Detailed microphysics modeling of the intense precipitation episode IOP7a observed during HYMEX experiment : study of the impact of pollution

Christina Kagkara

UNIVERSITE CLERMONT AUVERGNE
ECOLE DOCTORALE DES SCIENCES FONDAMENTALES

THÈSE

présentée pour obtenir le grade de

DOCTEUR D'UNIVERSITÉ

Spécialité : Météorologie, Océanographie, Physique de l'Environnement

Par **KAGKARA Christina**

Diplômée du Master Physique spécialité Sciences de l'Atmosphère et Environnement

---

Modélisation microphysique détaillée de l'épisode de précipitation intense IOP7a observé lors de l'expérience HYMEX : Etude de l'impact de la pollution

---

Soutenue publiquement le 13 février 2019, devant la commission d'examen.

Président du jury

Joël VAN BAELEN	Directeur de Recherche CNRS, LaMP, Clermont-Ferrand

Rapporteurs

Brice BOUDEVILLAIN	Physicien adjoint CNAP HDR, IGE, Grenoble
Nikos HATZIANASTASSIOU	Professeur Associé, UoI, Ioannina, Grèce
Evelyne RICHARD	Directrice de Recherche CNRS, LA, Toulouse

Directeurs de thèse

Andrea FLOSSMANN	Professeur, UCA, LaMP, Clermont-Ferrand
Céline PLANCHE	Maître de conférences, UCA, LaMP, Clermont-Ferrand

UNIVERSITY CLERMONT AUVERGNE
DOCTORAL SCHOOL OF FUNDAMENTAL SCIENCES

PhD. THESIS

presented to obtain the degree of

DOCTOR OF UNIVERSITY

Specialty: Meteorology, Oceanography, Physics of the Environment

By **KAGKARA Christina**

Master's Degree in Physics specialty Atmospheric Sciences and Environment

---

Detailed microphysics modeling of the intense precipitation episode IOP7a observed during HYMEX experiment: Study of the impact of pollution

---

Defended the 13th February 2019

President of the committee

Joël VAN BAELEN	Director CNRS, LaMP, Clermont-Ferrand

Reviewers

Brice BOUDEVILLAIN	Associate Physicist, IGE, Grenoble
Nikos HATZIANASTASSIOU	Associate Professor, UoI, Ioannina, Greece
Evelyne RICHARD	Director CNRS, LA, Toulouse

PhD Supervisors

Andrea FLOSSMANN	Professor, UCA, LaMP, Clermont-Ferrand
Céline PLANCHE	Associate Professor, UCA, LaMP, Clermont-Ferrand

Acknowledgements

Undertaking a PhD in a foreign country is not the easiest decision to take. When the trip to Clermont-Ferrand was finished, the real journey was begun for me. By reaching my destination, I assure that a PhD is a life-changing experience.

I have now the pleasure to express my sincere gratitude to my thesis supervisor Andrea Flossmann for providing me the opportunity to work on the topics of my interest: cloud microphysics and precipitation. I truly appreciate her trust on my ability to undertake this PhD, her contributions of time, her patience and advice. Her guidance and scientific knowledge were crucial for the successful progress of my thesis. I gratefully acknowledge the funding that I received towards my PhD from the ANR MUSIC project. I would also like to express my special appreciation to my co-supervisor Céline Planche. She introduced me to the large and complex DESCAM-3D model and she helped me to get familiar with its use. I always enjoyed our regular meetings and inspiring discussions and I am grateful for the scientific knowledge, motivation and useful advice for the writing of my thesis. I am also indebted to Wolfram Wobrock for his critical contribution on the realization of the present thesis. I also thank him for his constant interest and support throughout the whole duration of my PhD.

I would like to thank the director of LaMP, Joël Van Baelen, for his support since my arrival in the laboratory and for being the president and examiner of my dissertation committee. To continue with the reviewers of my thesis, I am thankful to Brice Boudevillain for the support and advice about observations data of precipitation, but also for his crucial remarks and comments. I am also grateful to Evelyne Richard for her interest and for the valuable feedback that she provided on my thesis through insightful questions and useful comments.

Profound gratitude goes to Nikos Hatzianastassiou, who first had the idea to send me to LaMP for a 2-month placement via the Erasmus program at the end of my Master's degree and for his encouragement in my decision to undertake this PhD. I am thankful for his constant interest and for being one of my thesis reviewers. I also thank him for his remarks and questions.

I would like to express my appreciation to Clémence Rose for sharing her knowledge and methods on the analysis of aerosol particle measurements and for contributing on the present work. It was also a pleasure to collaborate with Sandra Banson on the analysis of ground-based HYMEX observations. She was always available to provide me the information and help that I needed. I am also thankful to Frédéric Tridon for sharing his knowledge on the technical details of the MRR instruments and for his useful advice on the analysis of their observations. Many thanks to Jimmy Zwiebel, as well, for providing me HYMEX data in the beginning of my thesis and for his useful and clear explanations. A sincere "thank you" to Thibault Hiron for sharing his knowledge about the DESCAM code and for the advice and support. Finally, I am thankful to Evelyn Freney for her responses to my questions, to Aurélie Colomb for giving me the opportunity to participate at the "fête de la science", as well as to Nadège Montoux for her advice about my final presentation.

I would like to say also a big “thank you” to the lab mates that helped me to deal with the administrative stuff that were needed in order to be registered/installed at the university/laboratory, but also in Clermont-Ferrand. I express my deep appreciation to Florence who, as the secretary of the LaMP until 2018, she always kindly helped me with every issue. I am equally grateful to Françoise and Catherine for their kindness and availability to provide their help, as well as to Edouard for his support with informatics issues. Many thanks to Flora, for helping me to find my first apartment and to Mickael for kindly offering me his help in order to get installed in Clermont-Ferrand.

I couldn’t forget to include in this text my office mates and lunch-mates, who made this procedure more pleasant with their company, soirées, randonées, courses à pied, slackline, and so many. In alphabetical order: thanks to Alexandre, Alexis, Anaïs, Angelica, Antoine, Aurèlien, Brice, Danni, Gwennolé, Hélène, Ibrahim, Jimmy, Kevin, Maija, Manon, Miao, Pamela, Pièrre and Thibault. Of course, I cannot exclude the LPC team: Alex, Anne, Boris, Cédric, Florian, Guillaume and Mark. My thoughts are also with Alaa, Alessia, Arianne, Bayetoulaye, Maher, Matilde, Mylène and Yannick. Many thanks to the “Greek team” of Clermont-Ferrand: Maria, Myrto, Niki, Rhea and Vasiliki, who made me feel like home, as well as to my friends from Greece: Amalia, Artemis, Chryssoula and Marialena.

This dissertation could not have been undertaken without the love, patience, and endless support of my family. My deepest “thank you” goes to my parents who encouraged me all over the difficult way that I chose, for waiting for more than one year to see me and for finally making the trip to France to celebrate the end of my PhD. Special thanks to my family “in-law”, as well, for their love and support during the last year of my thesis.

Enfin, un très grand merci à mon Arthur pour son soutien et son calme pendant les moments durs, aussi que pour un amour qui durera.

~ To my parents

~ Στους γονείς μου

Contents

1 Introduction

The Mediterranean region consists of an almost closed maritime basin which is surrounded by coastlines with a varied relief. Situated between three continents and connected with the Atlantic Ocean and the Black Sea, it is a region of great meteorological interest. Exchanges of energy between sea and land results in the development of various weather phenomena which are often intense. Some of these phenomena are severe rainfall events and are caused by atmospheric processes at different scales. Local convection, mesoscale convective systems and upper synoptic-scale-level troughs are some of the principal factors that induce severe rainfall episodes in this region (Dayan et al. 2015). The South of France, with a large coastline in the Mediterranean Sea and various topographical characteristics (e.g. Massif Central and Alps) is also influenced by heavy rainfall events, especially in autumn. The Cévennes-Vivarais region, which is part of the Massif Central, is affected by this kind of rain episodes, which are known as “Cévenols”. These episodes can induce natural disasters, such as flash floods in the numerous rivers of this area and landslides, with important economic consequences and even life losses (Llasat et al. 2013). In a changing climate with a confirmed global warming of at least 1.5°C (IPCC 2018), the frequency of such meteorological events may increase in the future. Therefore, the forecasts of such events have to be accurate spatially and timely.

Prediction of intense rainfall events by Numerical Weather Prediction (NWP) models has been greatly improved during the last years (Sun et al. 2014; Sokol et al. 2016; Brousseau et al. 2016; Simonin et al. 2017). However, uncertainties are still present, particular regarding the strength of such episodes. One of the issues regarding the reduction of forecast errors of precipitation is the improvement of microphysical

parameterizations in NWP models. In this context, the project MUSIC (MUltiscale process Studies of Intense Convective precipitation events in Mediterranean) was financed by the National Research Agency of France (ANR, French acronym). ANR MUSIC aims to improve the knowledge and the modelling of intense precipitation events in the Mediterranean region. The ANR MUSIC is relying on HYMEX (HYdrological cycle in the Mediterranean EXperiment). HYMEX (Drobinski et al. 2014) was an international program launched in 2007, dedicated to the water cycle and its related processes in the Mediterranean. The HYMEX experiment provided a large observation dataset from various instruments recording heavy precipitation events (HPE). LaMP (Laboratoire de Météorologie Physique) participated in HYMEX and is one of the partners of the ANR MUSIC. The objective of this thesis is by exploiting the HYMEX dataset to provide a better understanding of microphysical processes that govern intense precipitation episodes and their interaction with atmospheric aerosol particles.

The cloud microphysical properties are influenced by the atmospheric aerosol particles. Indeed, aerosol particles are necessary for the formation of clouds via the heterogeneous droplet nucleation process and therefore, precipitation. Aerosol particles serving as cloud condensation nuclei (CCN) in supersaturated environment are activated in order to nucleate cloud droplets. Different number of aerosol particles in the atmosphere implies that different number of CCN can be activated. Thus, development and evolution of clouds can be altered and, consequently, aerosol particles can influence precipitation, too (Twomey 1977; Stevens and Feingold 2009). It has been reported in the literature that, in general, an increased aerosol particle concentration decreases precipitation (Teller and Levin (2006); Planche et al. 2010; Kogan et al. 2012), as well as the opposite (Guo et al. 2014). However, there are still uncertainties concerning the impact of aerosol particles on the precipitation (Khain 2009; Tao et al. 2012; Wall et al. 2013). The way that aerosol properties influence clouds and precipitation vary strongly among types of clouds which are mainly controlled by atmospheric dynamics and thermodynamics (Fan et al. 2016). Therefore, a question is raised: What is the role of the atmospheric aerosol particle concentration on heavy precipitation events? More precisely, how does the number of aerosol particles present in the atmosphere impact the cloud life time and the quantity, intensity and spatial distribution of precipitation? To answer this question, interactions between aerosols, cloud and precipitation need to be examined. However, generally precipitating clouds do not contain only liquid water, but also solid hydrometeors (e.g. ice crystals, graupel, and hail). The understanding of mechanisms concerning the ice phase in clouds is, consequently also important, as e.g. the nucleation of ice crystals. Thus, another question is about the impact of aerosol particle concentration on the ice content of the cloud and the associated precipitation.

Modeling of cloud microphysics is a way to address these questions because it permits to simulate the general atmospheric features in order to study the impact of the aerosol concentration on both the liquid and the ice phase of the clouds and their precipitation. However, NWP models use parameterizations to represent cloud microphysics. Only specific cloud models consider the aerosol concentration in order to simulate the evolution of clouds and precipitation. One of these models, the so-called "bin-resolved cloud models" is the DESCAM-3D (Flossmann and Wobrock; 2010). The present study focuses on the investigation of: (i) the importance of different concentration of aerosol particles on the formation and evolution of an intense precipitating convective cloud system and (ii) the role of pollution (high aerosol particle concentration) on the ice phase of such a cloud system. For this purpose, HYMEX observations were compared with results from a cloud model with detailed microphysics, DESCAM-3D. The special characteristic of the selected precipitation episode, the IOP7a, is the presence of pollution in the atmosphere. This characteristic allows to perform model sensitivity studies with different concentration of aerosol particles and investigate its role on heavy precipitation.

The present thesis is organized in five chapters. The first one (chapter 2) introduces cloud modeling at different atmospheric scales, as well as representation of microphysics in various cloud models from the literature. A complete description of the DESCAM-3D model is included at the end of this chapter. Chapter 3 presents and describes the intense precipitation event selected for this study, the HYMEX IOP7a, and the observations that took place during this event. Simulation of IOP7a with DESCAM-3D is detailed in Chapter 4. In this chapter, model results are evaluated by being compared to HYMEX observations from various instruments. Finally, Chapter 5 presents the sensitivity study of the impact of pollution on the precipitation and on the solid and liquid phase of the cloud system. General conclusions and perspectives are presented at the end of this dissertation.

2 Numerical modeling of clouds and precipitation

The need to understand and predict phenomena that take place in the Earth's atmosphere lead to the construction of numerical models which simulate physical, chemical, dynamical and radiative atmospheric processes. These processes are represented by a full set of equations that describe the atmospheric properties and whose integration is performed by numerical computing techniques. The categorization of the atmospherical models depends on their objective and consequently, the processes that they focus on (e.g. radiative, microphysical), the technical representation of the atmospheric motion (Eulerian or Lagrangian models), the assumptions that they make (e.g. barotropic, thermotropic, (non-)hydrostatic) and their resolution (e.g. global or regional models).

The complexity of the atmospherical processes and/or their immensely fine scales introduces additional difficulties in their physical representation in models. For this reason, such processes are often replaced by simplified concepts in the context of methods called "parameterizations". Different parameterizations interact with each other and can notably influence the model simulations and forecasts. During the last 50 years, remarkable efforts have been made for the development and the improvement of atmospherical models concerning their spatial resolution, numerical techniques, as well as parameterizations for various atmospheric processes.

This chapter is dedicated to the state-of-the-art of cloud modeling and the presentation of the model that is used for this thesis. First, an overview of various cloud models at different scales is presented and then, possible methods to represent cloud

dynamics and microphysics in models are discussed. Complex and still uncertain, the representation of the ice nucleation processes in the different cloud models and schemes is addressed. Finally, a detailed description of the model which is used for the present study and its special features terminates this chapter.

2.1 Modeling of cloud dynamics at all scales

A cloud is a visible mass of liquid and/or solid hydrometeors suspended in the atmosphere. Clouds, which have different vertical and horizontal extensions according to the 29 existing species given in the World Meteorological Organization's (WMO) International Cloud Atlas[1] are a critical component for life on Earth. They control the equilibrium of energy of the Earth-atmosphere system by reflecting, absorbing and emitting parts of the shortwave (solar) and longwave (terrestrial) radiation. The Earth's climate is determined by exchanges of energy between the atmosphere, the oceans and the land which make up the hydrological cycle, where clouds are a major component. Also, several chemical reactions that take place in cloud hydrometeors influence air pollution (e.g. Iribarne and Cho 1989; Gong et al. 2011).

In order to simulate the formation and the evolution of a cloud, different model approaches are needed considering its temporal duration and its spatial extension. Moreover, depending on the studied atmospheric processes, the model time step is also adapted. When focusing on the formation of clouds, the time scale of the microphysical processes is on the order of magnitude of microseconds. On the contrary, the investigation of the impact of clouds on climate requires studies on a multiannual level. **Figure 2.1** summarizes the multi-scale approach of the different atmospheric phenomena. For example, climate variation and the El Niño Southern Oscillation (ENSO) phenomena take place on the largest time scales (> 10^8 s) and horizontal spatial scales (10^5 – 10^8 m), whereas the spatial scale of turbulent eddies varies from a few hundred meters to millimeters and they last only for some seconds or minutes. To address this issue, different types of cloud models were conceived and are described hereafter. However, it is important to note that covering the entire Earth's atmosphere at every scale in space and time is impossible.

[1] https://cloudatlas.wmo.int/home.html

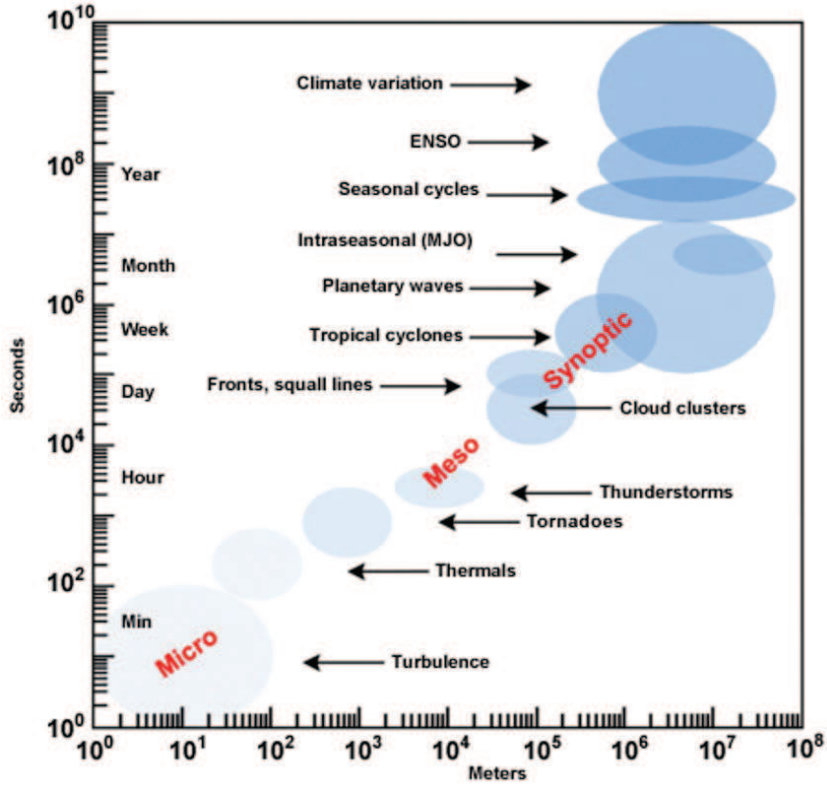

Figure 2.1: The different scales (micro, meso and synoptic) of atmospheric processes. The various atmospheric phenomena are presented as a function of their temporal duration and spatial extension (source[2]: The COMET® program, UCAR).

The configuration of cloud models varies depending on the study objectives. The most simplified one, the air parcel (or 0-D) considers an adiabatic and homogeneous volume of air in free convection (Monier et al. 2006). This kind of dynamics permits to explicitly study the evolving microphysics. A 1-D dynamics framework is based on the concept of a cylindrical model which consists e.g. of two concentric cylinders: one that represents the convective cell (inner), where the microphysical processes are simulated, and the second (outer) that represents the surrounding compensating downdraft region. Sensitivity studies for microphysics schemes can be performed by using a 1-D dynamics framework (Asai and Kasahara 1967). A 2-D dynamics framework consider two dimensions (i.e. x and z) and they are mainly used for studies of 2-D flow fields e.g. a topography influence (Jung et al. 2015). Finally, the 3-D dynamics framework permits the most complete simulation of the atmospheric phenomena, by considering the 3 spatial coordinates with the vertical one following the topography, as well as the curvature of the Earth and Coriolis force.

[2] http:// kejian1.cmatc.cn/vod/comet/tropical/textbook_2nd_edition/navmenu.php_tab_2_page_8.1.0.htm

On the large-scale of atmospheric motion, the Atmospheric Global Circulation Models (AGCM) cover the entire Earth's atmosphere and are mainly used for climate change predictions. Some of them are coupled to Oceanic Global Circulation Models (OGCM), also known as "coupled atmosphere-ocean models" or "Atmosphere–Ocean General Circulation Models" (AOGCMs), such as the ARPEGE-Climate model (Action de Recherche Petite Echelle Grande Echelle, (Déqué and Piedelievre 1995; Gibelin and Déqué 2003) and the Hadley Centre Coupled Model version 3 (HadCM3, Gordon et al. 2000; Collins et al. 2001). Lately, the AOGCMs tend to be expanded to Earth System Models (ESM) which include representation of biogeochemical cycles such as those involved in the carbon cycle (IPCC 2018). Due to their coarse spatial resolutions (100 x 100 km^2), sub-grid processes in climate models (e.g. turbulence, radiation and microphysics) which require grid increments at fine scale (i.e. $\simeq$ 100 m) cannot be explicitly resolved on existing computers. Even if climate models are nowadays capable to simulate aerosol particle properties (mass, number, size distributions), such as in Liu et al. (2012) and quantify their effective radiative forcing (Grandey et al. 2018), important limitations remain for the treatment of aerosol-cloud interactions, processes that require parameterizations.

Numerical Weather Prediction (NWP) models simulate the synoptic and meso-scale atmospheric motions (see **Figure 2.1**). These models use current weather observations as initial conditions in order to produce weather forecasts. They often have the ability to focus on smaller regions inside the large model domain (nested domain configuration) with horizontal grids of fine resolution (1/3 to 1/5 smaller than the resolution of the large domain). Vertically the domains of NWP models are composed of staggered grids with fine resolution at least in the boundary layer, where the small-scale motions play important role for the simulations. The "frequency" of the simulations and the size of the needed domain depend on the type of the weather predictions. For example, short-range forecasts require horizontal spatial resolutions of 1 to 5 km and simulations performed every few hours, whereas to obtain long-range forecasts, resolutions of several dozens of kilometers are needed and the simulations are performed at a daily scale. NWP models use so-called cumulus parameterizations and/or bulk schemes in order to represent cloud and precipitation.

Some NWP models with global coverage are Integrated Forecasting Systems (IFS), ARPEGE integrated within the ARPEGE-IFS (Déqué et al. 1994) software, and Weather Research and Forecasting (WRF). There are also mesoscale NWP models such as the French Meso-NH (Mesoscale-Non Hydrostatic) and regional models such as the AROME (Applications of Research to Operations at Mesoscale, Seity et al. 2011) which are in

operational at Météo-France. Finally, another NWP model is the Clark-Hall (Clark 1977; Clark and Hall 1991) which is described in detail in **section 2.3.1**.

One of the most widely used mesoscale model for both research and operational purposes is the aforementioned WRF. According to Skamarock et al. (2008), WRF provides the ability to describe atmospheric properties using several physics schemes (i.e. about the atmospheric radiation, turbulence, cloud microphysics etc.). Another example of mesoscale model used for research purposes is Meso-NH (Lafore et al. 1998). It is a non-hydrostatic core mesoscale model which allows studies with horizontal resolutions from 10 m to 10 km.

Note that AROME-France was developed as a complement to ARPEGE and the Aire Limitée Adaptation Dynamique Développement International (ALADIN-France) model. Its physical parameterizations were extracted from the Meso-NH model. A version of the AROME model, namely AROME-WMED (West MEDiterranean sea, Fourrié et al. 2015), was developed in order to provide daily forecasts to the HYMEX operational center in order to decide for observation strategy. An analysis[3] was produced every 3 hours with a horizontal resolution of 2.5 km and once per day, at 00:00 UTC, AROME-WMED provided 48-h numerical weather predictions for HYMEX.

As already mentioned, the study of aerosol-cloud interactions requires an explicit treatment of the microphysical processes that occur mostly at sub-grid scales and timescales of minute to an hour. For this purpose, so-called “bulk” and “bin-resolved” models were developed. These models can describe interactions between liquid and solid hydrometeors. The use of bin-resolved models requires a lot of computing time and memory, especially when their dynamics are described in three dimensional fields. In the following section, these two different microphysical approaches are detailed.

2.2 The representation of microphysics in cloud models

Microphysics is a fundamental part of cloud modeling and critical factor in numerical weather prediction. In climate models, microphysics influence the radiative impact through the interactions between aerosols, clouds and radiation, whereas in NWP models microphysics determines the precipitation forecasts. The bin and bulk microphysics representations are discussed along with their use in different cloud models. This section also focuses on the representation of the aerosol-cloud interactions,

[3] The AROME-WMED outputs are available in the HYMEX database: http://mistrals.sedoo.fr/HyMeX

especially in the droplet nucleation and heterogeneous ice nucleation processes, in the various types of microphysics schemes.

2.2.1 "Bulk" and "bin" microphysics

Bulk and bin-resolved cloud models use different approaches for the simulation of the formation, growth and sedimentation of the hydrometeors. The choice between these approaches depends on the objective of each study.

2.2.1.1 Bulk microphysics

Bulk microphysics schemes predict moments of the size distribution for a number of categories of hydrometeors: cloud drops, rain drops, ice crystals... A so-called "particle size distribution" in an analytic form is considered for each category and therefore, one or more bulk quantities (cloud water, rain water, ice content...) are predicted using the moments of the corresponding particle size distribution. The determination of the moment *M* at the power of *i* of a particle size distribution *N(D)* is given in the equation 2.1, where *D* is the diameter of the hydrometeors.

$$M^i = \int_0^\infty D^i N(D) dD \qquad 2.1$$

Consequently, the 0th moment of size distribution (equation 2.2) corresponds to the total number concentration of the hydrometeors *N*, the 3rd moment (equation 2.3) is proportional to the liquid water content *LWC* and the 6th moment (equation 2.4) determines the radar reflectivity factor *Z*, usually called "reflectivity".

$$N = \int_0^\infty N(D) dD \qquad 2.2$$

$$LWC = \int_0^\infty \frac{4}{3} \pi \rho_w \frac{D^3}{2} N(D) dD \qquad 2.3$$

$$Z = \int_0^\infty D^6 N(D) dD \qquad 2.4$$

These moments are commonly used in bulk schemes but other moments can be calculated, i.e. Milbrandt and McTaggart-Cowan (2010). According to the number of moments simulated, different bulk schemes with different complexity exist. There are one-moment (or single-moment) schemes which provide information only about the

mass mixing ratio of some hydrometeor species by calculating only the 3rd moment of the size distribution, (e.g. Kessler 1969). Two-moment schemes provide information about both the mass mixing ratio and the number concentration of hydrometeors (0^{th} and 3^{rd} moment of the size distribution), as in Cohard and Pinty (2000), Morrison et al. 2008, Lim and Hong (2009), Saleeby and Van Den Heever (2013). Also, three-moment schemes give in addition the radar reflectivity factor (6^{th} moment of the size distribution), as in Milbrandt and Yau (2005). Other schemes, as i.e. the Thompson et al. (2008) scheme, use a single-moment microphysics representation with the exception of the cloud ice and rain variables that are represented with two moments, so this scheme predicts the mixing ratios of cloud water, rain, cloud ice, snow and graupel, as well as the number concentration of rain and cloud ice. The majority of bulk schemes use a gamma distribution in order to represent the hydrometeor size distribution presented in the equation 2.5:

$$N(D) = N_0 D^{\mu} e^{-\lambda D} \qquad 2.5$$

where N_0 is the distribution intercept, μ is the shape parameter and λ is the slope parameter. In the bulk schemes (one or two moments), the gamma distribution is often used for cloud drops whereas the precipitating particles are represented thanks to an exponential distribution, i.e., $\mu = 0$ in equation 2.5, as for example in Morrison et al. (2008). Nevertheless, an assumption can be used, as in Kessler (1969), where the cloud droplets are represented with a monodisperse distribution whereas the rain drops are represented with an exponential distribution (Marshall and Palmer 1948).

Considering the computational efficiency of bulk microphysics schemes due to the small number of prognostic variables that they contain, they are widely used in NWP models (meso-scale and large-scale), even in climate models (in simplified versions); limitations remain, though. For example, the process of drop-breakup is still unclear, as well as the diffusional growth of the liquid water, which is associated with the evaporative cooling rates. Uncertainties are also found in the number and type of the classes for the solid hydrometeors which can affect the accuracy of the simulation of convective precipitation systems. Moreover, most bulk schemes do not focus on the aerosol-cloud interactions. In this framework, during the last decade, few improvements were done, as e.g. in the scheme of Thompson and Eidhammer (2014), where the activation of aerosol particles as cloud condensation nuclei (CCN) and ice nuclei (IN) have been incorporated thanks to the prediction of the number concentration of cloud droplets and two aerosol variables (one for CCN and one for IN). The "removal" of CCN from the aerosol reservoir has been considered in the two-moment parameterization of Kogan (2012) and in Lebo and

Morrison (2013). Also, efforts on the development of "multimodal" schemes have been done, as e.g. in the quasi double-moment aerosol microphysical scheme LIMA[4] (Liquid, Ice, Multiple Aerosols, Vié et al. 2016). More details about the representation of the aerosol-cloud interactions in cloud models are available in the next section.

2.2.1.2 Bin-resolved microphysics

Bin-resolved microphysics approach (or size-resolving microphysics) describes in detail the evolution of the hydrometeors and the microstructure of the cloud that is important for the studies of convective precipitation systems. All the microphysical processes that take place during the cloud lifetime (i.e. CCN activation, droplet and ice crystal formation, particle growth, collision-coalescence, sedimentation…) are taken into account in this kind of approach. The aerosol-cloud interactions are often described by considering the aerosol budget, as well as the transport and sink of the aerosol particles of different sizes.

Both the aerosol particles and the hydrometeors are divided into size categories (so-called bins) where the evolution of each information in a bin is calculated separately. The number of size bins is either fixed or with varied boundaries, but is always high, with in a range from some dozens up to hundreds of bins. The predicted variables represent distributions for each considered hydrometeor, thus the use of bin approaches require very high computing memory and huge computation time; consequently their operational use is prohibitive. To compare with the bulk schemes, bin approaches require more computer time, depending on the complexity of the different bulk schemes. However, a bin approach provides the most realistic microphysical representation and the maximum possible information about all the processes that take place, such as the growth and the terminal velocities of the hydrometeors.

Bin approach is used in, e.g., the Hebrew University Cloud Model (HUCM, Khain et al. 2004, 2010) that was first coupled to the fifth-generation Pennsylvania State University–NCAR Mesoscale Model (MM5), a precursor to WRF (Lynn et al. 2005). HUCM predicts size distributions for eight types of hydrometeors (drops, freezing drops, graupel, hail, three types of ice crystals and snow). Also, bin microphysics is used in DESCAM (DEtailed SCAvenging Model, Leroy et al. 2007; Flossmann and Wobrock (2010); Planche et al. 2014) that is used for the present thesis, coupled to the Clark-Hall model (Clark and Hall 1991) and is described in detail in **section 2.3**.

[4] LIMA is derived from the ICE3 scheme (Pinty and Jabouille (1998); Caniaux et al., 1994) and it is the most recently developed scheme that is used in Meso-NH.

Finally, to achieve the accuracy of a bin approach with the efficiency of a bulk scheme, a « mixed » approach has been proposed. So-called hybrid schemes use a combination of bulk parameterizations and bin approach. For instance, Onishi and Takahashi (2011) developed a bin–bulk hybrid cloud microphysical model which they implemented in the atmospheric component of the Multi-Scale Simulator for the Geo-environment (MSSG-A, Baba et al. 2010). In this hybrid model, warm microphysical processes are described by a bin approach, whereas a bulk parameterization describe cold microphysical processes. However, hybrid schemes have still too high computational cost to be used in NWP models.

2.2.2 The representation of aerosol – cloud interactions in cloud models

When investigating the interactions between aerosols, cloud and precipitation, the aerosol particle properties such as the total number and their size must be taken into account in the model. The reason for this is the influence of the aerosol budget on the cloud microstructure and macrostructure and thus, the cloud lifetime and precipitation through various ways (Twomey 1974; Albrecht 1989). Twomey (1977) has also pointed out that an increase of CCN (which implies increase of the initial aerosol particle concentration) in shallow and warm clouds leads to the formation of more numerous but smaller cloud droplets, assuming that the liquid water content of the cloud remains constant. Activation of CCN and cloud droplet nucleation have been described by Köhler (1936), whose theory is fundamental for aerosol-cloud interactions and has been widely used in cloud models (see also Pruppacher and Klett 1997). However, a precise representation of the aerosol – cloud interactions, through the CCN activation process, is not always feasible in cloud models. Hereafter in this section, the way that the aerosol – cloud interactions are described in some different bulk and bin approaches is discussed.

The bulk scheme of Thompson and Eidhammer (2014) incorporates the activation of aerosol particles as cloud condensation (CCN) and ice nuclei (IN) so that the number concentration of cloud droplets, as well as the number concentrations of two aerosol variables (one each for CCN and IN) can be predicted. It includes a cloud droplet nucleation from an explicit aerosol number concentration[5] and it uses a lookup table of CCN activation fractions determined by the predictions of a parcel model (Feingold and

[5] The aerosol number concentrations are derived from multiyear global model simulations (Colarco et al. 2010) in which particles are sulfates, sea salts, organic carbon, dust, and black carbon. A simplified aerosol treatment considers dust as hydrophobic ice-nucleating particles, whereas other species besides black carbon are combined as an internally mixed hydrophilic cloud droplet-nucleating particles.

Heymsfield 1992) for temperature, vertical velocity and number of aerosols. A predetermined hygroscopicity parameter (Petters and Kreidenweis 2007) is also included, as well as a mean aerosol radius, which is equal to 0.04 μm. The lookup table was created by an explicit treatment of the Köhler activation theory. Thus, the CCN activation takes place at the cloud base and anywhere inside the cloud where the corresponding value of the lookup table is greater than the existing droplet concentration and for a minimum upward velocity of 1 cm s^{-1}. In two-moment schemes the prediction of the number concentration of cloud droplets is based on the Köhler theory, whereas the population of activated CCN is assumed to be single-mode and spatially homogeneous. Nevertheless, in the LIMA scheme, the process of cloud droplet activation is based on a prognostic multimodal, heterogeneous aerosol population represented by the superimposition of several aerosol modes (each mode is designed by its chemical composition and its ability to act either as CCN or as IN depending on solubility (as in (Thompson and Eidhammer 2014). The parameterization of the CCN activation is based on Cohard et al. (1998) extended to a multimodal population of CCN. This parameterization is based on an approximation for the maximum ambient supersaturation and on an extension of Twomey's law (Twomey 1977). Vié et al. (2016) presents further computations leading to a formula for the modeling of the CCN activation of multimodal aerosol particle spectra.

In the bin microphysics cloud model HUCM (Khain et al. 2004, 2009), the size distribution function f_k of the k^{th} mass category is given by the equation 2.6:

$$\frac{\partial f_k}{\partial t}+\frac{\partial u f_k}{\partial x}+\frac{\partial (w-V_{tk}) f_k}{\partial z} = \left(\frac{\partial f_k}{\partial t}\right)_{nucl}+\left(\frac{\partial f_k}{\partial t}\right)_{\underline{\underline{c}}}+\left(\frac{\partial f_k}{\partial t}\right)_{\underline{\underline{d}}}+\left(\frac{\partial f_k}{\partial t}\right)_{col}+\left(\frac{\partial f_k}{\partial t}\right)_{\underline{\underline{f}}}+\left(\frac{\partial f_k}{\partial t}\right)_{break} \quad 2.6$$

where V_{tk} is the terminal velocity of hydrometeors belonging to the k^{th} mass bin and u, w represent the horizontal and vertical component of V_{tk}. Nucleation (*nucl*), condensation/evaporation (*c/e*), deposition/sublimation (*d/s*) of ice particles, collisions (*col*), freezing/melting (*f/m*), and breakup (*break*) of drops are considered on the right-hand side of the equation 2.6.

The empirical power low of Twomey (1977) given by the equation 2.7 links the total number of the activated CCN (N_{CCN}) to the supersaturation with respect to water, S_w, is being used.

$$N_{CCN} = C S_w^k \quad 2.7$$

In this equation, k and C are observed constants, as a function of the air mass. S_w is calculated at each time step at all grid points and is used for the calculation of the critical CCN radii according to the Köhler theory. CCNs whose radii exceed the critical value are activated.

2.2.3 The representation of the heterogeneous ice nucleation

The ice phase and its related processes for the formation of clouds and precipitation are still not clear in the scientific community, especially regarding ice nucleation. According to the new terminology proposed by Vali (2015), the ice nucleation occurs when an *embryo*, *a thermodynamically unstable aggregate of water molecules in a structure that favors further development into stable ice,* which is larger than the critical[6] size, is found in an environment of supersaturated vapor or supercooled water; respectively, either deposition nucleation or freezing nucleation takes place.

Note that *ice nucleation without any foreign substance that aids the process* is called homogeneous. It is the spontaneous freezing of super-cooled droplets or aqueous solutions that takes place at temperatures colder than -35 °C (more details in Monier 2003).

The *ice nucleation aided by the presence of a foreign substance so that nucleation takes place at lesser supersaturation or super-cooling than is required for homogeneous ice nucleation* is called heterogeneous. Always according to Vali (2015), there are two main modes of the heterogeneous ice nucleation: deposition nucleation and freezing nucleation. Deposition is the case of ice nucleation from supersaturated vapor on an ice nucleating particle (INP) without the existence of liquid, whereas ice nucleation in a body of supercooled liquid ascribed to the presence of an INP (or equivalent[7]) is called freezing. The main modes of heterogeneous freezing nucleation are the immersion, contact and condensation freezing. At the same time, evidence of further heterogeneous ice freezing modes, such as evaporation and collision freezing, has been reported. **Figure 2.2** summarizes the different modes of the heterogeneous ice nucleation, as explained above.

[6] *"The size at which the probability of growth of an embryo becomes equal to the probability of decay"* (Vali, 2015).
[7] "*Ice nucleating molecule (INM), entity (INE), material, substance, object, item, unit or other, assumed to be the agent responsible for heterogeneous ice nucleation"* (Vali 2015).

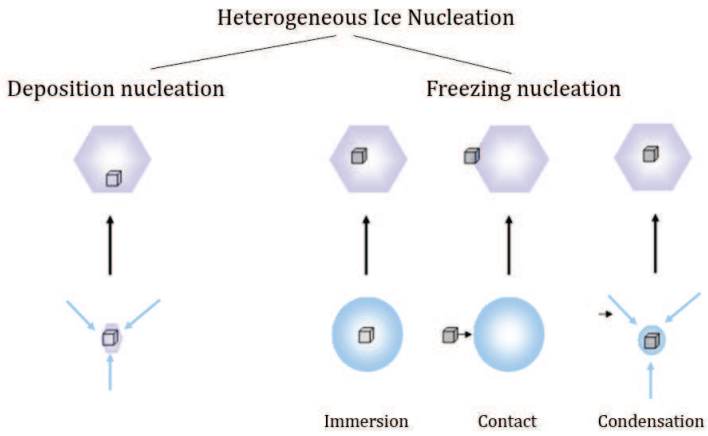

Figure 2.2: Schematic representation of the different modes of heterogeneous ice nucleation (Seifert et. al 2009).

The various microphysics approaches in cloud models use specific parameterizations that express these ice nucleation processes. Considering the complexity of representing the heterogeneous ice nucleation, as well as the fact that homogeneous freezing is more important at very cold temperatures, the focus in this section is given to heterogeneous ice formation.

Heterogeneous ice nucleation is considered in various microphysics schemes as e.g. in the approach of Lin et al. (1983). In this scheme, each precipitating hydrometeor species (i.e. rain, snow and hail) is assumed to follow an exponential size distribution ($\mu = 0$ in the equation 2.5). In this approach, the size distribution for small ice crystals is assumed to be monodisperse, which means that all ice crystals have the same mass. The collision-freezing mechanism that is responsible for graupel and hail formation follows Bigg (1953), with a probabilistic freezing of rain. The single-moment microphysics scheme ICE3 (Caniaux et al. 1994; Pinty and Jabouille 1998) is also based in this approach to represent heterogeneous ice nucleation. The ICE3 has been deployed in AROME, AROME-WMED and Meso-NH models.

The most commonly used parameterization for heterogeneous ice nucleation (for condensation freezing and deposition nucleation) in both bulk and bin approaches is from Meyers et al. (1992), where the number of pristine ice crystals n_{id} is a function of the ice saturation ratio, S_i (equation 2.8):

$$n_{id} = exp\{-0.639 + 0.1296[100(S_i - 1)]\} \qquad 2.8$$

Also, according to Meyers et al. (1992), the number of IN that result from immersion and contact freezing are of the same order. However, contact freezing is supposed to be less efficient than immersion freezing because of the small magnitude of the collision efficiency. As an example, in the bulk scheme of Thompson et al. (2004), (deployed in WRF), the Meyers et al. (1992) parameterization is being also used along with the measurement-based formula of Cooper (1986) which calculates the number of ice crystals that are formed due to deposition nucleation and condensation freezing (equation 2.9).

$$n_{Cooper} = 0.005exp[0.304(T_0 - T)] \quad 2.9$$

where T_0=273.15 K and T is the ambient temperature (in K). The same parameterizations are included in (Thompson and Eidhammer 2014).

The Meyers et al. (1992) approximation for the IN activation is also used in the HUCM microphysics scheme (Khain et al. 2010; Ilotoviz and Khain 2016) that was implemented in WRF.

The empirical heterogeneous ice nucleation parameterization of Phillips et al. (2008), that was revised in Phillips et al. (2013) is used in LIMA. The formulas of this parameterization take into account the saturation ratio of water vapor with respect to ice, which is a function of the ambient temperature.

The different modes of the heterogeneous ice nucleation are explicitly treated in Hiron and Flossmann (2015) for DESCAM with a 1D1/2 dynamics. They use Meyers et al. (1992) to represent deposition nucleation, condensation freezing and contact freezing. For the immersion freezing, the dependence of the drop freezing process on the drop volume proposed by Bigg (1953) was considered. Hiron and Flossmann (2015) find that deposition nucleation and contact freezing play a negligible role with respect to the other ice-nucleating mechanisms, while homogeneous freezing shows similar qualitative behavior than classical immersion freezing.

In the next section, the DESCAM bin microphysics scheme coupled with a 3D dynamics will be described. This numerical model is the main tool used in the present work.

2.3 The DESCAM-3D model

Precipitation mechanisms are better understood if the microphysical and dynamical processes are examined in a coupled system (Rogers and Yau 1989). The simulation tool for the present study is the DESCAM-3D model which is composed by the detailed microphysics scheme DESCAM coupled to the 3D dynamic model of Clark and Hall (1991). In the following sections, before the complete description of the bin microphysics of DESCAM, the governing equations and specific scheme characteristics of the dynamic model is detailed.

2.3.1 The dynamic model

The non-hydrostatic three-dimensional cloud physics model of Clark and Hall (Clark 1977, 1979; Clark and Farley 1984; Clark and Hall 1991) is deployed as the dynamical framework of the DESCAM-3D module. Since the beginning of its development in 1974, the dynamical model of Clark and Hall has been improved and used in several research projects (Leroy et al. 2009; Planche et al. 2010).

In the present dynamical framework, the atmosphere is not considered to be in hydrostatic equilibrium; therefore the vertical acceleration of the atmospheric air is taken into consideration. Moreover, according to the anelastic approximation, the air density is assumed to be horizontally homogeneous which permits to eliminate acoustic waves, thus very small time steps for explicit numerical integration can be avoided. A terrain-following coordinate system is being used for the equations to be solved in a domain that has an irregular lower boundary.

Indeed, in order to follow the topography and treat irregular surface terrain features, the model equations are transformed into non-orthogonal coordinates through the equation 2.10:

$$\bar{z} = \frac{(z - h(x,y))H}{H - h(x,y)} \qquad 2.10$$

where h is the height above ground (i.e. the topography) and H is the height of the model's integration domain, which is constant (i.e., upper and lower boundaries).

Focusing on specific regions is achieved through the use of nested domain configuration, so as to obtain higher spatial resolution with computational efficiency (Clark and Hall 1991). Finally, operational NWP model outputs, such as those from the IFS by the ECMWF

(European Centre for Medium-Range Weather Forecasts) can be imported and used for the large-scale initialization of the model (Clark et al. 1996).

The evolution of the air's potential temperature θ, the atmospheric pressure P, the air density ρ, the air absolute temperature T and the water vapor mixing ratio q_v is being predicted by the model. The aforementioned thermodynamic variables are represented by the equations 2.11 to 2.15, that are in perturbation form and written in Cartesian coordinates:

$$\theta = \underbrace{\bar{\theta}(z)}_{TERM\ I} + \underbrace{\theta'(z)}_{TERM\ II} + \underbrace{\theta''(x,y,z,t)}_{TERM\ III} \quad 2.11$$

$$P = \underbrace{\bar{P}(z)}_{TERM\ I} + \underbrace{P'(z)}_{TERM\ II} + \underbrace{P''(x,y,z,t)}_{TERM\ III} \quad 2.12$$

$$\rho = \underbrace{\bar{\rho}(z)}_{TERM\ I} + \underbrace{\rho'(z)}_{TERM\ II} + \underbrace{\rho''(x,y,z,t)}_{TERM\ III} \quad 2.13$$

$$T = \underbrace{\bar{T}(z)}_{TERM\ I} + \underbrace{T'(z)}_{TERM\ II} + \underbrace{T''(x,y,z,t)}_{TERM\ III} \quad 2.14$$

$$q_v = \underbrace{\overline{q_v}(z)}_{TERM\ I} + \underbrace{q_v'(z)}_{TERM\ II} + \underbrace{q_v''(x,y,z,t)}_{TERM\ III} \quad 2.15$$

In the equations 2.11 to 2.15, terms I represent dry adiabatic atmospheric conditions, terms II represent the difference between the actual hydrostatically balanced environmental sounding and the isentropic sounding (constantly stable atmosphere) and terms III constitute those terms that evolve with time.

The momentum equation is defined as in the equation 2.16, where $\vec{\boldsymbol{V}}$ is the three-dimensional vector of the wind, $\vec{\boldsymbol{\Omega}}$ is the Earth's angular rotation vector and $\overline{\boldsymbol{\tau_{ij}}}$ is the stress tensor due to subgrid-scale turbulence processes that is determined by the equation 2.17 (Smagorinsky 1963). Also, $\vec{\boldsymbol{k}}$ is the vertical unit vector, K_M is the eddy mixing coefficient and γ expresses the fraction of the air's specific heat at constant pressure to the air's specific heat at constant volume ($\gamma = {}^{c_p}/_{c_v}$).

$$\bar{\rho}\frac{d\vec{\boldsymbol{V}}}{dt} + 2\bar{\rho}\vec{\boldsymbol{\Omega}} \times \vec{\boldsymbol{V}} = -\boldsymbol{\nabla}p' + \vec{\boldsymbol{k}}\bar{\rho}g\left(\frac{\theta'}{\bar{\theta}} - \frac{p'}{\gamma\bar{p}}\right) + \nabla \cdot \bar{\bar{\tau}} \quad 2.16$$

$$\overline{\boldsymbol{\tau_{ij}}} = \bar{\rho}K_M\left(\frac{\partial v_i}{\partial x_j} + \frac{\partial v_j}{\partial x_i} - \frac{2}{3}\delta_{ij}\frac{\partial v_k}{\partial x_k}\right) \quad 2.17$$

The continuity equation is defined in the equation 2.18:

$$\frac{\partial}{\partial x_i}\bar{\rho}u_i = 0 \quad 2.18$$

where $\vec{V}(u_i, u_j, u_k)$ is the wind.

Finally, the conservation of energy and water vapor is expressed in 2.19:

$$\frac{\partial}{\partial t}\bar{\rho}\theta + \frac{\partial}{\partial x_j}(\rho\overline{u_j} \cdot \theta) = \frac{L}{C_p\bar{T}}\frac{\delta M}{\delta T} + \frac{\partial}{\partial x_j}\left(\bar{\rho}K_m\frac{\partial q_v}{\partial x_j}\right)$$

$$\frac{\partial}{\partial t}\bar{\rho}q_v + \frac{\partial}{\partial x_j}(\rho\overline{u_j} \cdot q_v) = -\frac{\delta M}{\delta T} + \frac{\partial}{\partial x_j}\left(\bar{\rho}K_m\frac{\partial q_v}{\partial x_j}\right) \quad 2.19$$

Where the term $\frac{\delta M}{\delta T}$ corresponds to the mass of water vapor (ρq_v) that condenses, per unit of time, and L is the latent heat.

Different microphysics schemes can be coupled to this dynamic model, i.e. bulk scheme as in Planche et al. (2013) and Labbouz et al. (2013) or bin schemes as the DESCAM module which is described hereafter.

2.3.2 The detailed microphysics cloud model DESCAM

The microphysical aspect in cloud lifetime is described by the DEtailed SCAvenging Model (Flossmann et al. 1985; Leroy et al. 2007, 2009; Flossmann and Wobrock 2010; Planche et al. 2014) which is a bin microphysics scheme that uses logarithmic grids for aerosol particles, drops and ice crystals. During the past 30 years, DESCAM has been used for several research studies in combination with models of various dynamics (i.e. 1D, 2D, 3D).

DESCAM considers different distribution functions for the warm and cold phase of the cloud which are discretized in 39 bins (classes) and follow the information about aerosols and hydrometeors with equivalent radii in the size ranges of 1 nm - 7μm and 1 μm - 12 mm respectively. The size range that was defined for the aerosols corresponds to Aitken, accumulation and coarse mode, whereas the selected size range for the hydrometeors corresponds to the most common sizes of hydrometeors in the atmosphere. The aerosol particles and the hydrometeors have 18 bins in common between 1 μm and 7 μm.

The temporal evolution of the number density distribution function of droplets $f_d(m)$ and the distribution function of the aerosol particle mass inside droplets $g_{APd}(m)$ are described by the equations 2.20 and 2.21 respectively:

$$\frac{\partial f_d(m)}{\partial t} = \underbrace{\frac{\partial f_d(m)}{\partial t}\Big|_{dyn}}_{TERM\ I} + \underbrace{\frac{\partial f_d(m)}{\partial t}\Big|_{\substack{act \\ desact}}}_{TERM\ II} + \underbrace{\frac{\partial f_d(m)}{\partial t}\Big|_{\substack{cond \\ eva}}}_{TERM\ III} + \underbrace{\frac{\partial f_d(m)}{\partial t}\Big|_{coal}}_{TERM\ IV} + \underbrace{\frac{\partial f_d(m)}{\partial t}\Big|_{nucl,ice}}_{TERM\ V} + \underbrace{\frac{\partial f_d(m)}{\partial t}\Big|_{rim}}_{TERM\ VI} + \underbrace{\frac{\partial f_d(m)}{\partial t}\Big|_{melt}}_{TERM\ VII} \tag{2.20}$$

$$\frac{\partial g_{APd}(m)}{\partial t} = \underbrace{\frac{\partial g_{APd}(m)}{\partial t}\Big|_{dyn}}_{TERM\ I} + \underbrace{\frac{\partial g_{APd}(m)}{\partial t}\Big|_{\substack{act \\ desact}}}_{TERM\ II} + \underbrace{\frac{\partial g_{APd}(m)}{\partial t}\Big|_{\substack{cond \\ eva}}}_{TERM\ III} + \underbrace{\frac{\partial g_{APd}(m)}{\partial t}\Big|_{coal}}_{TERM\ IV} + \underbrace{\frac{\partial g_{APd}(m)}{\partial t}\Big|_{nucl,ice}}_{TERM\ V} + \underbrace{\frac{\partial g_{APd}(m)}{\partial t}\Big|_{rim}}_{TERM\ VI} + \underbrace{\frac{\partial g_{APd}(m)}{\partial t}\Big|_{melt}}_{TERM\ VII} \tag{2.21}$$

Knowing $f_d(m)$ and $g_{APd}(m)$ allows to calculate the mean aerosol particle mass $\bar{m}(m)$ inside a droplet of mass m, which is given by the equation 2.22:

$$\bar{m}(m) = \frac{g_{APd}(m)}{f_d(m)} \tag{2.22}$$

Thus, the size of the aerosols is being considered in the calculation of the drop growth rate.

The number of aerosol particles is explicitly followed by means of the moist aerosol particle number distribution function $f_{AP}(m_{AP})$, given in the equation 2.23:

$$\frac{\partial f_{AP}(m_{AP})}{\partial t} = \underbrace{\left.\frac{\partial f_{AP}(m_{AP})}{\partial t}\right|_{dyn}}_{TERM\ I} + \underbrace{\left.\frac{\partial f_{AP}(m_{AP})}{\partial t}\right|_{\substack{act \\ desact}}}_{TERM\ II} + \underbrace{\left.\frac{\partial f_{AP}(m_{AP})}{\partial t}\right|_{nucl,ice}}_{TERM\ V} + \underbrace{\left.\frac{\partial f_{AP}(m_{AP})}{\partial t}\right|_{\substack{cond \\ eva}}}_{TERM\ III} \quad 2.23$$

As for the ice crystals with mass m_i and for the mass of aerosol particles inside ice crystals, the number distribution functions are simulated by the equations 2.24 and 2.25 respectively.

$$\frac{\partial f_i(m_i)}{\partial t} = \underbrace{\left.\frac{\partial f_i(m_i)}{\partial t}\right|_{dyn}}_{TERM\ I} + \underbrace{\left.\frac{\partial f_i(m_i)}{\partial t}\right|_{nucl,ice}}_{TERM\ V} + \underbrace{\left.\frac{\partial f_i(m_i)}{\partial t}\right|_{dep/sub}}_{TERM\ VIII} + \underbrace{\left.\frac{\partial f_i(m_i)}{\partial t}\right|_{rim}}_{TERM\ VI} + \underbrace{\left.\frac{\partial f_i(m_i)}{\partial t}\right|_{melt}}_{TERM\ VII} \quad 2.24$$

$$\frac{\partial g_{APi}(m_i)}{\partial t} = \underbrace{\left.\frac{\partial g_{APi}(m_i)}{\partial t}\right|_{dyn}}_{TERM\ I} + \underbrace{\left.\frac{\partial g_{APi}(m_i)}{\partial t}\right|_{\substack{dep \\ sub}}}_{TERM\ VIII} + \underbrace{\left.\frac{\partial g_{APi}(m_i)}{\partial t}\right|_{nucl,ice}}_{TERM\ V} + \underbrace{\left.\frac{\partial g_{APi}(m_i)}{\partial t}\right|_{rim}}_{TERM\ VI} + \underbrace{\left.\frac{\partial g_{APi}(m_i)}{\partial t}\right|_{melt}}_{TERM\ VII} \quad 2.25$$

In the general equations 2.20, 2.21 and 2.23 to 2.25, term I is used to express the dynamic tendencies (i.e. transport, mixing, sedimentation…).

Term II represents the activation and deactivation processes. The activation process in DESCAM is simulated via the Köhler equation (Pruppacher and Klett 1997) and has been described in Leroy (2007) and Planche (2011). The critical radius for activation $r_{act}(r_N)$ is calculated as a function of the mean dry radius r_N of the wet aerosol particles inside the drops (Leroy et al. 2007). After the activation, the growth of droplets continues as long as the ambient air remains supersaturated. Activated wet aerosol particles whose radius is smaller than 1 µm are placed in the first class of drops (**Figure 2.3**). In case of subsaturation and if the droplet radius r is smaller than the activation radius due to evaporation, the droplet is transferred back to the wet aerosol particle reservoir. To

ensure that there will be no overloading of aerosol particles in the last class of the aerosol particle spectrum, DESCAM uses a scheme developed by Leroy (2007) which permits the re-calculation of the equilibrium radius according to Köhler theory. A drop is deactivated if its radius after evaporation ($r + \frac{dr}{dt} dt$) is smaller than the activation radius (r_{act}).

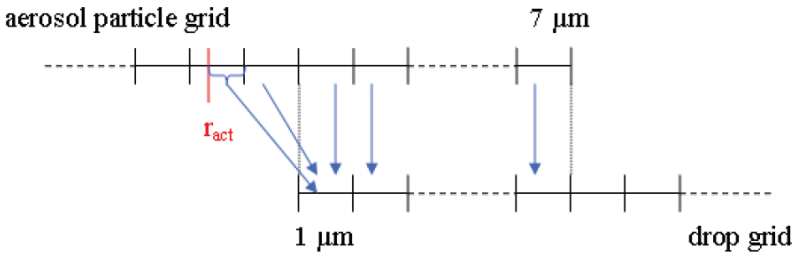

Figure 2.3: Schematic representation of the activation process in DESCAM (source: Leroy 2007).

The growth of the drops by condensation (term III) is treated as in Pruppacher and Klett (1997):

$$\left.\frac{\partial f_{wat}(m, m_{AP})}{\partial t}\right|_{cond} = -\frac{\partial}{\partial m}\left[f_{wat}(m, m_{AP}) \left.\frac{dm}{dt}\right|_{wat}\right] \qquad 2.26$$

In the relation 2.26 the term $\left.\frac{dm}{dt}\right|_{wat}$ is used to represent the growth velocity and is determined by the equation 2.27.

$$\left.\frac{dm}{dt}\right|_{wat} = 4\pi r \frac{\left(S_w - \frac{A}{r} + \frac{Br_N^3}{r^3 - r_N^3}\right)}{\left(\frac{RT}{D_v^* M_w e_{sat,w}} + \frac{L_e}{k_r^* T}\left(\frac{L_e M_w}{RT} - 1\right)\right)} \qquad 2.27$$

The mechanism of collision-coalescence is expressed by the term IV. For its numerical solution the technique of Bott (1998) was applied.

In the general DESCAM model equations, term V represents the ice nucleation. Homogeneous nucleation is considered in DESCAM by the parameterization of Koop et al. (2000) and does not depend on the composition of the droplet solution but only on the water activity of the solution. The process is a function (equation 2.28) of the water activity α_w (which in equilibrium with water vapor is equivalent to the relative humidity) and the homogeneous ice nucleation rate coefficient J_{hom} (in cm^{-3} s^{-1}). In the equation 2.29, α_w^i is the water activity of a solution in equilibrium with ice (given by equation 2.30).

According to Koop et al. (2000), *the kinetic (non-equilibrium) ice nucleation process is driven entirely by the thermodynamic (equilibrium) quantity* $\Delta\alpha_w$. Thus, the term $\Delta\alpha_w$ is called a "water-activity criterion" for homogeneous ice nucleation and is given by the equation 2.29.

$$log(J_{hom}) = -906.7 + 8502\Delta\alpha_w - 26924(\Delta\alpha_w)^2 + 29180(\Delta\alpha_w)^3 \quad 2.28$$

with

$$\Delta\alpha_w = \alpha_w - \alpha_w^i \quad 2.29$$

$$\alpha_w^i = exp\left[\frac{10^7}{RT}(210368 + 131.438T - 3.32373 \times 10^6 T^{-1} - 41729.1ln(T))\right] \quad 2.30$$

Where R=8.3144598 J mol^{-1} K^{-1} (gas constant) and T is the temperature.

The different types of heterogeneous ice nucleation (deposition, condensation freezing, contact freezing and immersion freezing) are not distinguished in this version of DESCAM. In the model, the heterogeneous nucleation is described globally by the formula of Meyers et al. (1992) in which the number of pristine ice crystals N_{IN} (cm^{-3}) is related to the fractional ice supersaturation S_i (equation 2.31).

$$N_{IN} = 10^{-3} exp(0.639 + BS_i) \quad 2.31$$

with B=12.96

The growth of ice crystals by deposition of water vapor is represented by the term VIII. Term VI corresponds to the growth of ice crystals by riming, a process that involves the collection of supercooled droplets on the surface of large ice crystals. As soon as the ice crystals cross the isotherm of 0° C, they melt instantaneously (term VII) and they are transferred in the reservoir of drops. Therefore, ice crystals in DESCAM are always dry. Aggregation process that is most efficient around 0°C, when ice particles develop a pseudo-liquid layer (Pruppacher and Klett, 1997), is consequently neglected. The use of a new parameterization of a non-instantaneous melting process developed by Planche et al. (2014) showed no important change on the development of a mostly icy cloud. Finally, the splintering of ice crystals is not considered yet in DESCAM model.

In the following chapters, this numerical tool will be used in order to study the impact of aerosol number changes on the formation and evolution of a convective

orographic precipitating system observed over the Cévennes-Vivarais region (France) during the HYMEX campaign. The following chapter presents the field experiment of this project.

3 Presentation of the HYMEX experiment and the IOP7a case study

Field campaigns are usually organized in order to study problematic and poorly understood atmospherical phenomena, e.g. in intense or extreme weather conditions, pollution episodes, etc. Modeling studies are an essential element for understanding, analysis and generalization of the findings. Also, observations contribute to making more realistic the model configuration and validate (or not) the simulation results as well as the quality of instruments, their calibration and/or the observation strategy.

This chapter presents the HYMEX experiment that was organized to study the extreme precipitating systems often observed over the South of France, which provide the framework of the present thesis. The selected case study, which was an episode of intense precipitation observed during HYMEX, is being described along with its unique features, synoptic and climate background. Afterwards, the instrumentation used to record the case study is presented, as well as the respective observation products. The observations are evaluated for further use in this work.

3.1 The HYMEX program and the SOP1 field campaign

For a better understanding of the water cycle and its related processes in the Mediterranean, the HYMEX (HYdrological cycle in the Mediterranean EXperiment) program was launched in 2007 by the French scientific community. During the program

a large set of atmospheric, oceanic, hydrological and biochemical variables were observed during two SOPs (Special Observation Period) that lasted several months each: the SOP1 took place in autumn 2012 (Ducrocq et al. 2014) and the SOP2 in winter 2013 (Estournel et al. 2016), both in northwestern Mediterranean. The case study analyzed hereafter was observed during the SOP1, so only the instrumental set up deployed during this SOP will be described.

The SOP1 which was dedicated to study heavy precipitation and flash-flooding, consisted of 20 IOPs (Intense Observation Period) in France, Spain and Italy. Within a domain of 1400×700 km^2 at the northwestern Mediterranean, 8 target sites were considered for observations (**Figure 3.1**a) during the IOPs. In these target sites, 165 research ground instruments were deployed and 3 research aircrafts performed in total 251 flying hours in order to provide also in-cloud measurements. Moreover, about 850 soundings were launched from ground, ship and mobile coastal stations to refine the description of the mesoscale environment. It is worth noting that during the SOP1 there were 20 days with daily rainfall accumulation that exceeded 100 mm somewhere in its observation domain.

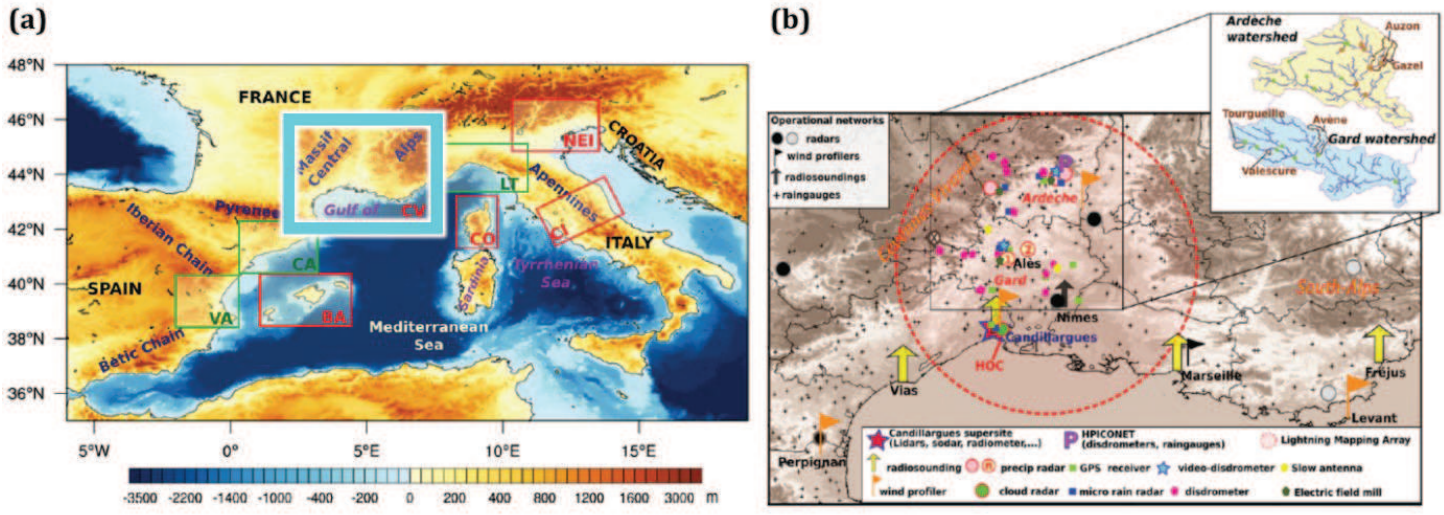

Figure 3.1: (a) The broader western Mediterranean region together with the HyMeX observation sites. The light blue frame indicates the target site of interest for this study, which is the CV (Cévennes-Vivarais). (b) Ground instrumentation deployed at the CV region during the SOP1, together with the operational meteorological networks from Météo-France and other agencies (Services de Prévision des crues) (source: Ducrocq et al. 2014).

One of the 8 target sites was the Cévennes-Vivarais (CV) region (**Figure 3.1**b), where dense observation networks were deployed. Indeed, according to Frei and Schär (1998), this site is one of the five rainiest areas in the region extending from the Massif Central to the eastern Alps. Moreover, Nuissier et al. (2008) have shown that the number

of days during which the daily surface rainfall exceeded 200 mm over the CV reaches 20-25 in 46-years scale. The CV site covered the south-eastern side of the Massif Central (France), especially the Cévennes Mountains and the Vivarais Mountains where the highest peaks are the Pic de Finiels, the Gerbier de Jonc and the Mézenc (see **Figure 3.2**). This mountain relief plays the key role for the formation of heavily precipitating systems. The Cévennes-Vivarais is, therefore an ideal region for studies of heavy orographic precipitation.

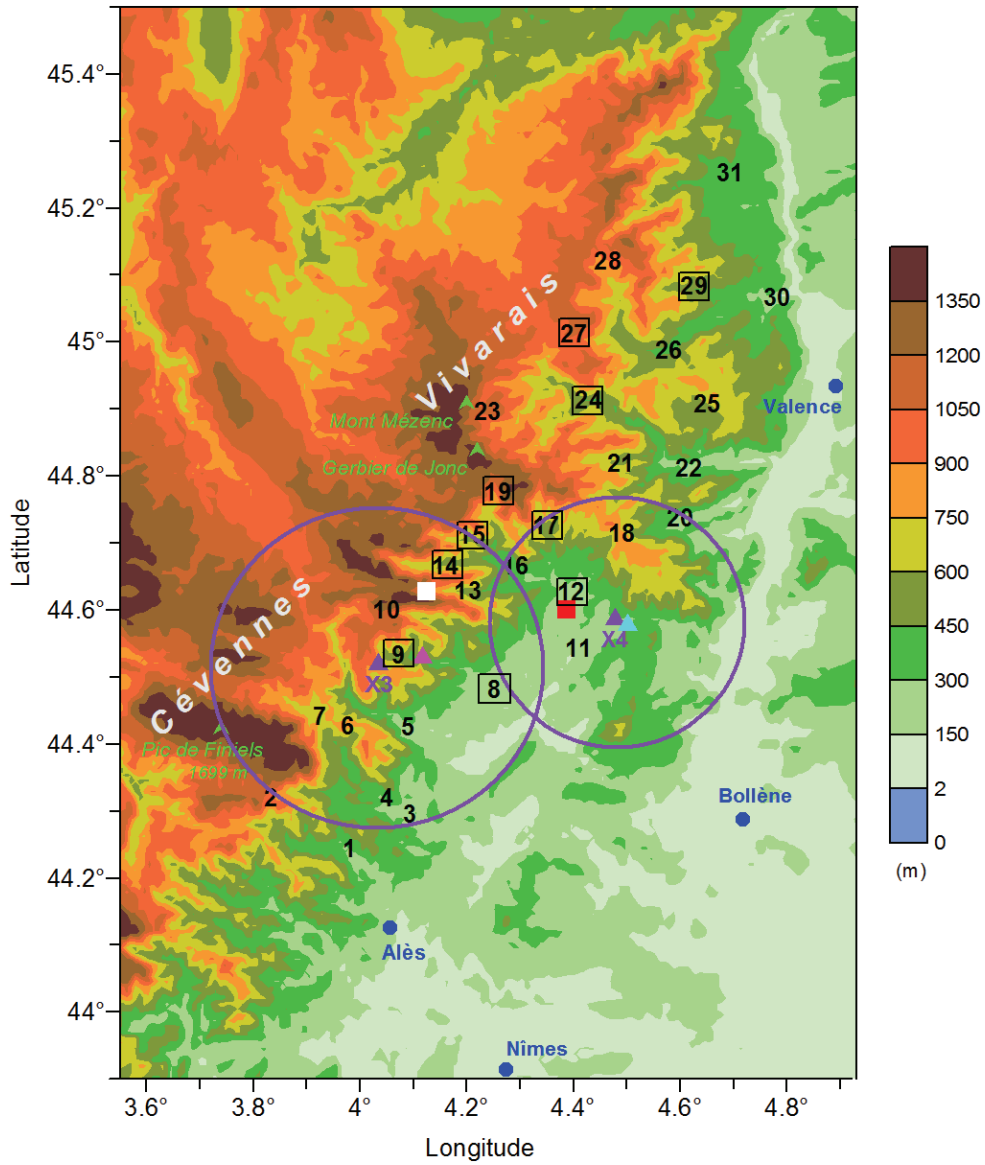

Figure 3.2: Summary of the HYMEX ground-based instruments in the Cévennes-Vivarais region used for the present study. The **numbers** indicate the positions of rain gauges. The **numbers in rectangles** indicate the rain gauges presented in **Figure 3.8**. The **white rectangle** represents the Parsivel S. The purple circles indicate the observation fields of the X-band radars. The instruments from LaMP are represented by triangles. The highest mountain peaks and cities of this region are indicated.
▲: X-band radars ▲: MRR8 and Parsivel8 (Le Pradel) ▲: MRR9 and Parsivel9 (Saint Mélany)
■: MRR10 and Parsivel10 (Saint-Etienne de Fontbellon, Aubenas)

3.2 IOP7a: Intense orographic precipitation event

This study focuses on the heavy precipitation episode of the HYMEX IOP7a, observed over the CV area (see **Figure 3.1**) on the 26th September 2012. The selection of this event as the reference case for this work is based on its nature, intensity, location, and on the availability of ground-based instrumentation, as well as airborne observations. During IOP7a a high amount of orographic rain fell in a short time period in the morning of the 26th September 2012 over the Cévennes-Vivarais region. According to composite observations of hourly cumulative rainfall by Météo-France, rain rate values up to 60 mm h^{-1} occurred, therefore the rainfall was characterized as intense.

The most remarkable feature of this event is that for the first time aircraft measurements were undertaken in and above the cloudy system over the Cévennes-Vivarais region. Moreover, most of the instruments deployed by LaMP (Laboratoire de Météorologie Physique) were able to measure this precipitation event (see **Figure 3.2** for locations). Spatially and temporally highly resolved X-band radar measurements were continually performed across of strongest precipitation, allowing to follow the evolution of convective cells responsible for the high rainfall rates.

Before a description of the main features of the IOP7a intense precipitation system, the synoptic conditions favorable to its formation are detailed.

3.2.1 Synoptic conditions of the IOP7a event

In the first hours of 26th September 2012 an upper-level low pressure system was centered over the British Isles and its edges were reaching France while propagating eastwards. The presence of this low barometric system favored the development of a cold front at the west of the Cévennes-Vivarais region, over Spain and the South of France, as seen in **Figure 3.3**. The values of the convective available potential energy (CAPE) were between 0.5 and 1 kJ kg^{-1} over the CV site (as given by the Global Forecast System (GFS) analysis in Zwiebel (2015), therefore the atmospheric air characterized as potentially unstable.

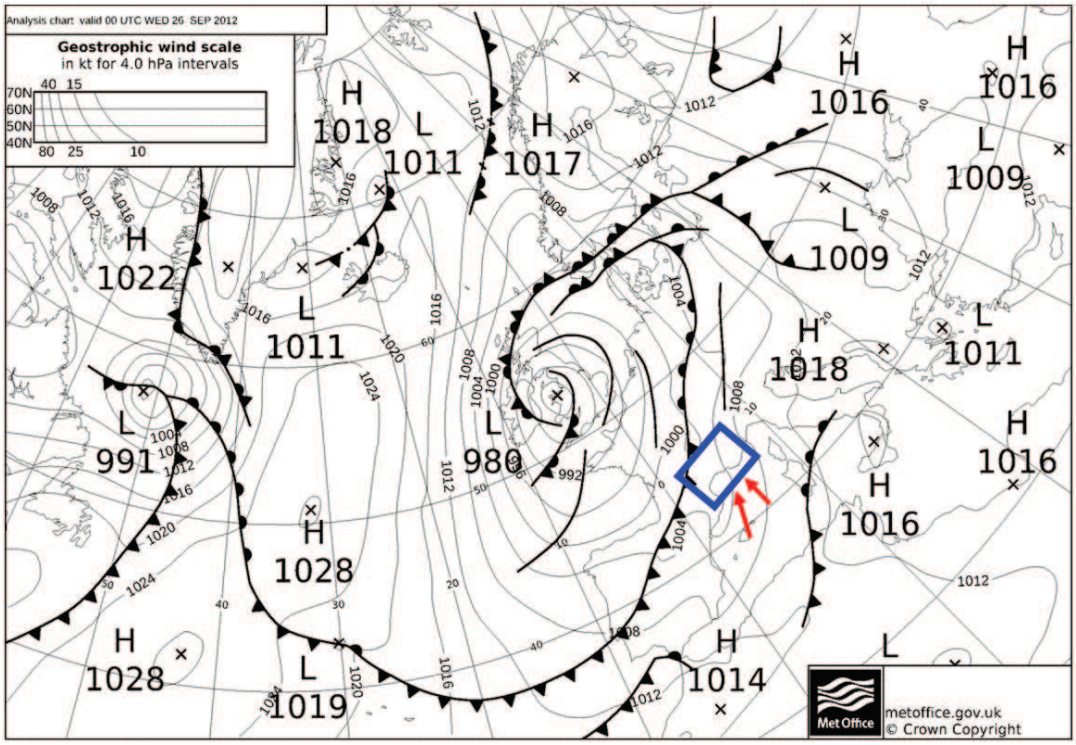

Figure 3.3: Mean sea-level pressure over Europe and the North Atlantic Ocean on 26th September 2012 at 00:00 UTC. Weather fronts are indicated. The blue square represents the CV site and the red arrows show the southerly humid and moist air flow from the Mediterranean Sea (source: www.wetter3.de).

Figure 3.4 shows that the dynamic conditions close to the surface resulted in the formation of a strong southwestern horizontal flow over the southern regions of France. By passing over the Mediterranean Sea the horizontal wind transported moist, warm and relatively unstable air masses to the CV area, i.e., the Cévennes-Vivarais Mountains. The location and the orientation of these mountains (**Figure 3.2**) enhanced the development of a small convective system which produced large orographic rain amounts in a few hours.

According to the synoptic conditions and the intense precipitation observed (more details in **section 3.3.1**), the IOP7a was characterized as a heavy precipitation event (HPE), also named as a "Cévenol" episode. Cévenols occur in the beginning of autumn in the region of Cévennes-Vivarais. In this kind of event, Bresson et al. (2012) showed that the intensity of the rainfall over the mountain slopes of the Massif Central is proportional to the horizontal wind and the humidity of the air flow. Moreover, the convective system may remain at the same location if the low-level flux is maintained. The Cévenol episode of the HYMEX IOP7a is described next.

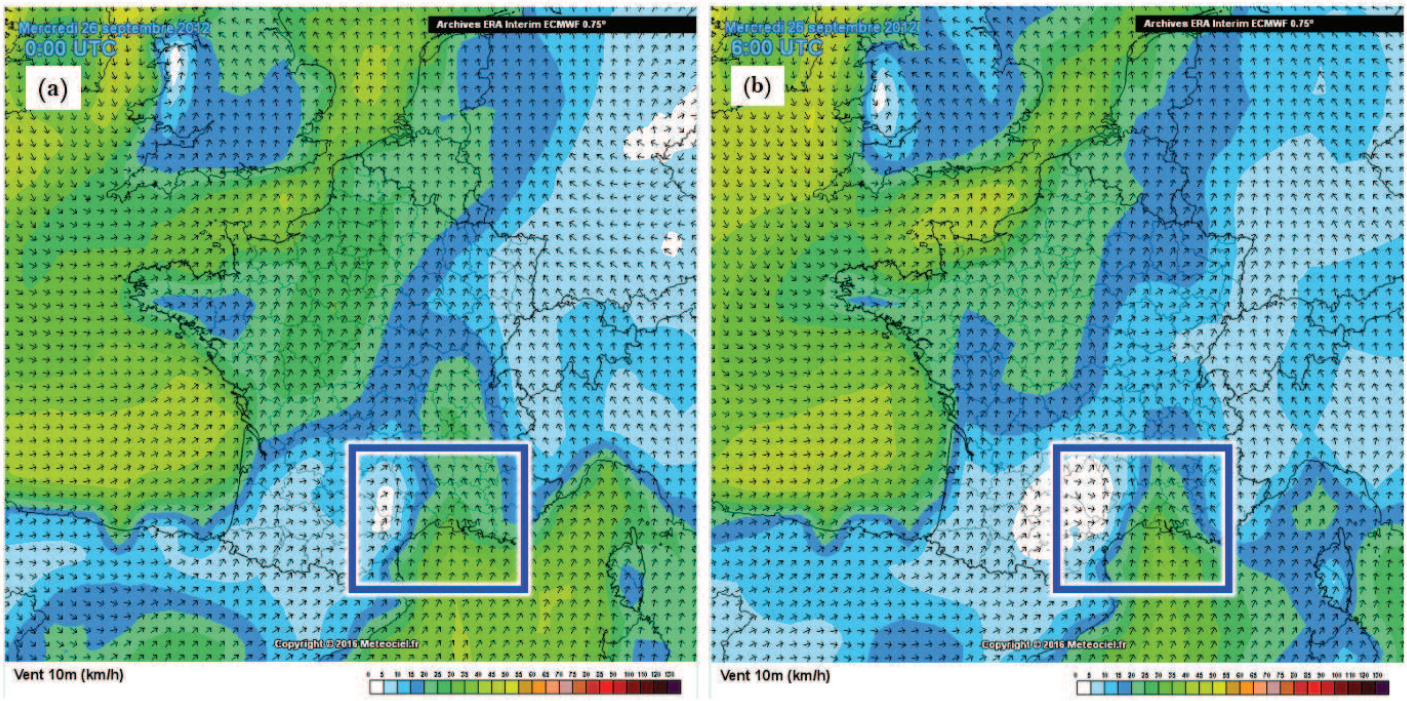

Figure 3.4: Horizontal wind (km h^{-1}) at the surface over France (a) at 00:00 UTC and (b) at 6:00 UTC provided by the ECMWF ERA-Interim archives[8]. The square represents the CV target site.

3.2.2 Description of the evolution of the IOP7a convective system

During the morning of the 26th September 2012, the convective system was formed over the non-mountainous area at the east of the Cévennes Mountains and over the eastern part of Vivarais Mountains (see **Figure 3.5**a). At 6:00 UTC the rainfall had started (see **Figure 3.5**). Between 6:00 UTC and 7:00 UTC the observations (details in **section 3.3.1**) showed that up to 60 mm of rain fell locally in only one hour (**Figure 3.5**a).

[8] http://www.meteociel.fr/modeles/archives/archives.php

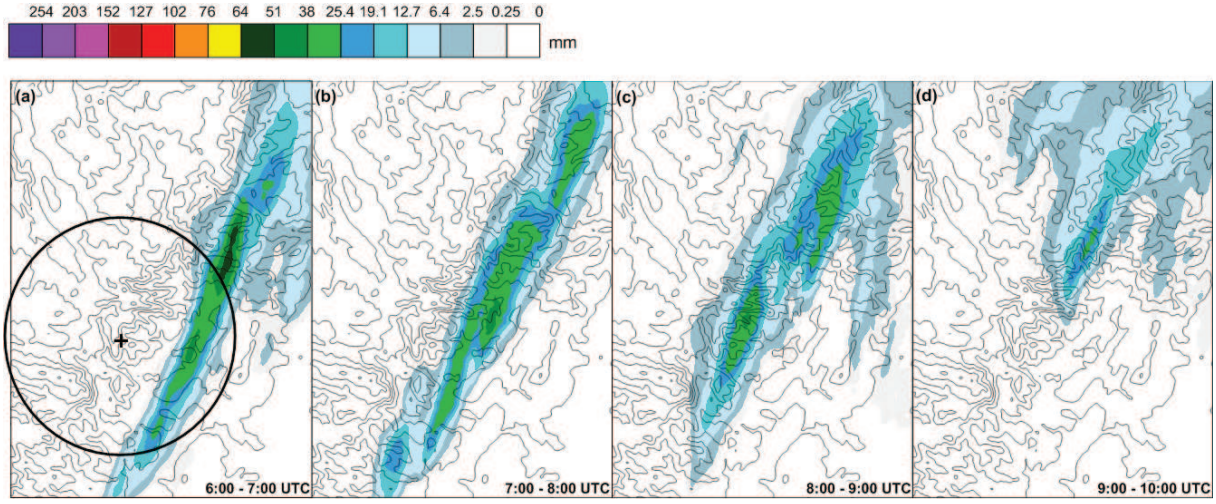

Figure 3.5: Hourly rain accumulation (in mm) by the KED QPE (see **section 3.3.1**). (a) From 6:00 UTC to 7:00 UTC, (b) from 7:00 UTC to 8:00 UTC, (c) from 8:00 UTC to 9:00 UTC and (d) from 9:00 UTC to 10:00 UTC. The cross represents the position of the X-band radar X3 (see **section 3.3.5**) and the circle corresponds to its observation field.

Between 7:00 UTC and 9:00 UTC the rain field was moving slightly to the west and towards the mountain slope, while being spread out over the affected region. The system began to change its organization at 8:00 UTC, as two cells over the mountain ridge are visible in **Figure 3.5**b and **Figure 3.5**c. The major part of the precipitation fell until 9:00 UTC. The amount of the recorded rain accumulation was less intense after 9:00 UTC (**Figure 3.5**d). Until 11:00 UTC light rain continued falling over the mountain slope and the plain area at the east of the mountain ridge and over the mountains of Vivarais. According to **Figure 3.6**b, up to 114 mm of rain were observed locally from 00:00 UTC of the 26th September until noon of the same day.

In order to obtain additional details about the rain intensity, **section 3.3.2** shows rain gauge data that provide rain rate at a higher temporal resolution locally.

In the following sections, the available observations during the HYMEX IOP7a are described together with details about the used instruments.

3.3 Ground-based observations of the IOP7a system

Most of the ground-based observations from HYMEX are used to document the evolution of the IOP7a precipitation system: rain gauges, radars, disdrometers... The associated observed parameters are the rain accumulation, radar reflectivity and drop size distributions that provide information about the temporal and spatial evolution of

the amount, the microstructure and the intensity of the precipitation. The main criteria for the instrument selection were their location, the data availability during the hours of interest, as well as the comparability of the observations with the simulated parameters of the cloud model. **Figure 3.2** illustrates the position of the ground-based instruments.

Moreover, the Mediterranean Hydro-meteorological Observatory of the Cévennes-Vivarais (OHM-CV, French acronym) was also involved in the HYMEX program by providing the products of other ground-based instruments which are part of operational networks.

This section begins with the presentation of rainfall observations from the OHM-CV. Afterwards, the individual ground instruments used during HYMEX for the measurement of precipitation are presented.

3.3.1 Quantitative precipitation estimation (QPE) product from OHM-CV

The rainfall reanalysis is a product of approximating the amount of precipitation that has fallen at a location or across a region. Maps of the estimated amount of precipitation are compiled using several different data sources including, e.g. radars data and rain gauges measurements. In this framework, the OHM-CV developed a product from the merging of radars and rain gauges measurements that provides quantitative precipitation estimation (QPE). The observations provided by the radars (Table 3.1) of the French ARAMIS (Application Radar à la Météorologie Infra-Synoptique) network (Tabary et al. 2013), as well as by rain gauges over this domain were merged through a geostatistical method called KED (Kriging with External Drift) method (Boudevillain et al. 2011, 2016; Delrieu et al. 2014) over the domain presented in the **Figure 3.7**. The two C-band and two S-band Doppler radars which are considered in the rain product provide cumulative rainfall observations every 5 min.

	Bollène	**Nîmes**	**Montclar**	**Sembadel**
Radar type	S-band	S-band	C-band	C-band
Altitude	324.5 m	78 m	678.5 m	1141 m

Table 3.1: Specifications about the type and the altitude of the 4 operational radars of the Météo-France ARAMIS network which are used in the OHM-CV rain product.

The merging of this data was achieved by the systematic implementation of the following concurrent methods:

- Exploitation of the 5-minute C-band and S-band radar data (QPE radar product)
- Processing of the hourly rain gauge data by the climatological Ordinary Kriging (OK) technique
- Coupling of the radar and rain gauge data by the Kriging with External Drift[9] (KED) method

A regular assessment of these three estimation methods with a cross-validation exercise by Boudevillain et al. (2016) proved that the KED QPEs were consistently equivalent and often better than the best QPEs based on radar and rain gauges separately (methods i and ii), both in terms of bias and spatial–temporal correlation.

The KED QPE method was applied on observations during intense rainfall events obtained by 250 hourly and 160 daily rain gauges, as well as by the aforementioned operational radars from the Météo-France ARAMIS network. A rainfall event was defined as "intense" when its daily rain accumulation exceeded 30 mm locally according to rain gauge data with non-zero mean rainfall during one or several successive days. In that case, the rain product provides 1, 2, 4 and 6-h estimation of rain accumulation in millimeters. The rainfall during IOP7a was characterized as an intense event and QPE data are available for this day. **Figure 3.5** presented the hourly rain accumulation provided by the KED QPE product from 6:00 to 10:00 UTC on the 26th September 2012 and **Figure 3.6** illustrates the cumulative rainfall from 00:00 to 6:00 UTC and from 00:00 to 11:00 UTC. In both **Figure 3.5** and **Figure 3.6** the focus is made on the area where the most intense rainfall occurred. Therefore, the aforementioned domain is smaller than the OHM-CV domain (**Figure 3.7**). The resolution of the rain product is 1 km x 1 km.

[9] Spatial prediction technique that combines a regression of the dependent variable on auxiliary variables (such as parameters derived from digital elevation modelling, remote sensing/imagery, and thematic maps) with kriging of the regression residuals. The auxiliary predictors are used directly to solve the kriging weights.

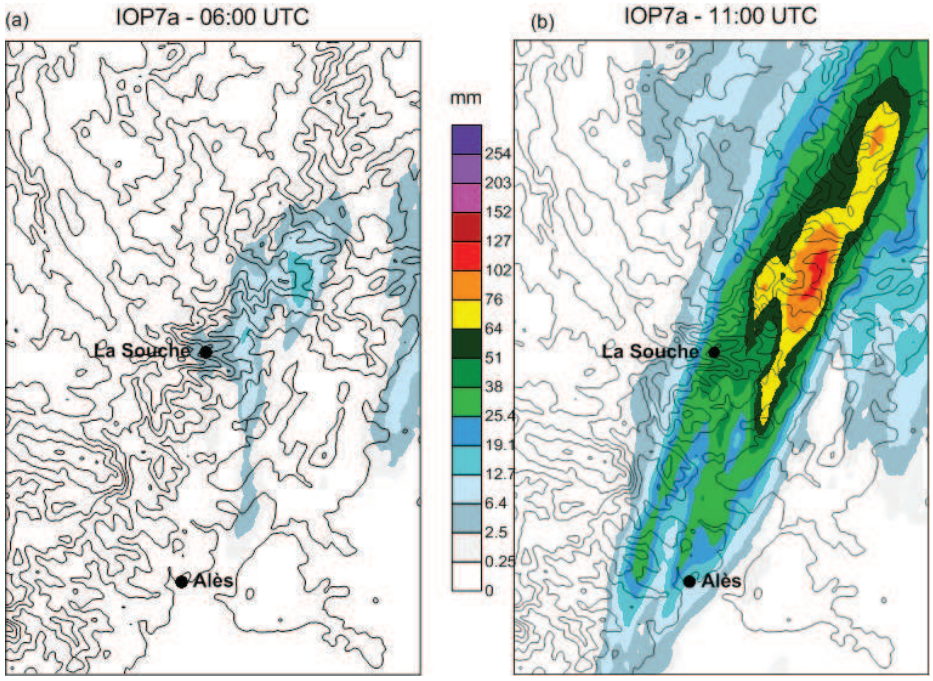

Figure 3.6: Cumulative rainfall (in mm) observed at the surface during the IOP7a (a) from 00:00 UTC to 06:00 UTC and (b) from 00:00 UTC to 11:00 UTC. The maximum values are 18 mm and 114 mm respectively.

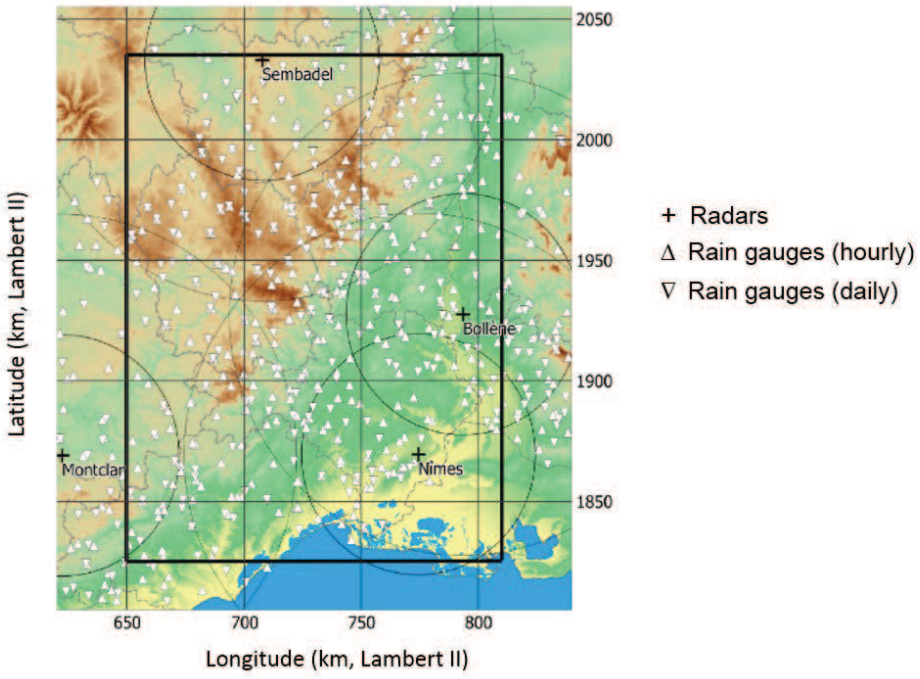

Figure 3.7: The OHM-CV domain in Southeastern France together with a map of the rainfall observation system superimposed on the topography. The triangles refer to the rain gauges and the + signs along with the 50 and 100-km range markers refer to the 4 operational radars of the Météo-France ARAMIS network. The thick black frame delineates the estimation domain of the rain products (source: Boudevillain et al. 2016).

3.3.2 Rain gauges

In this section, the measurements obtained by rain gauges located over the domain of this study (**Figure 3.2**) are discussed. Before that, the operating principle of the rain gauge instrument is detailed.

A rain gauge is a meteorological instrument (**Figure 3.9**a) which gathers and measures the amount of precipitation over a set period of time. It consists of a small measuring tube and a cylinder which contains a funnel. The amount of precipitation reaching the ground is represented in terms of the vertical depth that the water would have if it covered a horizontal projection of the soil surface of 1 m^2. It is measured in millimeters, with a recommended resolution of 0.2 mm (=0.2 L m^{-2}). Therefore, when more than 0.2 mm of rain has fallen, a tipping bucket gauge sends a signal to a recorder.

Although the rain gauge provides one of the most accurate rain measurement, the rainfall observations provided by this instrument can be underestimated due to several atmospheric parameters: wind and temperature of the surrounding air can cause evaporation in case of low precipitation. Also, solid precipitation (snow or hail) reaches the measurement system with difficulties and the heating system used to measure this kind of precipitation after its melting can also cause evaporation.

Moreover, the maintenance of the rain gauge is an important factor that determines the quality of the measurements in order to avoid closing of the rain gauge and a bad horizontality of the cone that decreases the capture surface.

The sparseness of the rain gauges can result in less accurately capturing of the high spatial and temporal variability of precipitation systems (Villarini et al. 2008). During HYMEX, in order to well capture the rainfall properties, a dense network of 302 rain gauges (by Météo-France, EDF (Electricité De France) and by the SPC GD (Service de Prévision des Crues Grand Delta)) is used to estimate, e.g. hourly time rate.

Figure 3.8 shows the temporal evolution of 5-minute rain rate measured by several rain gauges located over the domain of this study (**Figure 3.2**). Only the most intense rain rates are represented in this figure. The measurements from other rain gauges are presented in **Appendix**. The different panels of the **Figure 3.8** show that the associated precipitations of the IOP7a convective system are quite intense and highlight the temporal evolution of this system. The intense precipitation was just observed over the Cévennes mountain, and then, close to Aubenas (see **Figure 3.2**) and over the Vivarais mountain.

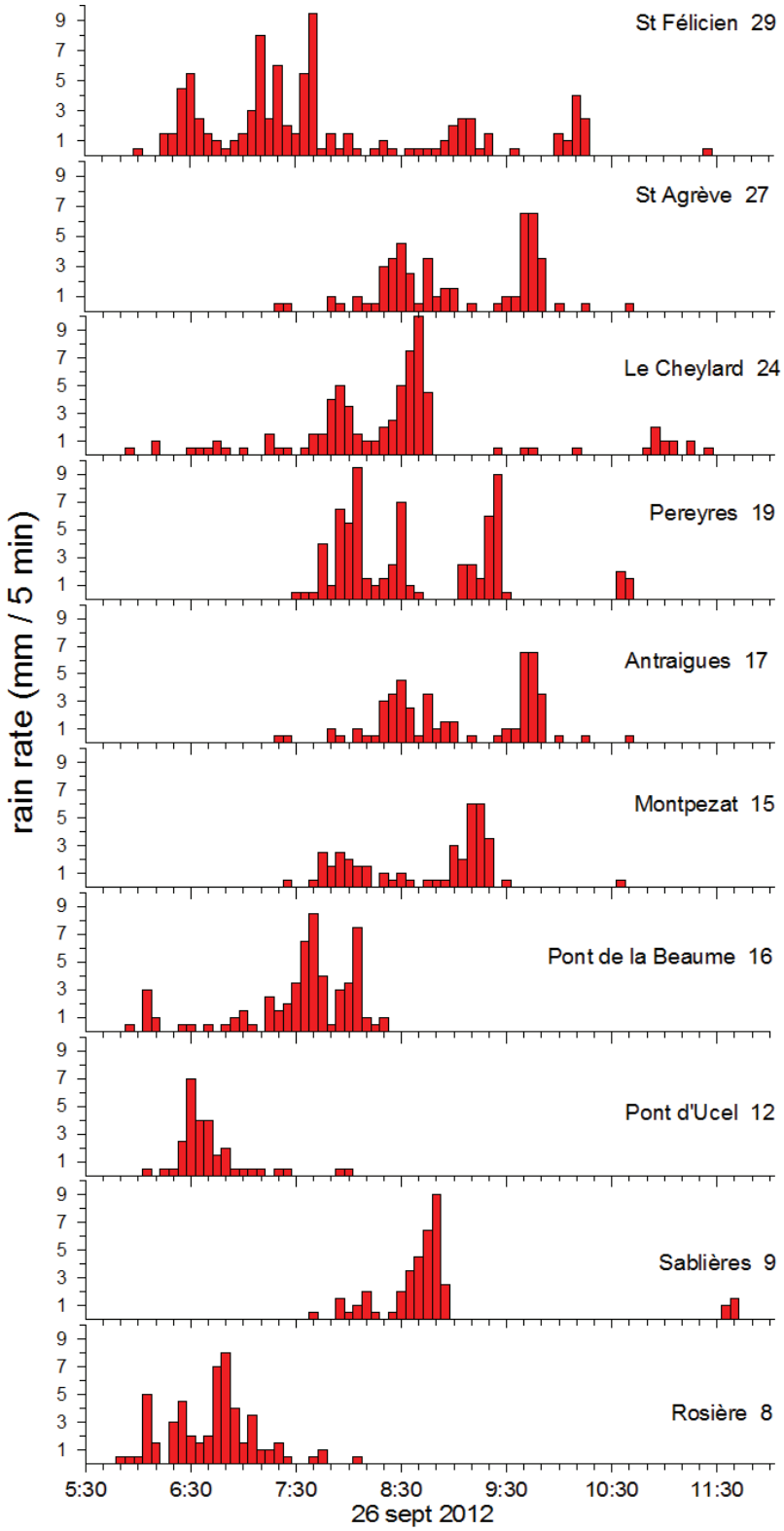

Figure 3.8: Temporal evolution of 5-minute rain rate observed by rain gauges located in the Cévennes-Vivarais region (see **Figure 3.2** for specific locations). The panels represent the measurement of rain gauges located from the North (top panel) to the South (bottom panel) of the Cévennes-Vivarais Mountains.

Note that in the period from 7:00 to 8:00 UTC, the rain gauge located at the Le Cheylard measured 39 mm of rain whereas at the same point the hourly rain accumulation from the KED QPE product is 18 mm (**Figure 3.5**b). The coarser resolution used for the QPE slightly smooths the rain observations from rain gauges.

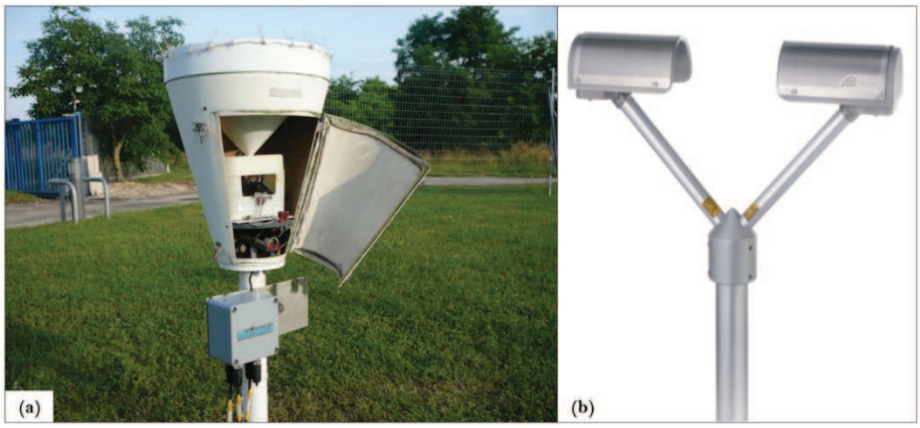

Figure 3.9: (a) Typical autonomic rain gauge by Météo-France in the Rhone-Alps region in France. (b) Schematic representation of the OTT Parsivel disdrometer.

3.3.3 Parsivel disdrometers

In addition to rain gauges, disdrometers can measure rain properties at the surface.

Disdrometers are instruments that measure the drop size distributions and thus permits to quantify the microstructure of the precipitation, by using either laser or microwave technology. The OTT[10] Parsivel (PARticle SIze and VELocity), whose observations are used in this study, is a laser-based optical disdrometer (Löffler-Mang and Joss 2000) which measures simultaneously the diameter and the vertical velocity of all the falling liquid and solid hydrometeors by sensing their shadow (**Figure 3.9**b). The fall speed of the particles is determined by the duration of their detection. The measurements are classified into 32 bins whose range varies from 0 to 24 mm for the drop diameter and between 0.2 m s^{-1} and 20 m s^{-1} for the vertical velocity. The raw data are used to retrieve parameters concerning the type, amount, intensity and kinetic energy of the precipitation, the visibility, as well as the equivalent radar reflectivity factor.

Figure 3.10 shows the temporal evolution of the rain rate (RR) measured by three different Parsivel disdrometers (see locations in **Figure 3.2**) using corrected 1-minute

[10] Albert Ott was founder of the "Mathematical-Mechanical Institut" in Germany (1873), which became the OTT Company. OTT (member of the Hydromet Group) provides measuring systems for hydrometry, meteorology and environmental monitoring.

data (Raupach and Berne 2015). These measurements show that the precipitation is intense at the location of Parsivel 10 and over the relief (Parsivel S), as already seen with rain gauges.

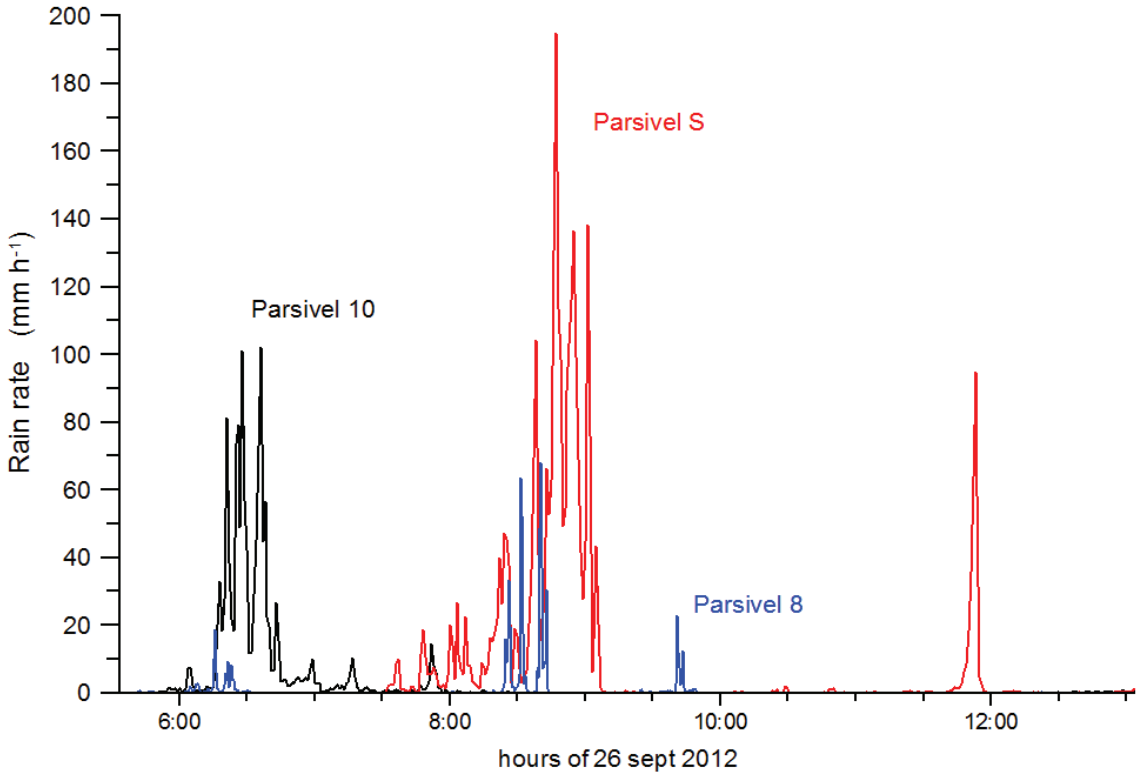

Figure 3.10: Temporal evolution of the rain rate (mm h^{-1}) observations by the disdrometers Parsivel 8 (in blue), Parsivel 10 (in black) and Parsivel S (in red) as a function of the time during the IOP7a.

The advantage of the use of the Parsivel disdrometer is the ability to acquire and process precipitation in a wide spectrum from drizzle to tropical rain with extreme rain rates up to 1200 mm h^{-1}. It is also a low cost, durable, and reliable in all environmental and weather conditions instrument which allows to investigate the small-scale variability of the drop size distribution (Löffler-Mang and Joss 2000). Nevertheless, the Parsivel measurement technique considers that the detected particles will be ellipsoidal and that only one particle will be in the beam at once (Battaglia et al. 2010). However, these conditions were not always met (flattering of falling drops).

3.3.4 Micro-rain radars (MRR)

In addition to the radars from the ARAMIS French national network, other radars were deployed during the SOP1, as Micro-rain radars (MRR) that provide details about the vertical profile of rain. The MRR is a vertically pointing FM-CW (Frequency Modulated Continuous Wave) Doppler K-band (24.1 GHz) radar (Van Baelen et al. 2009; Tridon et al. 2011) for the measurement of drop size distribution profiles from which rain rates, liquid water content and terminal velocity can be retrieved. The FM-CW technique permits the change of the radar's operating frequency whereas continuous transmission power is radiated. Every 1 min it detects droplets of 46 bins in the size range of 0.246 mm-5.8 mm, resolved into 32 range gates with a vertical resolution of 100 m. The droplet number concentration N(D) in each drop-diameter bin D is derived from the backscatter intensity in each corresponding frequency bin by using the relation between terminal velocity and drop size (Atlas et al. 1973).

Despite the advantages of its exploitation, uncertainties can be found in MRR observations. The analysis of Peters et al. (2002) suggests that the MRR can be used to support quantitative rain rate estimates with weather radars, noting that limitations with respect to the applied drop size retrieval are caused by non-zero vertical winds and turbulence. In particular, Tridon et al. (2011) have shown that aliasing errors in the measured spectra can be detected automatically and be used to identify the presence of strong vertical winds and eliminate retrievals which are incorrect. However, the retrieved drop size distributions from MRR during stratiform precipitation events, where the updraft regime is less intense than in convective systems, are in agreement with theoretical distributions, as in the study of Wang et al. (2017). Peters et al. (2005) have also showed that for vertical wind velocities lower than 2 m s^{-1}, the MRR data averaged over 1 min intervals provide good estimates of the drop size distribution. Also, measurements by MRR instruments are influenced by attenuation. Overall, making use of the MRR data for the study of a convective precipitation system implies that the aforementioned uncertainties which may cause underestimation of the retrieved parameters are taken into consideration.

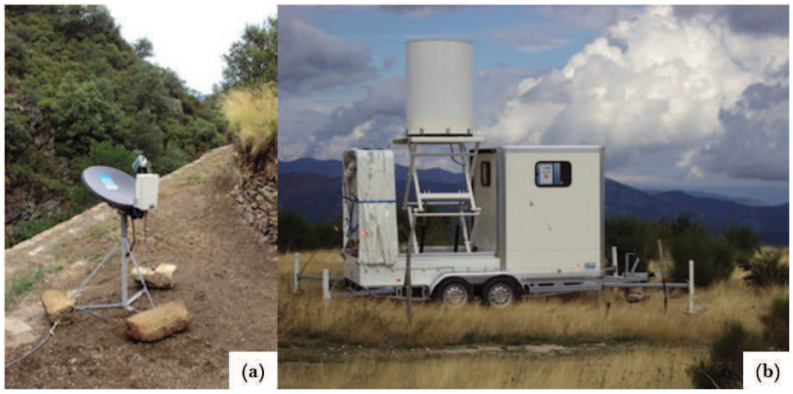

Figure 3.11: Instruments of LaMP that were deployed for observations during HyMeX SOP1 and the IOP7a: (a) The MRR9 and (b) the X-band radar at La Bombine.

In the area of interest, two MRR instruments operated during the IOP7a: the MRR9 (**Figure 3.11**a) and the MRR10. Their locations are indicated in the **Figure 3.2**. The precipitating system of the IOP7a was detected by the MRR10 between 6:15 UTC and 6:45 UTC and one hour later by the MRR9, as seen in the **Figure 3.12**a and **Figure 3.12**b, respectively. Indeed, according to the rain accumulation retrieved from observations in **Figure 3.5**a, no rain fell at the location of the MRR9 (see also **Figure 3.2**) between 6:00 and 7:00 UTC.

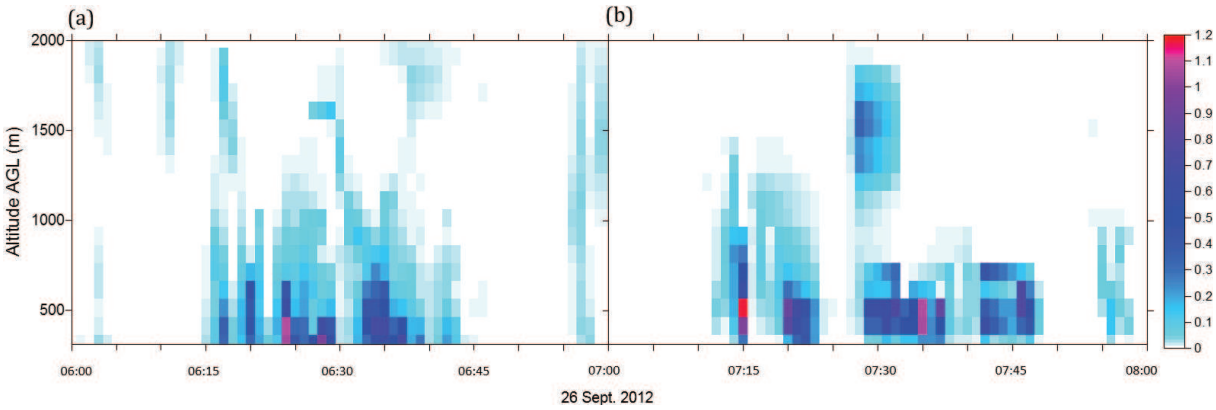

Figure 3.12: Temporal evolution of the rain water content (RWC, in g m^{-3}) during the IOP7a as a function of the altitude (AGL, in m) retrieved by the observations of (a) the MRR10 and (b) the MRR9.

The retrieved rain water content (RWC) attains higher values close to the surface and the RWC decreases by a factor of 10 from the surface to 1000 m AGL.

Furthermore, the RR can be retrieved from the MRR observations thanks to the equation 3.1, where the $v(D)$ is the terminal velocity of the cloud drops and was calculated by the formula of Beard (1976).

$$RR = \frac{\pi}{6}\int \mathrm{N}(D)v(D)D^3 dD \qquad 3.1$$

Figure 3.13 presents the retrieved rain rate from the MRR10 at 3 different levels (which correspond at the altitudes of 210 m, 310 m and 410 m AGL) along with the rain rate observed by the disdrometer Parsivel 10 at the surface. Even though the two instruments were situated at the same observation site, the difference of the observation altitude affects the intensity of the observed rain rate; it is, therefore, expected that the closer to the surface, the higher the RR. The coherence of the observations is satisfactorily encouraging the use of the data for further studies. Nevertheless, the MRR10 data should be used with caution because RR difference reaches 50 % between the disdrometer data and the MRR10 measurements at the lower level.

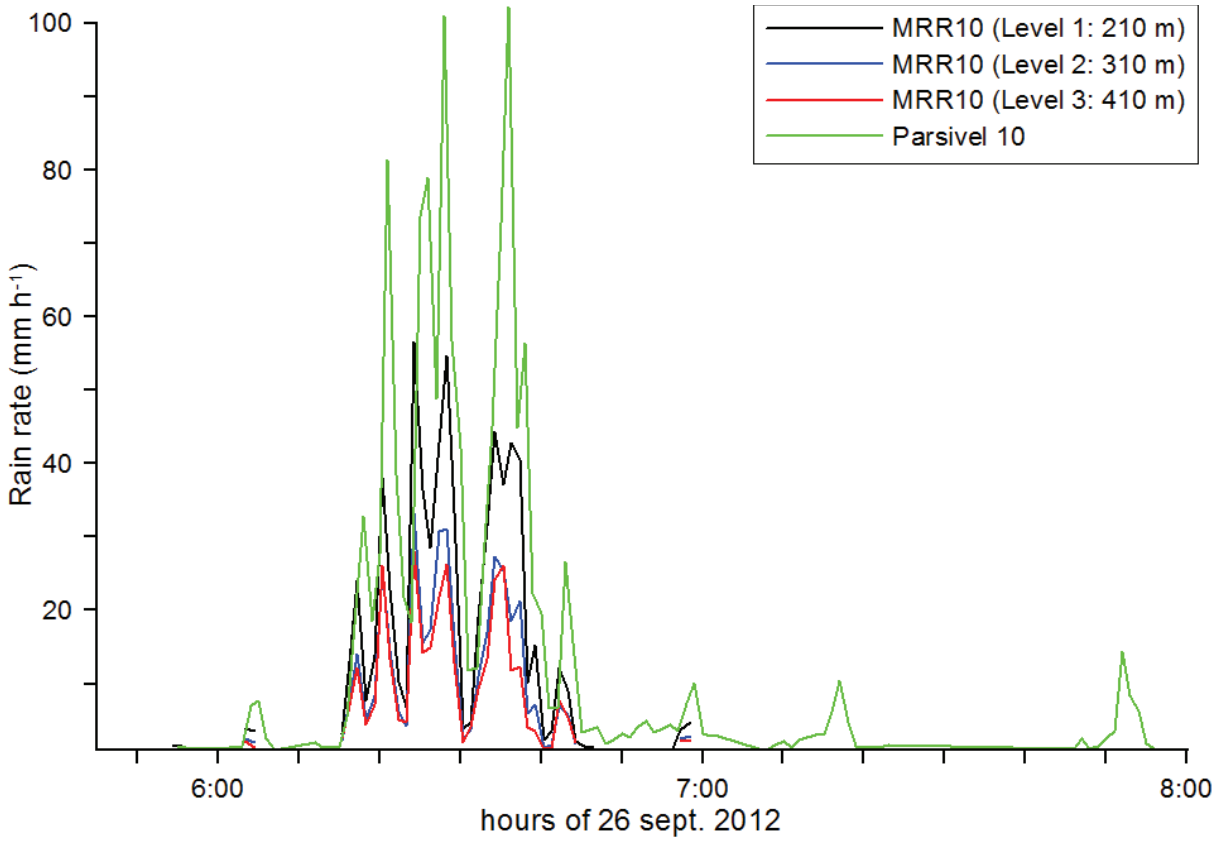

Figure 3.13: Rain rate (in mm h^{-1}) during IOP7a, as observed by the "Parsivel 10" disdrometer (green line) and retrieved by the observations from the instrument MRR10 at 3 levels (black line: at 210 m AGL, blue line: at 310 m AGL, red line: at 410 m AGL). All time series use a 1-min temporal resolution.

On the contrary, the same comparison would not be possible to be done for the instrument MRR9, due to the lack of instruments installed close to it that could provide comparable observations. Moreover, the MRR9 is close to the relief where the dynamics is more

complex and where MRR9 data could be affected by, e.g., the vertical wind. Consequently, in order to avoid misinterpretation, the MRR9 is not further used in the present study.

3.3.5 X-band radars

The X-band radars were deployed in order to provide precipitation features at high-resolution over a small catchment basin.

The X-band radar is a compact weather radar which operates at a frequency of 9.41 GHz. It provides observations of precipitating systems at very high resolution, enabling their small-scale dynamics to be documented.

Its operating principle (Zwiebel 2015) is the same as for other meteorological radars; it consists of a transmitter, an antenna and a receiver. A microwave signal is generated by the transmitter and is being focused into a small beam by the antenna. The radar beam is thus a series of short pulses that are being scattered by the target of interest (raindrops, hail, etc.). A small portion of the scattered energy is directed back toward the radar (echo) to be received by the antenna and analyzed by the radar signal processor. The return signal is proportional to the diameter (to the power of six) of the particles in the target echo.

The two X-band radars of LaMP (Laboratoire de Météorologie Physique) were placed at the northwest of the Cévennes-Vivarais, close to the mountain slope (see **Figure 3.2**). In particular, the radar X3 (placed at La Bombine) is located at the mountainous region, at the altitude of 975 m and the radar X4 (placed at Le Chade) is located at the altitude of 330 m. The vertical coverage of the radar X3 is restricted to a single elevation of 1.5° and its horizontal range is 36 km. It provides one image for every 30 s. Respectively, the X4 radar scans at 1°, 2° and 4° of elevation, it has a horizontal range of 21.6 km and a scan cycle of 3 min.

Figure 3.14 shows the radar reflectivity field observed by the X3 at four different moments during the IOP7a. These observations highlight the complex structure of the convective system and its spatial and temporal evolution.

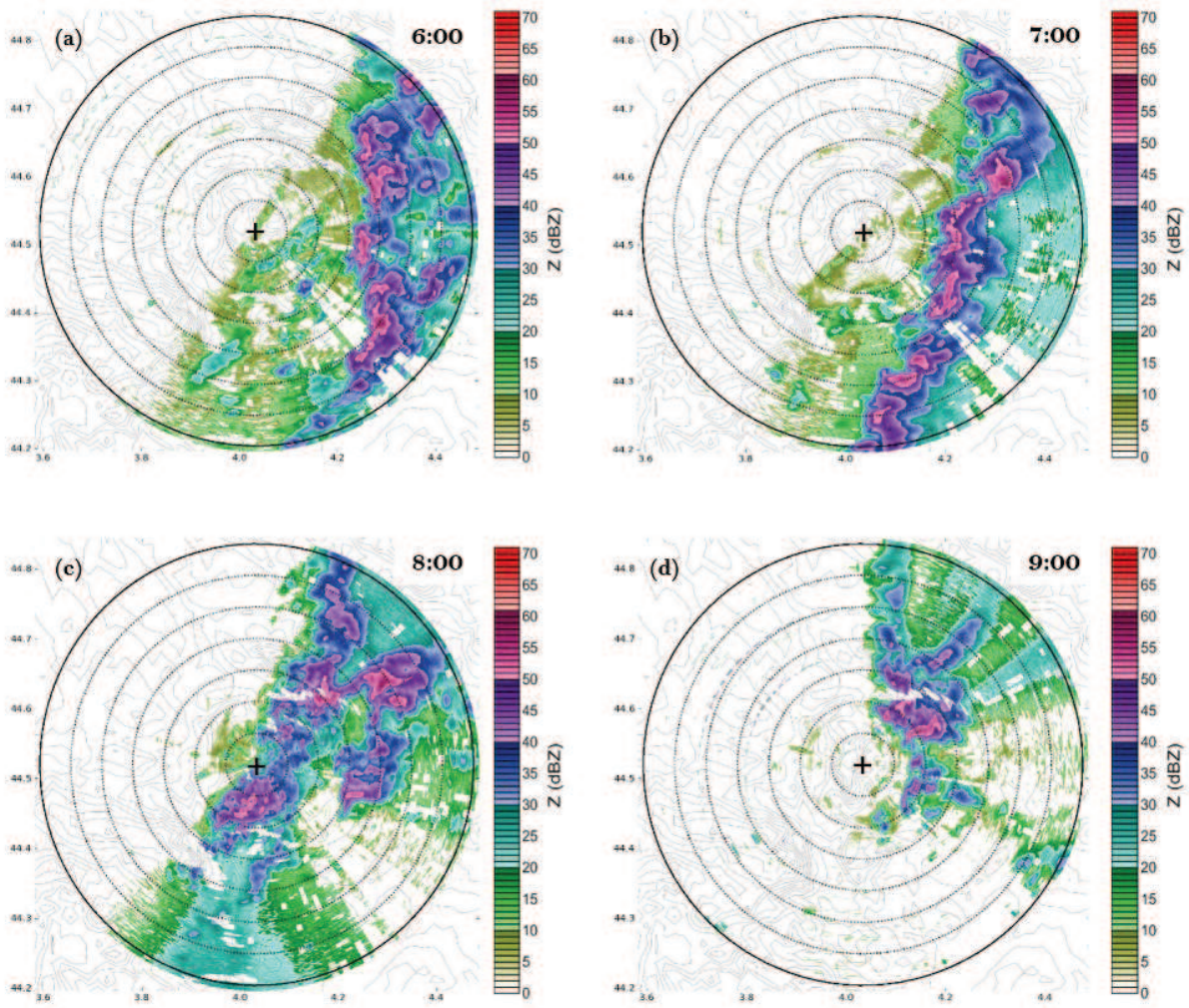

Figure 3.14: Plan position indicator (PPI) images of the observed radar reflectivity (in dBZ) from the X3 radar. The radar position is indicated by the cross in the center, whereas the concentric circles correspond to the different elevations of the radar beam at every 5 km to the radar position. The maximum height of the radar beam (external circle in bold black) is 1892 m. The grey lines represent the topography. Observations are presented here (a) at 6:00 UTC, (b) at 7:00 UTC, (c) at 8:00 UTC and (d) at 9:00 UTC.

Due to the location and the range of the X-band radars, their observational area have a common coverage, as shown in **Figure 3.2**. **Figure 3.15** shows the radar reflectivity field obtained with the X3 radar and with the X4 (with the 4° beam elevation) at 7:00 UTC. In the common observational area, a small convective cell (yellow circle on both panels) is observed with both radars. The altitude of the measurement at this point for the X4 is at 1030 m AGL and at 1500 m AGL for the X3. Note that the radar reflectivity of this cell is approximately 35 dBZ according to the X3 whereas it reaches 70 dBZ according to the X4. With a shift of only 460 m in the altitude of the radar beams, the increase of reflectivity by more than 35 dBZ seems not realistic. A deeper investigation of the X-band data shows a systematic overestimation of the reflectivity measured by the X4.

The radar team is still working on this overestimation, so the data of the X4 will not be used in this work.

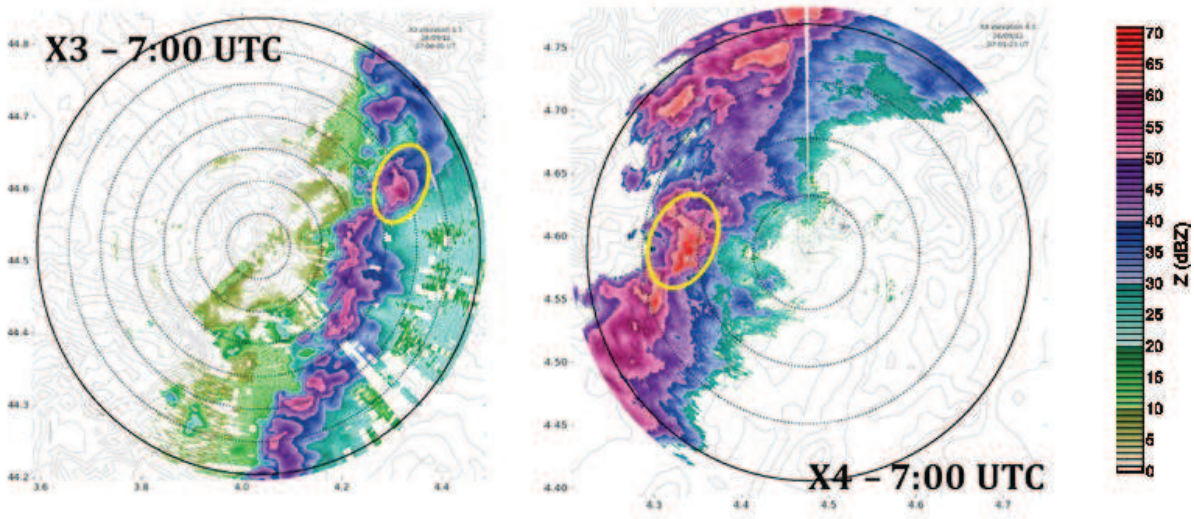

Figure 3.15: PPI images of the observed radar reflectivity (in dBZ) on 26th September 2012 at 7:00 UTC from the radars X3 (on the left) and X4 (on the right). For both radars, the concentric circles correspond to the different elevations of the radar beam at every 5 km to the radar position. The yellow circle indicates a convective cell observed by both radars in their common observational area.

Overall, the IOP7a was characterized by several ground-based instruments that provide details about rain properties. **Figure 3.16** summarizes the available instruments together with their main characteristics and associated observations.

In addition to these ground-based instruments, airborne measurements were performed on the 26th September 2012 in order to study the IOP7a convective system. These observations are presented in the next section.

	Radar X3	Radar X4	Parsivel S	MRR8	Parsivel 8	MRR9	Parsivel 9	MRR10	Parsivel 10
Location	La Bombine	Le Chade	La Souche	Le Pradel	Le Pradel	Saint Mélany	Saint Mélany	Saint Etienne de Fontbellon	Saint Etienne de Fontbellon
Altitude	975 m	330 m	900 m	303 m	303 m	313 m	313 m	210 m	210 m
Range/surface/vertical coverage	36 km	21,6 km	54 cm^2	403 m - 3403 m ASL	54 cm^2	413 m - 3413 m ASL	54 cm^2	210 m – 3210 m ASL	54 cm^2
Availability during IOP7a	Yes	Yes	Yes	No	Yes	Yes	No	Yes	Yes
Evaluated parameters	Radar reflectivity (dBZ)	Radar reflectivity (dBZ)	Rain rate (mm h^{-1})	-	Rain rate (mm h^{-1})	RWC (g m^{-3})	-	RWC (g m^{-3}), rain spectra	Rain rate (m mh^{-1}), rain spectra
Selected for this study	Yes	No	Yes	No	No	No	No	Yes	Yes

Figure 3.16: Summary of the specifications of the individual ground instruments for precipitation observations during HYMEX IOP7a, their availability, evaluated parameters and information about their use (or not) in the present study.

3.4 Airborne and in-cloud observations

Two French research airplanes performed flights during the IOP7a over the Cévennes region, equipped with different instrumentation. The ATR-42 was deployed for aerosol measurements and the instruments on-board the Falcon 20 provided information about cloud physical properties, such as the condensed water content, either measured directly or retrieved from the cloud radar reflectivity. The aircrafts were both operated by SAFIRE (Service des Avions Français Instrumentés pour la Recherche en Environnement). The trajectory of the Falcon 20 over the Cevennes-Vivarais is illustrated in **Figure 3.17**. More details about the ATR-42 flight track are given in **chapter 4**.

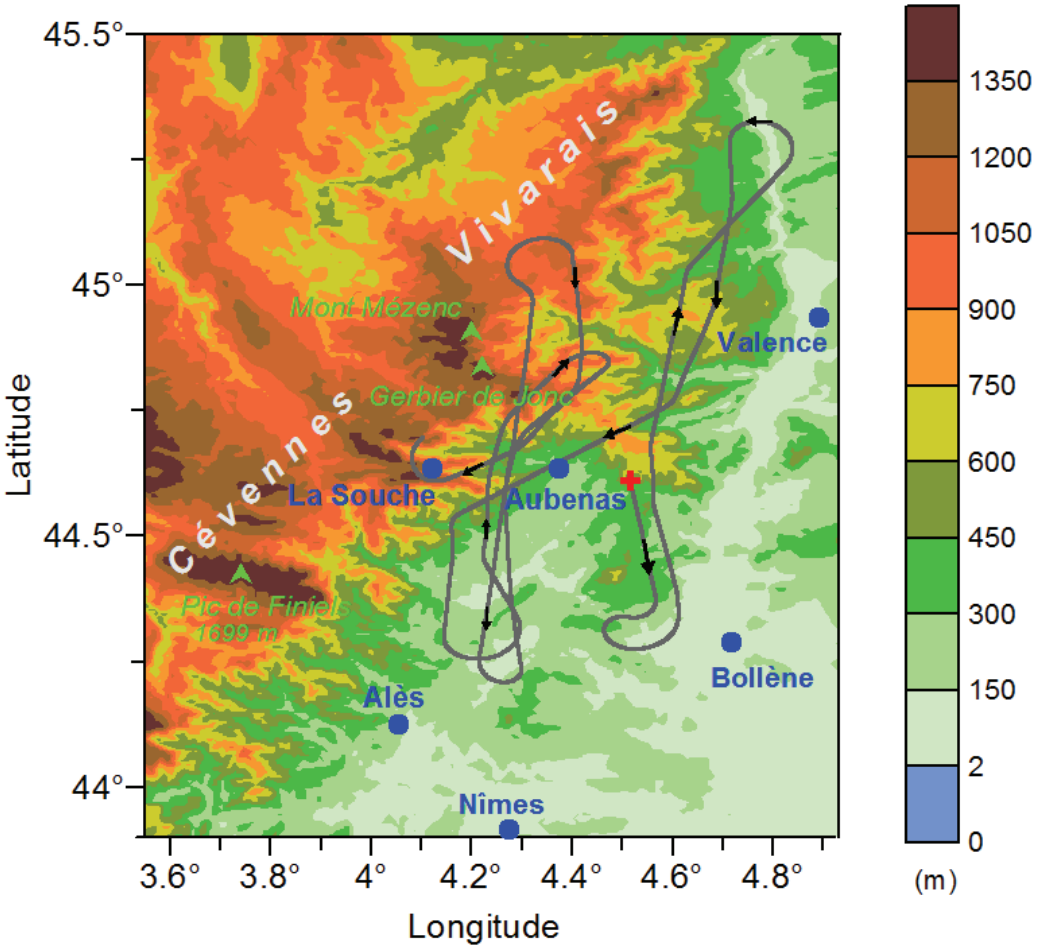

Figure 3.17: The part of the Falcon 20 flight track (grey line) over the Cévennes-Vivarais during IOP7a from 8:00 UTC (the position of the aircraft at this moment is indicated by the red cross) to 9:20 UTC. The black arrows indicate the direction of the aircraft.

The advantage of the airborne in-situ instruments is that they provide the most direct observation of cloud-related phenomena, as well as the microstructure of the precipitating systems. However, research flights also underlie air traffic regulation which

prohibits flights in levels below 3000 m a.s.l. and in fields of strong precipitation. Thus, the in-situ measurements of the Falcon 20 could only be performed in elevated altitudes between 3500 and 11000 m. The impossibility of flying inside the precipitating system during the entire flight time and the change of flight level leads to important limitations.

The present section starts with the description of the aerosol measurements from the instruments on-board the ATR-42. Afterwards, observations performed with instruments on-board the Falcon 20 are detailed.

3.4.1 Aerosol particle measurements

The ATR-42 performed 28 flights during the SOP1, between 11 September and 4 November 2012 (Rose et al. 2015). The airplane was equipped with an instrumental set-up including a Scanning Mobility Particle Sizer (SMPS) and a GRIMM Optical Particle Counter (OPC).

The SMPS spectrometer (Crumeyrolle et al. 2010) is widely used as the standard method to measure airborne particle size distributions. The measuring principle is based on the mobility of a charged particle in an electric field. When the particles enter the system, they are neutralized so that they have an equilibrium charge distribution. After they pass through a differential mobility analyzer (DMA), where each aerosol particle is classified according to its electrical mobility, only the particles of a narrow size range of mobility exit through the output slit. These particles are finally counted by a condensation particle counter (CPC) which determines their concentration at that size. The measuring method is independent of the refractive index of the particle and has a high degree of measurement repeatability.

The GRIMM OPC measures the size resolved number concentration per cubic centimeter of particles. The measuring principle of the OPCs is based on the fact that when a particle passes through a beam of light, some of the light is being scattered. Then, the pulses of the scattered light that reach the detector are being counted in order to determine the number of particles.

The SMPS provides particle size distributions with diameters from 20-485 nm with a time resolution of 130 s, whereas the GRIMM OPC measures in a range from 300 nm to 2 μm every 6 s. All the size distributions that are recorded at a constant altitude during the IOP7a can be fitted over the entire size range with 3 lognormal modes according to the same method as in Rose (2014). **Figure 3.18** summarizes the observations of the

aerosol particle concentrations by both the SMPS and the GRIMM OPC during the IOP7a at different altitudes from 200 m to 3700 m.

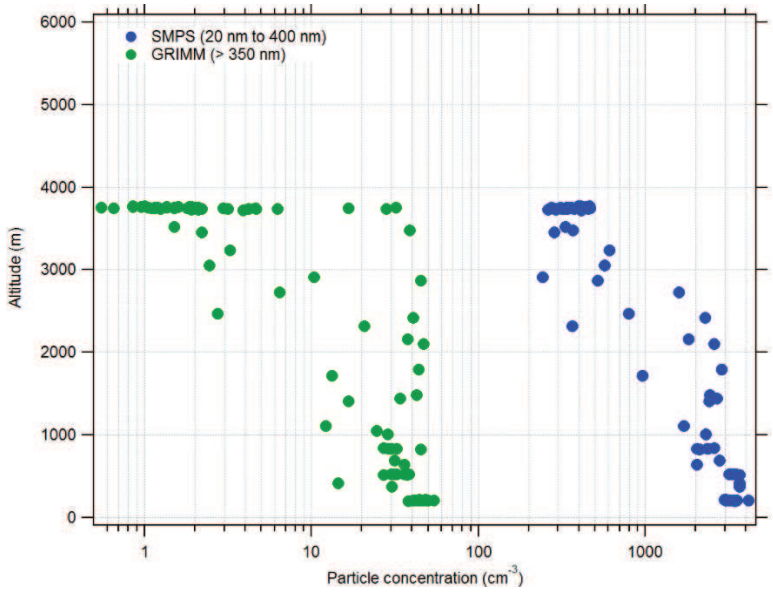

Figure 3.18: Observations of the aerosol particle concentration (number of particles per cm^3) as a function of the altitude a.s.l. (in m) by the SMPS and GRIMM OPC during the IOP7a. Each dot presents a measurement of the particle size distribution during 210 s.

This kind of observations are used in the present study for the model initialization. The obtained aerosol particle size distributions as well as the details about their 3 modes are further described in **chapter 4**. This section continues with the observations of the aircraft Falcon 20, used for comparison with model results.

3.4.2 Cloud hydrometeor probes

Two Optical Array Probes (OAPs) were on-board the Falcon 20 research aircraft. The 2D Stereo Probe (2D-S) by the Stratton Park Engineering Company (SPEC) provided hydrometeor measurements in a size range of 10-1280 µm (± 5 µm). The Precipitation Imaging Probe (PIP) by Droplet Measurement Technologies (DMT) provided measurements of larger cloud particle sizes in the range of 100–6400 µm (± 50 µm). The merging of the two imagers permits the sampling of a size range from 10 µm to 6400 µm, covering almost the entire size range of the hydrometeors in the atmosphere (cloud and precipitation).

The 2D-S imager (Lawson et al. 2006) is composed of 2 laser-diode array pairs which are placed perpendicular to each other and the strips are composed by 128 diodes with a

resolution of 10 µm. The PIP consists of a laser and a diode bar which includes 64 diodes with a resolution of 100 µm.

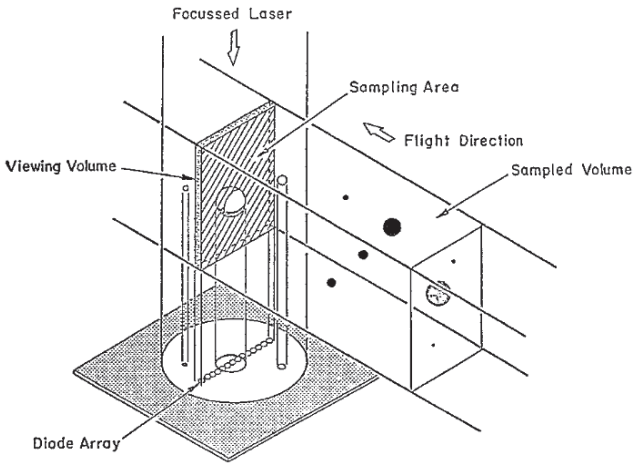

Figure 3.19: The optical shadowing principle of an OAP (Source: Baumgardner and Korolev 1997)

During the flight, the measuring system of the OAP (**Figure 3.19**) permits the passage of the hydrometeors between the diodes and the laser. This results in the darkening of some of the diodes which get a zero binary value in contrast with those that stay illuminated and have a binary value of 1 (i.e., **Figure 3.20**).

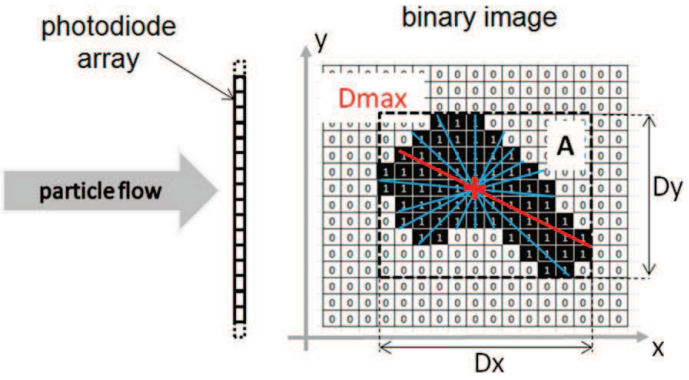

Figure 3.20: Definition of particle dimensions that are extracted from OAP binary images. The blue lines illustrate some possible diameters passing through the center of the image, whereas the red line is defined as the maximum dimension of the hydrometeor, D_{max}. (Leroy et al. 2016)

The values are updated every 500 ns (sampling speed: 200 m s^{-1}) and every 60 ns (sampling speed: 170 m s^{-1}) for the PIP and the 2D-S, respectively. This mechanism creates a black and white image representing the shadow of the particle (i.e. **Figure 3.21**) from which the maximum dimension[11] (D_{max}, **Figure 3.20**) of the hydrometeors is being retrieved. The number distribution of the hydrometeors $N(D_{max})$ and the distribution of

[11] The maximum dimension of the hydrometeor is defined as the longest straight line that covers the particle image and crosses at the same time the barycenter of the particle image (Fontaine et al. 2014).

particle aspect ratio[12] $A_s(D_{max})$ are calculated as a function of the D_{max}. From these two parameters, the in-situ particle size distribution is calculated that permits the retrieval of the reflectivity (for more details, see Drigeard et al. 2015). Finally, considering that the hydrometeor mass obeys the power-law relationship of the equation 3.2, the condensed water content (CWC) can be determined (equation 3.3).

$$m = aD_{max}^{\beta} \tag{3.2}$$

$$CWC = \int_{50\mu m}^{6400\mu m} N(D_{max}) a\, D_{max}^{\beta} dD_{max} \tag{3.3}$$

Coefficients α and β are determined by a variational calculation from the comparison of observed and calculated radar reflectivity (see Fontaine et al. 2014).

Figure 3.21a and **Figure 3.21**b show the 2-D images of hydrometeors obtained by in-cloud measurements during the HYMEX IOP7a, when the Falcon 20 was flying at the altitude of 3.7 km and 5.5 km, where the temperature was -2°C and -12°C respectively. The irregular shape of the particle images demonstrates that the ice phase seems to dominate in the measurements, and so, the CWC is probably equivalent to the ice water content (IWC). For this reason, these measurements will refer hereafter to IWC. Note that measurements of only liquid water content (LWC) are not available. The IWC calculated from the hydrometeor probe measurements (Fontaine et al. 2014) corresponds to the mean value of ten particle spectra (each one collected with 1 Hz). Due to this 10 s sampling time the IWC presents thus an average over a flight distance of 1.6 km.

[12] The particle aspect ratio A_s is defined by the quotient H/D_{max}, where H is the extension of the particle image which is perpendicular to the D_{max} and crosses the barycenter of the hydrometeor.

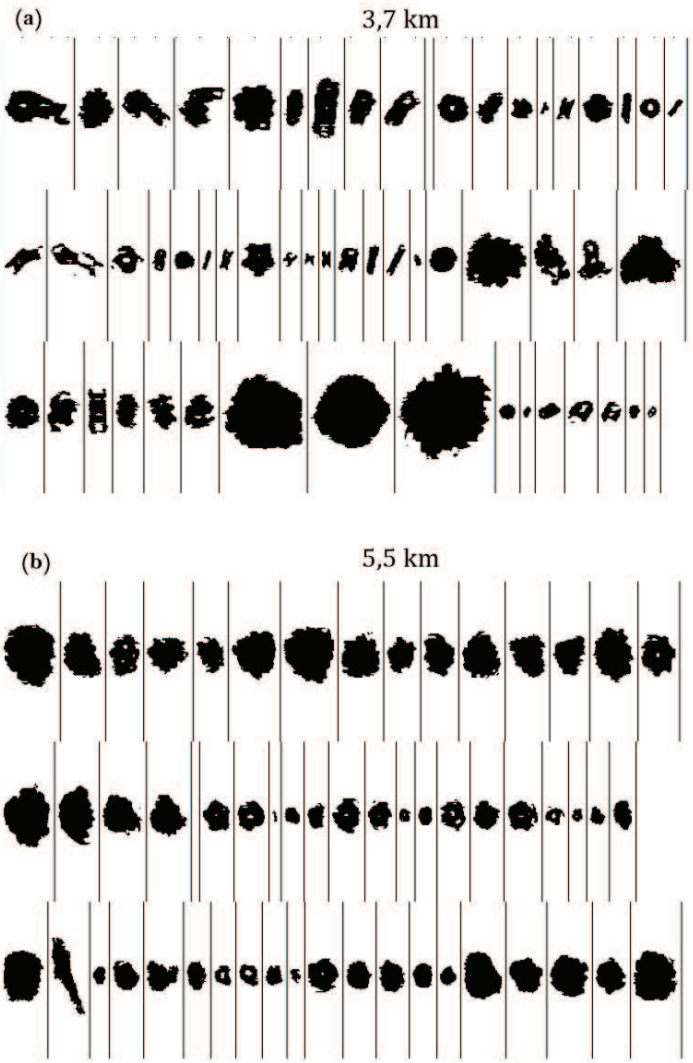

Figure 3.21: Hydrometeor observations by the 2D-S during the IOP7a at the altitude of (a) 3.7 km where the temperature was -2°C and (b) 5.5 km where the temperature was -12°C. The vertical bars indicate the maximum size of 1 mm.

In order to create a vertical profile from the individual in-situ data, the aircraft altitude was allocated to a vertical grid with a constant spacing of 300 m. The results of the observed in-situ IWC are displayed in the **Figure 3.22**, where the red curve shows the resulting profile of the mean in-situ IWC. The label of each altitude corresponds to the number of samples available for each selected altitude z (± 150 m). During this flight about 400 particle spectra were sampled with IWC larger than 0.03 g m^{-3}. Most spectra (65 %) were observed in the altitudes 3.75, 5.25 and 5.55 km (± 150 m). These measurements were taken during the time period from 8:18 UTC to 9:12 UTC, as depicted by **Figure 3.23**. For certain grid layers (e.g. between 4 to 5 km) no data are available. According to the standard deviation, IWC fluctuates significantly, in particular at flight altitudes between 5 km and 6 km with ± 0.6 g m^{-3}. For many levels above 5.7 km the number of samples stays

quite low and the resulting mean value of the retrieved IWC has thus only a limited significance. Mean IWC values calculated with a more significant sample size are given for altitudes of 7.05 km and 8.25 km, each covering a vertical range of ± 150 m.

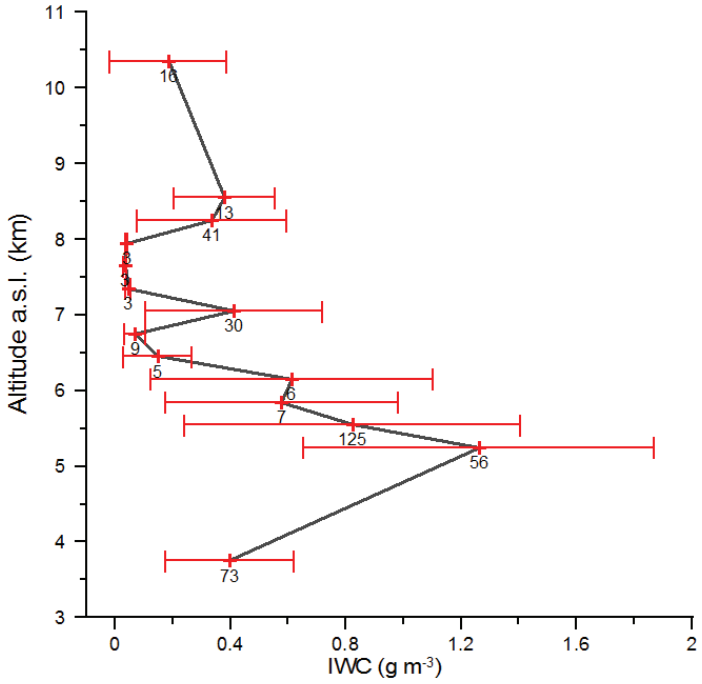

Figure 3.22: Mean vertical profile of the in-situ IWC (black line, in g m^{-3}) by the OAPs during the whole flight time of the Falcon 20 of the IOP7a along with the standard deviation of the measurements (in red color). The numbers indicate the number of particle spectra (10 s mean) that were used for the calculation of the mean vertical profile of the CWC.

The measurements of the mean IWC depend significantly on the location of the flight track inside the convective system. The samples of data at the altitude of 5.25 km were measured when the aircraft flew over the Vivarais mountains (surface elevation 1000-1200 m) where the strongest precipitation developed during IOP7a. The long flight track at 5.45 km however went along the foothills of Cevennes and Vivarais mountains, where the topography was typically below 500 m and the convective activity was significantly weaker during IOP7a.

Along with the hydrometeor probes, Falcon 20 carried also the cloud radar RASTA, whose description and observation products are presented in the next section.

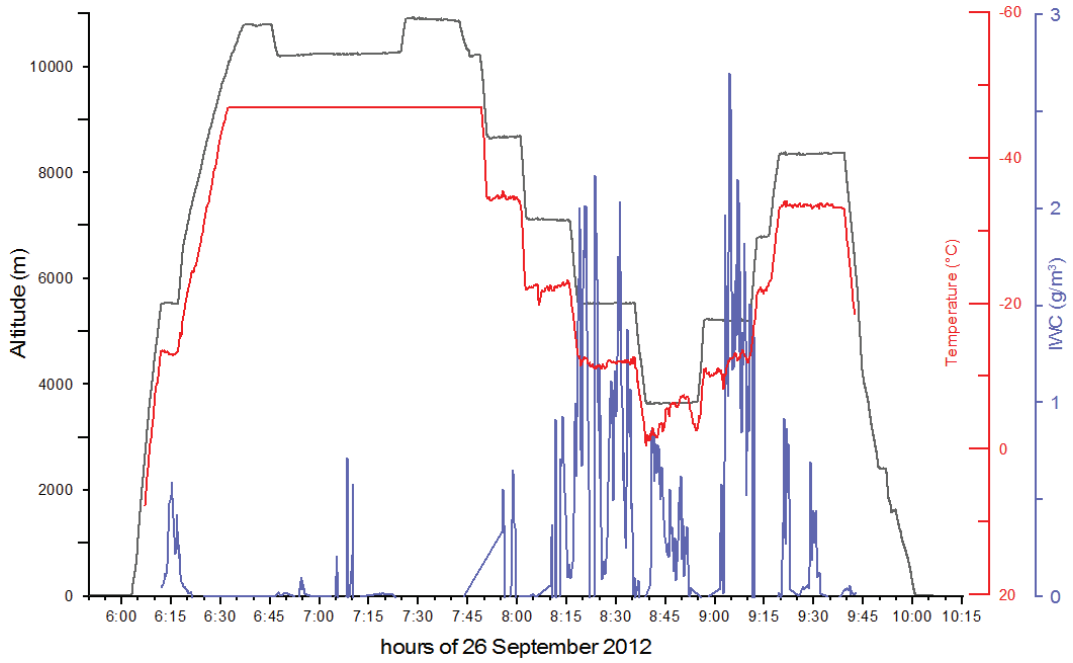

Figure 3.23: The measured temperature (red line, in °C) and the retrieved IWC (blue line, g m^{-3}) from the OAP observations during the IOP7a as a function of the time and the altitude (a.s.l.). The grey line corresponds to the flight altitude of the Falcon 20 aircraft which carried the instruments.

3.4.3 Cloud radar RASTA

RASTA (Radar Aéroporté et Sol de Télédétection des Propriétés Nuageuses) is a 94 GHz (W-band) Doppler cloud radar constructed by the Laboratoire Atmosphères, Milieux, Observations Spatiales (LATMOS) and deployed on board the Falcon 20 aircraft during the IOP7a.

It consists by 6 antennas with different viewing angles (**Figure 3.24**), 3 of which aiming upwards and 3 downwards. The radar reflectivity (the fraction of power backscattered by the clouds and precipitation) as well as the displacement speed are being restored with a resolution of 60 m along the sighting. RASTA scans at a range of 15 km with an integration time of 250 ms.

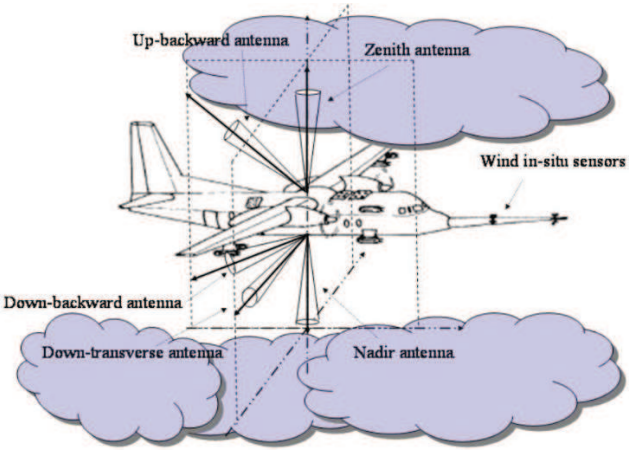

Figure 3.24: The cloud radar RASTA and its 6-beam configuration (Source: Delanoë et al. 2012)

The multi-beam antenna system of RASTA allows the measurement of the reflectivity by using the RadOnvar technique (Delanoë et al. 2007; Delanoë and Hogan, 2008) and the retrieval of the dynamic field of the clouds in 3 dimensions. **Figure 3.25** shows the temporal evolution of the radar reflectivity, as well as the regime of the vertical wind (updraft and downdraft structures), both as a function of the altitude, during the whole flight time of the IOP7a.

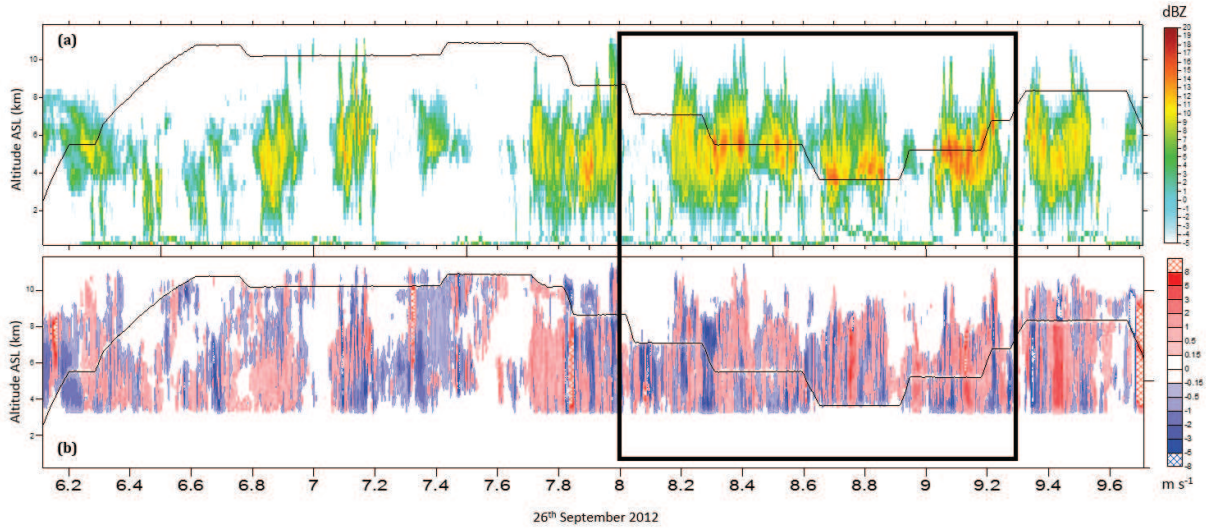

Figure 3.25: Observations of (a) Cloud radar reflectivity factor (in dBZ) and (b) Vertical wind (in ms^{-1}) by the RASTA radar during the IOP7a as a function of the time (decimal) and the altitude above sea level (in km). The flight altitude is represented in both figures by the black line. The black square illustrates the flight period presented in the **Figure 3.26**.

RASTA cloud radar provides reflectivity profiles with a time resolution of 1.5 s. Note that as its spatial and temporal resolution is much finer than the model resolution (which is discussed in **chapter 4**), the observed data were averaged over 6 s in time and over 300 m in the vertical. The aircraft speed was about 160 - 170 m s^{-1}, therefore the averaged

profiles of reflectivity and of other retrieved parameters present a mean over a horizontal distance of about 1 km. These data are obtained after the calibration of RASTA, that is described in Bouniol et al. (2008). Moreover, the gaseous attenuation is computed using the model by Liebe (1985) with the cumulated attenuation to be the saved variable for each radar gate as a function of the distance from the aircraft. The rain attenuation is considered, too, in RASTA data as a function of the gaseous attenuation (for more details see RASTA product description 2016, private communication with J. Delanoë).

In the present analysis the data which originate from the 4 first radar gates below and above the aircraft are excluded. Indeed, as explained in Bouniol et al. (2008), the radar does not provide reliable measurements for these radar gates because the receiver is obstructed during emission. Therefore, the data next to the aircraft height were calculated by interpolation from the reflectivity that was observed 240 m (or 180 m) below and above the aircraft.

3.4.3.1 RASTA Radar reflectivity

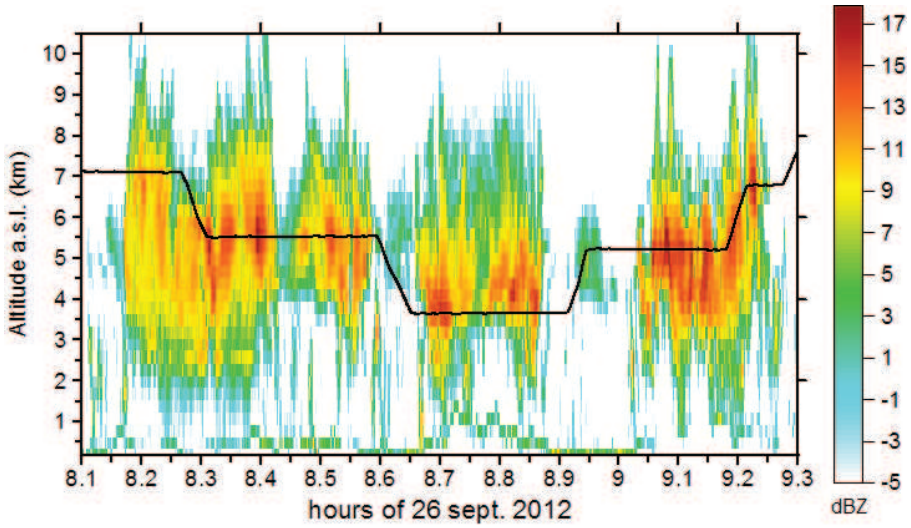

Figure 3.26: Zoom of the 95GHz cloud radar reflectivity observations from RASTA in the time period from 8:00 UTC to 9:20 UTC.

As seen in the **Figure 3.25**, the Falcon 20 was flying at altitudes higher than 8 km for almost half of the flight time. After 8:00 UTC, the aircraft descended to an altitude of 7 km where it stayed for about 15 min and then it reached the cloud system, according to **Figure 3.23**, which show high values of the observed cloud radar reflectivity and of the retrieved IWC. A zoom in the time period when highest values of radar reflectivity

occurred, from 8:06 to 9:20 UTC, is depicted in the **Figure 3.26**. This zoom illustrates the vertical structure of the cloud field encountered during IOP7a over the Cévennes Mountains (see **Figure 3.17**).

According to **Figure 3.26**, it seems that for most of the time the highest cloud radar reflectivity occurred in immediate vicinity of the aircraft location. It seems, thus, that the signal decreases with increasing distance from the aircraft, i.e. the more the cloud target is distant from the aircraft, the signal is attenuated. A retrieval technique developed by J. Delanoë (private communication) allows to take into account this attenuation of the signal. The corrected reflectivity forward modeled from the retrieval results is shown in the **Figure 3.27**. The regions which are next to the aircraft and below the melting level (around 3.6 km) were omitted in this figure, as attenuation below the melting level becomes more important. We can note that the magnitude of the reflectivity increases significantly, even reaching unrealistic values, at several locations (up to 50 dBZ, not shown in the **Figure 3.27**).

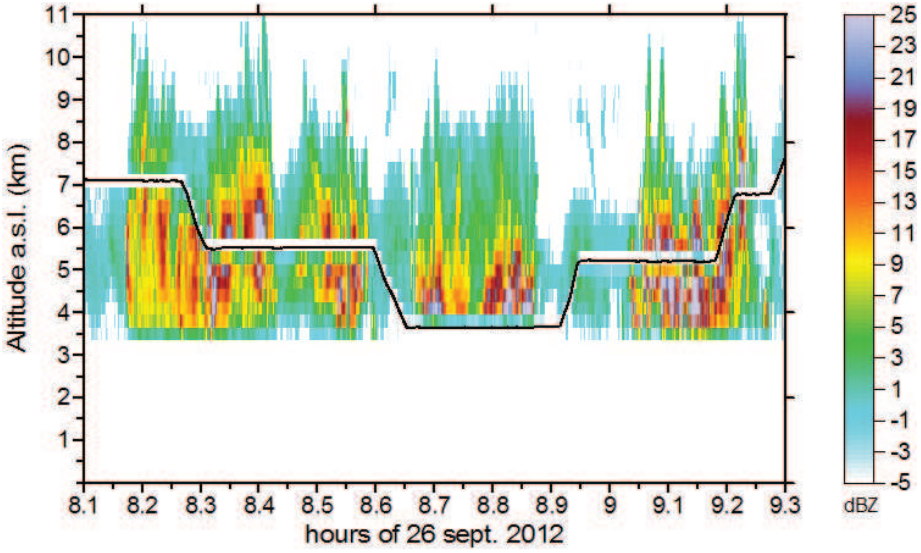

Figure 3.27: Forward modelled 95GHz cloud radar reflectivity corrected for attenuation for the time period from 8:00 UTC to 9:20 UTC.

In order to better illustrate the effect of attenuation, the variation of the reflectivity (as in **Figure 3.26**) was analyzed as a function of the distance from the aircraft. The reference level ($Z^*_{aircraft}$) is given by the equation 3.4:

$$Z^*_{aircraft} = Z^{time}_{aircraft} \pm 240\ m \qquad 3.4$$

and this omits the deficient reflectivity measurements just above and below the aircraft.

The distance between the reference level ($Z^*_{aircraft}$) and any level above (or below) is called Δz and it represents the ordinates in **Figure 3.28**. The difference of reflectivity $\delta Z_{95}(\Delta z)$ is defined as in equation 3.5:

$$\delta Z_{95}(\Delta z) = Z_{95}(Z^*_{aircraft}) - Z_{95}(\Delta z) \qquad 3.5$$

The term $\delta Z_{95}(\Delta z)$ expresses the variation of Z_{95} with increasing distance Δz from the aircraft. Negative values of $\delta Z_{95}(\Delta z)$ indicate weaker reflectivity compared to the aircraft level, whereas positive values of $\delta Z_{95}(\Delta z)$ indicate stronger reflectivity compared to the aircraft level.

Figure 3.28a and **Figure 3.28**b show the variation of reflectivity δZ_{95} observed in the first 3.5 km above the aircraft, while it was flying in the center of the clouds (at altitudes between 3.5 km and 7 km) and at altitudes higher than 7 km. This data analyses restricts to observations for which $Z_{95}(Z^*_{aircraft})$ > 2 dBZ and this means that the aircraft was inside cloudy air or very close to the clouds.

Both **Figure 3.28**a and **Figure 3.28**b clearly show that the majority of $\delta Z_{95}(\Delta z)$ values is positive. A clear tendency of decrease in reflectivity with increasing altitude can be detected. This behavior is even more pronounced for the results presented in the **Figure 3.28**b. It is most likely due to the fact that cloud density (i.e., hydrometeor concentration and size) decreases in the upper layers when approaching cloud top.

Figure 3.28c and **Figure 3.28**d illustrate the variation of reflectivity measured below the aircraft. The flight levels selected for the **Figure 3.28**c restrict to the range from 5 to 7 km in order to stay above the terrain height (maximum of 1500 m). This illustration displays the same finding for δZ_{95} as in the **Figure 3.28**a and **Figure 3.28**b: most of the points demonstrate that reflectivity decreases with increasing distance from the aircraft. This is most surprising as in the range Δz from 2 to 3.5 km below the aircraft the encountered reflectivity $Z_{95}(\Delta z)$ comes from altitudes where the temperature is higher than 0°C i.e., where raindrops are present. As the backscatter of raindrops is larger than for ice hydrometeors, an increase of the reflectivity would be expected there, and hence a decrease of δZ_{95}. This is a clear signature of a strong attenuation of the signal.

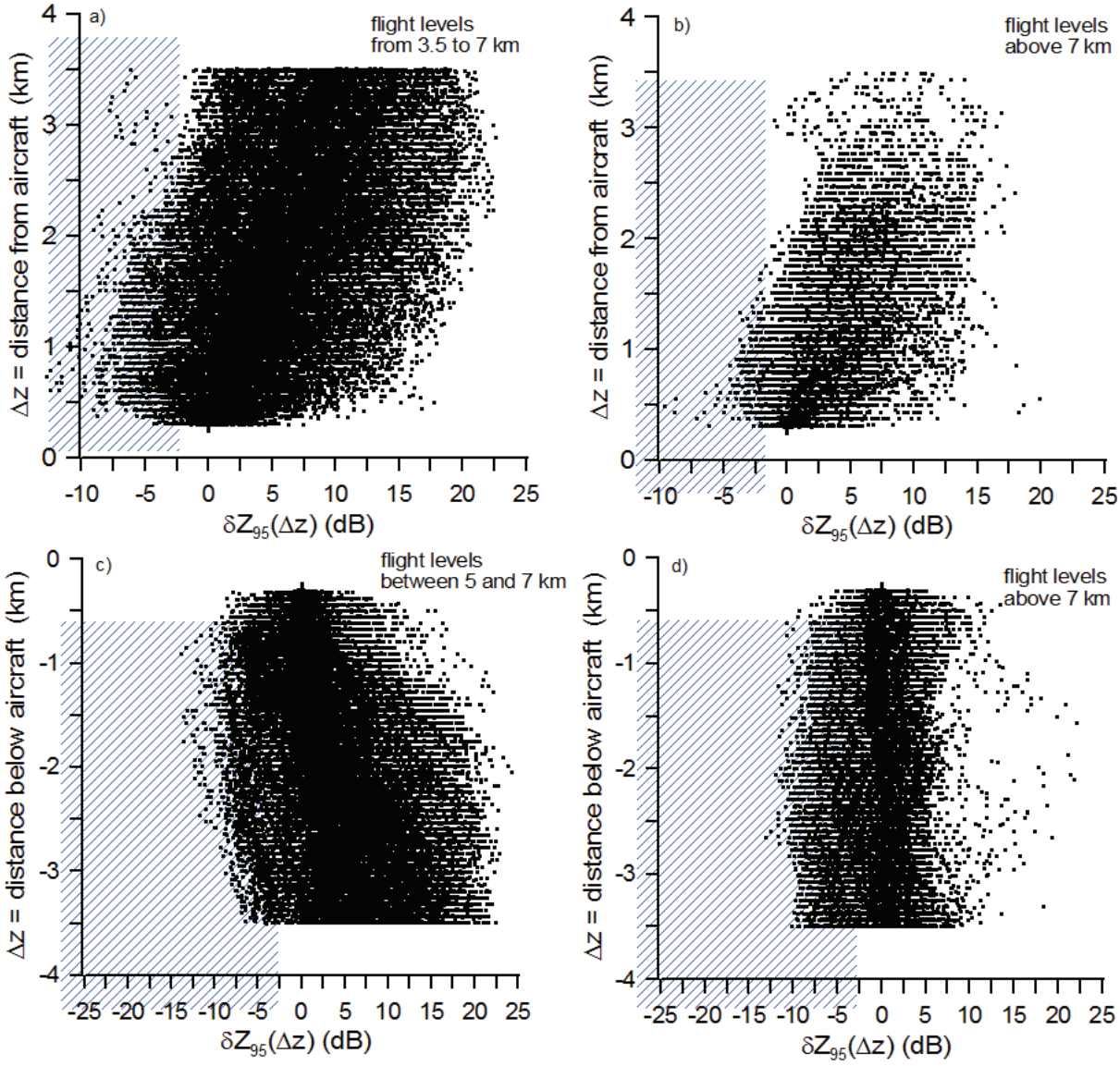

Figure 3.28: Difference ($\delta Z_{95}(\Delta z)$, in dB) between the reflectivity next to the aircraft and levels **ABOVE** the aircraft for flight altitudes (a) between 3.5 km and 7.0 km and (b) higher than 7 km. Also, difference ($\delta Z_{95}(\Delta z)$, in dB) between the reflectivity next to the aircraft and levels **BELOW** the aircraft for flight altitudes (c) between 5 km and 7 km and (d) higher than 7 km. Positive difference means the radar reflectivity is higher close to the aircraft, whereas negative difference means the radar reflectivity is higher at the considered altitude far from the aircraft.

Finally, **Figure 3.28**d shows the results of δZ_{95} looking downward from the elevated flight levels (7 to 11 km). In contrast to the previous figures the numbers of positive and negative δZ_{95} values are quite balanced in this scatter plot. As already mentioned, the **Figure 3.25** indicated that the aircraft flew most of the time at the cloud top (flight levels > 7 km occur before 8:00 UTC and after 9:30 UTC). Therefore, the reflectivity would be expected to increase essentially below these altitudes, leading to negative δZ_{95} values in

the **Figure 3.28**d. This however is not the case and this fact underlines again our suspect that strong attenuation influences the observations available from the 95GHz airborne radar.

3.4.3.2 Retrieved IWC from RASTA

Two different techniques were used by Delanoë et al. (2014) in order to determine the profiles of IWC from the RASTA observations during HYMEX SOP1. The first one is a retrieval technique (corresponding to retrieved IWC in **Figure 3.29**) which assumes that all the hydrometeors are ice crystals. According to this technique, the number distribution of the hydrometeors can be described in a normalized way by the mean volume weight diameter D_m, the scaled number concentration N^* and a modified gamma distribution representing the normalized shape of the distribution. The variations of N^* and D_m allow to find the spectrum which fits best the observed Z_{95GHz} values. Consequently, the IWC can be calculated using Delanoë et al. (2014), as shown in the equation 3.6:

$$IWC = \frac{\pi \rho_w}{6} N^* D_m \frac{\Gamma(4)}{4^4} \qquad 3.6$$

The second technique determines IWC from RASTA reflectivity observations (corresponding to parameterized IWC in **Figure 3.29**) using the parameterization from equation 3.7. However, the coefficients α and β in equation 3.7 can vary significantly depending on the type of ice clouds. For the calculations, a temperature dependency of the coefficients α and β was used (private communication with J. Delanoë).

$$IWC = \alpha Z_{95GHz}^{\beta} \qquad 3.7$$

As already mentioned, in order to calculate the mean profiles of IWC, the data were averaged over 300 m in the vertical and over 1 km in the horizontal (flight) direction. The present analysis was restricted to values not affected by attenuation and where only ice was present (according to the corresponding flags available in the data files). Furthermore, in order to focus on the cloud area, only IWC larger than 0.01 g m^{-3} are used hereafter.

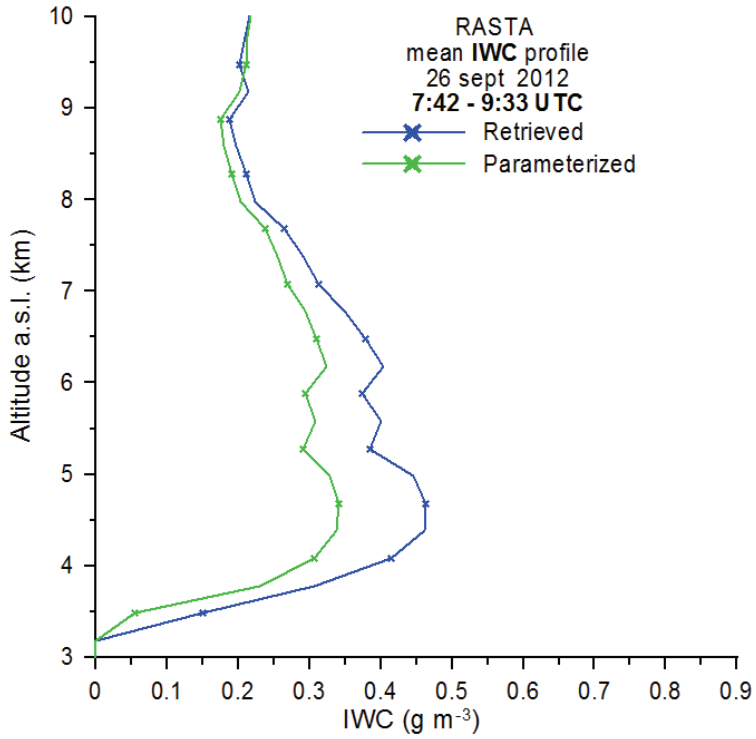

Figure 3.29: Mean vertical profile of IWC from RASTA reflectivity measurements. The blue curve includes all retrieved data above and below the aircraft (via equation 3.6) and the green curve shows the IWC profile using the parameterization of the equation 3.7.

Figure 3.29 shows the mean vertical profiles for the retrieved IWC (blue curve) and the parameterized IWC (green curve). According to this figure, the results for both IWC differ significantly in magnitude. The mean profile of the parameterized IWC is about 20% less that the retrieved one. Both profiles have a similar shape with a slight maximum in an altitude between 4 and 5 km and they decrease slowly in levels higher than 6 km. In contrast, the IWC decreases rapidly down to the melting level at 3.6 km. Both profiles also show a minimum in strength for levels between 5 and 6 km. An important part of the data ensemble was collected when the aircraft flew in altitudes around 5.3 and 5.6 km (see **Figure 3.25**). As reflectivity measurements close to the aircraft (± 240 m) are not reliable, these data were excluded from the construction of the mean IWC profiles and interpolations between observations below and above were done. **Figure 3.29** shows that the estimation of the IWC profiles is still affected, and hence suggests that more data might need to be excluded. The corresponding range of altitude will not be considered for the analyses in order to avoid misinterpretation.

3.4.3.3 Comparison between RASTA retrieved IWC and in-cloud observations of IWC

During the IOP7a, the derived CWC from in-cloud measurements (or microphysics probes) is considered equivalent to the IWC (see **section 3.4.2**). Thus, it can be compared with the RASTA retrieval of the IWC. **Figure 3.30** presents the mean vertical profile of the IWC retrieved by RASTA observations together with the corresponding IWC from the in-situ probes.

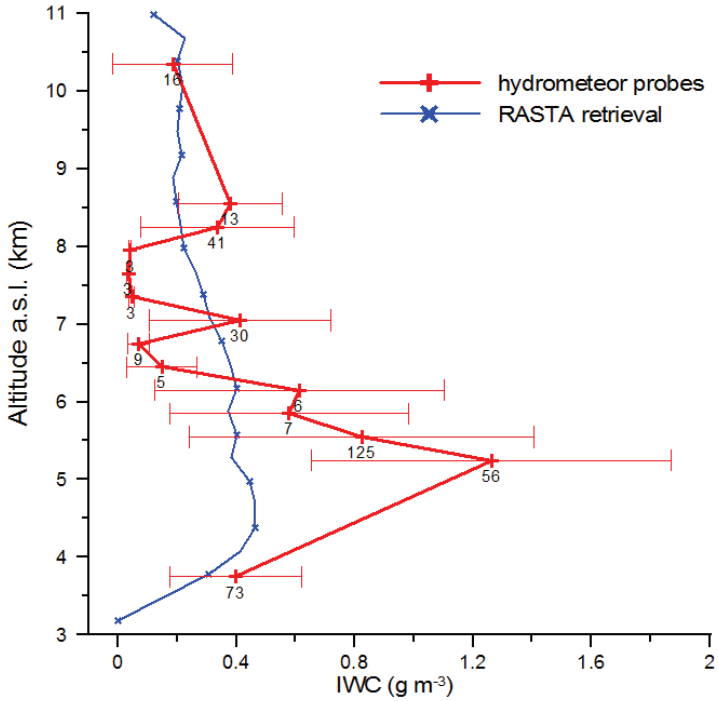

Figure 3.30: Mean vertical profile of the retrieved IWC (black line, in g m^{-3}) by the OAPs during the whole flight time of the Falcon 20 of the IOP7a along with the standard deviation of the measurements (horizontal thin red lines), as in **Figure 3.22**, and along with the mean vertical profile of the IWC retrieved by the RASTA observations.

Both mean vertical profiles were obtained by considering all the cloudy grid points (IWC ≥ 0.01 g m^{-3}). The IWC obtained by the hydrometeor probes exceeds the one obtained by RASTA except for the altitudes between 6 km and 8 km. In this layer, the values from the RASTA retrieval are about 50% smaller than the ones by the hydrometeor probes, except from the altitude of 7 km where the IWC from RASTA exceeds the value obtained by the hydrometeors. The biggest difference between the two IWC profiles is found at the altitude of 5 km and the smallest ones between 3 km and 4 km, as well as above the 10 km.

Thus, the available in-cloud measurements during the IOP7a and the corresponding IWC retrievals have significant differences and are attached with some uncertainties. Consequently, it is difficult to conclude about the precision and quality of the aforementioned products. However, regarding the absence of other measurements to characterize in-cloud properties (e.g. lidar) during the IOP7a, the present data is being used as indicative information when compared with model simulation results (see **chapter 4**).

3.4.3.4 Retrieved wind velocity from RASTA

RASTA measurements include also measurements of the Doppler wind velocity. Combining the observations of its multi-beam antenna system makes it possible to retrieve the 3D wind field in the cloud. The present analysis is restricted to the vertical wind component w. The resulting vertical wind field during the whole flight time w(z, t) is illustrated in **Figure 3.25**b. **Figure 3.31** shows the wind field over the time period between 8:00 and 9:20 UTC, when the aircraft was over the Cévennes-Vivarais area (see **Figure 3.17**). Note that the color scale used is different between **Figure 3.25**b and **Figure 3.31**. Locally, vertical wind can reach values up to +18 or down to -15 m s^{-1} (not shown).

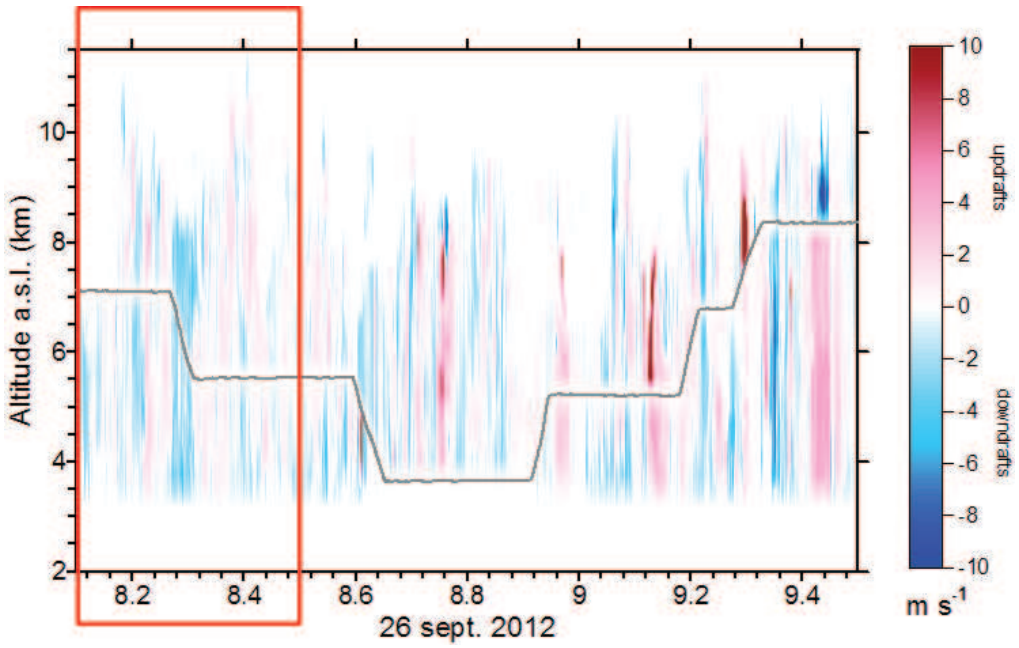

Figure 3.31: Temporal evolution of the vertical wind (w) retrieved from RASTA measurements during IOP7a for the time period between 8:00 UTC and 9:20 UTC as a function of the flight altitude (black line). The red rectangle presents the selected period shown in **Figure 3.32**.

However, a more detailed comparison of the vertical wind with the orientation of the aircraft shows that the retrieved vertical wind is strongly influenced by the roll of the aircraft. Indeed, in **Figure 3.32** the retrieved vertical wind field and the roll angle of the aircraft are plotted and illustrate the correlation between aircraft roll and intensity of the vertical wind. The time period 1 (indicated by green rectangle in **Figure 3.32**) with intense updrafts is associated to a roll angle that reaches up to 30° whereas the time periods 2 and 3 (indicated by pink and purple rectangle respectively in **Figure 3.32**) with intense downdrafts are associated to a roll of ~ -30°. In order to avoid this technical problems, the retrieved vertical wind should be considered when the roll is ~ 0°. Therefore, the retrieved vertical wind data usable in this study decreases significantly, especially if in-cloud data are selected. Thus, this data will not be further used for this study.

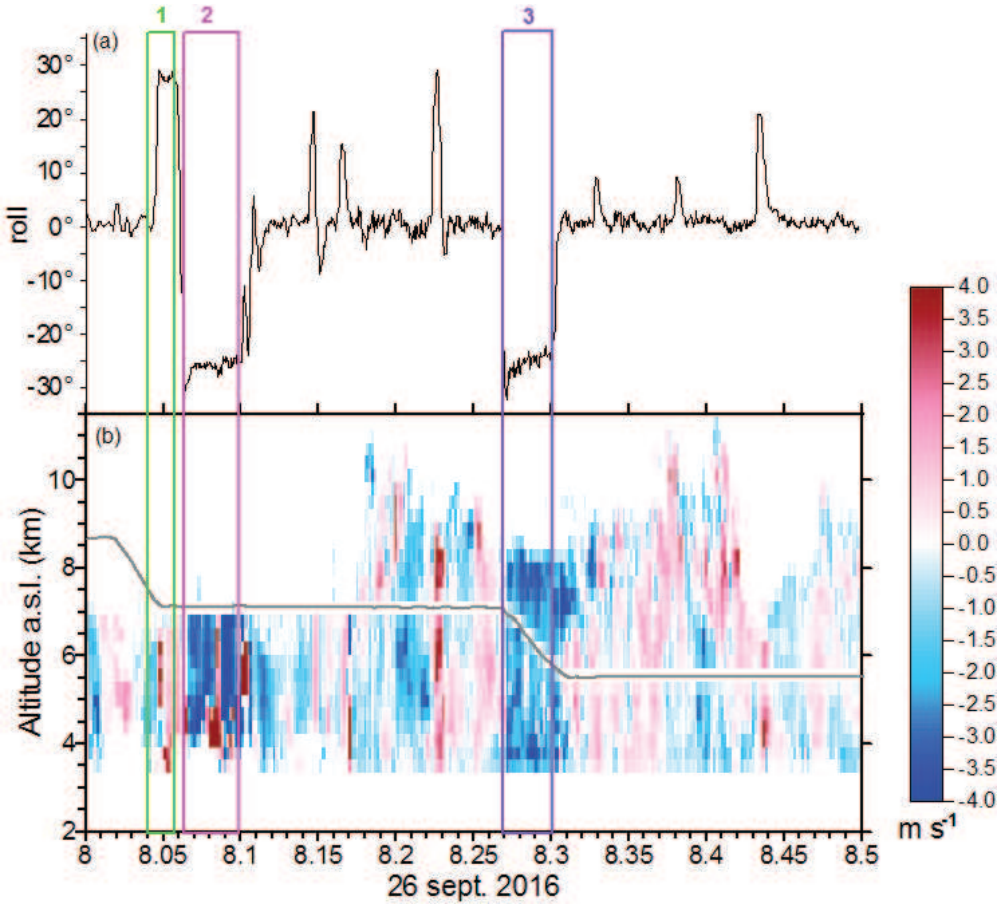

Figure 3.32: (a) Roll angle of the aircraft during the period indicated in **Figure 3.31**. (b) Retrieved vertical wind (in m s^{-1}) at the same time. Time is given in decimal format.

To sum up, in the present section the different observations from ground-based and airborne instruments were assessed. KED QPE and observations by the X-band radar X3 are considered as reliable and will be used in the next chapter to compare with model

results at the surface. The observations from the MRR10, Parsivel 10, Parsivel S and the ones from RASTA cloud radar, as well as the airborne measurements of hydrometeor spectra (2D-S and the PIP) will provide features of the in-cloud microphysics and additional constraints to model results.

4 Simulation of the HYMEX IOP7a heavy precipitation event with the DESCAM-3D cloud microphysics model

In the previous chapters, the prevailing synoptic conditions and the temporal and spatial evolution of the intense precipitation event of the HYMEX IOP7a have been discussed, as well as the characteristics of the detailed cloud model DESCAM-3D. The present chapter is dedicated to the simulation of the HYMEX IOP7a with the DESCAM-3D model. The analysis of the simulation results takes place in order to confirm the model's ability to provide detailed information on the process during this heavy precipitation episode.

In a first step, the set-up used in order to reproduce the features of the IOP7a system is described. Thereafter, the ability of DESCAM-3D to simulate this intense system is evaluated thanks to comparisons (both qualitative and quantitative) between simulation results and available HYMEX observations, presented in chapter 3. Finally, the impact of the initial large scale model set-up on the simulation results will be assessed.

4.1 Description of the model set-up

In order to make the simulation of the HYMEX IOP7a as realistic as possible, the atmospheric synoptic conditions which prevailed on the 26th September 2012 (during the IOP7a), as well as the observed aerosol particle regime were used for the initialization of

the model. These two aspects, as well as the domain properties of DESCAM-3D represent the model set-up and are being discussed hereafter.

4.1.1 Aerosol particle properties

The aerosol particle spectrum used for the present study was measured during the flight[13] of the ATR-42 aircraft thanks to SMPS and GRIMM OPC instruments (see **chapter 3**) in the morning of the 26th of September 2012 from 6:00 UTC to 9:30 UTC, over the Gulf of Lion. The area of measurements is presented in the **Figure 4.1**. The origin of the air masses that carried the measured aerosol spectra are also shown through their 3-day back trajectories (Rose et al. 2015) which were calculated every 5 min along the flight path with the Hybrid Single-Particle Lagrangian Integrated Trajectory (HYSPLIT) model. According to **Figure 4.1**, these air masses passed over continental and/or urban areas. All measured air masses followed the south-western horizontal air flow that characterizes a Cévenol episode (see **section 3.2**).

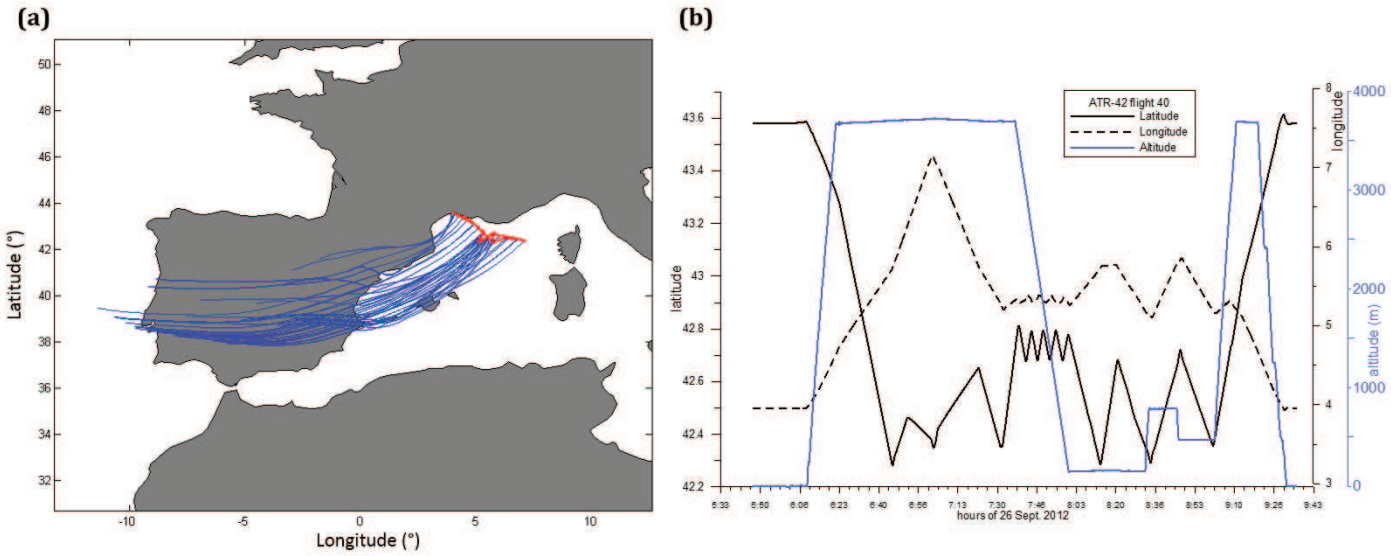

Figure 4.1: (a) Backward trajectories (blue lines) of the air masses of the measured aerosol particle spectrum on the 26th September 2012 (IOP7a). The part of the ATR-42 flight where the aerosol particle measurements took place is indicated by the red line. (b) Aircraft position of the ATR-42 as a function of the time (in hours) during the morning of the 26th September 2012 (corresponds to the red line of (a)). The black continuous line corresponds to the latitude, the black dashed line represents the longitude and the blue line indicates the altitude (in meters) of the aircraft.

The on-board instruments performed measurements at various altitudes from 0.2 km to 4.0 km. As an example, the number size distribution of the aerosol particle spectra at four

[13] This flight is marked in the HYMEX database as "ATR-42 flight 40".

different altitudes, which are 0.2 km, 0.4 km, 0.8 km and 3.7 km above sea level, together with their fittings is presented in **Figure 4.2**.

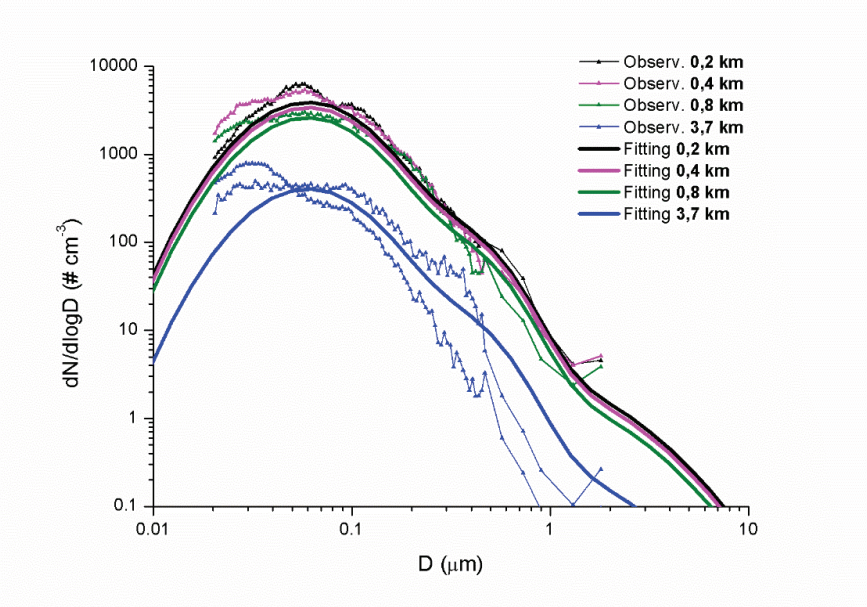

Figure 4.2: Number density distributions of the aerosol particle spectra (# cm^{-3}) observed by the SMPS and the GRIMM OPC at different altitudes (thin lines with triangles) together with the respective calculated fittings of each observed aerosol particle spectrum (thick lines).

For spectra observed close to the surface, the maxima are found for diameters of about 0.05 µm, whereas the maxima for spectra observed at higher altitudes (i.e. at 3.7 km) are found for diameters of about 0.02 µm, as seen in **Figure 4.2**.

For the present study, considering the necessary aerosol features for DESCAM initiation, the surface aerosol particle spectrum is required. **Figure 4.3** shows the aerosol particle distributions observed by SMPS and GRIMM at an altitude of 0.2 km (i.e. the lowest level of observations). The SMPS and GRIMM ranges of observations are different and permit to obtain aerosol properties in a diameter range from 0.02 µm to 2.0 µm. The fitting method gave 3 different modes characterizing the Aitken, accumulation and coarse modes of the aerosol particles (**Figure 4.3**).

The properties of each of the three modes, namely the concentration in number of aerosols, N_i, the geometric mean diameter, D_i, as well as the logarithm of the geometric standard deviation, σ_i were used for the initialization of DESCAM-3D and they are presented in **Table 4.1**. In DESCAM-3D model, the aerosol particles are assumed to be ammonium sulfate that is 40 % soluble with molecular weight of 132 g mol^{-1} and 60 % of insoluble silicates. Also, the aerosol concentration decreases exponentially up to 3.7 km

and is kept constant above this level. These assumptions are in agreement with the HYMEX observations during the IOP7a (e.g. **Figure 3.18**).

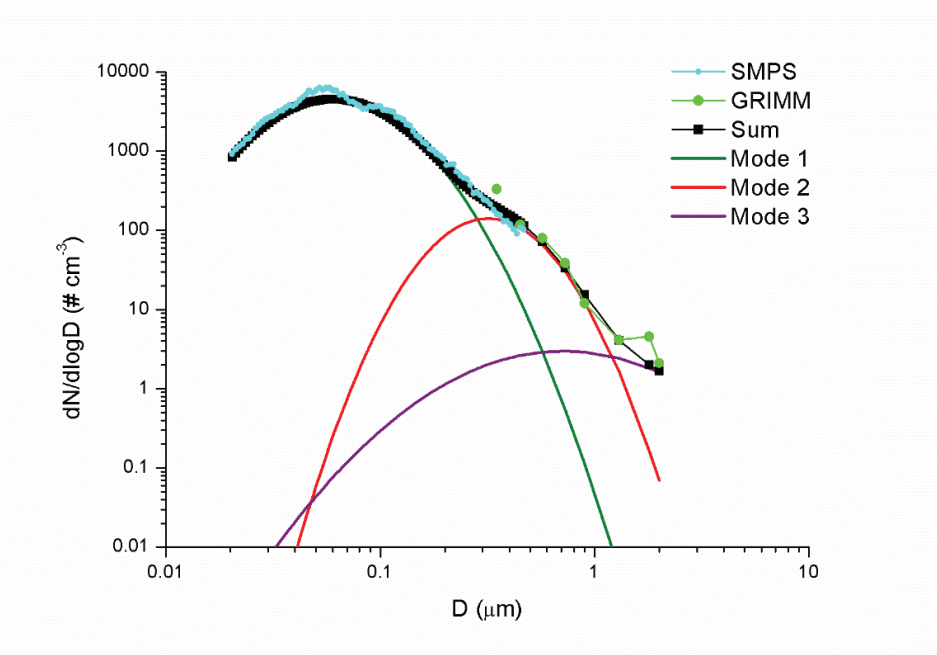

Figure 4.3: Number density distribution of the observed aerosol particles (# cm^{-3}) at 0.2 km by the SMPS (in light blue) and by the GRIMM OPC (in light green with round dots) together with the three fitted modes of the aerosol particle spectrum (Aitken mode in dark green, accumulation mode in red, coarse mode in purple) and the sum (in black).

	Mode 1	**Mode 2**	**Mode 3**
N_i (cm^{-3})	2900	72	3
D_i (nm)	0.06	0.32	0.72
logσ_i	0.26	0.20	0.397

Table 4.1: Properties of the lognormal distribution of the aerosol particle spectrum used in the simulation of the HYMEX IOP7a. The different modes, i, of each distribution are described by the concentration in number, N_i (cm^{-3}), the geometric mean diameter, D_i (μm), and the logarithm of the geometric standard deviation, σ_i.

The selected spectrum had a concentration of 2975 aerosol particles per cm^3. This was the highest aerosol particle concentration observed during HYMEX SOP1. This fact motivated to study the impact of a reduction of the aerosol particle number in the model simulations of the studied heavy precipitation episode. Thus, a less-polluted spectrum was also used in the DESCAM-3D initialization and the respective sensitivity studies are presented in **chapter 5**.

4.1.2 Initial synoptic conditions

The initial thermodynamic and dynamic conditions of the atmosphere during HYMEX IOP7a that were used for the initialization of DESCAM-3D were provided by the IFS ECMWF (operational analysis) data of the 26th September 2012 at 00:00 UTC. The used IFS ECMWF data give the temperature T, the water vapor mixing ratio Q_v, the geopotential height z and the horizontal wind components u and v for 25 pressure levels from 1000 to 10 hPa with a horizontal grid resolution of 0.5° in x and y directions. These data were available for 00:00 and 12:00 UTC on 26th September 2012. The temperature profile in the emagram (**Figure 4.4**) corresponds to a location in the Cévennes mountain region with geographical coordinates 44.5° N and 4.0° E at 00:00 UTC. There, the direction of the horizontal wind close to the ground was southerly and the relative humidity (RH) at the surface was 77 %, whereas in the atmospheric layer between 900 hPa and 950 hPa, the RH goes up to 100 %. Moreover, the positively buoyant region which is proportional to the convective available potential energy (CAPE) expands up to 250 hPa. Thus, the thermodynamic conditions that were introduced to initialize DESCAM-3D favor convection. Respective diagrams at other locations in the Cévennes-Vivarais region at 00:00 UTC showed a similar behavior.

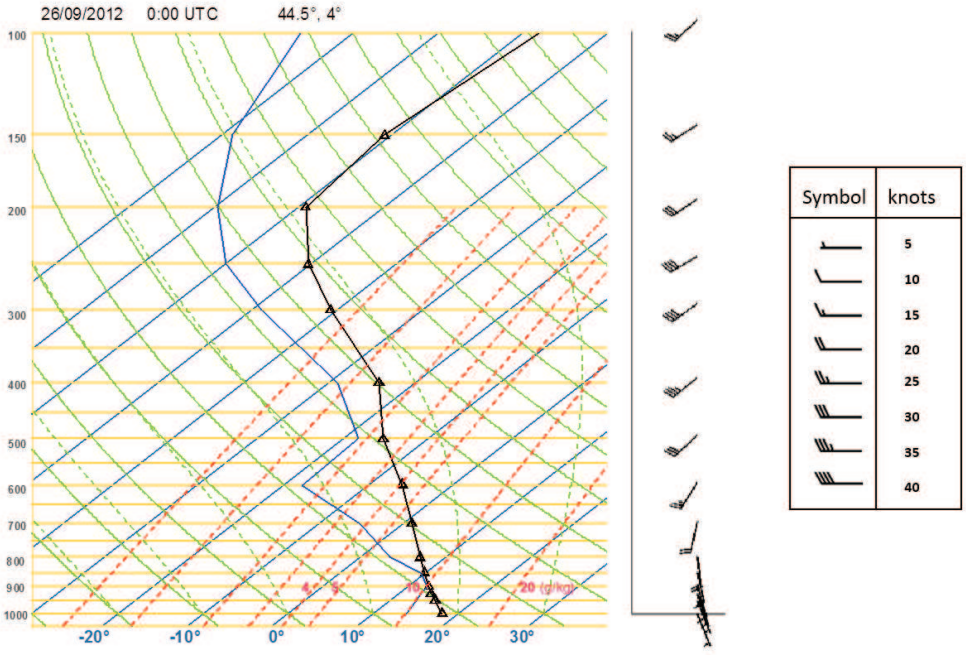

Figure 4.4: Indicative profile of the environmental temperature (black line) and the dew point (blue line) temperature provided by the IFS ECMWF for the 26th September 2012 at 00:00 UTC at the 44.5° N latitude and 4.0° E longitude. The direction and intensity[14] of the horizontal wind at different altitudes (in hPa) is marked on the right.

[14] 5 knots = 9.26 km h^{-1}

4.1.3 Configuration of the reference (REF) simulations

In order to focus on the region of interest, a nested domain configuration is used. The outermost domain of DESCAM-3D, which refers to "D1" (**Figure 4.5**), covers a geographical region of 1024 x 768 km^2 that corresponds to 128 x 96 grid points, including the north-western part of the Mediterranean Sea, the South of France, as well as parts of Spain and Italy. D1 has a coarse horizontal resolution of 8 km and its vertical extension is 22 km (using nearly 50 non-equidistant grid points). The size of the first nested domain (referred as "D2") is 512 x 384 km^2 (256 x 192 grid points) with a horizontal resolution of 2 km. The vertical grid goes up to 12 km (82 grid points). Finally, the second nested domain (referred as "D3") that focuses on the Cévennes-Vivarais region, covers a surface of 125 x 128 km^2 (256 x 256 grid points) with a horizontal resolution of 0.5 km and its vertical extension is similar to D2. The nesting is two-way for all the thermodynamical parameters and one-way for the microphysical parameters.

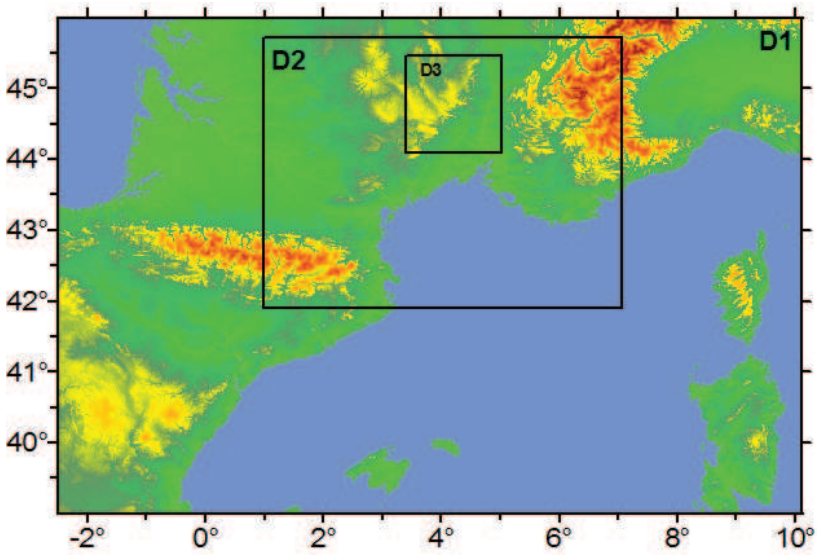

Figure 4.5: The three domains of DESCAM-3D used for the reference simulation of the HYMEX IOP7a. "D1" refers to the outermost domain, "D2" to the first nested domain and "D3" to the second nested domain.

4.2 Results for the DESCAM reference (REF) case

In the present section the simulation results for the reference (REF) case of IOP7a are presented and compared with the respective HYMEX observations. At first, the

temporal and spatial evolution of the simulated system of the 26th September 2012 is being described. Afterwards, the available ground-based observations, as well as in-situ measurements from HYMEX (**chapter 3**) are being compared with the respective model results. The assessed variables concern the cumulative surface rainfall, X-band radar reflectivity and rain spectra, as well as cloud radar reflectivity, cloud water content and hydrometeor spectra.

4.2.1 Temporal horizontal evolution of the precipitating system

As discussed in **chapter 3**, the ECMWF ERA-Interim archives (**Figure 3.4**b) show that southerly horizontal wind was prevailing at 6:00 UTC at the surface over the South of France and the geographical region of Cévennes-Vivarais. **Figure 4.6** shows the horizontal cross section of the simulated horizontal and vertical wind in the beginning of the rainfall, both at the surface and at the altitude of 1.0 km for the innermost domain (D3, see **Figure 4.5**) where results are obtained with a resolution of 0.5 km.

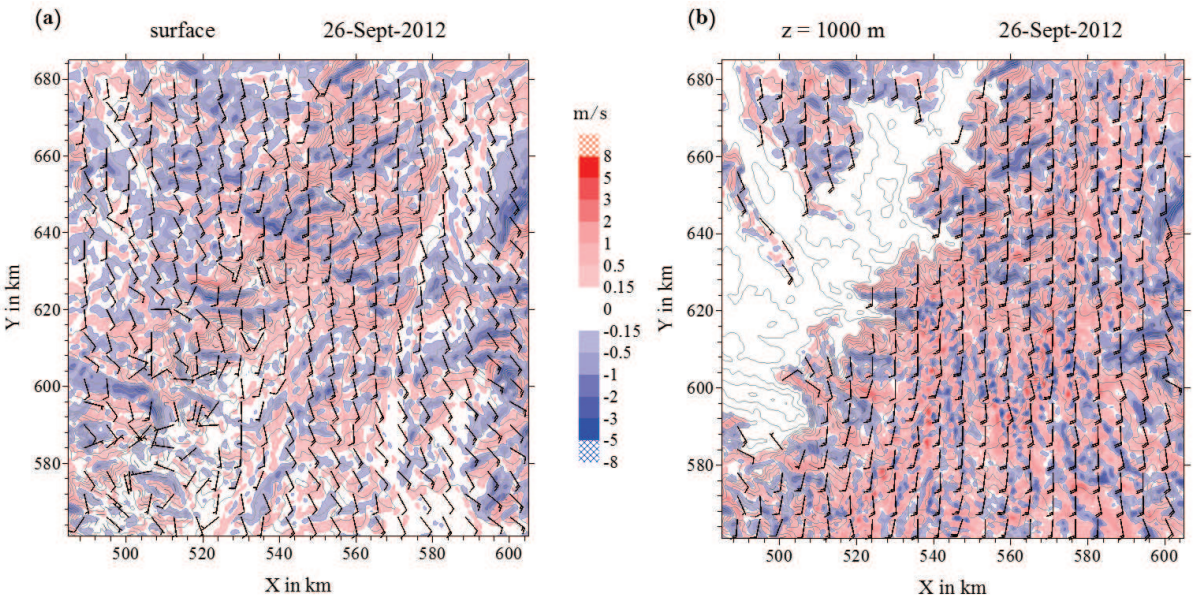

Figure 4.6: Horizontal wind (barbs) and vertical wind (color scale, m s^{-1}) as simulated in D3 for REF case by DESCAM-3D at 06:00 UTC (a) at the surface and (b) at the altitude of 1 km. The white zone in (b) corresponds to elevations > 1 km.

According to **Figure 4.6**, the direction of the horizontal wind at the surface is SSE to SE in the region that is located at the east of the Cévennes Mountain. Particularly, over the mountain slope and the mountain ridge the prevailing horizontal wind has a southern direction, whereas over the highest mountain peaks of Cévennes (in the southern part of

the domain) the horizontal wind seems to be perturbed by the relief. There, horizontal wind varies strongly due to topographical effect and velocity values are smaller than 2 m s^{-1}, while in the rest of the geographical region the values of the horizontal wind speed at the surface range between 2.5 m s^{-1} and 10 m s^{-1}.

At the same time, the direction of the horizontal wind at the altitude of 1 km was mainly southerly (**Figure 4.6**b) and the average velocity is 10 m s^{-1}. The altitude of the mountain peaks are higher than 1000 m (see **Figure 3.2**), therefore the relief influences the direction and the speed of the horizontal wind over these regions. For this reason, in the south-western part of the domain, wind barbs of various directions appear and the velocity of the horizontal wind is not higher than 5 m s^{-1}.

Figure 4.6a and **Figure 4.6**b also present the vertical wind features. The updrafts are marked with red colors and the downdrafts in blue. In this illustration, and in particular in **Figure 4.6**b, the strongest updrafts (up to 5 m s^{-1}) are observed mainly at the east of Cévennes Mountains and over non-mountainous regions.

Next, the temporal evolution of the convective system horizontally is described. The modeled variables used for this description is the cloud water mixing ratio and the IWC.

The cloudy regions of the D3 are represented by the cloud water mixing ratio at the altitude of 5.4 km above sea level, where the highest values are found, at different hours (**Figure 4.7**). Both cloud drops and ice crystals exist at the altitude of 5.4 km. The development of the system started prior to 7:00 UTC over the slopes of Cévennes, whereas at 8:00 UTC the system was well developed over the mountain range and stays until 10:00 UTC. Afterwards, the system starts to dissipate in the southern part of the Cévennes until 12:00 UTC. The orientation of the cloud system follows the mountain ridge with an angle of approximately 60° with respect to the axis X during its entire lifetime.

It is clear in **Figure 4.7** that the most and highest values of cloud mixing ratio are seen at 8:00 UTC and at 9:00 UTC. Moreover, this corresponds to the time period when the highest IWC was observed in the aircraft measurements, as seen in **chapter 3**. Thus, next, the focus is given on this time span, with the analysis of the temporal horizontal evolution of the IWC.

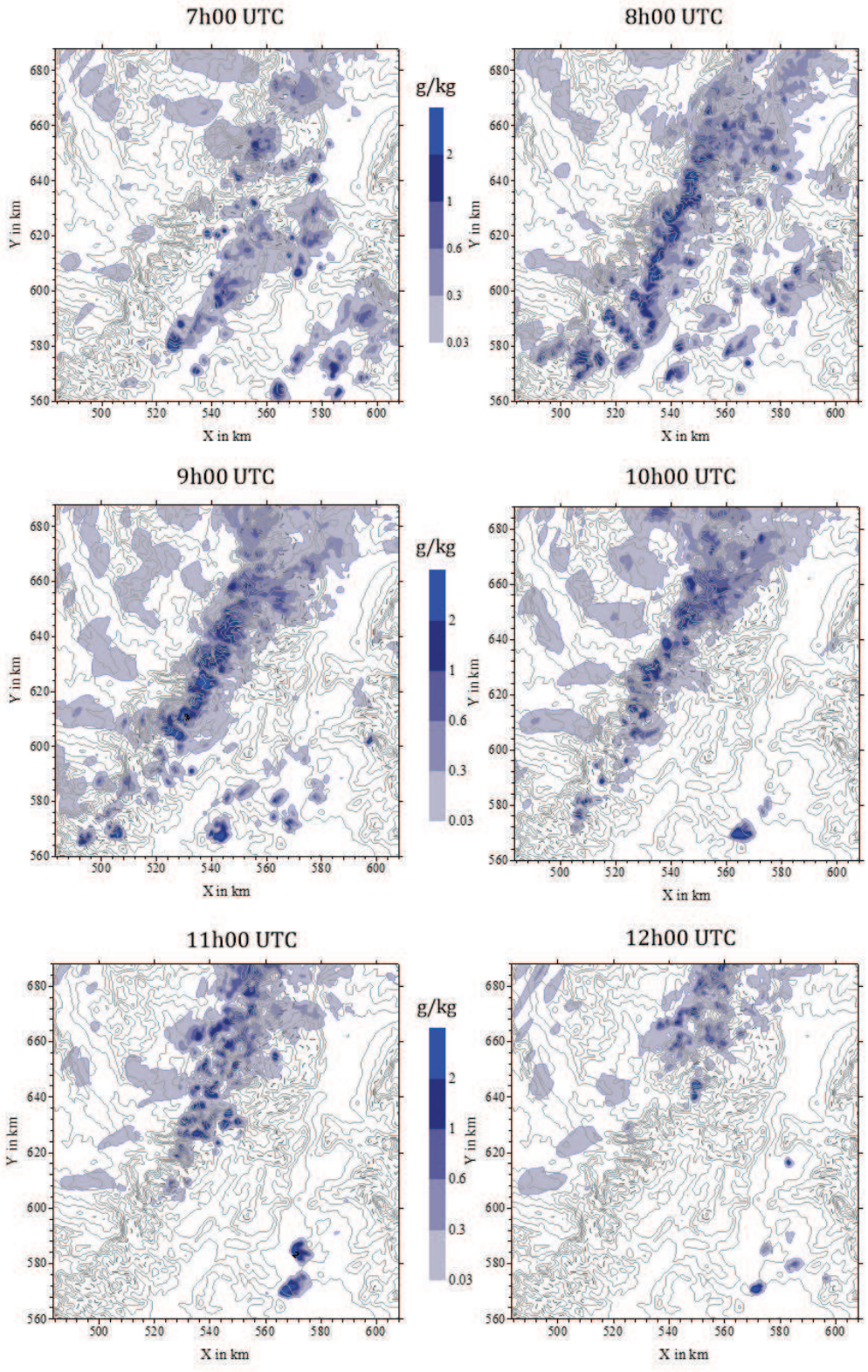

Figure 4.7: Spatial and temporal evolution of the simulated cloud (liquid) water mixing ratio (g kg^{-1}) every hour from 7:00 UTC to 12:00 UTC for the DESCAM-3D reference (REF) case. The horizontal cross section corresponds to the altitude of 5.4 km a.s.l. of D3. The black contours represent the topography.

Figure 4.8 shows the evolution of the IWC between 8:00 UTC and 9:00 UTC at an altitude of 4.4 km and 5.7 km above sea level. This atmospheric layer corresponds to where highest values of IWC were observed (discussed in **chapter 3**). In the simulation, IWC values between 0.4 g m^{-3} to 0.6 g m^{-3} were found over the north-eastern area of the D3 in the aforementioned atmospheric layer. In this layer, the maximum values of IWC were 2.8 g m^{-3} to 3 g m^{-3} and they are located over the mountainous region. IWC of 0.6 g m^{-3} to 1 g m^{-3} were also found over the mountain ridge and particularly over Vivarais Mountains.

According to the results presented in this section, it is seen that the model simulates correctly the southern horizontal wind flow that resulted in the development of the convective system. Also, the cloudy region is found to be over and along the Cévennes-Vivarais Mountains, as expected from the observations presented in **chapter 3**. Finally, the presence of ice in the atmospheric layer 4 to 6 km is seen mostly over the Vivarais Mountains, therefore, the analysis of the IWC is focused on this region, as will be presented later in this chapter, but also in **chapter 5**.

The present chapter continues with the comparison between the HYMEX observations presented in chapter 2 and the respective model results. The comparison starts with variables at the surface, i.e. rain accumulation, X-band radar reflectivity and rain spectra.

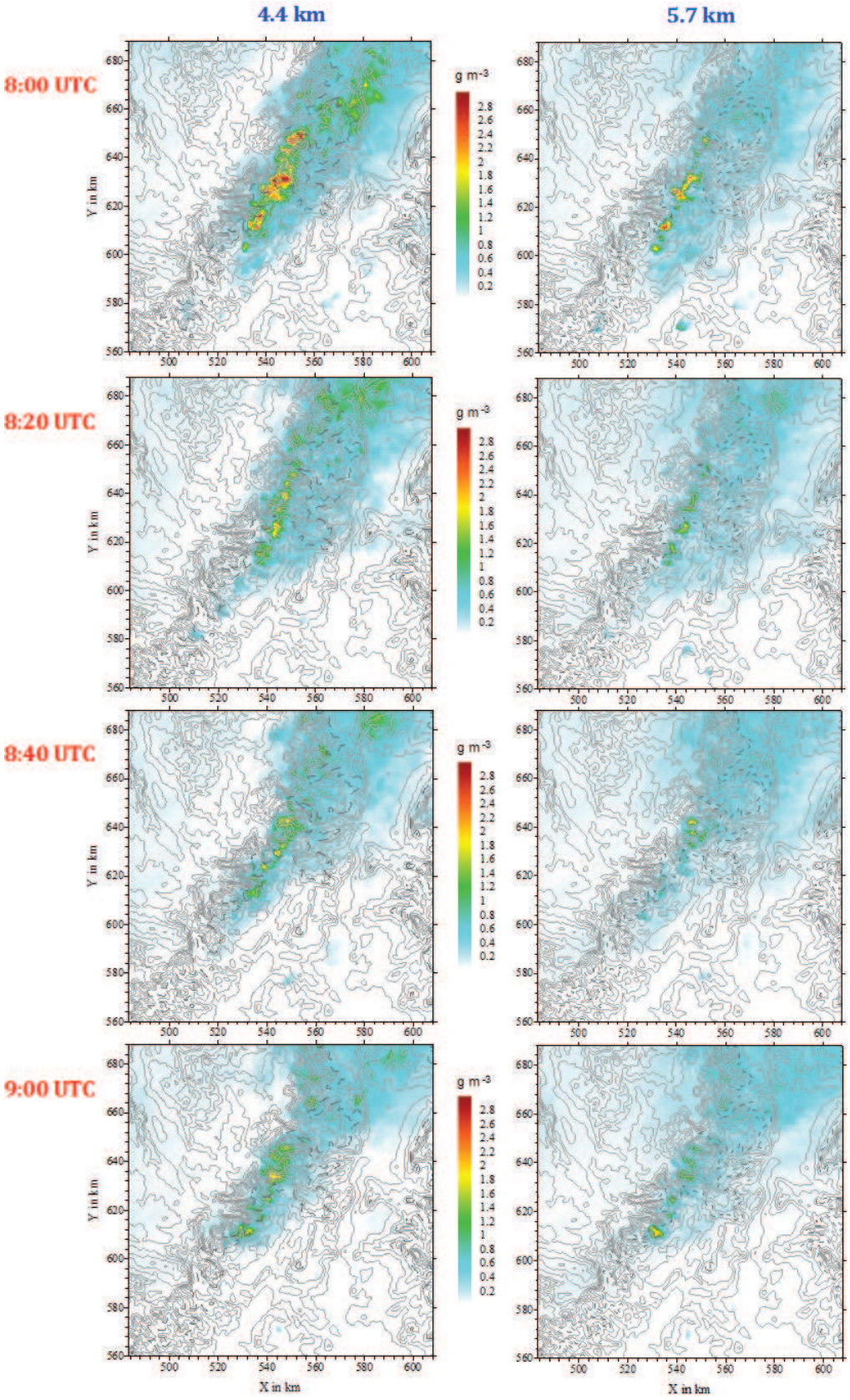

Figure 4.8: Spatial and temporal evolution of the simulated IWC (g m^{-3}) between 8:00 UTC and 9:00 UTC for the DESCAM-3D reference (REF) case in D3. On the **left**, the horizontal cross section was taken at 4.4 km and at 5.7 km a.s.l. on the **right**.

4.2.2 Comparison between DESCAM-3D model results (REF) and HYMEX ground-based observations

The observations of precipitation by the ground instrumentation of HYMEX described in **chapter 3** are now compared to the results of the simulations. For a better understanding of the evolution of the precipitating system, the present section starts with the analysis of the cumulative rainfall on the ground and its comparison with the KED QPEs. Afterwards, the observed X-band radar reflectivity is compared to the modeled one and finally the simulated droplet spectra is compared to the observations from disdrometers and MRR instrument.

4.2.2.1 Surface rain accumulation

The present analysis compares the cumulative rainfall that was provided by the KED QPE (see **section 3.3.1**) and the simulated by DESCAM-3D. **Figure 4.9** gives in the left column the observations and in the right one the results of the REF simulations. In this figure, the hourly rain accumulation is presented for the period between 7:00 and 9:00 UTC.

From 7:00 UTC to 8:00 UTC, intense rainfall takes place with a maximum of 48.7 mm on the mountain slope, according to the observations (**Figure 4.9**a). During the same time period, the simulation yields rain accumulation up to 17 mm mainly over the mountainous region of Cévennes (**Figure 4.9**b).

Between 8:00 UTC and 9:00 UTC, maxima can be found over the Cévennes Mountains, with a value of 42 mm in the southern area (**Figure 4.9**c). As seen in **Figure 4.9**d, during the same time period, up to 52 mm of rain fell in the model and the center of the precipitating system is found close to the position of the northern cell of the KED QPE. It is worth noting that the orientation of the precipitating system is reasonably reproduced by the model.

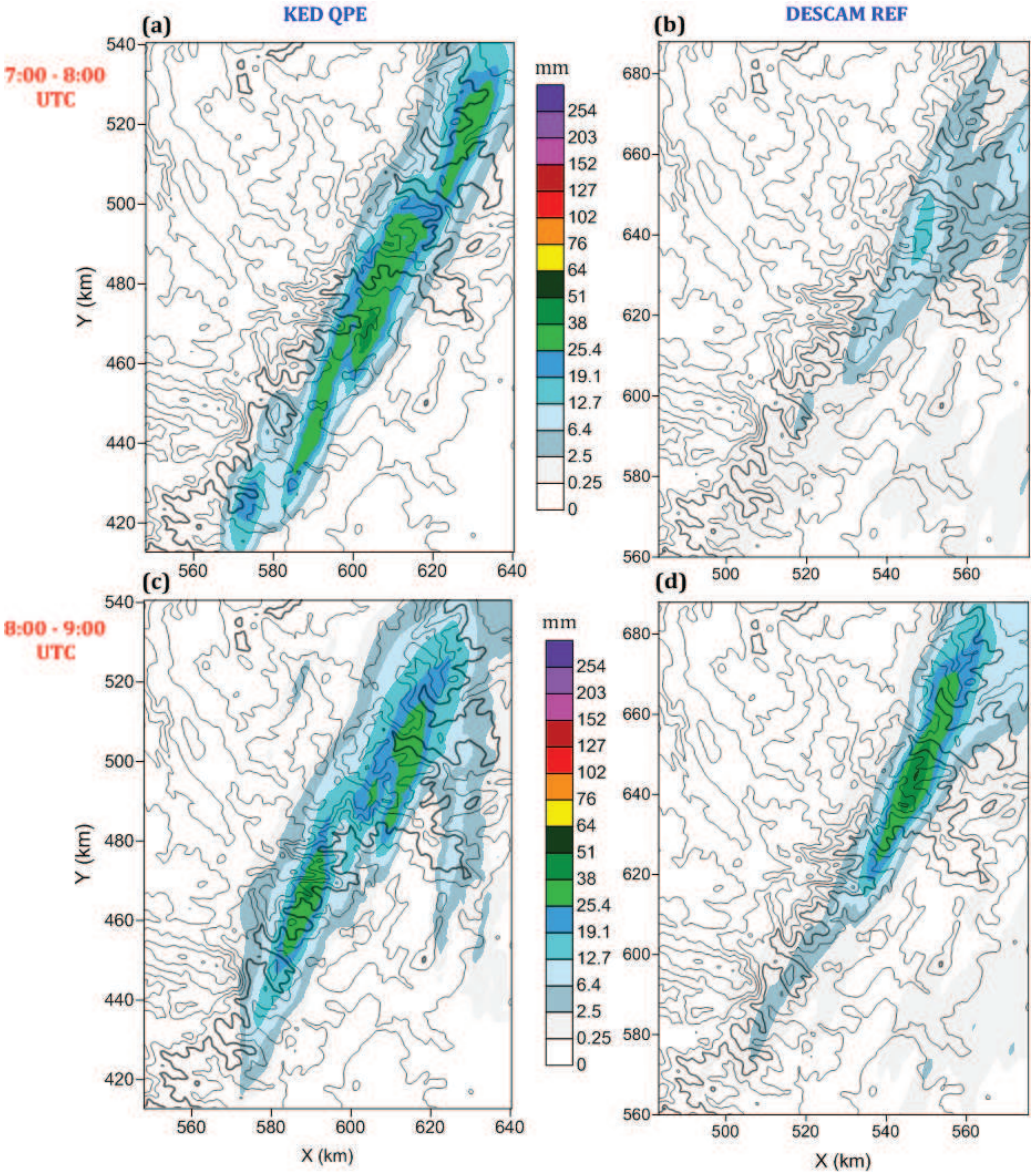

Figure 4.9: Hourly rain accumulation (in mm) between 7:00 UTC and 8:00 UTC (a, b) and between 8:00 UTC and 9:00 UTC (c, d) by the KED QPE and the DESCAM-3D model results. The solid black lines represent the topography. The grey thick line corresponds to the altitude of 600 m.

The heavy rainfall over the Cévennes Mountains continues in the model simulation results between 9:00 UTC and 10:00 UTC, as seen in the **Figure 4.10**b, whereas the observed precipitation is less intense during this time period (**Figure 4.10**a). The maximum modeled value is 55.4 mm while the respective observations show up to 28 mm locally. However, the center of the precipitating system in the model results is found to be almost at the same place with the observations.

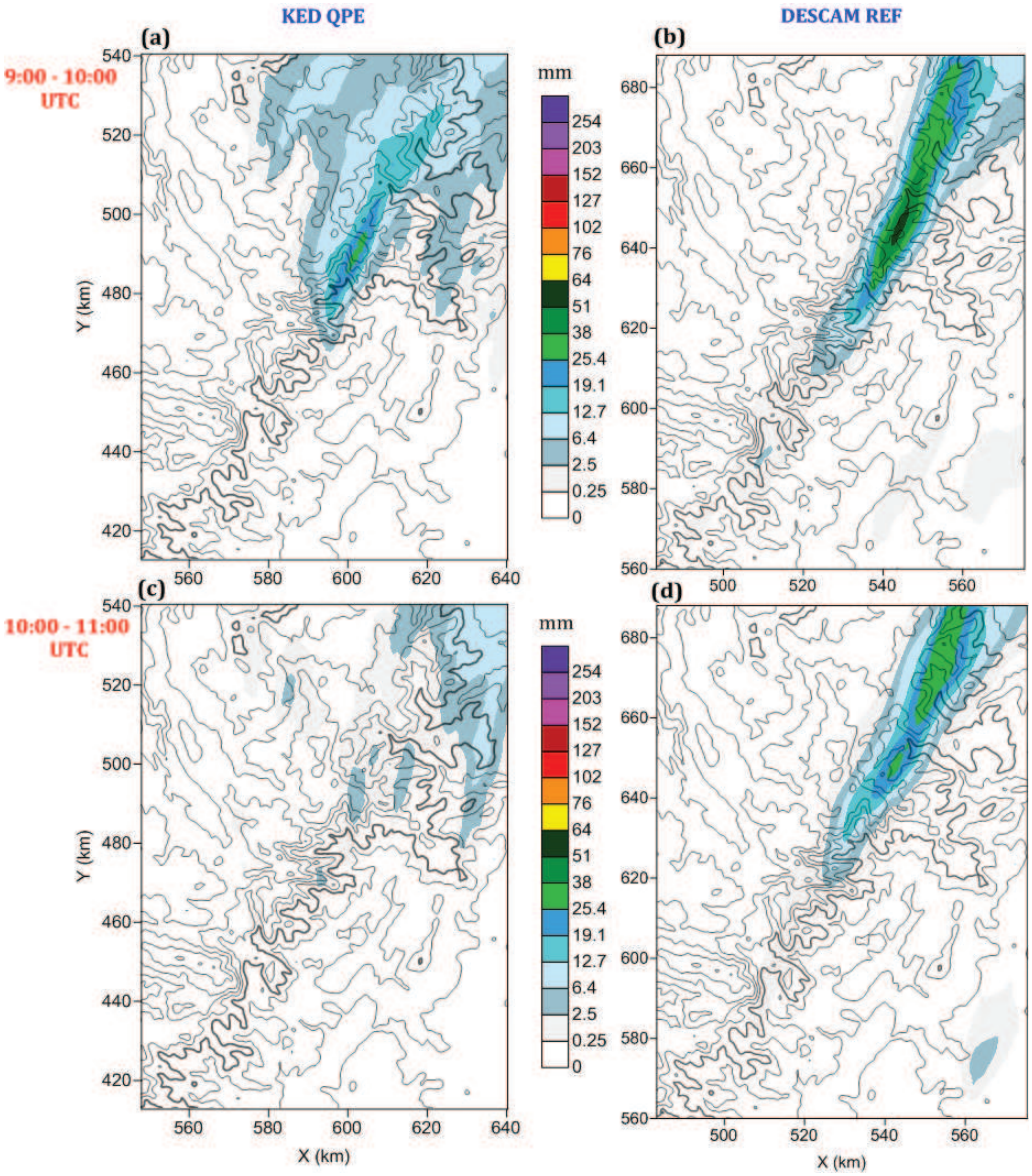

Figure 4.10: Hourly rain accumulation (in mm) between 9:00 UTC and 10:00 UTC (a, b) and between 10:00 UTC and 11:00 UTC (c, d) by the KED QPE and the DESCAM-3D model results. The solid black lines represent the topography. The grey thick line corresponds to the altitude of 600 m.

Between 10:00 UTC and 11:00 UTC (**Figure 4.10**c) no more than 10 mm of maximum rain at the surface are obtained in the KED QPE. On the contrary, the model gives a maximum of cumulative rainfall which is three times higher (**Figure 4.10**d). Nevertheless, the area where the rain falls is reasonably simulated by DESCAM-3D. These differences in the quantity of the cumulative rainfall can be attributed to a 1-hour delayed onset of the rainfall in the simulation results. This 1-hour time shift can be linked to the initial synoptic conditions that were used for the model simulations. The precipitation in the model simulation continued until 12:00 UTC, while at the same time, between 11:00 UTC and 12:00 UTC the observed rainfall has almost ended.

Figure 4.11a and **Figure 4.11**b present the total cumulative rainfall at the surface from 00:00 UTC to 12:00 UTC by the KED QPE and the model results, respectively. The comparison of these two figures shows that the model results for the total rain accumulation after 12 hours of integration, at the end of the heavy precipitation event, are reasonable. The main precipitating cell in the simulation results is shifted about 10 km to the north-west with respect to the observations. The horizontal extension of the rain field is underestimated particularly in the northern region of the domain. The maximum cumulative rainfall in the model results is 118 mm locally, whereas the respective maximum value of the KED QPE is 114 mm. The location and orientation of the modeled cumulative precipitation at the surface is in agreement with the respective observations.

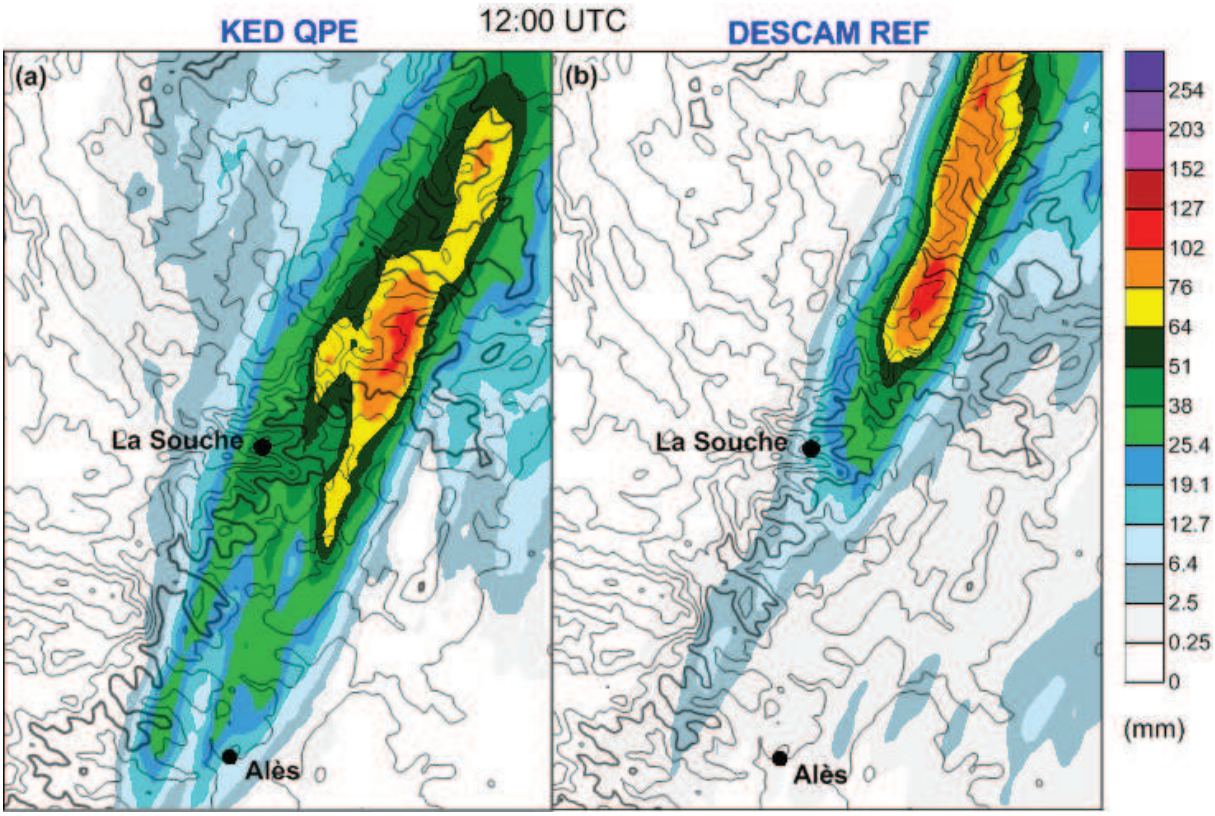

Figure 4.11: Cumulative rainfall from 00:00 UTC to 12:00 UTC of the 26th September 2012, as estimated by (a) the QPE observations and (b) the DESCAM-3D model. The solid black lines represent the topography and the black circles show the position of La Souche and Alès. The grey thick line corresponds to the altitude of 600 m.

For a more quantitative comparison between the simulated and observed rain accumulation, the frequency distribution of the total rainfall in classes (bins) of 1 mm is calculated and presented in **Figure 4.12** (cumulative rainfall from 00:00 UTC to 12:00 UTC).

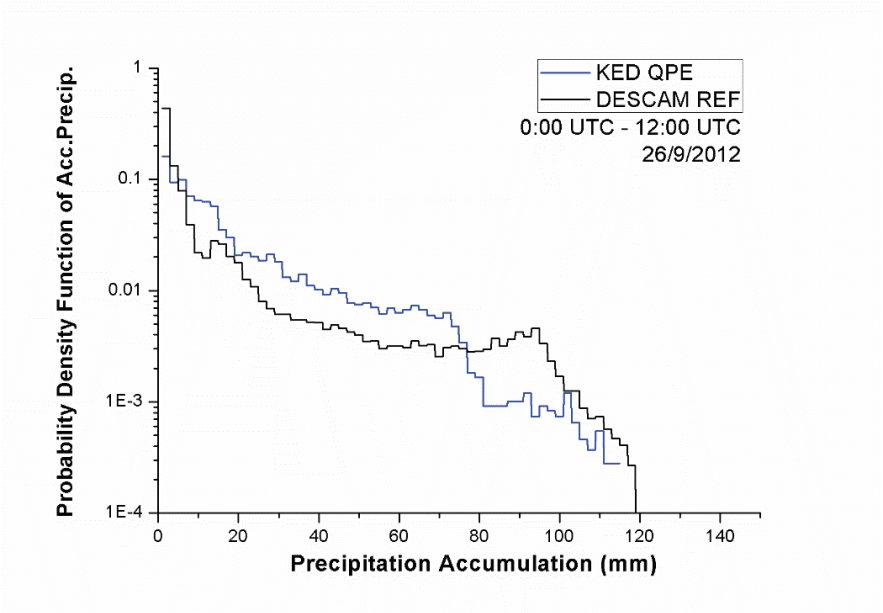

Figure 4.12: Probability density function of the rain accumulation on the surface between 00:00 UTC and 12:00 UTC of the 26th September 2012 for the QPE observations (blue line) and the DESCAM-3D model results (black line).

The frequency distributions of the two cases follow similar tendencies, except from values between 80 mm and 100 mm, which are overestimated by the model results compared to the observations. It can be also seen that the cumulative rainfall values from 20 mm to 80 mm are about 50 % underestimated by the model results. The differences between the two cases may appear also due to the fact that the model provides results of different horizontal resolution than the observations. However, the frequency of strongest and the weakest rain spots is well reproduced by the model results.

4.2.2.2 X-band radar reflectivity

The calculation of the X-band radar reflectivity is achieved by considering the hydrometeor number distribution *N(D)* that is simulated by DESCAM-3D. The radar reflectivity factor Z for liquid hydrometeors is given by the equation 4.1, whereas for solid hydrometeors the equation 4.2 proposed by Delanoë et al. (2005) is being used. In the equation 4.2, the terms $|K_i|^2$ and $|K_w|^2$ represent the di-electrical constants for ice and the liquid water and they equal to 0.176 and 0.93 respectively. The density of ice, ρ_i equals to 0.9 g/cm^3.

$$Z[mm^6m^{-3}] = \int N(D)D^6dD \qquad 4.1$$

$$Z[mm^6m^{-3}] = \frac{|K_i|^2}{|K_w|^2}\left(\frac{\rho_w}{\rho_i}\right)^2 \int N(D)D^6dD \qquad 4.2$$

Finally, the comparability of the radar reflectivity factor Z with the X-band radar observations was achieved via the conversion to the normalized radar reflectivity Z_{dBZ} according to the equation 4.3, where Z_0= 1 mm^6 m^{-3}.

$$Z_{dBZ} = 10\log\left[\frac{Z[mm^6m^{-3}]}{Z_0}\right] \qquad 4.3$$

The resulting radar reflectivity Z_{dBZ} by DESCAM-3D at different moments is presented in the right column of the **Figure 4.13** and **Figure 4.15**. The left column displays the X-band measurements at the same time. The simulation results herein were restricted to the area covered by the X-band radar X3 and using the same beam elevation[15] (PPI images).

Figure 4.13a shows that intense rainfall has already started at 6:40 UTC, according to the high radar reflectivity values observed by the X3 instrument with a maximum of about 58 dBZ locally over the Cévennes mountain slopes. The precipitating system is formed at the east and towards the Cévennes-Vivarais with an angle of about 60° with regard to the horizontal axis X. The respective model results (**Figure 4.13**b) show radar reflectivity values from 10 dBZ to 40 dBZ and a maximum of 43 dBZ locally. At the same time the system is occurring more to the east. The quantitative differences of the radar reflectivity at 6:40 UTC can be seen in **Figure 4.14**a, where the probability density functions[16] of the observed and simulated values are presented. Note that considering the delayed onset of the simulated precipitation by one hour, in **Figure 4.14** the probability density functions of the observations are compared to the model results one hour later. However, in **Figure 4.14**, only some indicative comparisons during the period of most intense precipitation are being shown. The behavior of observed and modeled reflectivity presented in **Figure 4.14**a are quite similar for values smaller 25 dBZ, larger reflectivity that corresponds to values higher than 45 dBZ, however, is underestimated in the simulations.

[15] mean altitude of the beam
[16] In order to avoid "noise" of the instrument, the probability density functions were calculated considering 1 dBZ bin classes and only for reflectivity higher than 10 dBZ and lower than 70 dBZ.

At 7:20 UTC, radar reflectivity measurements still reach up to 55 dBZ, as seen in **Figure 4.13**c and in **Figure 4.14**b. The system is slightly shifted by about 0.1° to the west in direction to the mountain crest. In the respective model results, (**Figure 4.13**d), the system also moves to the west and increases its horizontal extent.

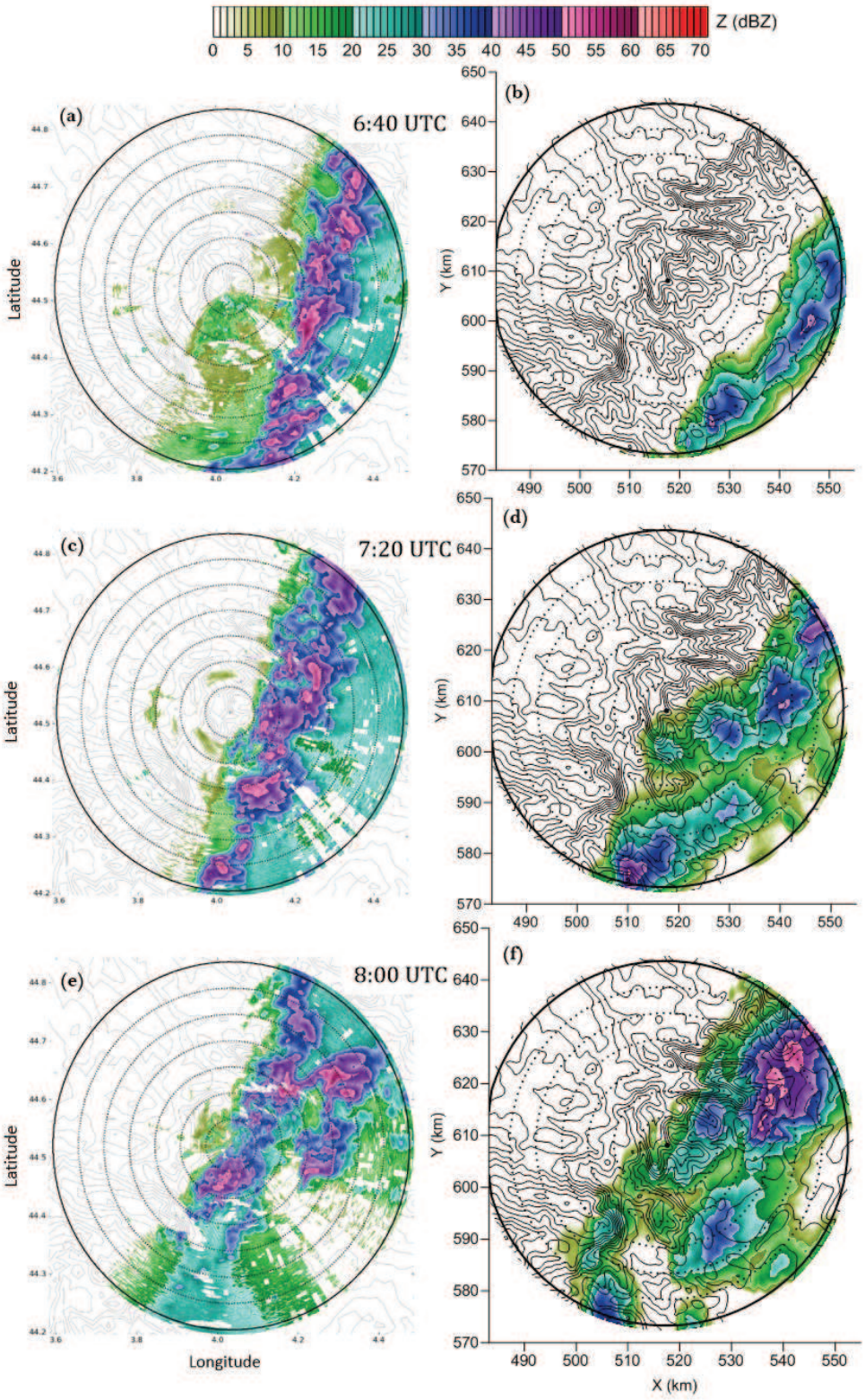

Figure 4.13: PPI images of the radar reflectivity observed by the X-band radar during the HYMEX IOP7a at (a) 6:40 UTC, (c) 7:20 UTC and (e) 8:00 UTC and simulated by DESCAM-3D (reference case - REF) at the same specific times (b, d and f). The solid black lines represent the topography and the concentric circles correspond to the different altitudes of the radar beam at every 5 km to the radar position. The maximum height of the radar beam (external circle in bold black) is 1892 m.

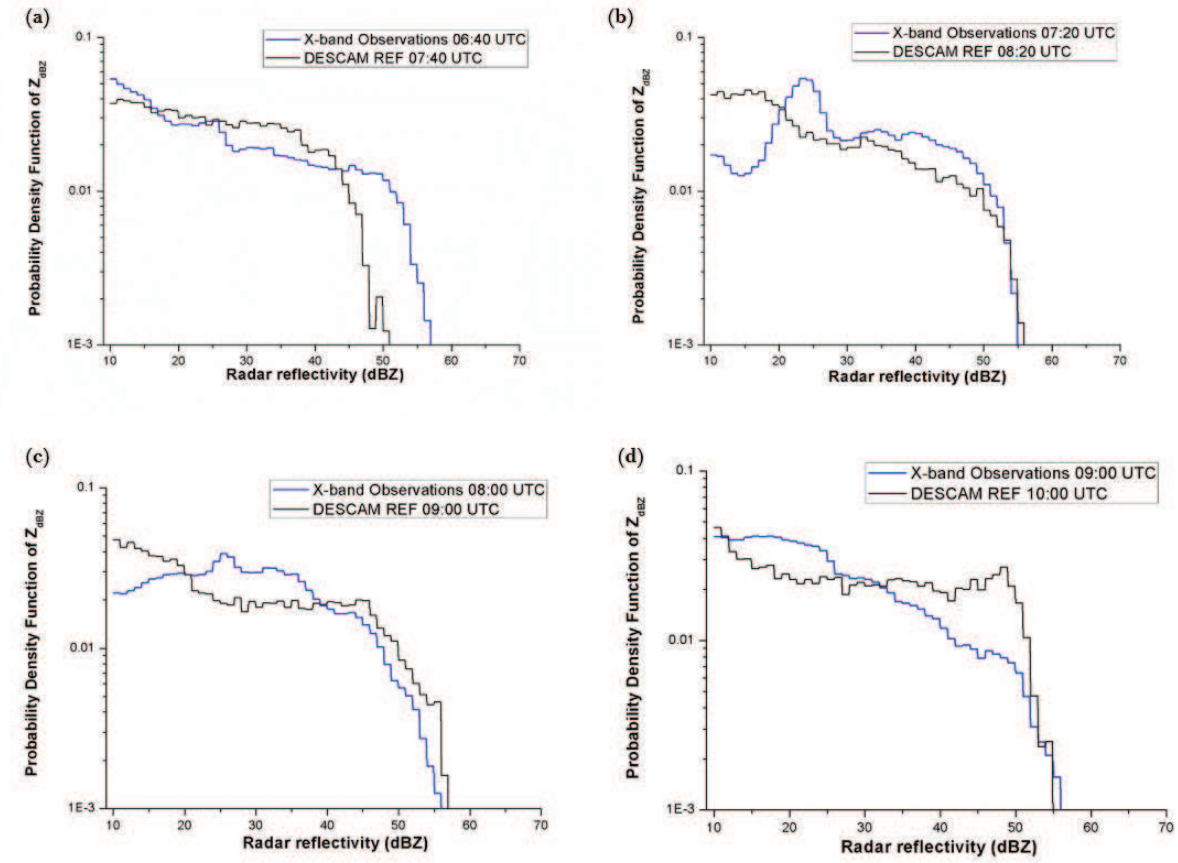

Figure 4.14: Probability density function of the X-band radar reflectivity observations (blue lines) and the respective DESCAM-3D model results (black lines) of the reference simulation (REF) at (a) 6:40 UTC for the observations and at 7:40 for the model results, (b) 7:20 UTC for the observations and at 8:20 for the model results, (c) 8:00 UTC for the observations and at 9:00 for the model results and (d) 9:00 UTC for the observations and at 10:00 for the model results.

At 8:00 UTC, the precipitating system is changing its organization. The dominant cells move and scatter in NE direction (**Figure 4.13**e) and maximum reflectivity values remain quite high, up to 56 dBZ. In the respective simulation results, the orientation of the precipitating system is similar to the observed one, as seen in **Figure 4.13**f. Furthermore, the secondary cell of the convective system at the north-east is well estimated by the model simulation. The increasing similarity between observations and simulation results can be also seen in the statistical comparison. According to **Figure 4.14**c, the differences of the probability density function for the two cases are small and they mainly occur for reflectivity values below 35 dBZ.

Twenty minutes later, at 8:20 UTC, the precipitating system is weakened. According to **Figure 4.15**a, two main precipitating cells are found; one located between 44.4° and 44.5° in latitude and 4.0° in longitude (close to the X3 radar position) with maximum values of 50 dBZ and a second one located at the north-east with maximum values of 56 dBZ. Similar

precipitating cells are also found in the respective model results (**Figure 4.15**b). The maximum reflectivity of each cell agrees with the observations. The northern precipitating cell is located more eastward in the model results than in the observations. The orientation of the precipitating system of the observations is similar with the one in the model results.

At 9:00 UTC there is almost no rain at the southern part of the radar observation field (**Figure 4.15**c). In the respective model results (**Figure 4.15**d), the system is also weakened over the aforementioned area, but there is still reflectivity mostly in the range of 15-20 dBZ. According to **Figure 4.14**d, the model simulation seems to overestimate values in the range of 35 dBZ to 50 dBZ, whereas there is a good agreement for values between 25 dBZ and 33 dBZ, as well as for the highest values.

Finally, at 10:00 UTC the X-band radar observations in **Figure 4.15**e show that the system has almost disappeared and only some small cells are located at the north-east. In this region, high reflectivity values are found in the simulation results (**Figure 4.15**f). Nevertheless, the model results show that the rainfall continued in the south, with the precipitating system still organized at 10:00 UTC.

Comparing the time evolution of the radar reflectivity observations with the simulated ones in **Figure 4.13** and **Figure 4.15** suggest again that the onset of the modeled precipitation system started with a time delay (as already seen in **Figure 4.9**) and consequently still presented at 10:00 UTC when the observed one already disappeared.

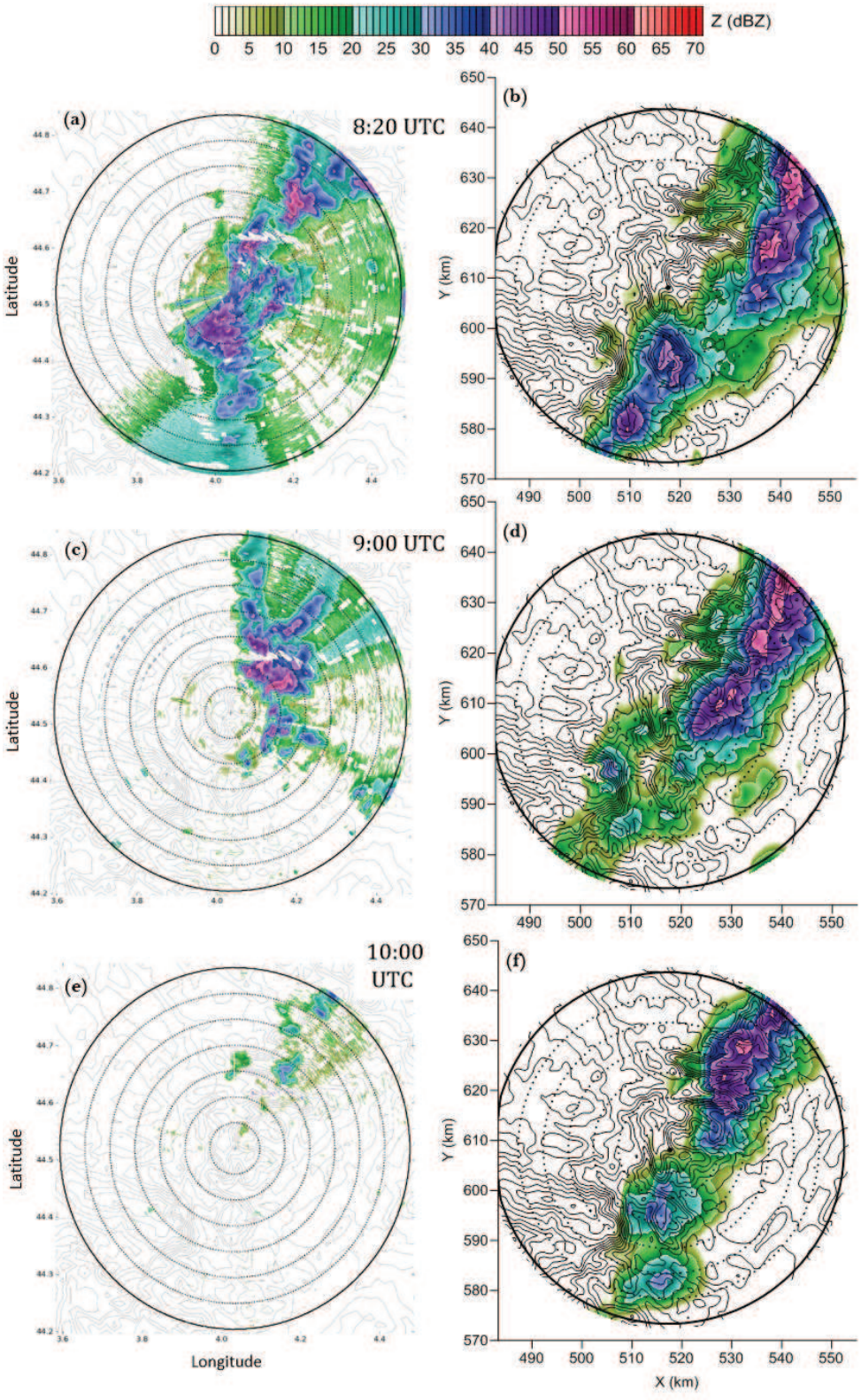

Figure 4.15: PPI images of the radar reflectivity observed by the X-band radar during the HYMEX IOP7a at (a) 8:20 UTC, (c) 9:00 UTC and (e) 10:00 UTC and simulated by DESCAM-3D (reference case - REF) at the same specific times (b, d and f). The solid black lines represent the topography and the concentric circles correspond to the different altitudes of the radar beam at every 5 km to the radar position. The maximum height of the radar beam (external circle in bold black) is 1892 m.

By focusing on the time period when the reflectivity was high, namely between 6:40 UTC and 9:00 UTC, it is seen that the averaged probability density function of the modeled X-band radar reflectivity follows the same tendency with the respective mean frequency distribution of the observations (**Figure 4.16**a). Small differences are found for values between 20 and 25 dBZ, where the observed radar reflectivity exceeds the modeled ones. This behavior can be explained by a possible over-correction of the attenuation in the observations (e.g. regions in light blue situated behind intense echoes that represent precipitating cells, visible in PPI images). Small differences are also seen for values between 40 and 50 dBZ that can be attributed to the 1-hour time shift of the simulated rainfall.

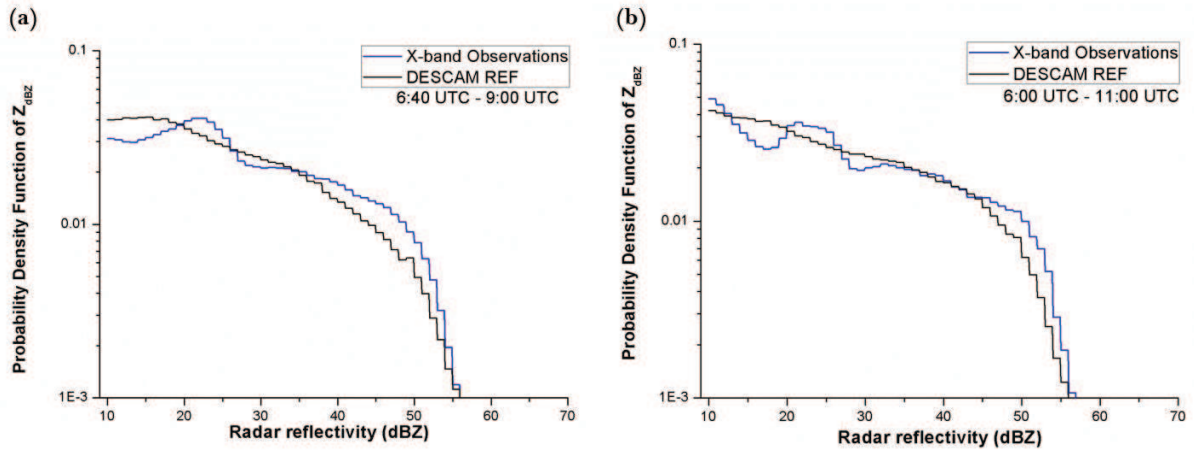

Figure 4.16: Averaged probability density function of the X-band radar reflectivity observations (blue lines) and the respective DESCAM-3D model results (black lines) of the reference simulation (REF) for the time periods of (a) 6:40 UTC – 9:00 UTC and (b) 6:00 UTC – 11:00 UTC.

The comparison of the averaged probability density function between the X-band observations and the modeled radar reflectivity during the time period from 6:00 UTC to 11:00 UTC is presented in **Figure 4.16**b. The consideration of the radar reflectivity values during the entire duration of the precipitation of the IOP7a results in smaller differences between the observations and the model results. The main differences are found for values between 15 and 25 dBZ and around 50 dBZ for the reasons explained for **Figure 4.16**a, whereas for values between 35 and 45 dBZ the model results are in agreement with the observations. As explained for **Figure 4.13** and **Figure 4.15**, the period of the intense rainfall in the simulation results starts almost one hour later than in the observations and therefore it continues later. Consequently, by taking into account the radar reflectivity values until 11:00 UTC, the probability density function of the observations resembles more the one of the model results.

After the analysis of the horizontal and three-dimensional temporal evolution of the rainfall, the focus will be given on the microphysics of the precipitation. In the next section, the comparison between the observed and modeled rain spectra is presented.

4.2.2.3 Analysis of the raindrop spectra

Drop size distribution is a key component for the study of heavy precipitation episodes. As seen in **chapter 3**, disdrometers and MRR instruments provide information about characteristics of the rain spectra. In this section, rain spectra observations from the two available disdrometers (see **Figure 3.16**), Parsivel 10 and Parsivel S, as well as from the instrument MRR10 are compared to the respective model simulation results. Parsivel 10 and Parsivel S that were installed in the Cévennes-Vivarais region (see **Figure 3.2**), provided the temporal evolution of the rain rate that is presented in **Figure 3.10**.

As seen in **chapter 3**, the different locations of the available instruments in combination with the passage of the precipitating system at these locations and at different moments, results in different detection time of the rainfall by the various instruments. The highest rain rates were observed by the Parsivel 10 between 6:18 UTC and 6:42 UTC and between 8:00 UTC and 9:06 UTC by the Parsivel S. Consequently, according to the observations, six different time periods from 6:18 UTC to 9:06 UTC were selected for the analysis of the respective number and mass size distributions of the liquid hydrometeors and their comparison with the model results. The time periods 1 and 2 correspond to observations by the Parsivel 10, whereas the time periods 3 to 6 correspond to the observations from Parsivel S. The average RWC (retrieved using equation **2.3**) during each of the selected time periods by each of the two instruments is presented in **Table 4.2**.

	Parsivel 10	**Parsivel S**
Period 1 **6:18 – 6:30 UTC**	1.95 g m^{-3}	-
Period 2 **6:30 – 6:42 UTC**	1.46 g m^{-3}	-
Period 3 **8:00 – 8:09 UTC**	-	0.66 g m^{-3}
Period 4 **8:18 – 8:30 UTC**	-	0.93 g m^{-3}
Period 5 **8:43 – 8:58 UTC**	-	4.32 g m^{-3}
Period 6 **8:36 – 9:06 UTC**	-	3.25 g m^{-3}

Table 4.2: Mean rain water content observed by the disdrometers Parsivel 10 and Parsivel S during different time periods.

Observed droplet spectra are compared with modeled ones, as seen in **Figure 4.18** and **Figure 4.19**. The modeled droplet spectra are calculated at moments when there was rainfall in the simulation, but at altitudes that correspond to the instruments' location. As the simulated rain field deviates spatially from the observed, modeled rain spectra averaged over a horizontal area of 20 x 20 km² in the vicinity of observations are used for the comparison (see **Figure 4.17**). This area was selected in order to focus on the area where precipitation occurred in the model results.

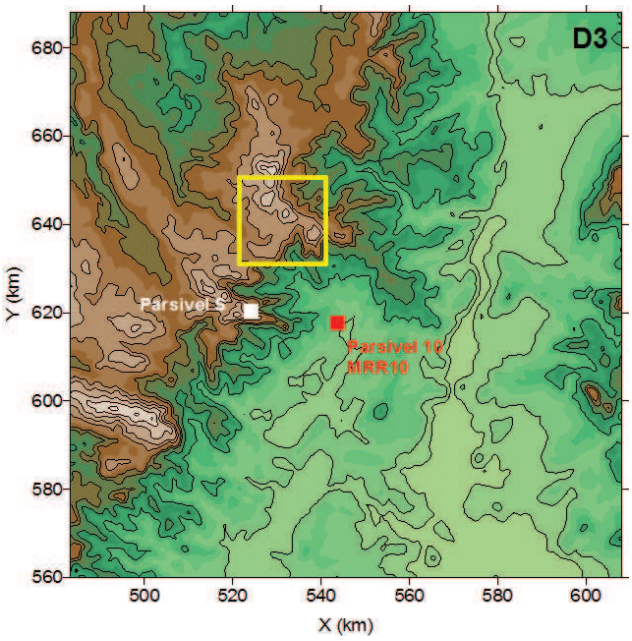

Figure 4.17: The 20 x 20 km² horizontal area (yellow frame) selected for the calculations of the modeled rain spectra. The positions of the instruments whose observations are compared with the model results are indicated by the white square (Parsivel S) and the red square (Parsivel 10 and MRR10).

In **Figure 4.18**a, the number size distributions observed during the periods 1 and 2 by the Parsivel 10 (208 m a.s.l.) are shown along with the modeled number size distributions at different moments during the rainfall. The Parsivel 10 observed up to 1000 droplets m^{-3} mm^{-1} for diameters smaller than 1 mm during both period 1 and period 2, whereas the respective modeled maximum values that correspond to these diameter sizes are less than 300 droplets m^{-3} mm^{-1}. For droplets with diameters which are bigger than 1 mm, the number size distribution is decreasing exponentially for both the observed and the modeled rain spectra, as e.g. described by a so-called Marshall-Palmer distribution (Marshall and Palmer 1948). According to **Figure 4.18**a, for the droplet diameter range between 2 mm and 3 mm, all the modeled rain spectra are in the same order of magnitude as the observed ones.

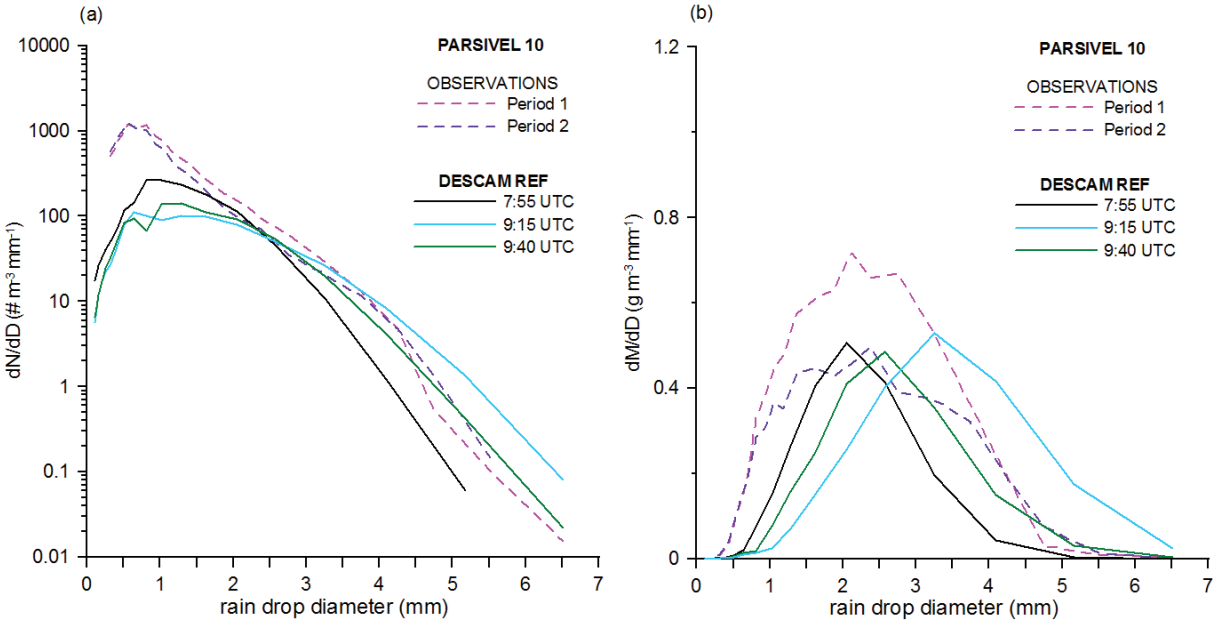

Figure 4.18: (a) Number density distributions of droplets (m^{-3} mm^{-1}) by the Parsivel 10 observations (dashed lines) during the Period 1 and Period 2 and the DESCAM reference (REF) simulation results at different moments and (b) corresponding mass size distributions (g m^{-3} mm^{-1}). The simulated mean rain water content at 7:55 UTC, at 9:15 UTC and at 9:40 UTC is 0.97 g m^{-3}, 1.35 g m^{-3} and 1.11 g m^{-3} respectively.

In the modeled spectrum of 7:55 UTC the number of the biggest droplets seems to be 10 % to 80 % underestimated with regard to the observations. On the contrary, in the modeled rain spectrum of 9:40 UTC, the number of droplets with diameters > 2 mm is in agreement with the observations. The third spectrum displayed for 9:15 UTC exceeds the observed spectra for diameters > 4 mm but also falls below the observations for diameters < 2 mm.

The same modeled rain spectrum provides the mass distribution (**Figure 4.18**b) which is most similar to the observed one during period 2. The mass distribution of the modeled spectra illustrate that the smallest drop sizes (< 1 mm) contribute very few to the rain mass, less than in the observed spectra. For all distributions (modeled and observed) the maximum droplet mass is found for droplets with diameter sizes between 2 mm and 3 mm. The model seems to underestimate the mass of the droplets with diameters smaller than 2 mm, whereas droplets with diameters bigger than 3.5 mm are overestimated in the modeled spectrum of 9:15 UTC, but underestimated at 7:55 UTC. However, according to the observations of the period 1, the main droplet mass is found to have a maximum of 0.7 g m^{-3} mm^{-1} which is not found in any of the modeled rain spectra close to the surface.

The observations from Parsivel S are characterized by extremely high numbers of small droplets (< 1 mm), which are up to 4000 m^{-3} mm^{-1} during periods 5 and 6 (**Figure**

4.19a). During periods 3 and 4, however not more than 1000 droplets m^{-3} mm^{-1} were encountered. Simulated DSDs were selected from surface grid points which are located between 900 and 1000 m. As over La Souche (Cévennes region) no rain occurred in the model (visible in **Figure 4.9**b and **Figure 4.9**d), the simulated DSDs considered here were taken from the Vivarais regions where strong rain was simulated in elevations above 800 m (shown in **Figure 4.17**).

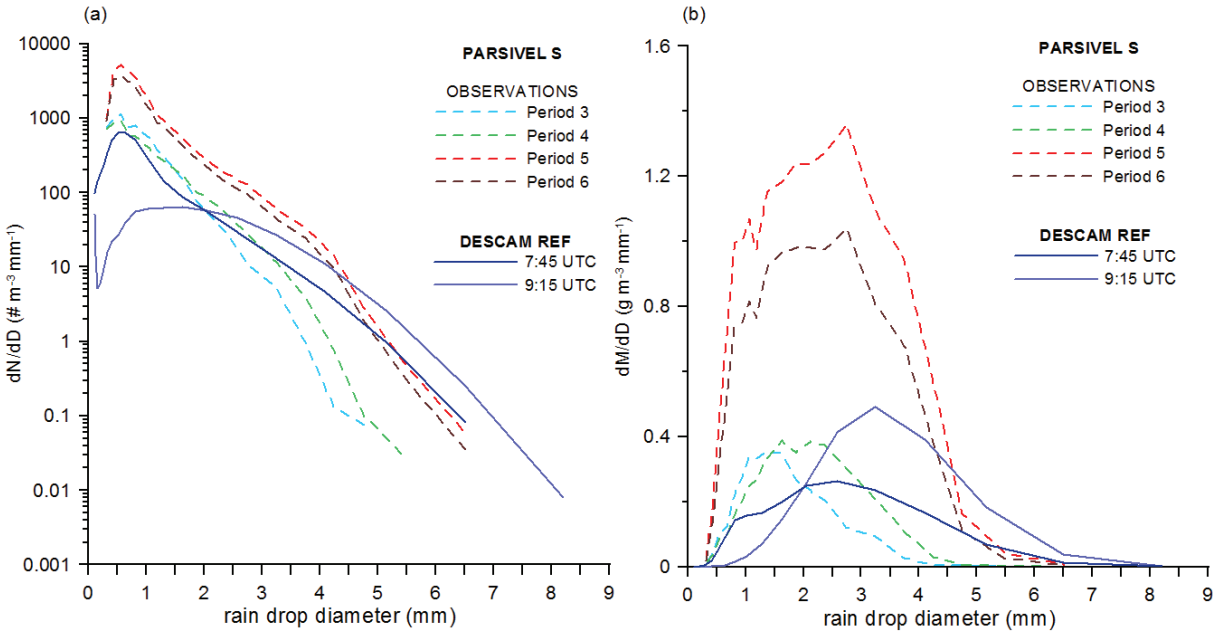

Figure 4.19: (a) Number size distributions of droplets (m^{-3} mm^{-1}) by the Parsivel S (dashed lines) during the Periods 3 to 6 and the DESCAM reference (REF) simulation results at different moments and (b) corresponding mass size distributions of droplets (g m^{-3} mm^{-1}). The simulated mean rain water content at 7:45 UTC and at 9:15 UTC is 0.92 g m^{-3} and 1.47 g m^{-3} respectively.

The maximum modeled droplet number is 500 m^{-3} mm^{-1} at 7:45 UTC (**Figure 4.18**a). The mass distributions from the observations during periods 5 and 6 are also extremely high compared to these of periods 3 and 4, as well as to the model results (**Figure 4.19**b). No more than 400 droplets m^{-3} mm^{-1} are found in the modeled spectrum of 9:15 UTC, while in this spectrum there is a maximum of 0.5 g m^{-3} mm^{-1} of droplets with diameters around 3 mm, which is slightly higher than in the observations of the periods 3 and 4. In the modeled spectra of 9:15 UTC (**Figure 4.19**a), the big droplets seem to be overestimated either with regard to the observations.

Due to the quite high observed number concentrations in the range from 500 µm to 1 mm it can be concluded that the Parsivel S was not away from the cloud base. The model results, on the contrary, indicate the extinction of this size class of cloud particles

in all rain spectra presented here before. Similar comparisons with rain spectra observed by the MRR10 are discussed next.

The MRR10 that was installed at the same place as the Parsivel 10 provided also number size distributions of the liquid hydrometeors during the IOP7a (as discussed in **chapter 3**).

During the periods 1 and 2, when precipitation was detected by the MRR10, there is no rain in the model results in this area. Thus, modeled spectra at different times, during the period when rain occurs, are selected to be compared with MRR10 observations. In **Figure 4.20**, the mean number size distribution by the MRR10 at two different levels (at 210 m and at 310 m above the surface) are compared with DESCAM results in the respective atmospheric layer. The observational periods for the MRR10 correspond to the occurrence of the maximum rainfall as illustrated by period 3 and 4 of **Figure 4.19**a.

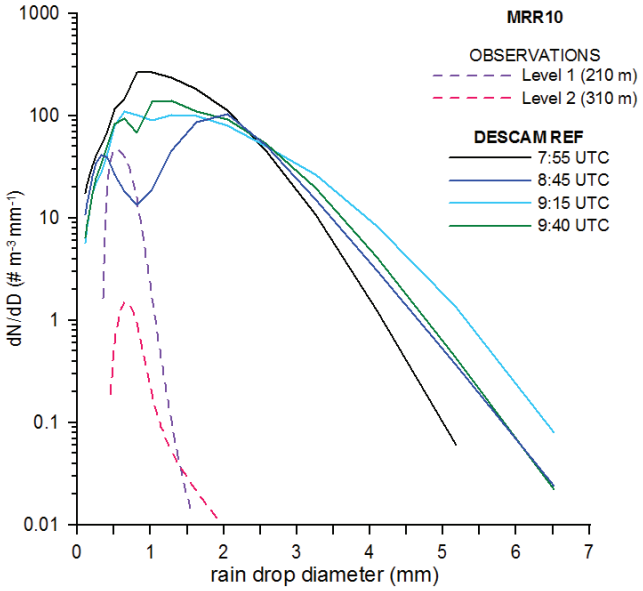

Figure 4.20: Number density distributions of droplets (m^{-3} mm^{-1}) at 210 m and 310 m ASL (i.e. closest levels at the surface) by the MRR10 (dashed lines) and the DESCAM reference (REF) simulation results at the surface for different times (solid lines).

Most of the raindrops in the MRR observations have diameters of about 0.5 mm, whereas a spectrum of 40 raindrops m^{-3} mm^{-1} with diameter of 0.4 mm was also found in the first maximum of the modeled spectrum at 8:45 UTC. As seen in **Figure 4.20**, the observations do not detect rain drops with diameters larger than 2 mm, while in both the disdrometer observations and the model results the maximum diameter size is in the range 6.5 mm to 8 mm. Furthermore, it has to be mentioned that no bigger rain drops were observed by the MRR spectra at higher levels, as demonstrated by two examples in **Figure 4.21**.

A maximum of 70 drops m^{-3} mm^{-1} with diameter of 0.5 mm is observed by the MRR10 at the altitude of 610 m, as well as a secondary maximum of 0.7 drops m^{-3} mm^{-1} with diameter of approximately 1 mm (**Figure 4.21**a). Except from the primary maximum at this level, the respective modeled values are much higher than in the observations at the altitude of 610 m as well as higher at 910 m (**Figure 4.21**b) with a clearly wider spectrum.

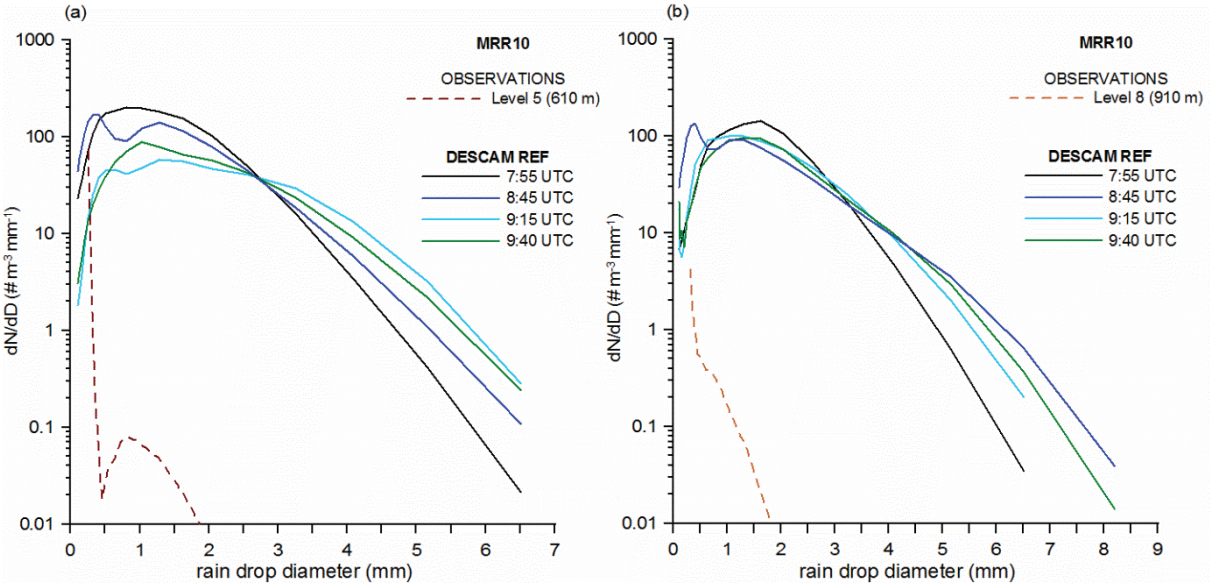

Figure 4.21: Number density distributions of droplets (m^{-3} mm^{-1}) at (a) 610 m and (b) at 910 m from the instrument MRR10 (dashed lines) and the respective DESCAM reference (REF) simulation results at different times (solid lines) for the same altitudes.

Overall, although precipitation was observed at a similar time by the MRR10 and the Parsivel 10, their observations differ significantly. Concerning that the MRR10 was located on the mountain slope, which is an area with a presence of strong vertical wind, it can be concluded that its observations were probably affected by this factor. Indeed, under such atmospheric conditions, MRR observations suffer by aliasing errors and therefore, their retrieved parameters, too (Tridon et al. 2011). Furthermore, attenuation seems to influence significantly the observations. Thus, in this case, the observations of the MRR10 cannot be trusted to evaluate the model results due to dynamical reasons.

To conclude, compared to ground-based observations, the model results are rather reasonable. Next, aircraft observations are compared to the respective simulation results.

4.2.3 Comparison between DESCAM model results (REF) and aircraft observations

After evaluating the model results at the ground, the in-cloud ones are analyzed. In this section, cloud radar reflectivity, IWC and ice crystal spectra are investigated

compared to HYMEX aircraft observations (e.g. from cloud radar RASTA and hydrometeor probes).

4.2.3.1 95 GHz cloud radar reflectivity

As DESCAM models the spectra of drops and ice particles in a bin resolved way, zenith and nadir observations performed by the airborne cloud radar can be determined from the simulated hydrometeor spectra. In order to compute from model the so called reflectivity factor, Z_{95GHz}, provided by RASTA measurements (see **Figure 3.26**) the following steps must be considered. The reflectivity factor Z_{95GHz} (in dBZ) can be determined from the equivalent radar reflectivity z_e by the equation 4.4.

$$Z_{95GHz} = 10 log z_e \qquad 4.4$$

The equivalent radar reflectivity z_e (in $mm^6\ m^{-3}$) can be calculated by means of the backscattering coefficient σ_B and the number distribution of the hydrometeors dN/dD, as in the equation 4.5 (Penide 2010):

$$z_e = 10^{18} \frac{\lambda^4}{\pi^5 |K_w|^2} \int \sigma_B \frac{dN}{dD} dD \qquad 4.5$$

where the normalization constant $|K_w|^2$ is equal to 0.75 at 95 GHz. The backscattering coefficient σ_B is a function of the radar wavelength λ (for 95 GHz: λ = 3.15 mm), as well as a function of the hydrometeor size D and of the optical properties of the hydrometeor given by the real and imaginary part of the complex refraction index. σ_B is calculated by using Mie (1908), therefore a spherical form is assumed for the shape of the hydrometeors. The values for the refractive index were taken for water from Ray (1972), those for ice from Warren (1984). Equations 4.4 and 4.5 allow the calculation of the Z_{95GHz} for all cloudy areas in the model results.

Depending on the phase and the size of the hydrometeors, the electromagnetic wave that is emitted by the cloud radar can be strongly attenuated, as seen in **chapter 3**. In order to consider this effect in the model simulation, the extinction coefficient of the simulated hydrometeor spectra σ_{ext} is recalculated next to the backscatter coefficient σ_B (Penide 2010). The so called "one way attenuation factor A" (Gosset and Sauvageot 1992) can be calculated for each modeled grid point as a function of the extinction coefficient, as in the equation 4.6.

$$A = \int_{100\mu m}^{D_{max}} \sigma_{ext} \frac{dN}{dD} dD \quad 4.6$$

The lower limit in 4.6 is set to 100 μm, as 95 GHz reflectivity is not sensitive to particles with D_{max} < 100 μm.

The attenuation of the electromagnetic wave is given by the integration of the attenuation factor for the path from the flight level ζ_0 to the level of the cloud target ζ_T and back. The attenuated radar reflectivity $z_{e,atten}$ can thus be determined by the equation 4.7:

$$z_{e,atten} = z_{e,0} exp\left[-2\int_{\zeta_0}^{\zeta_T} A d\zeta\right] \quad 4.7$$

The index 0 corresponds to the signal received without attenuation. The transformation to the reflectivity factor Z_{95GHz} (in dBZ) as in the equation 4.4, leads to equation 4.8:

$$Z_{95,atten} = Z_{95GHz,0} - 8.68\int_{\zeta_0}^{\zeta_T} A d\zeta \quad 4.8$$

where the factor $Z_{95GHz,0}$ corresponds to the non-attenuated values (as presented in **Figure 4.22**a).

The importance of the attenuation in the reflectivity values can be appreciated i.e. from **Figure 4.22**, where the modeled non-attenuated (**Figure 4.22**a) and attenuated (**Figure 4.22**b) reflectivity is presented, both at 8:20 UTC. In **Figure 4.22**b the assumption that the level of the flight was at 5600 m above sea level is made for the calculation of the $Z_{95,atten}$.

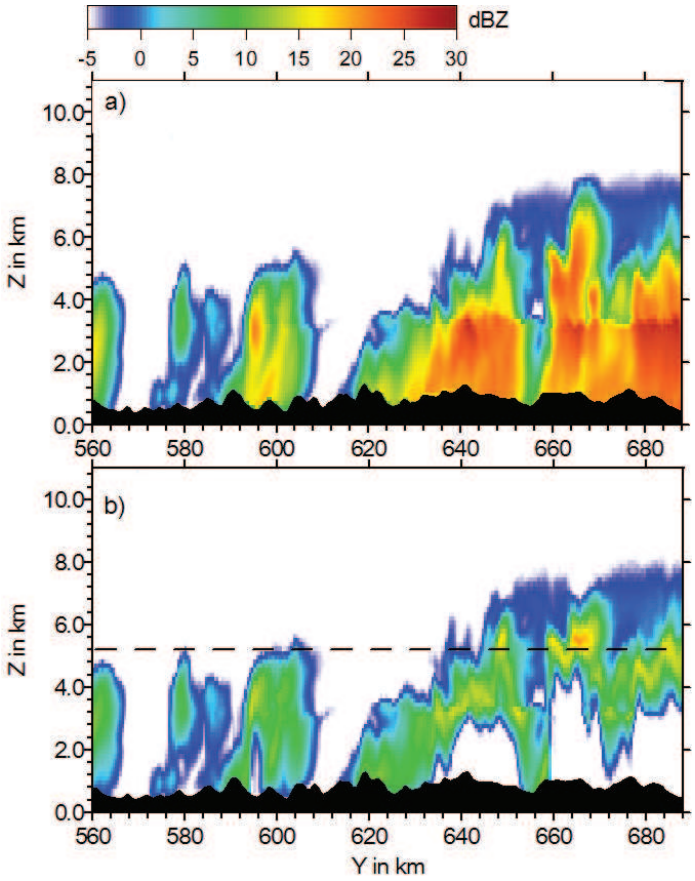

Figure 4.22: Vertical cross section from SSW to NNE at 8:20 UTC (a) of the modeled non-attenuated reflectivity Z_{95GHz} and (b) of the modeled attenuated reflectivity $Z_{95GHz,atten}$ assuming a flight level of 5.6 km (dashed line).

Comparing **Figure 4.22**a and **Figure 4.22**b, a reduction of the reflectivity factor due to the attenuation can be detected. For regions with precipitation below the melting level the strong Z_{95GHz} has completely disappeared when comparing with $Z_{95,atten}$. The observed reflectivity signals break off at about 2 - 3 km below the aircraft, thus signals reaching altitudes below 2 km do rarely occur. It is certainly not evident that clouds and precipitation were present in the reflectivity free zone between the ground and the aircraft position. Finally, in **Figure 4.22**b, a discontinuity in the model results appears at the melting level, as the model treats the transition of the precipitating ice to water as an instantaneous process when temperature becomes larger than 0°C. Consequently, strongest reflectivity occurs just below the melting level.

The comparison between the attenuated and the non-attenuated simulated reflectivity at 95 GHz indicates that the signals encountered during IOP7a by the airborne cloud radar are strongly influenced by attenuation. Attention has to be taken into account for the RASTA products.

The blue line in **Figure 4.23** illustrates the vertical cross section in DESCAM results of **Figure 4.22** at 8:20 UTC. This vertical cross section is applied focusing on the location of the precipitating system (see **Figure 4.9**d).

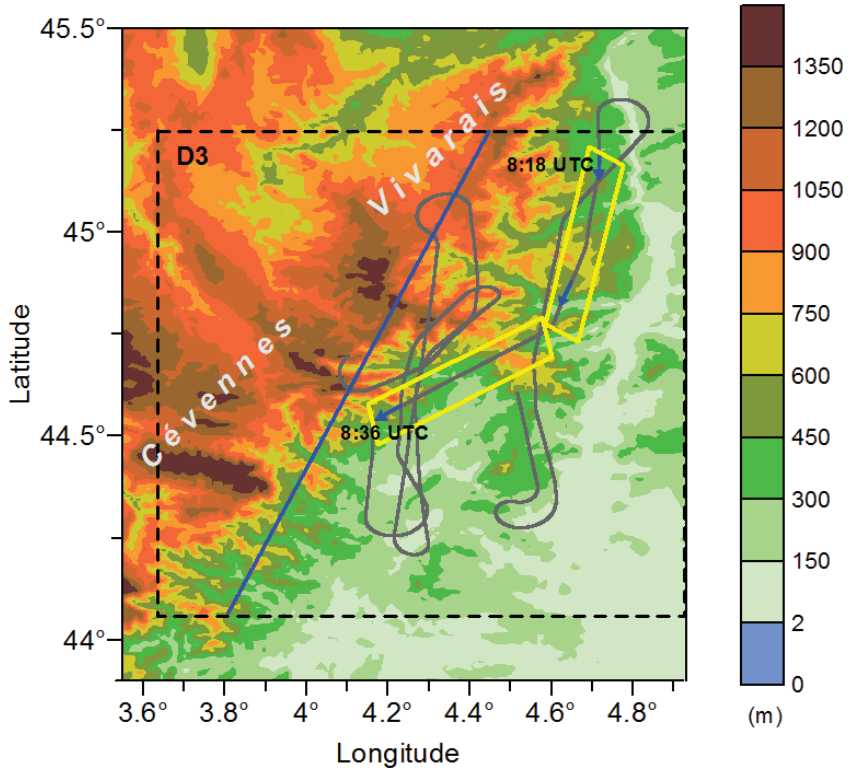

Figure 4.23: Position of the Falcon 20 (in grey) from 8:00 to 9:20 UTC. The parts of the trajectory in the yellow frames correspond to the aircraft position between 8:18 and 8:36 UTC. The blue line indicates the vertical cross section of **Figure 4.22** in D3 (dashed frame).

At this time, Falcon 20 with RASTA on-board was flying from NE to SW over the region indicated by the yellow frames in **Figure 4.23** at an altitude of 5.6 km above sea level. The observed radar reflectivity during this part of the trajectory is shown in **Figure 4.24**.

By comparing **Figure 4.24** with **Figure 4.22**a, it is seen that the modeled non-attenuated reflectivity reaches values up to 30 dBZ whereas the observed one does not exceed 18 dBZ. The observed values are closer to the ones in **Figure 4.22**b of the simulated attenuated reflectivity. This confirms that attenuation in RASTA observations must be considered. Moreover, modeled reflectivity (both attenuated and non-attenuated) reaches levels up to 8 km, whereas RASTA observes reflectivity up to 10 km, which can be attributed to the presence of ice crystals at those levels. To investigate this, the retrieved by RASTA IWC is compared to the model results, next.

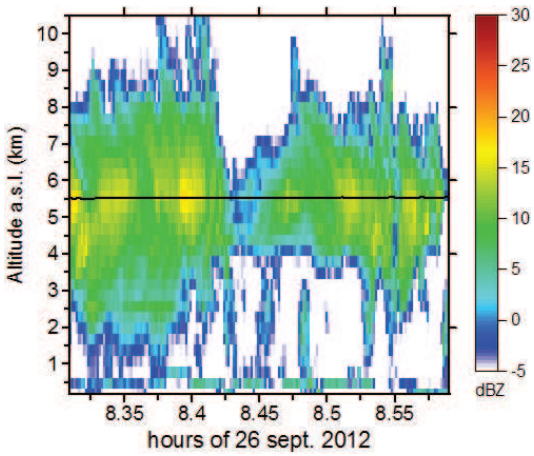

Figure 4.24: Observed radar reflectivity (in dBZ) from RASTA from 8:18 UTC to 8:36 UTC (as indicated in) at the altitude of 5.6 km.

4.2.3.2 Ice water content (IWC)

Here, the IWC profile determined by means of the cloud hydrometeor probes and from the cloud radar will be compared to the mean profiles resulting from the model calculation. In order to do so, a limited area in the innermost model domain was selected wherein clouds and precipitation continuously appeared between 7:30 UTC until 11:00 UTC. This area is indicated by the triangle of **Figure 4.25**.

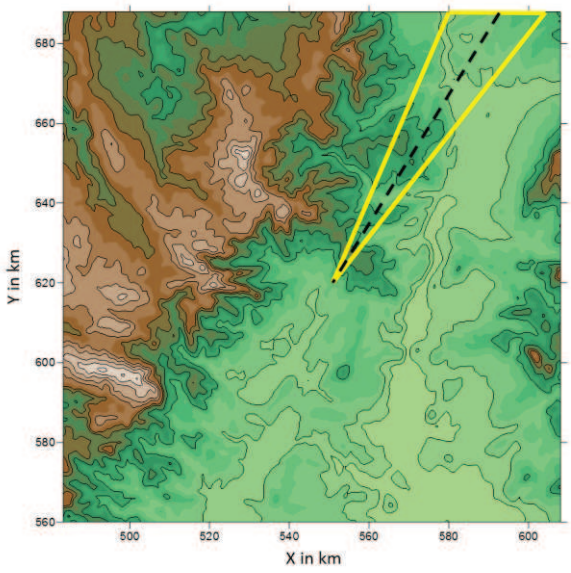

Figure 4.25: The inner model domain (D3) along with the focus-area (indicated by the yellow triangle) for the calculation of the mean simulated IWC profiles and the ice crystal spectra. The black dashed line indicates the vertical cross section of the figure 4.26.

Indeed, a vertical cross section in this area (dashed line in **Figure 4.25**) shows modeled IWC values up to 1.5 g m^{-3}, as shown in **Figure 4.26**a, in the atmospheric layer between 3.5 and 4 km at 8:20 UTC. **Figure 4.26**a shows also that the melting level is found at 3.2 km above sea level.

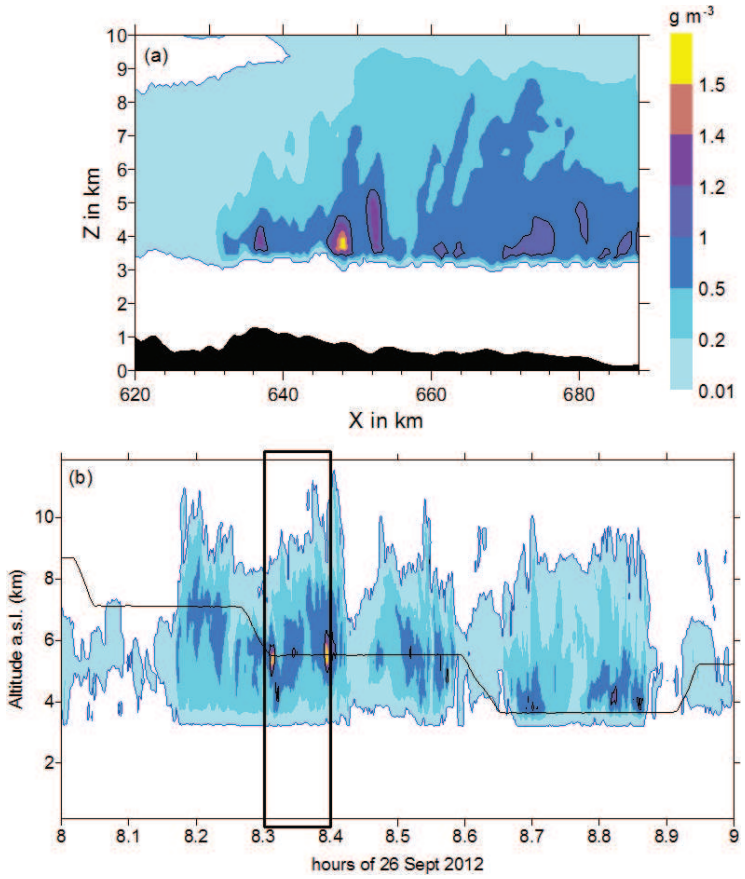

Figure 4.26: (a) Vertical cross section (as in **Figure 4.25**) of modeled IWC (in g m^{-3}) at 8:20 UTC. (b) Retrieved IWC (in g m^{-3}) by RASTA cloud radar from 8:00 UTC to 9:00 UTC. The black frame indicates the flight part which corresponds to (a). The black line illustrates the altitude (in km) of the aircraft.

Figure 4.26b shows the retrieved IWC by RASTA as a function of the time and the altitude. By focusing on the time period that corresponds to **Figure 4.26**a, it is seen that the observations are qualitatively in agreement with the model results. The maximum IWC from 8:00 to 9:00 UTC was observed at 8:24 UTC (1.9 g m^{-3}) and it is 17 % higher than the maximum of the modeled IWC (1.6 g m^{-3}) at 8:20 UTC. Comparing **Figure 4.26**a with **Figure 4.26**b, it is observed that values in the range 0.2 – 0.5 g m^{-3} are found up to 9 km above sea level, whereas these values rarely exceed the 8.5 km in the RASTA retrieval. Nevertheless, the melting level is similar in the observations and the model results.

During the period of strongest precipitation, model results were stored every 5 minutes. For the present analysis, a time span from 7:55 to 9:20 UTC was selected, which

covers quite well the period of the aircraft measurement discussed in **chapter 3**. Thus, 18 individual model times/outputs (t_i, i=1,18) were used for the calculation of the time averaged ice water content $\overline{IWC}$. For each individual output time t_i the IWC profile was determined by averaging horizontally over the limited area displayed in **Figure 4.25**. Only grid points with IWC larger than 0.01 g m^{-3} were considered for this analysis (see **Figure 4.26**a).

In order to compare the model results with the airborne observations, it must be respected that the aircraft, for security reasons, avoided zones of strong reflectivity, i.e. regions with high concentrations of ice and water. Thus, Rayleigh reflectivity Z_{Ray} was also calculated from the simulated particle spectrum for each grid point. Only data points with Z_{Ray} below 35 dBZ were selected for the calculation of the mean modeled IWC(t_i). Both conditions yielded about 1500-2000 single profiles which contributed to the calculation of each individual vertical profile of IWC(t_i) to avoid zones that were not accessed by the aircraft.

In **Figure 4.27**, the modeled IWC profile averaged in space and in time is displayed. The standard deviation from the temporal mean is represented by the error bars. In order to better illustrate the strong temporal variation of the IWC, two further profiles at different times are shown; the red dashed line represents the mean profile at 8:20 UTC, whereas the green dashed line corresponds to 9:10 UTC. All curves present spatial averages over the triangular area shown in **Figure 4.25**. The comparison between modeled profiles and profiles provided from the airborne cloud radar indicate similarity in their vertical shape, however, the modeled IWC is significantly higher in lower levels from 3.5 to 7 km. On the contrary, at elevated altitudes above 8.8 km the retrieved IWC from RASTA exceeds with values of 0.2 g m^{-3} the model results. This can be caused by a strong difference in data volume between observation and model results. While the model results rely on typically 2000 data points for each level, retrieved or parameterized radar data above 8.5 km only have a sample volume of 100 to 50 observational points (decreasing with altitude).

The individual profiles presented in **Figure 4.27** at 8:20 UTC and 9:10 UTC demonstrate the variability in IWC profile during the temporal evolution of the convective system. At the end of the development phase, at 8:20 UTC, very high IWC accumulated in altitudes from 4 to 6 km leading to important precipitation during this period, as discussed in the **chapter 3**. 50 minutes later, at 9:10 UTC, the IWC has strongly decreased in the layer from 4 to 6 km, but more IWC was formed or transported to the uppermost regions of the cloud system.

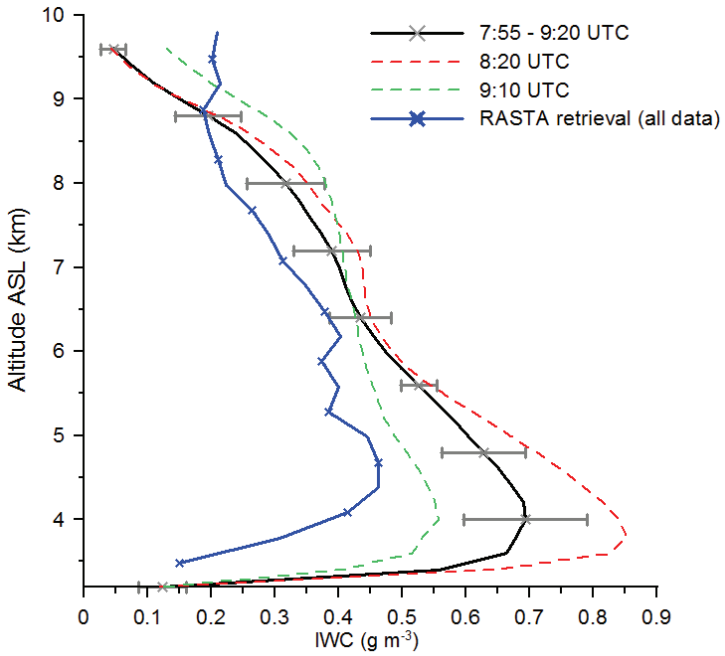

Figure 4.27: Vertical profiles of the modeled and retrieved IWC. The black curve gives the mean modeled value over the main period of precipitation. The error bars show the standard deviation in time. Red and green dotted lines correspond to the individual profiles at 8:20 and 9:10, respectively. The blue line corresponds to the RASTA retrieval (as already presented in **Figure 3.29**).

This comparison shows that the model results yield higher ice water content than the retrieval techniques applied to the cloud radar observations. This result is not surprising, as the analysis of the radar reflectivity observations from RASTA has demonstrated that Z_{95GHz} signals are strongly attenuated, especially in altitudes below 7 km (and perhaps not totally corrected).

Another possibility to assess the accuracy of the modeled IWC is the comparison with the in-situ measurements of cloud microphysics. The measurement techniques of the hydrometeor probes and the method for calculating IWC from the observed ice particle size distributions are described in section **3.4.2**. The comparison between the observed and the modeled mean IWC are presented in **Figure 4.28**, where the modeled mean vertical IWC profile is illustrated by the black line.

The highest mean IWC with a value of 1.26 g m^{-3} was found for the in-situ observation in between 5.1 and 5.4 km. This value, which was based on 56 individual samples, exceeds significantly the modeled one, as well as the retrieved IWC from RASTA, as seen in **Figure 4.28**. In the grid layer between 5.4 km and 5.7 km, where most samples were taken, the mean IWC decreases clearly to 0.82 g m^{-3}. With increasing altitude the decline in IWC becomes obvious. The uncertainty of the observations with low sample numbers (< 10)

in levels from 6.5 to 8 km has the effect that the remaining profile of in-situ IWC seems to agree with the modeled one. All in-situ observations of IWC exhibit important fluctuation. Taking into account the high variability of the IWC, it can be noticed that most modeled IWC is well located in the range of the observed fluctuations of in-situ IWC. The differences in space and also in time occurring for the airborne observations make the comparison with the model results quite challenging.

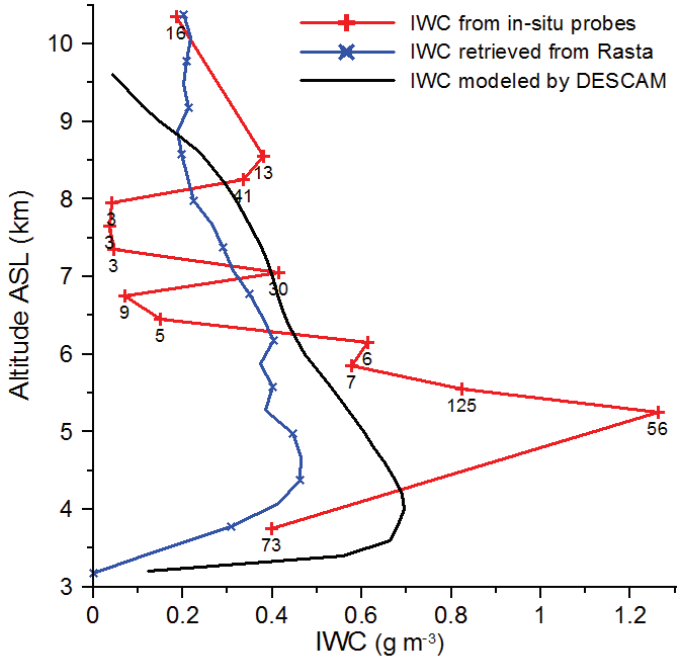

Figure 4.28: Mean IWC profiles provided by different methods: by the RASTA retrieval (blue line), as in **Figure 4.27**, by the calculation from hydrometeor probes measurements (red line) and by the DESCAM REF simulation averaged over the time period 7:55 UTC to 9:20 UTC (black line) and over the triangular area shown in **Figure 4.25**. The labels for the in-situ IWC (red curve) give the number of 10 s samples encountered in the different altitudes.

4.2.3.3 Ice crystal spectra

As explained in **chapter 3**, the in-situ measurements of the hydrometeor probes consisted of numerous individual samples of hydrometeor (ice) spectra. In the present section, the mean ice crystal spectra at different altitudes, are being compared with the respective simulated ice crystal spectra.

The selected region of the model domain for the present calculations is the same than was used for the calculation of the mean IWC profile, (**Figure 4.25**). Considering the large variation of the in-situ probe measurements (i.e. **Figure 4.28**), the interest here is focused on the number distribution of ice crystals in the atmospheric layer from 5 km to 6 km, where most of the ice spectra were sampled. In **Figure 4.29**, the number density

distributions of the observed spectra are presented along with the modeled ones in different levels in the aforementioned atmospheric layer. In particular, **Figure 4.29** shows the mean modeled ice crystal spectra for the period 8:00 to 9:00 UTC at different altitudes.

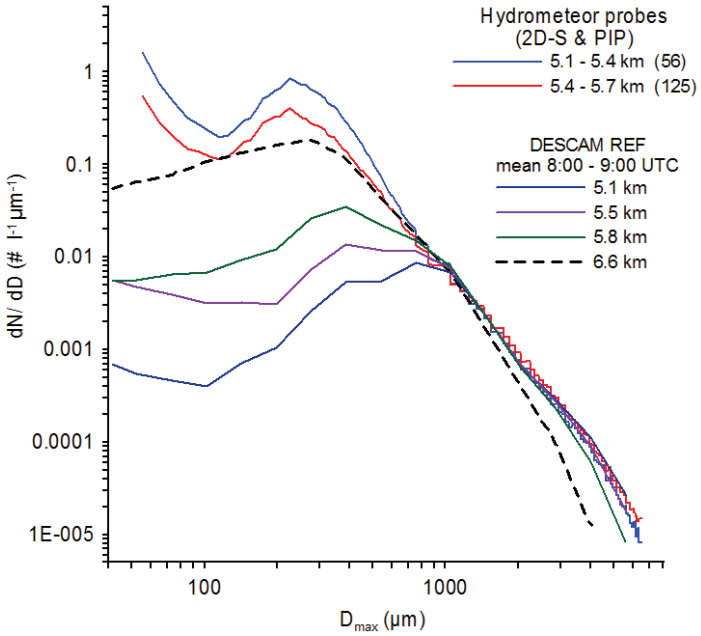

Figure 4.29: Number density distributions of ice crystals (l^{-1} μm^{-1}) as a function of the maximum dimension (D_{max}) from the hydrometeor probes' in the atmospheric layers between 5.1 km and 5.4 km (blue line) and between 5.4 km and 5.7 km (red line). Mean number density distributions of modeled ice crystals from 8:00 UTC to 9:00 UTC are plotted for altitudes of 5.1 km, 5.5 km, 5.8 km and 6.6 km.

As expected, the number of the sampled ice crystals exceeds the modeled ones in the layer from 5 to 6 km (see **Figure 4.28**) continuously during the whole time period from 8:00 UTC to 9:00 UTC. This fact is more pronounced for small ice crystals (D_{max} < 500 µm), whereas the number distributions of the large ice crystals (D_{max} > 500 µm) are generally in agreement with the sampled ones.

However, at the altitude of 6.6 km, it can be clearly seen that the mean ice crystal spectrum is closer to the observed ones. In this mean spectrum, the maximum is found for crystals with diameters of 200 - 300 µm, as in the observations. At this altitude (6.6 km) the highest maximum in all modeled ice crystal spectra is found. The tendency of the modeled spectra is in agreement with the observed ones, but with definite underestimation of the number of the small ice crystals (< 200 µm), as well as of the largest ones (> 2000 µm). This behavior is confirmed by the presence of higher modeled values of mean IWC at this altitude than in the observations from the hydrometeor probes, as shown in **Figure 4.28**. Also, the larger vertical extension of the modeled IWC (i.e. **Figure 4.26**) justifies that the

mean modeled spectrum at 6.6 km is rather in agreement with spectra observed at lower altitudes by 1 km.

In general, the comparisons between observations and model results confirmed a reasonable simulation of the heavy precipitation of IOP7a by DESCAM. Nevertheless, studies have shown that the domain configuration of NWP models influences the simulation results in cases of heavy rainfall (Bray et al. 2010). Most recently, Chu et al. (2017) investigated the reproduction of an extreme precipitation event by using three different horizontal domain configurations of the WRF model. They concluded that the simulation results are sensitive to the domain size, with the one that merely covers the area of interest to not completely allow the development of small-scale features. However, there is lack of information from respective sensitivity studies for detailed cloud models. In the last section of this chapter, that follows hereafter, the influence of modifications of the model domain configuration is investigated.

4.3 Influence of the DESCAM domain modifications

As explained in **chapter 3**, a critical factor that causes the Cévenols heavy precipitation events (such as HYMEX IOP7a) is the humid and moisture air flow from the Mediterranean Sea. The impact of the Mediterranean Sea will be studied by considering a smaller part of this region, shifted to the west. The question of how such a modification of the lateral boundaries will influence the formation and evolution of the HYMEX IOP7a precipitating system in space and time with respect to the reference simulation motivated the following sensitivity study.

4.3.1 Description of the model set-up

For this study, DESCAM-3D was initialized by considering a smaller outermost domain D1A that was shifted to the west with regard to the parent domain D1 of the reference simulation (**Figure 4.30**). In particular, the center of D1A for the sensitivity simulation is located 3.3° to the west in comparison with the center of the D1 of the reference simulation and 0.75° to the north, respectively. The coordinates of the center of

the domains for the two cases are given in **Table 4.3**. The model simulations for which this domain configuration has been used for their initialization will refer hereafter to SSD (for Smaller Shifted Domain).

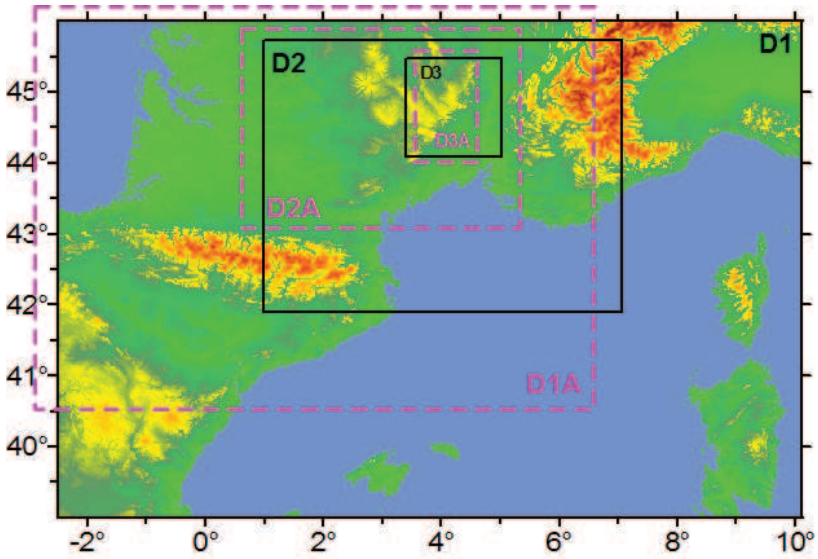

Figure 4.30: Comparison between the nested domain configuration of DESCAM-3D for the reference (REF) and the sensitivity simulation SSD, expressed as a function of latitude and longitude. The three domains of the REF case are indicated by the black frames and the domain configuration of the SSD case is indicated by the pink dashed frames. In both figures, "D1" corresponds to the outermost domain, "D2" refers to the first nested domain and "D3" to the second nested domain.

	REF	**SSD**
Domain size: **D1** **D2** **D3**	 1024 x 768 km^2 512 x 384 km^2 128 x 128 km^2	 784 x 656 km^2 386 x 322 km^2 97 x 161 km^2
Center of D1: **(latitude, longitude)**	 42.5°, 4.8°	 43.25°, 1.5°

Table 4.3: Specifications about the domain set up of the reference simulation (REF) and the sensitivity simulation SSD.

The consideration of a smaller and shifted outermost domain results in differences concerning atmospheric dynamics (i.e. horizontal wind, relative humidity). **Figure 4.31** illustrates the intensity and direction of the horizontal wind at the surface, as well as the regime of the relative humidity (RH) at the beginning of the simulations REF and SSD, in

their outermost domains. According to this figure, the dynamical field of the SSD simulation is characterized by the presence of up to 20 % higher RH over the sea, at the south of Cévennes-Vivarais region, compared to REF. Indeed, the less humid air masses situated over the north-east coasts of Spain (seen in **Figure 4.31**a) are not taken into consideration in the smaller outermost domain of the SSD. The SSW horizontal wind that prevails over the north-west Mediterranean Sea, transfers drier air masses at the South of France, in REF simulation, thus the percentage of RH is lower than in SSD. Also, the southern horizontal wind over the sea area at the South of France appears about 10 km h^{-1} less intense in SSD simulation than in REF.

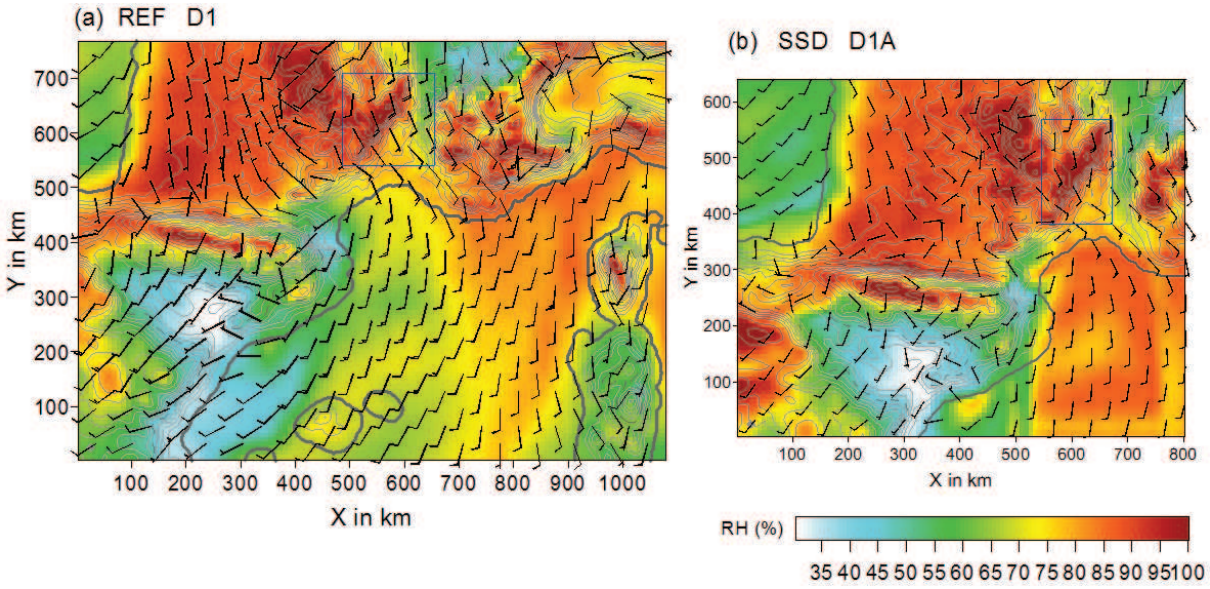

Figure 4.31: (a) Horizontal wind barbs and percentage of relative humidity (RH) at the surface of the outermost domain D1 of REF simulation at 01:00 UTC. The blue frame indicates the D3. (b) Same variables at the surface of the outermost domain D1A of SSD simulation. The blue frame illustrates the D3A.

In order to investigate possible differences of the SSD configuration in the simulation results, in the following section, the modeled radar reflectivity and cumulative rainfall are being compared to the output of the simulation REF, as well as to the respective observations.

4.3.2 Comparison between REF and SSD simulation results

Modeled radar reflectivity from the REF and the SSD cases are presented for different times of integration and compared to the respective observations in **Figure 4.32**, **Figure 4.33** and **Figure 4.34**.

The consideration of a smaller outermost domain that is shifted to the west results in differences in the modeled X-band radar reflectivity with respect to the one from the reference (REF) case. In particular, at 6:40 UTC, high radar reflectivity values up to 55 dBZ are found in the SSD results, as seen in **Figure 4.32**c, where the precipitating system is horizontally larger than in the reference case (**Figure 4.32**b). The maximum modeled reflectivity values are slightly shifted to the west, compared to the observations shown in **Figure 4.32**a. The orientation of the precipitating system of the SSD case is similar to the observed one.

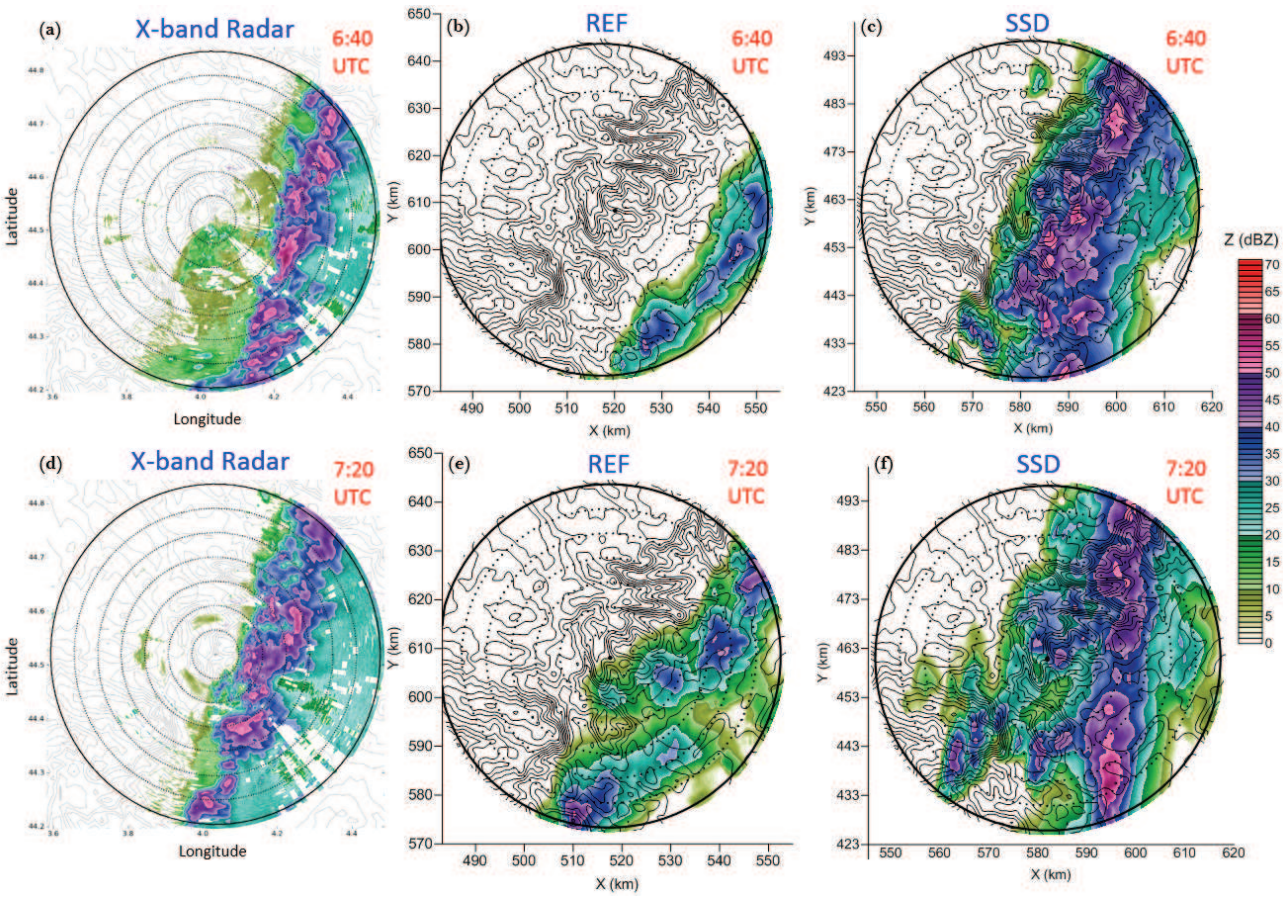

Figure 4.32: PPI images of the radar reflectivity observed by the X-band radar during the HYMEX IOP7a (a, d), simulated by DESCAM-3D for reference case (b, e) and simulated by DESCAM-3D for SSD case (c, f). The PPI images are obtained at two specific hours: at 6:40 UTC (a, b, c) and at 7:20 UTC (d, e, f).

Forty minutes later, at 7:20 UTC, the convective system for the SSD simulation is found in the southern part of the model domain (**Figure 4.32**f), whereas high reflectivity values of 40 to 50 dBZ are also seen in the north-eastern part of the domain, similar to the observations (**Figure 4.32**d). At that moment, the system in SSD is almost perpendicular to the X axis. On the contrary, lower radar reflectivity values were found in REF simulation (**Figure 4.32**e), mostly from 10 to 30 dBZ, but the system's orientation and the position

of the southern cell are closer to the observations than in the SSD case. However, some high reflectivity values up to 50 dBZ are found in REF simulation, locally, at the south.

The highest reflectivity values in SSD simulation results at 8:00 UTC are found in the eastern part of the domain, as seen in the **Figure 4.33**c, at similar location as in REF (**Figure 4.33**b). At the same time, most reflectivity values seen in SSD results are between 10 and 20 dBZ and correspond to light rain, almost all over the presented part of the domain. The high radar reflectivity values observed at the south-west of the radar position (**Figure 4.33**a) are not seen in the REF results neither for the SSD case.

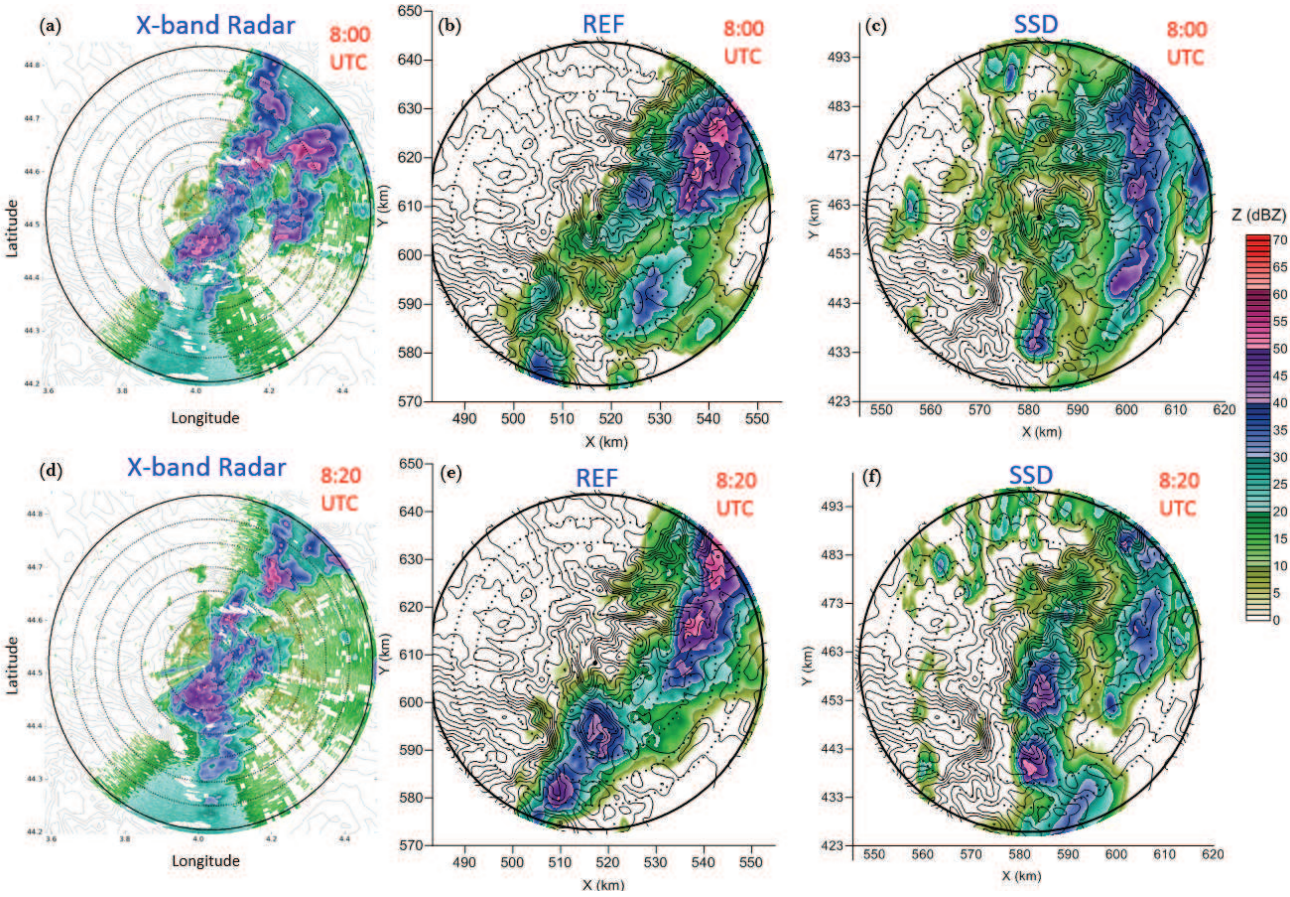

Figure 4.33: PPI images of the radar reflectivity observed by the X-band radar during the HYMEX IOP7a (a, d), simulated by DESCAM-3D for reference case (b, e) and simulated by DESCAM-3D for SSD case (c, f). The PPI images are obtained at two specific hours: at 8:00 UTC (a, b, c) and at 8:20 UTC (d, e, f).

At 8:20 UTC, the main precipitating cell observed at the north-eastern part of the domain in the figure **Figure 4.33**d is found more to the south in the SSD results (**Figure 4.33**f). However, it is well-estimated by the REF simulation results (**Figure 4.33**e). A secondary precipitating cell was observed to the south of the radar position, which is also seen in both simulations, whereas in the SSD results it is found to be shifted by about 10 km to the east.

The SSD simulation results at 9:00 UTC in **Figure 4.34**e show that the precipitating system was located at the same region as in the previous results of 8:20 UTC. However the system is slightly reinforced at the northeast, with reflectivity values from 30 to 50 dBZ over a large area. The maximum observed values (**Figure 4.34**a) are about 10% higher than for the SSD case. In the southern part of the radar observation field, precipitating clouds already disappeared.

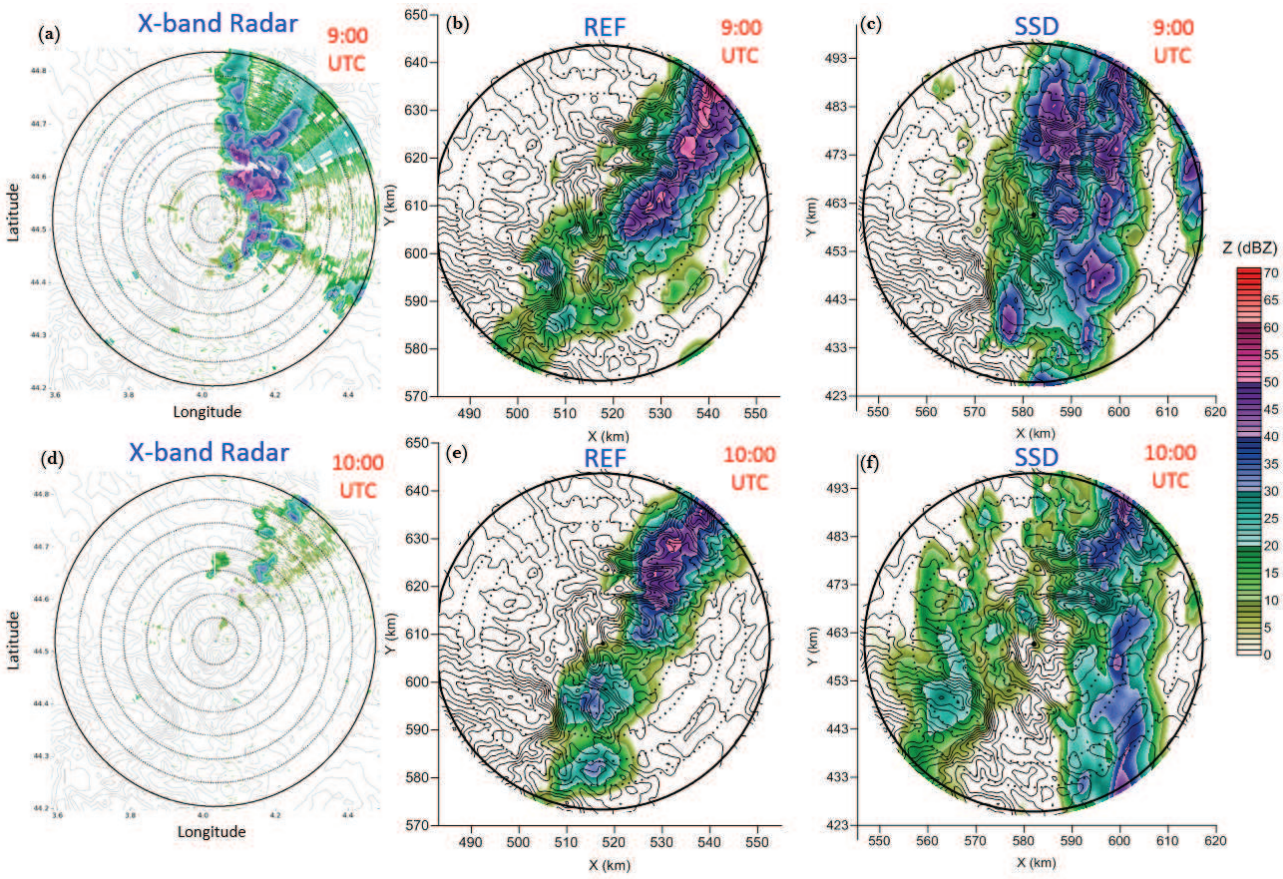

Figure 4.34: PPI images of the radar reflectivity observed by the X-band radar during the HYMEX IOP7a (a, d), simulated by DESCAM-3D for reference case (b, e) and simulated by DESCAM-3D for SSD case (c, f). The PPI images are obtained at two specific hours: at 9:00 UTC (a, b, c) and at 10:00 UTC (d, e, f).

At 10:00 UTC the precipitation system disappeared totally in the observations. For both simulations, however, precipitation continued at 10:00 UTC over the radar observation field (**Figure 4.34**e and **Figure 4.34**f). Some small precipitating cells over both the mountainous regions and areas of low altitudes are seen in the SSD results in **Figure 4.34**f.

Regarding the quantitative comparison between the observations and the two model simulations, the mean probability density function of radar reflectivity for the time period from 6:00 UTC to 11:00 UTC is presented in **Figure 4.35**. Except from the

reflectivity between 35 dBZ and 45 dBZ, the values around 25 dBZ, as well as the highest reflectivity bins (> 55 dBZ), the SSD results either underestimates or slightly overestimates the respective observed values. As the SSD case simulates a high precipitation event, the detection of reflectivity between 50 to 60 dBZ is more important. In this range, REF simulation reproduces reflectivity fields which are more in agreement with the observations.

Next, the impact of the modification of the domain configuration on the cumulative rainfall is discussed.

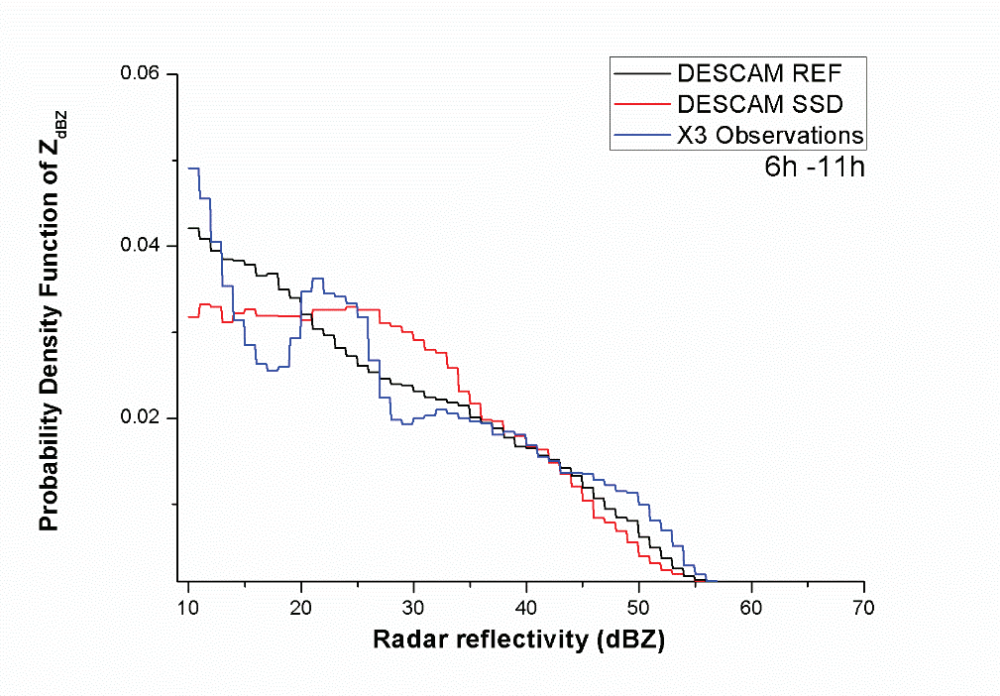

Figure 4.35: Averaged probability density function of the X-band radar reflectivity observations (blue lines) and the respective DESCAM-3D model results of the reference simulation (REF, black line) and the SSD simulation (red line) for the time period of 6:00 UTC – 11:00 UTC.

Figure 4.36 illustrates the cumulative rainfall at the surface until 11:00 UTC by the KED QPE, the REF and the SSD simulation. According to this figure, the convective system was developed along the Cévennes mountain ridge during both model simulations, as the observations showed. The system's orientation in the SSD results is different than in the observations and the REF simulation; it has an angle of 75 degrees related to the X axis whereas the respective angle of the observed one was approximately 60 degrees. The region of the highest rain accumulation is well determined in the SSD results, but is shifted about 10 km to the south and 5 km to the east compared to REF results and 15 km to the west compared to the KED QPE. A secondary precipitating cell to the south is occurring in the SSD results (**Figure 4.36**c) which does not exist neither in the observations (KED QPE)

nor in the REF simulation results. The maximum cumulative rainfall in the KED QPE is 114 mm, while the maxima in the REF and SSD simulation results are 116 mm and 121 mm respectively. Even if the maxima are quite close, the rain distribution in SSD is different than the observed or simulated in REF.

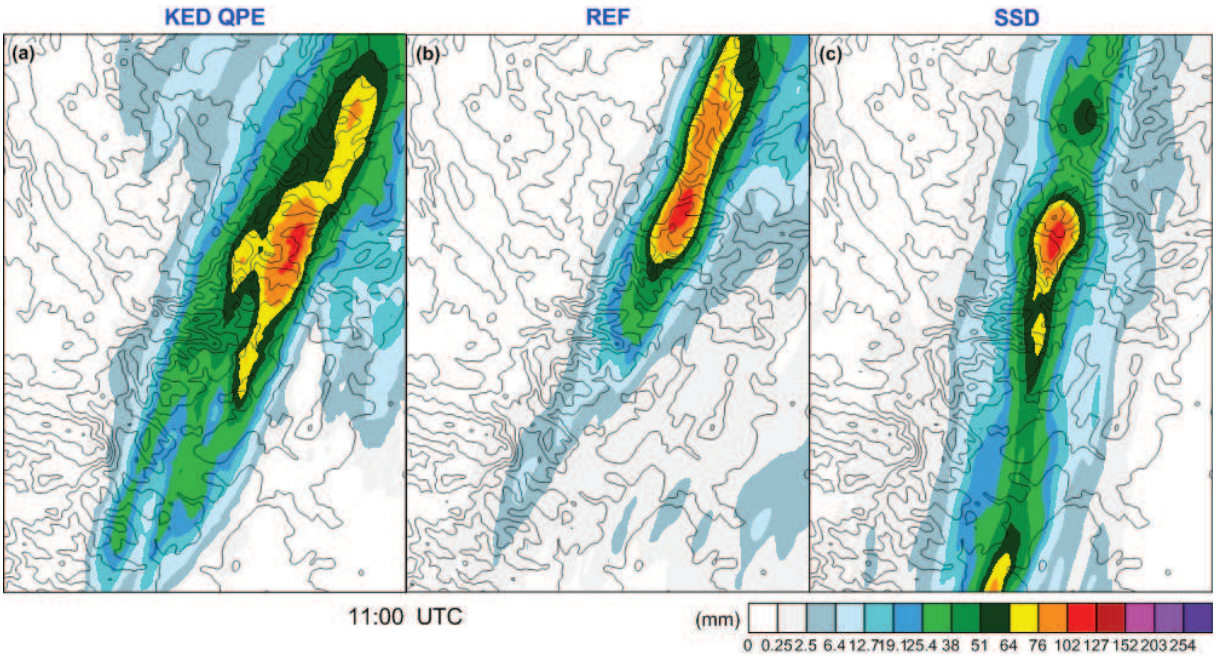

Figure 4.36: Cumulative rainfall from 00:00 UTC to 11:00 UTC of the 26th September 2012, as estimated by (a) the QPE observations, (b) the REF simulation by DESCAM-3D and (c) the SSD simulation by DESCAM-3D.

Finally, the probability density function of the accumulated precipitation for the SSD case (**Figure 4.37**, red curve) shows that the frequency of the rain spots from 1 mm to 40 mm is well reproduced in comparison to the observations. On the contrary, the strongest rain spots (> 50 mm) are rather underestimated by the SSD simulation. However, a descending trend is seen in both quantitative estimations of the model simulation, which is in agreement with the observations.

It is concluded that dynamics play important role in the simulation of this heavy precipitation episode. The boundaries of the outermost model domain must be determined carefully including, in this case, the entire southerly wind flow. Otherwise, the simulated system has quite different orientation and spatial distribution. The SSD simulation will be further investigated in **chapter 5**, by studying at the same time the impact of different scenarios of pollution.

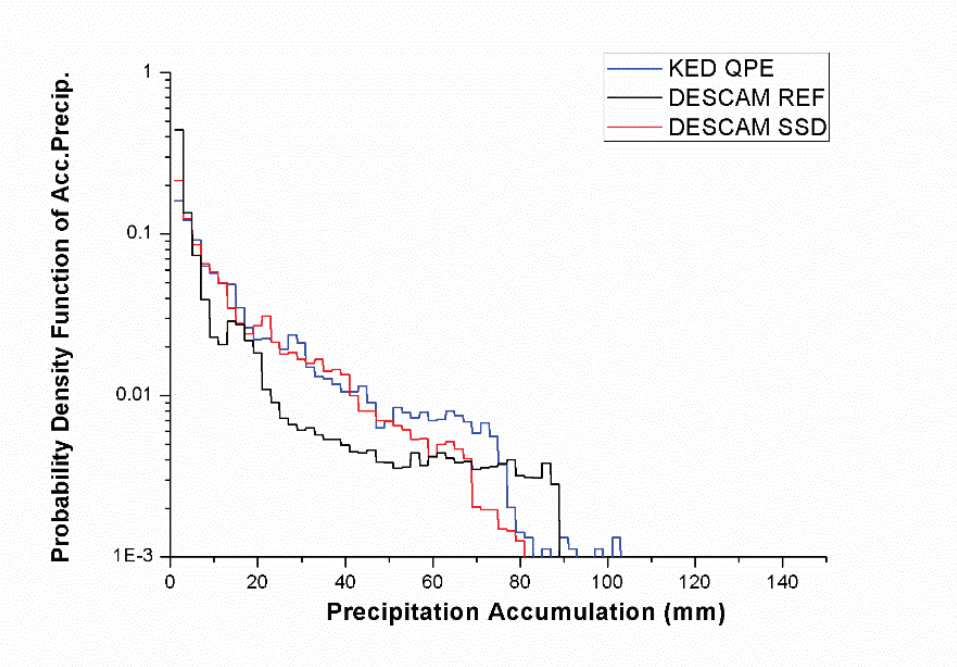

Figure 4.37: Probability density function of the rain accumulation on the surface between 00:00 UTC and 11:00 UTC of the 26th September 2012 calculated for the QPE observations (blue line) and the DESCAM-3D model results of the reference simulation (black line) and the SSD simulation (red line).

4.4 Conclusions

In the present chapter, the details about the model initialization in order to simulate the heavy precipitation episode of IOP7a were described, as well as the simulation results in comparison to the respective HYMEX observations and in-situ measurements. The aim of this work was the investigation of the characteristics of the precipitating system, as well as the validation of the model simulation.

The reference (REF) simulation reproduced well the prevailing southern horizontal wind flow at the beginning of the rainfall, which resulted in the development of an orographic precipitating system along the Cévennes mountain ridge and over the Vivarais Mountains.

Despite the delayed onset of the precipitation with a time shift of one hour compared to the observations, the total rain accumulation at the ground at the end of the episode was in good agreement with the one observed. Also, the orientation of the modeled system was similar to the observed one with a main precipitating cell located close to the observed one. The horizontal extension of the rain field seemed to be quite

underestimated by the simulation. Nevertheless, the frequency distribution of the cumulative rainfall showed a good agreement with the KED QPE. The frequency of the strongest and the weakest rain spots are well simulated.

The delayed onset of the precipitation was also confirmed by the high-resolution analysis of X-band radar reflectivity. The modeled reflectivity during the period of the strongest rainfall was, nevertheless, in agreement with the observations qualitatively as well as quantitatively. The main differences in the frequency distribution of reflectivity between the model results and the observations can be attributed to the different number of values and/or due to the fact that the observations include numerous values of reflectivity in the range 20 - 25 dBZ. The existence of these values indicates noise in the observations, particularly in zones behind strong precipitation. An over-correction of the attenuation in the observations at these zones is possible. The reflection by the topography can be also a reason of the existence of a small part of these values.

Concerning the modeled rain spectra which are compared to observations from two disdrometers located at different altitudes, it was seen that the number and the mass of the smallest rain drops (< 1 mm) is somewhat underestimated by the model. However, it has to be noted that the number of droplets observed from the Parsivel S was extremely high, probably because during the observations this instrument was close to the cloud base (altitude = 900 m). Comparing observed ice crystal spectra with modeled ones, it was seen that the small ice crystals (< 200 μm) are rather underestimated by the model. Ice crystals of large sizes (> 1000 μm) however were in agreement with the observations. Also, the ice spectra observed between 5.4 km and 5.7 km are better represented by the modeled ones at higher altitude, at 6.6 km, because of the larger vertical extension of the modeled IWC.

The accordance between RASTA reflectivity and modeled reflectivity is confirmed by the comparison between retrieved and modeled IWC. Mean vertical IWC profiles calculated for model results were compared with respective profiles for observations from hydrometeor probes, as well as for the RASTA retrieval. The mean IWC profile calculated by hydrometeor probes showed a large variation, with high values appearing between 5 and 6 km but very small values between 7 and 8 km. The retrieved mean IWC vertical profile by RASTA showed lower values than the modeled ones all over its vertical extent, except elevated altitudes. This difference can be a result of the impact of attenuation in reflectivity observations that probably influence the retrieval of IWC.

Overall, it is concluded that the model reproduces satisfactorily the precipitating system of the IOP7a. A modification of the model's large scale set-up significantly influences the structure and the orientation of the precipitating system, as well as the

position of the precipitating cells. Quantitatively, cumulative rainfall at the ground and reflectivity differ slightly from the ones of the reference simulation. This sensitivity study confirmed that in order to achieve a realistic simulation of the heavy precipitation episode, the outermost domain must include all the south-east part of the Mediterranean Sea with its meteorological characteristics (e.g. horizontal wind and relative humidity).

Once reference simulation is reasonable, sensitivity simulations can be performed in order to quantify the impact of the pollution on an intense precipitating system such as a Cévenol event. The next chapter is dedicated to the study of the role of the initial aerosol particle number on the formation and evolution of the IOP7a heavy precipitating system.

5 Impact of the initial aerosol particle number concentration on the formation and evolution of the HYMEX IOP7a

The atmospheric aerosols are suspensions of solid or liquid particles, derived from various kinds of natural and/or anthropogenic sources. Under suitable conditions of temperature and relative humidity, the aerosol particles can be activated as cloud condensation nuclei (CCN) and ice nuclei (IN) that can form warm clouds (CCN only) or mixed-phase clouds (CCN and IN). The understanding and estimation of the role of the aerosol particles in cloud formation and precipitation is a challenging topic in atmospheric physics.

Leroy et al. (2006) have studied the contribution of the air pollution in terms of the initial aerosol particle spectrum on the precipitation formation, as well as its influence on the development of the ice phase. The modification of the initial aerosol particle spectrum in a 1D1/2 model with detailed microphysics showed a strong influence on rain accumulation at the ground. Planche et al. (2010) concluded that for a convective precipitating system with low amount of ice, an increase of the initial number of aerosol particles is the principal parameter that influences the formation of the precipitation compared to changes on their solubility. The number of this kind of studies is still quite low and there is a lot of uncertainty regarding CCN and IN. As discussed in **chapter 3**, the

IOP7a was the most polluted case observed during the HYMEX SOP1. This fact provided a strong motivation to study scenarios with lower aerosol particle concentration but keeping the same initial synoptic conditions of the IOP7a (detailed in **chapter 3**).

The aim of the following study is to investigate the sensibility of a reduction of the initial aerosol particle number on the formation and the evolution of the IOP7a convective system by means of a 3D detailed microphysics model. For this purpose, two simulations named “background 1” and “background 2” were performed and their results are being compared with the reference simulation. The focus of this intercomparison will be put on the evolution of the precipitation and on the vertical structure of the cloud system.

The present chapter starts with the description of the initial conditions for aerosol particles used in the different sensitivity simulations. Then, a comparative analysis of their results with both the reference (REF) simulation results (discussed in **chapter 4**) and the respective HYMEX observations (available in **chapter 3**) is detailed. The discussed modeled variables, i.e. cumulative rainfall, radar reflectivity, IWC and RWC, will permit to show the impact of the aerosol particle number on the temporal and spatial (horizontal and vertical) structure of the IOP7a intense precipitation event.

5.1 Description of the aerosol initial conditions for the sensitivity simulations

Simulations “background 1” and “background 2”, called hereafter BK1 and BK2 respectively, were initialized by using the synoptic conditions described in **chapter 4** (i.e. large-scale set-up) that were the same as for the REF simulation. The aerosol properties of these two simulations are described below.

Simulation BK1 was initialized with the properties of an aerosol spectrum observed during the lowest polluted IOP event of HYMEX SOP1 (i.e. IOP16), in the morning hours (5:52 - 9:18 UTC) of the 27th October 2012, over the northwestern part of the Mediterranean Sea (**Figure 5.1**).

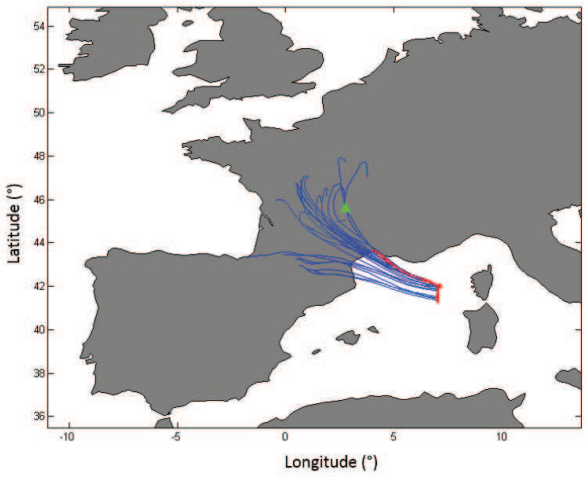

Figure 5.1: Backward trajectories (blue lines) of the air masses that contained the measured aerosol particle spectrum of the 27th October 2012 (IOP16) computed by (Rose 2014) with the Hybrid Single-Particle Lagrangian Integrated Trajectory (HYSPLIT) model. The part of the ATR-42 flight where the aerosol particle measurements took place is indicated by the red line. The green triangle indicates the position of the Puy de Dôme (PDD) research station.

This aerosol spectrum, whose origins were continental, was measured at the altitude of 200 m by the instruments SMPS and GRIMM OPC (see description in **chapter 3**) which were on-board the French research aircraft[17] ATR-42. The number size distribution of this aerosol spectrum, as well as its three modes are shown in **Figure 5.2**.

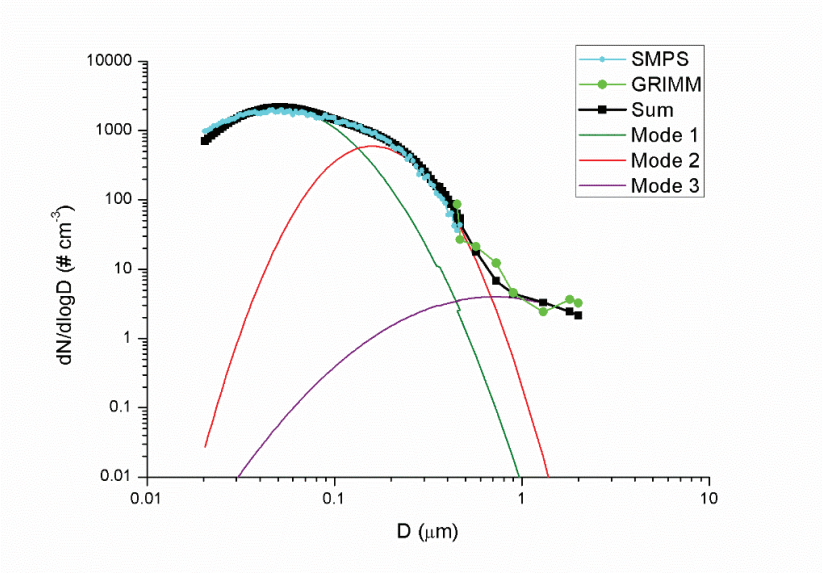

Figure 5.2: Number density distribution of the observed aerosol particles (# cm^{-3}) at 0.2 km during IOP16 by the SMPS (in light blue) and by the GRIMM OPC (in light green with round dots) together with the three fitted modes of the aerosol particle spectrum (in dark green, red and purple) and the sum (in black).

[17] This flight is marked in the HYMEX database as "ATR-42 flight 56".

As in REF simulation, concerning the variation of the aerosol particle number concentration it is supposed that the aerosol concentration decreased exponentially until the altitude of 3.7 km. The characteristics of each of the three modes (N_i, D_i, and the logarithm of σ_i) are presented in **Table 5.1**. The total number of this spectrum was 1704 aerosol particles cm^{-3}. However, this aerosol particle concentration characterizes a rather polluted spectrum. Moreover, both aerosol spectra of REF and BK1 cases were measured over the Mediterranean Sea. Thus, a scenario with a less polluted aerosol spectrum measured over continental region was necessary to complete this study. For this reason, scenario BK2 was introduced.

Case	**Mode 1**		**Mode 2**		**Mode 3**		**Total AP number cm^{-3}**
Reference (REF)	N_1	2900	N_2	72	N_3	3	2975
	D_1	0.06	D_2	0.32	D_3	0.72	
	$\log\sigma_1$	0.26	$\log\sigma_2$	0.20	$\log\sigma_3$	0.397	
Background 1 (BK1)	N_1	1400	N_2	300	N_3	4	1704
	D_1	0.05	D_2	0.16	D_3	0.72	
	$\log\sigma_1$	0.26	$\log\sigma_2$	0.198	$\log\sigma_3$	0.396	
Background 2 (BK2)	N_1	150	N_2	610	N_3	250	1010
	D_1	0.025	D_2	0.52	D_3	1.35	
	$\log\sigma_1$	0.146	$\log\sigma_2$	0.217	$\log\sigma_3$	0.176	

Table 5.1: Properties of the aerosol spectra used for the polluted reference case (REF) and the background cases (BK1 and BK2)

The aerosol particle spectrum whose properties were deployed for the simulation that corresponds to BK2 was observed at the Puy de Dôme (PDD) research station in Central France (45°46'N, 2°57'E, see **Figure 5.1**). These measurements were performed in Autumn (September-November) and the used values resulted from the log normal fitting procedure of the average nighttime (00:00 to 6:00) size distribution provided from the SMPS instrument, as described in Venzac et al. (2009). In **Table 5.1**, these aerosol size

properties are presented, as well as the ones that were used for the initialization of the reference (REF) simulation.

For the present study, the autumn season parameters were selected for compatibility reasons with the reference case. It should be noted that the "autumn nighttime" measurements present the lowest particle concentrations of all the observations encountered from January 2006 to December 2007 at the PDD station. To our knowledge, the selected aerosol spectrum corresponds, thus, to the cleanest atmospheric conditions documented for the southern part of France. As mentioned in the previous chapters, a concentration of almost 3000 cm^{-3} aerosol particles was measured near the surface at the altitude of 200 m during the IOP7a. The respective total aerosol particle concentration that was observed at the PDD research station (which is situated at the altitude of 1400 m) was 1010 cm^{-3}. For the studied cases, the aerosol spectra were modified homogeneously all over the model domain.

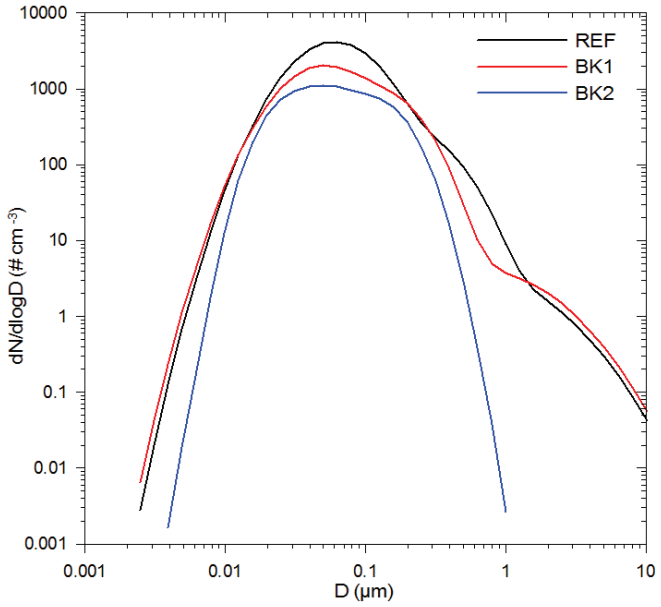

Figure 5.3: Number size distributions of the aerosol spectra for the initialization of the polluted REF case (in black), the background 1 (BK1) case (in red) and the "background 2 (BK2) case (in blue).

Figure 5.3 shows the number size distributions of the three model simulations that are compared in this chapter: the REF, the BK1 and the BK2. The majority of the observed aerosols for all the cases have a diameter of around 0.08 μm. Aerosols with diameter sizes that exceed the 1 μm were observed for the REF and BK1, when measurements were performed over the Mediterranean Sea. Nevertheless, there is no presence of particles larger than 1 μm for BK2, as the SMPS instrument used for that study measures in the

range of 0.01 – 0.5 μm. The results of the aforementioned simulations are presented and compared in the following sections.

5.2 Impact of the initial aerosol properties on precipitation fields

The focus on this study is given on the impact of the initial aerosol particle number on the temporal and spatial evolution of the precipitation field. For this reason, the modeled cumulative rainfall and radar reflectivity obtained for the cases BK1 and BK2 are being investigated and compared with the respective REF simulation results, in both a qualitative and a quantitative way.

5.2.1 Impact on the cumulative rainfall

At 6:00 UTC light rainfall had started according to all model simulations of the present chapter. The maximum values of rain accumulation on the ground from midnight until every hour from 6:00 UTC to 12:00 UTC for each of the three model simulations are presented in **Figure 5.4**. According to this figure, the initiation of the precipitation gives almost similar maximum values of rain on the ground, but rain accumulation for BK1 is the highest. However, after 7:00 UTC and until 12:00 UTC, BK2 has the highest maximum values of cumulative rainfall. The maximum cumulative rainfall on an hourly basis for each simulation is shown in **Figure 5.5**. The hourly evolution of the cumulative rainfall is illustrated for each of the three model simulations in **Figure 5.6** and **Figure 5.7**.

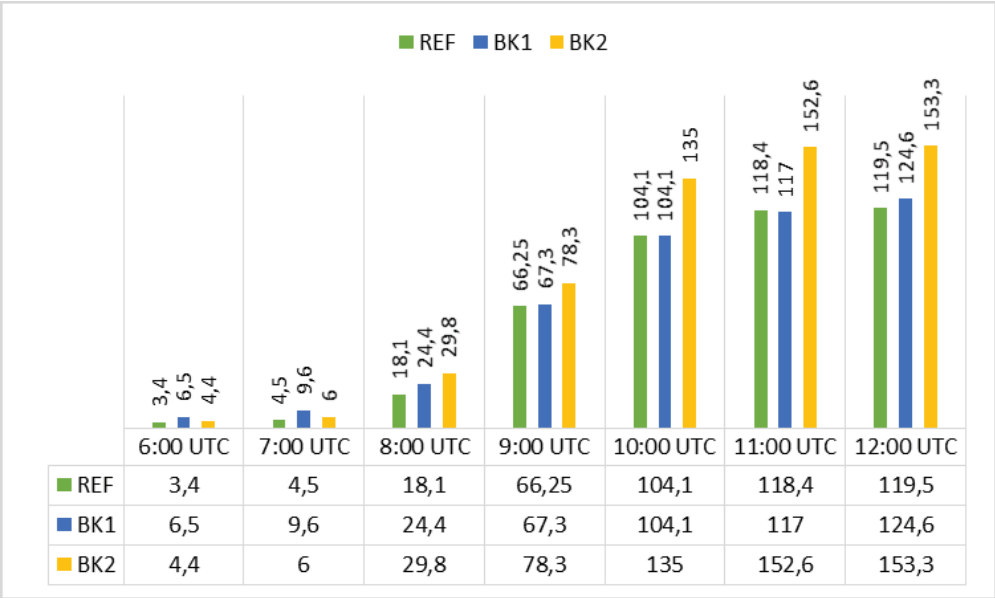

	6:00 UTC	7:00 UTC	8:00 UTC	9:00 UTC	10:00 UTC	11:00 UTC	12:00 UTC
REF	3,4	4,5	18,1	66,25	104,1	118,4	119,5
BK1	6,5	9,6	24,4	67,3	104,1	117	124,6
BK2	4,4	6	29,8	78,3	135	152,6	153,3

Figure 5.4: Maximum rain accumulation on the ground (in mm) from 00:00 UTC until every hour from 6:00 UTC to 12:00 UTC for the simulations REF, BK1 and BK2.

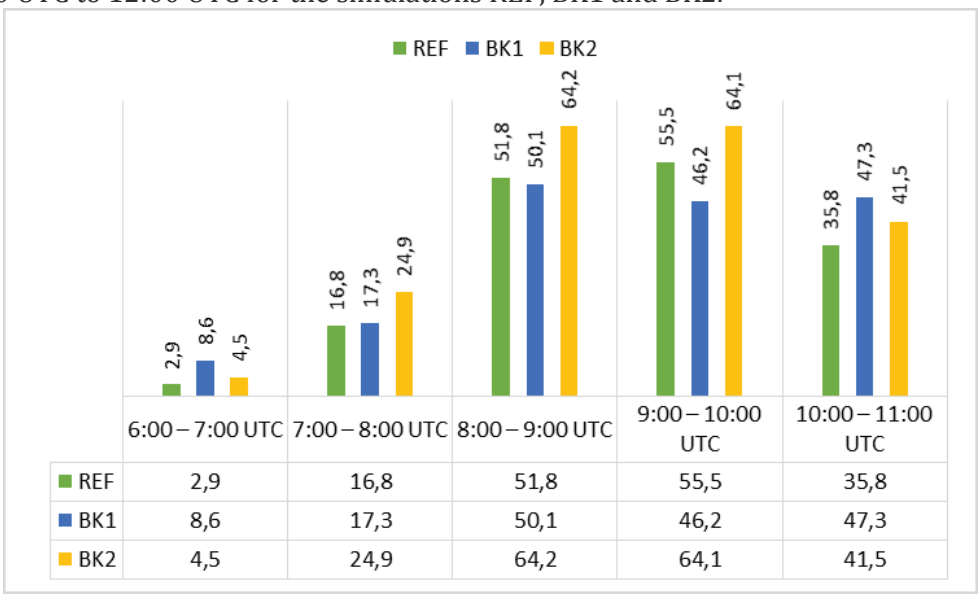

	6:00 – 7:00 UTC	7:00 – 8:00 UTC	8:00 – 9:00 UTC	9:00 – 10:00 UTC	10:00 – 11:00 UTC
REF	2,9	16,8	51,8	55,5	35,8
BK1	8,6	17,3	50,1	46,2	47,3
BK2	4,5	24,9	64,2	64,1	41,5

Figure 5.5: Maximum hourly rain accumulation on the ground (in mm) for the simulations REF, BK1 and BK2.

The rain accumulation from 6:00 to 7:00 UTC (**Figure 5.6**a, b and c) shows that the affected areas at the beginning of the precipitation are the mountain slope of Cévennes (southern part of the mountain ridge), the peaks of Vivarais (northern part of the mountain ridge), as well as the south-eastern part of the domain with lower altitude, at the east of Alès. Despite the fact that only light rain was prevailing during this time period, the highest cumulative rainfall is found in the BK1 simulation results with a maximum of 8.6 mm (see **Figure 5.5**). Both cases BK1 and BK2 show slightly higher values than the

REF results during this time period (maximum of 2.9 mm) and rainfall is found also in regions at the northern part of the model domain, over Vivarais Mountains.

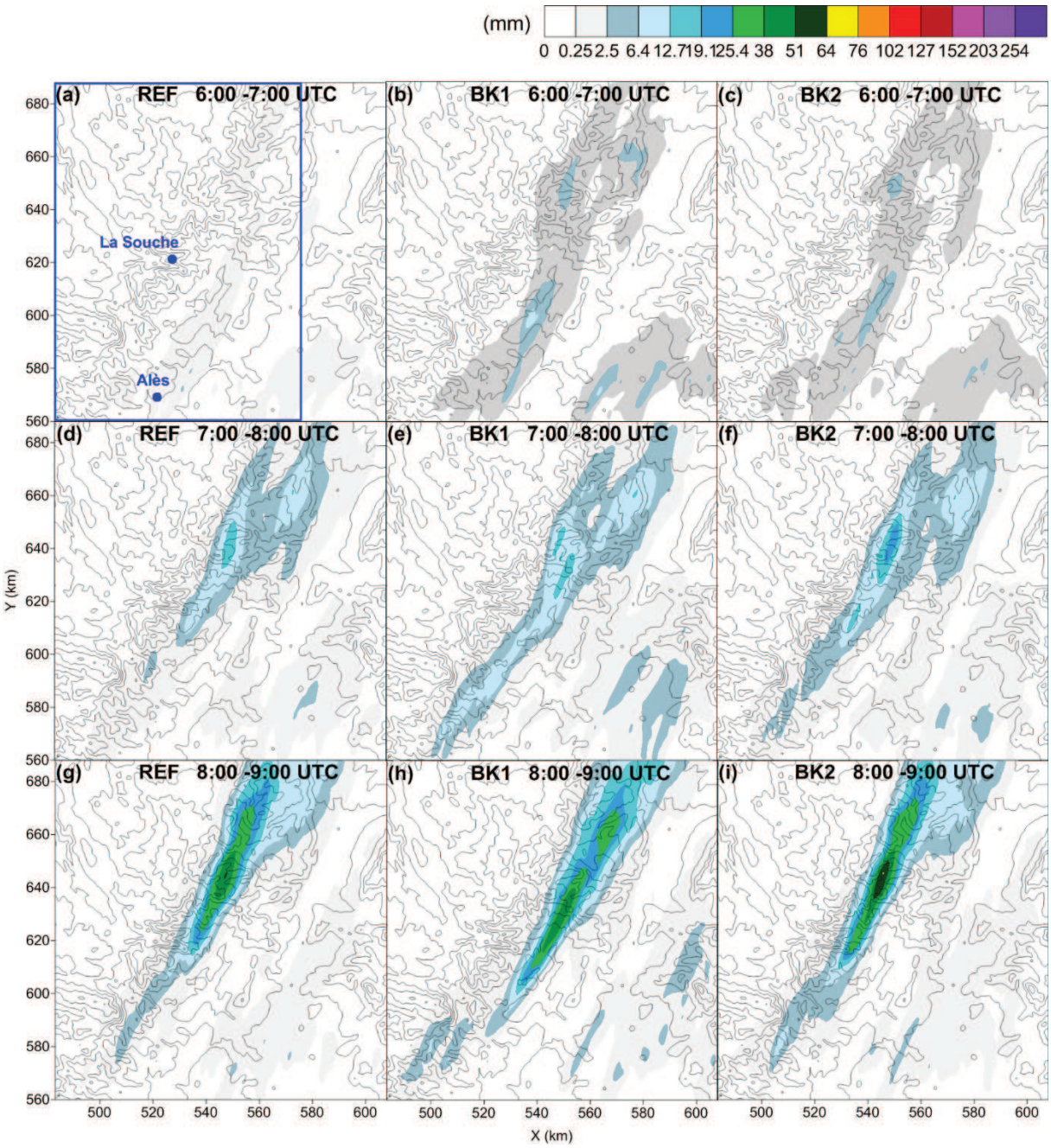

Figure 5.6: Modeled hourly cumulative rainfall on the ground (in mm) for the reference (REF) simulation (a) from 6:00 UTC to 7:00 UTC, (d) from 7:00 UTC to 8:00 UTC and (g) from 8:00 to 9:00 UTC, for the simulation BK1 (b, e and h) and for the simulation BK2 (c, f and i) at the same specific time periods. The blue frame in (a) indicates the observations domain that was presented in **Figure 4.11**.

The highest maximum of rain accumulation from 00:00 to 7:00 UTC is found for the case BK1 with almost 10 mm (**Figure 5.4**). At the same time, the maximum rain accumulation for the REF case is 4.5 mm and the respective value for the case BK2 is 6 mm. However,

the hourly precipitation between 7:00 and 8:00 UTC is stronger in BK2 simulation with almost 25 mm of rain on the ground. During this time period, the main convective cell at the north-west of La Souche is splitted, according to BK1 (see **Figure 5.6**e), and the rain is more enhanced over the south-east part of the domain (maximum up to 6 mm), which is in contrast to the REF and the BK2 case. Also, BK1 and BK2 cases both simulate light rain over the south-western part of the Cévennes Mountain (**Figure 5.6**e and **Figure 5.6**f), whereas for the REF simulation, this area is almost not affected during this time period (**Figure 5.6**d). The main precipitating cell is located over the same area according to the REF and the BK2 case, as seen in **Figure 5.6**d and **Figure 5.6**f. Furthermore, the orientation of the precipitating system is similar for the three cases.

From 8:00 to 9:00 UTC heavy rainfall takes place in all model simulations. The hourly rain accumulation is largest for the BK2 case, with a maximum of 64.2 mm locally, whereas the REF and the BK1 give maxima of 51.8 and 50.1 mm respectively. The main precipitating cell is located at the same place for the REF and the BK2 cases, over the Cévennes Mountain, whereas the strongest rain for the BK1 case is slightly shifted at the south-east (**Figure 5.6**g, i and h, respectively). According to the BK1 results, light rain falls over the mountainous region of the eastern part of the domain (590 km to 600 km on axis X), which is not shown for the REF and BK2 simulations. Two small precipitating cells are also seen at the south-western part of the domain (490 km to 510 km on axis X), whereas the REF and the BK2 cases simulate a single small precipitating cell at the north-west of Alès.

Heavy rainfall continues for all simulation results between 9:00 and 10:00 UTC. REF, BK1 and BK2 cases simulate up to 55.5 mm, 46.2 mm and 64.1 mm respectively. Compared to the REF case, the precipitating system of BK1 is shifted 10 to 20 km to the east, whereas the system of the case BK2 is located over the same region with the REF case, but extended up to 40 km to the south (see **Figure 5.7**a, b and c).

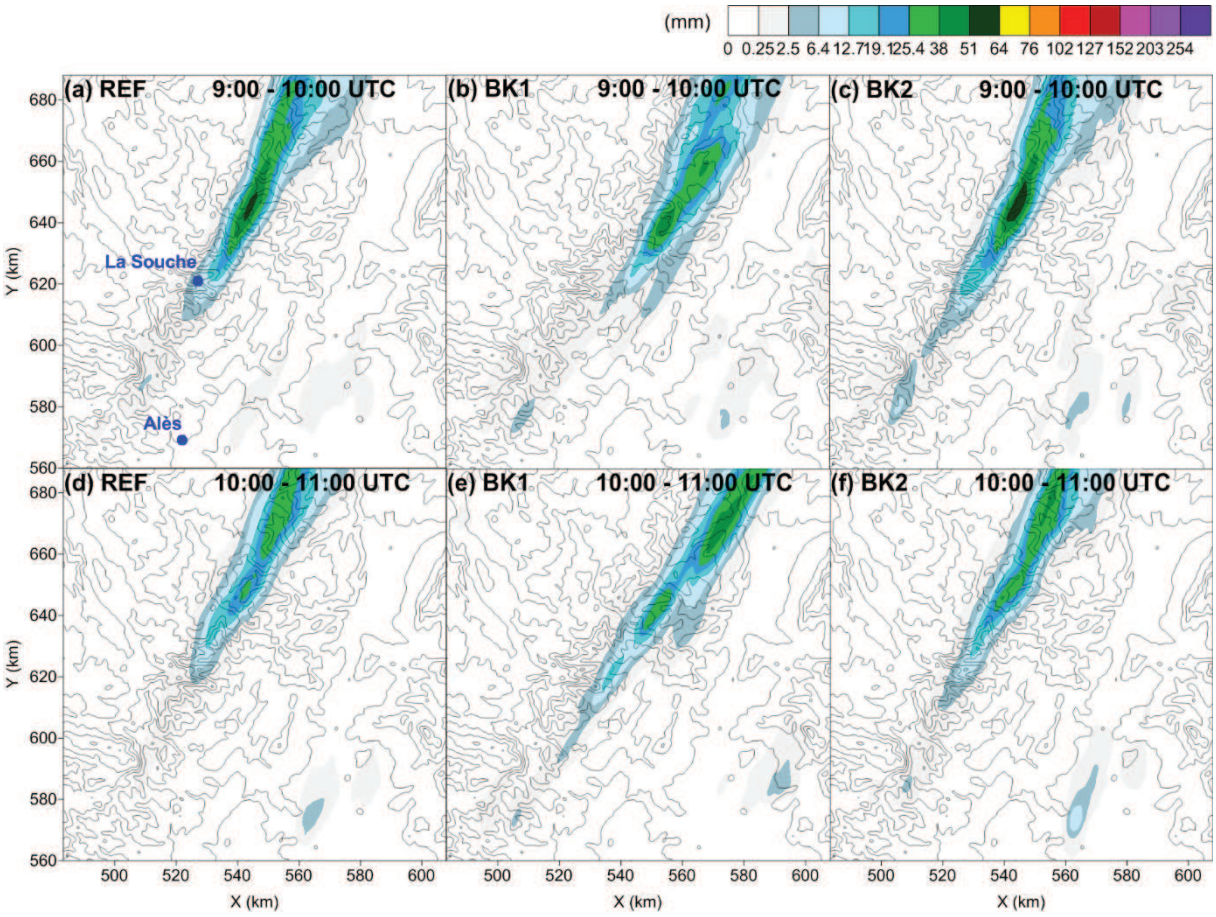

Figure 5.7: Modeled hourly cumulative rainfall on the ground (in mm) for the reference (REF) simulation (a) from 9:00 UTC to 10:00 UTC and (d) from 10:00 UTC to 11:00 UTC, for the simulation BK1 (b and e) and for the simulation BK2 (c and f) at the same specific time periods.

Finally, between 10:00 and 11:00 UTC, the main amount of rain falls mostly over the northern part of the Vivarais Mountains for all study cases (**Figure 5.7**d, e and f). Both REF and BK2 simulations reproduce similarly the position of the precipitating system, but for the BK1 simulation the system is found up to 20 km shifted to the east and extended up to 30 km more to the south. The precipitating cell is separated into two for all the studied cases and the orientation of the system is similar. Precipitation is lower during this time period with maxima between 36 and 47 mm of rain.

Figure 5.8 presents the cumulative rainfall on the ground from 00:00 to 12:00 UTC according to the three model simulations. **Figure 5.9** illustrates the spatial distribution of the absolute difference between the simulation results for the total rain accumulation.

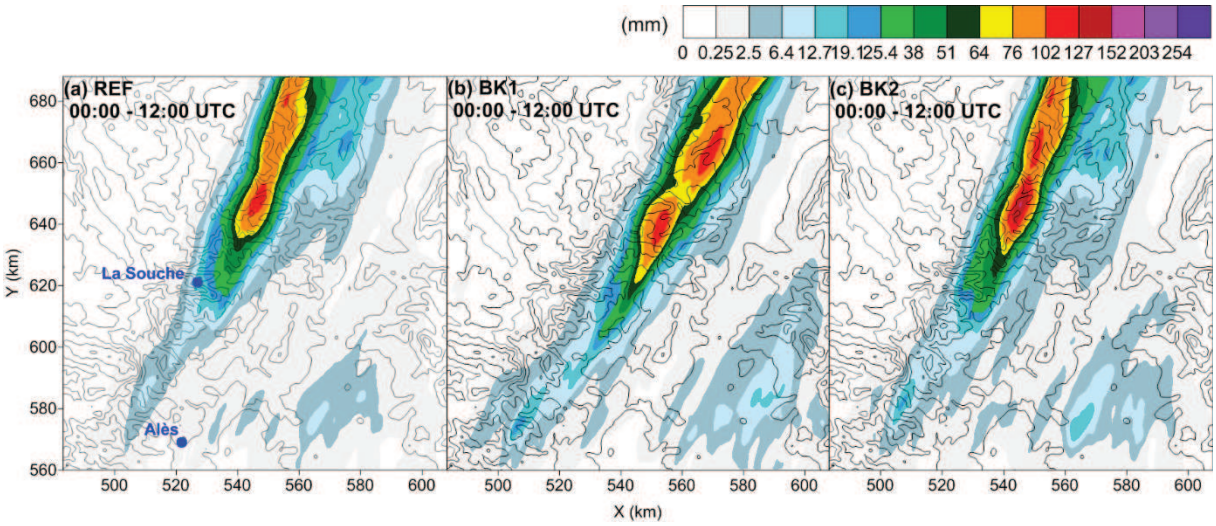

Figure 5.8: Modeled cumulative rainfall on the ground (in mm) from 00:00 UTC to 12:00 UTC of the 26th September 2012 for simulations (a) REF, (b) BK1 and (c) BK2.

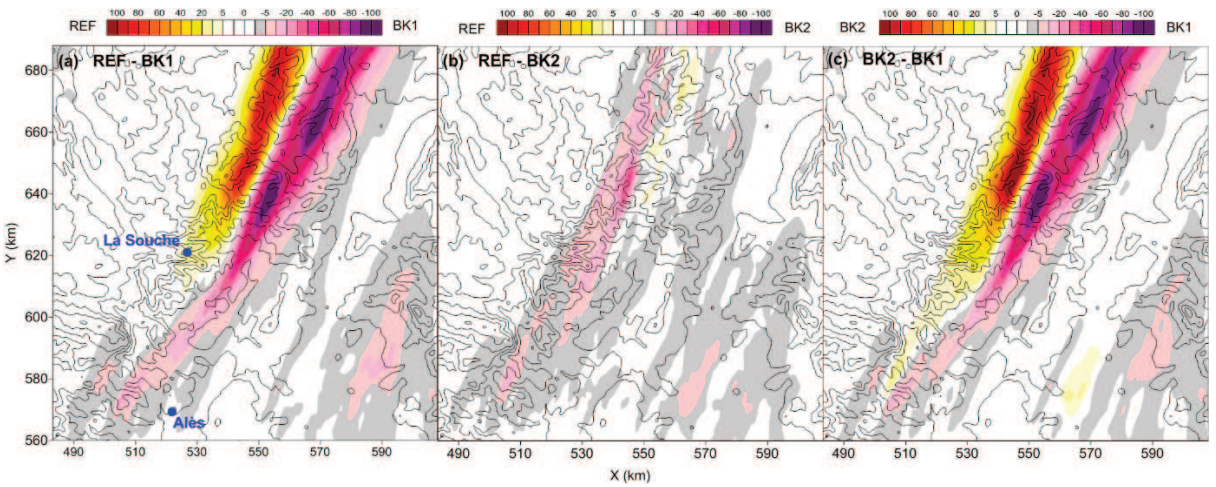

Figure 5.9: Absolute difference of the cumulative rainfall on the ground (in mm) from 00:00 to 12:00 UTC between (a) the REF and the BK1, (b) the REF and the BK2 and (c) the BK2 and the BK1. The positive values mean that the cumulative rainfall is greater in the REF case (for a and b) or in the BK2 case (for c).

At the end of the heavy precipitation event, i.e. after 12 hours of integration, the maximum modeled rain accumulation on the ground is 119.5 mm for the REF simulation, 124.6 mm for the case BK1 and 153.3 mm for the case BK2.

As seen in **Figure 5.8** and **Figure 5.9**a, a reduction of 43 % in the initial number of aerosol particles caused, i.e. between REF and BK1, apart from a higher maximum in the cumulative rainfall of 4 %, a shift of up to 20 km of the precipitating system to the east. Moreover, the system of the BK1 results is more extended to the south-west than in the REF results, by about 20 km. Finally, the orientation of the precipitating system of BK1 is

slightly different than in the REF results and the system is more narrow horizontally (about 10 km less wide than in REF), especially at its northern part.

A reduction of 66 % in the initial aerosol particle number, i.e. between REF and BK2, caused an increase of 22 % in the maximum cumulative rainfall for the case BK2. **Figure 5.9**c shows that even a third maximum is seen in the northern part of the domain, over the mountainous region of Vivarais. The position of the main precipitating cell is almost similar to the one of the REF simulation results. The rainfall during the BK2 case is more intense than in the REF results at the south-west (over the peaks of Cevennes), as well as over the south-eastern part of the domain.

It is, therefore, clear that a reduction of the initial number of aerosol particles influences strongly the evolution of the spatial rain distribution for an intense precipitating system as the one of IOP7a.

To better understand the influence of the initial aerosol changes on the precipitation field, **Figure 5.10** illustrates the total rain amount at the ground, in the whole model domain (D3), from 00:00 UTC to every hour from 7:00 to 12:00 UTC.

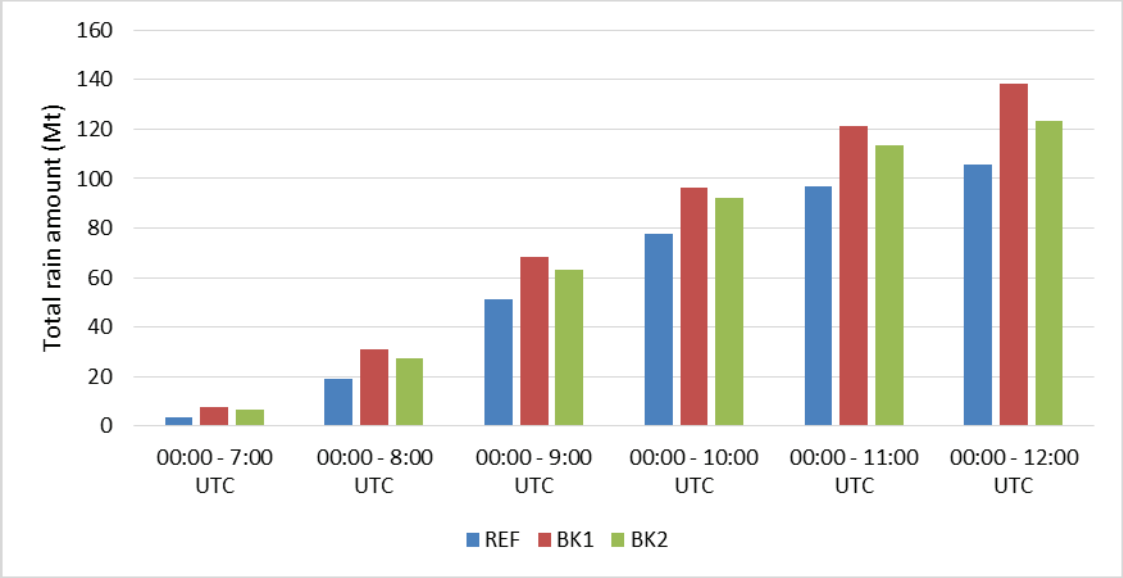

Figure 5.10: Total rain amount at the ground (in Mt) in the whole D3 for the simulations REF (in blue), BK1 (in red) and BK2 (in green) from 00:00 UTC to every hour from 7:00 to 12:00 UTC.

Despite the fact that BK2 has the highest maximum values of cumulative rainfall at the ground locally (as seen in **Figure 5.4**), the highest total rain amount is found for BK1, at every hour. At the end of the heavy precipitation episode, until 12:00 UTC, the highest total rain amount is fallen during BK1 simulation (138 Mt in the whole D3), which is 10 % higher than in BK2 and 30 % higher than in REF simulation.

It is, therefore, seen that the lower the number of aerosol particles at the beginning of the model simulation, the larger the rain quantity can be, however it should be noted that the increase is not proportional. The number of the aerosol particles determine the number of CCN that can form droplets inside the cloud. However, a large number of CCN can reduce the collection efficiency through the collision-coalescence process due to the large number of small cloud droplets nucleated, thus, the total rainfall is decreased. An explanation of the lower total rain amount in BK2 (least polluted case) than in BK1 is probably the different aerosol population of these cases. Indeed, the aerosol spectrum of BK1 was observed over the sea and it contained also large aerosols (as shown in **Figure 5.3**), whereas the aerosol spectrum of BK2 is continental and with smaller aerosols.

Moreover, compared to REF and BK2, the BK1 case has the highest frequency of rain spots between 50 and 120 mm, as seen in **Figure 5.11**, which presents the frequency distributions of the modeled cumulative rainfall from midnight to midday for simulations and observations (KED QPE).

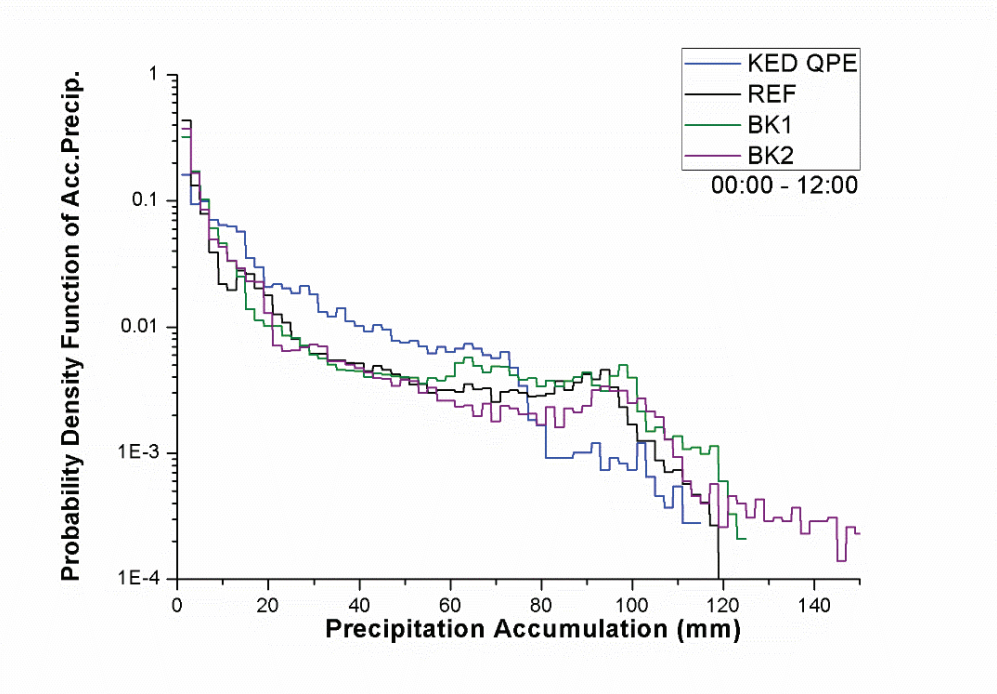

Figure 5.11: Probability density function of the rain accumulation on the surface between 00:00 UTC and 12:00 UTC of the 26th September 2012 calculated for the QPE observations (blue line) and the model results of the REF simulation (black line), the BK1 case (green line) and the BK2 case (purple line).

The frequencies of the rain spots between 25 and 50 mm are rather similar for all model simulations. The existence of strong rain spots (> 120 mm) for the BK2 case can be also seen in **Figure 5.11**, in contrast to the REF and BK1.

Nevertheless, in the same figure is shown that frequency distribution of the precipitation accumulation of the KED QPE displays differences with the model simulations; it is shown that rain spots from 20 to 70 mm are less frequent than in the observations.

Finally, **Figure 5.12** illustrates the total rain amount for the observations and the simulations (in their region in common) from midnight to midday. As seen in this figure, the model simulates lower rain quantity than in the observations. However, for this comparison, it has to be considered that the resolution of the observations (1 km x 1 km) is smaller than in the model (0.5 km x 0.5 km), so differences are rather expected. It is also worth-noting that in the common area of the OHM-CV observation field and the model simulations, the largest total rain amount is found for simulation BK2 (113 Mt). This happens because of the horizontal shift by 10 km in BK1 results that excludes part of the precipitation which is not found in the common model-observation area.

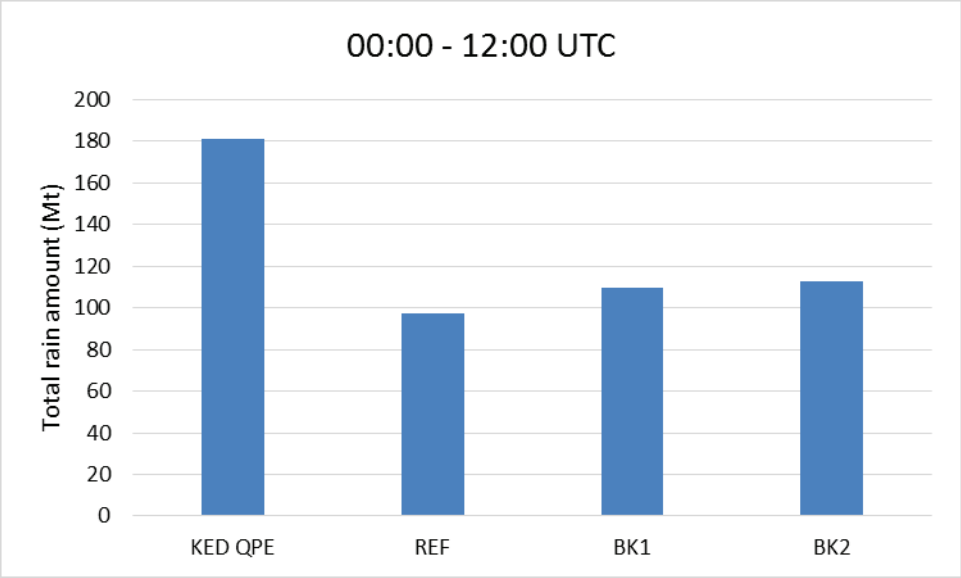

Figure 5.12: Total rain amount on the ground (in Mt) from 00:00 UTC to 12:00 UTC according to the KED QPE and the model simulations REF, BK1 and BK2 inside their geographical region in common.

Overall, according to the analysis of the rain accumulation on the ground, it is found that "pollution" influences both intensity and quantity of rainfall, as well as its spatial distribution during a heavy orographic precipitation event, such as IOP7a. Nevertheless, temporal evolution of the rainfall is not affected by changes of the initial aerosol particle concentration.

It is concluded that the highest the initial number of aerosol particles, the least the maximum cumulative rainfall. Particularly, a decrease of a factor of 2 in the initial aerosol particle concentration can cause an increase of up to 4 % in the maximum cumulative

rainfall until the end of the heavy precipitation episode. Nevertheless, a decrease of 66 % in the initial aerosol number lead to an increase of up to 22 % in the maximum rain accumulation.

Also, the horizontal structure of the precipitating system was affected, with a shift of the main precipitating cell by 10 km to the east and an extension of the system to the south for BK1 simulation. This deviation is caused by dynamical reasons. In particular, from midnight to 7:00 UTC, a bifurcation between temperature and RH field developed in BK1 simulation that caused a cloud and precipitation field which differ in location and evolution of the convective cells. Thus, a larger amount of precipitation fell earlier (from 6:00 to 7:00 UTC) than in the REF and the BK2 cases, as seen in **Figure 5.5**.

Finally, in BK1 simulation obtained the highest total rain amount of all model simulation, which is rather attributed to the population of its initial aerosol spectrum, as explained here before.

In order to investigate the aforementioned differences in a high resolution but also in a smaller domain, this study continues with the analysis of the evolution of the X-band radar reflectivity for the test simulations.

5.2.2 Impact on the radar reflectivity

The calculation of the X-band radar reflectivity by the model was described in **chapter 3**. In the present section, the focus is on the time period of the strongest precipitation, from 6:40 to 10:00 UTC (as in **chapter 4**, **Figure 4.13** and **Figure 4.15**). **Figure 5.13** and **Figure 5.14** compare the REF simulation with the respective results from the BK1 and the BK2 simulations at certain hours of integration which cover the period of most intense precipitation.

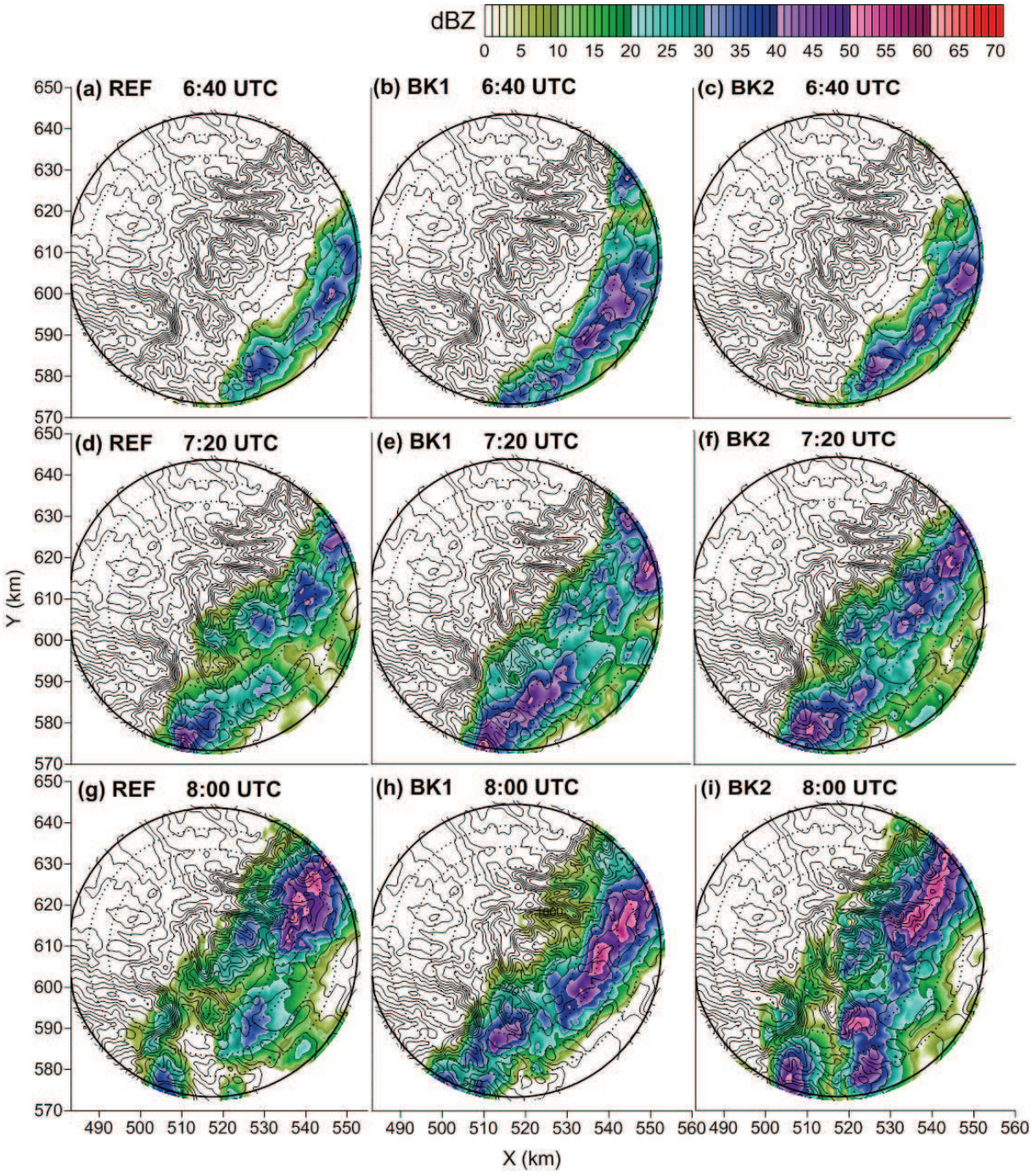

Figure 5.13: PPI images of the modeled radar reflectivity for the reference case (REF) at (a) 6:40 UTC, (d) 7:20 UTC and (g) 8:00 UTC, the simulation BK1 (b, e and h) and the simulation BK2 (c, f and i) at the same specific times. The solid black lines represent the topography and the concentric circles correspond to the different altitudes of the radar beam at every 5 km to the radar position. The maximum height of the radar beam (external circle in bold black) is 1892 m.

At 6:40 UTC (**Figure 5.13**a), in both results for BK1 and BK2, about 12 % more intense reflectivity is seen than REF case (locally), whereas all cases agree that the system has not reached yet the southern part of the Cévennes mountain ridge, but is located at its east, as seen in **Figure 5.13**a. The locations of the highest reflectivity values (up to 40 dBZ for the

REF case and up to 50 dBZ for the cases BK1 and BK2) are simulated with small differences on the horizontal axis which are not higher than 10 km.

All simulations agreed that a convective cell was located at the southern part of the domain at 7:20 UTC. The structure of the system according to REF simulation resembles more case BK2, whereas the last had higher values of reflectivity.

As already seen in **Figure 5.6**, there are no significant differences for the spatial evolution of the modeled reflectivity at 8:00 UTC and 8:20 UTC from the three simulations, according to **Figure 5.13**g, h and i and **Figure 5.14**a, b and c respectively. The main difference between these simulation results is the existence of high reflectivity values (40 – 50 dBZ) at a larger extent in the south during both BK simulations than in the REF one. This difference is more pronounced in the 8:00 UTC results, where convective cells are seen at locations up to 10 km (for BK1) and up to 30 km (for the BK2) more south than in REF.

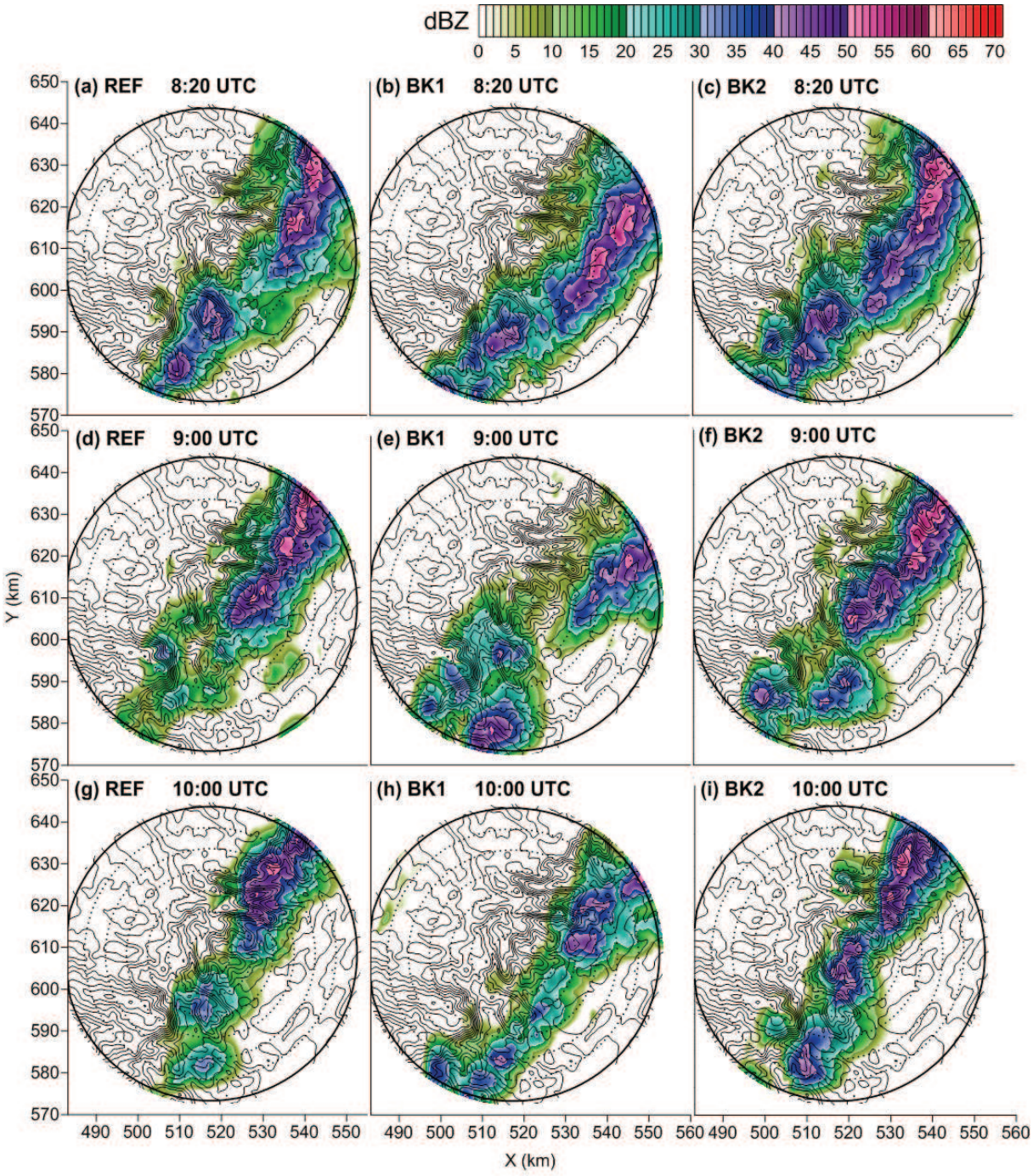

Figure 5.14: PPI images of the modeled radar reflectivity for the reference case (REF) at (a) 8:20 UTC, (d) 9:00 UTC and (g) 10:00 UTC, the simulation BK1 (b, e and h) and the simulation BK2 (c, f and i) at the same specific times. The solid black lines represent the topography and the concentric circles correspond to the different altitudes of the radar beam at every 5 km to the radar position. The maximum height of the radar beam (external circle in bold black) is 1892 m.

BK2 case shows the highest reflectivity values during this time period, but also at 9:00 UTC and at 10:00 UTC (up to 59 dBZ), as seen in **Figure 5.14**e and **Figure 5.14**b respectively. The highest reflectivity values are found at the same locations for REF and

BK2 results, whereas the structure of the system in BK1 results appeared shifted to the east by 10 km, both at 9:00 UTC and at 10:00 UTC.

Figure 5.15 presents the frequency distribution of the radar reflectivity computed for the three model simulations from 6.40 UTC to 10:00 UTC, including all model outputs during this time period (given every 20 minutes) and all the observations (given every 30 s) from the radar X3 (see **Figure 3.2** for location).

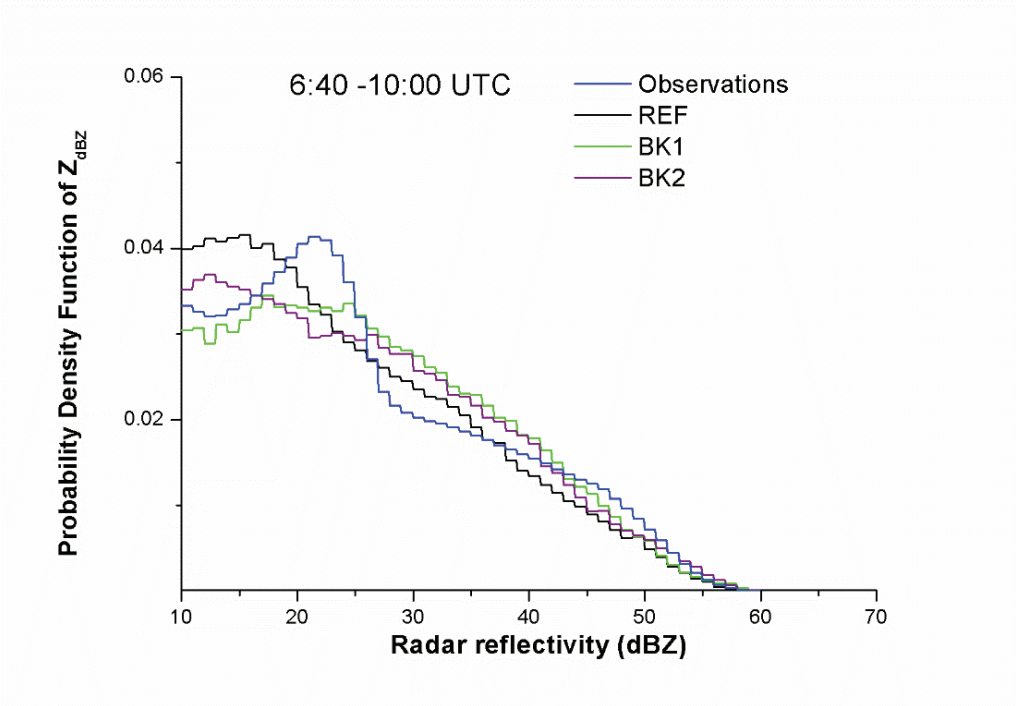

Figure 5.15: Averaged probability density function of the X-band radar reflectivity observations (blue line) and the respective model results of the REF simulation (black line), the BK1 case (green line) and the BK2 case (purple line) for the time period of 6:40 UTC – 10:00 UTC.

In the quantitative comparison of the modeled reflectivity, most of the differences between simulation results are found for low reflectivity values, in the range of 10 – 20 dBZ. Low reflectivity values appear mostly in REF results and least in BK1 results. The highest frequency of reflectivity in the range 25 – 50 dBZ is found for BK1 and frequency distribution of REF seems to be the lowest of the three simulations. BK2 shows the highest frequency of reflectivity values > 55 dBZ. This behavior can be linked to the general conclusion of the rain accumulation results shown in the previous section. REF simulation had the lowest maximum cumulative rainfall and lowest total rain amount of all simulations, whereas BK2 had the highest cumulative rainfall maximum and BK1 the highest total rain amount. However, compared to the observations, a descending trend for values > 30 dBZ is similar to all frequency distributions. Overall, changes on the initial aerosol particle number influence radar reflectivity results both quantitatively and

qualitatively. The difference between observed values in the range 15 to 25 dBZ and respective model results confirms the conclusions of section **4.2.2.2** about a possible over-correction of the attenuation in the observations.

The previous sections presented the differences in the modeled cumulative rainfall and X-band radar reflectivity through temporal and spatial horizontal variations of these fields according to changes on aerosol number concentration. In order to further analyze the impact of the initial aerosol number concentration on the simulation of the IOP7a event, the following section focuses on the vertical structure of the convective system by presenting its influence on the evolution of the IWC and RWC.

5.3 Impact of the initial aerosol particle number on the vertical structure of the system

In this section, liquid and ice phase of the convective system are studied in a 3D-field via the analysis of the RWC and IWC, respectively. In order to investigate the influence of the initial aerosol particle number on the vertical extent of the system, mean profiles of RWC and IWC (e.g. as in **chapter 4**) are presented for the REF simulation, but also for cases BK1 and BK2.

The 3D profiles illustrated in **Figure 5.16** and **Figure 5.17** were calculated by using model outputs every 20 minutes during the time period 8:00 UTC - 9:20 UTC and focusing on the triangular area of **Figure 4.25**.

For compatibility reasons with IWC from RASTA retrieval (see section **3.4.3.2**), IWC profiles in **Figure 5.16** were calculated only for levels where the modeled Rayleigh reflectivity Z_{Ray} was lower than 35 dBZ. In contrast to the 95GHz cloud radar reflectivity (Z_{95}), Rayleigh reflectivity permits also the detection of precipitating particles which are larger than 2000 μm (e.g. rain drops) and represents values seen by a rain radar[18]. Moreover, all profiles were calculated only for cloudy grid points with IWC > 0.01 g m^{-3}. Since melting level is always at 3.2 km a.s.l., altitude in figures of IWC profiles is restricted to this level. **Figure 5.16** illustrates the resulted time-averaged IWC for REF, BK1 and BK2 cases together with the RASTA retrieval.

[18] Airplanes fly in cloudy regions with $Z_{Ray} \leq 30$ dBZ.

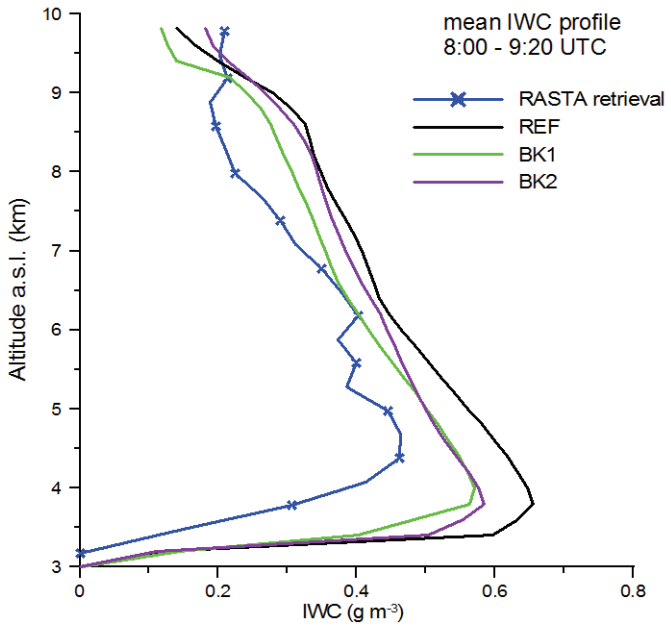

Figure 5.16: Time-averaged mean vertical profile of IWC (in g m^{-3}) in the time period 8:00 UTC – 9:20 UTC for simulations REF, BK1 and BK2 together with the RASTA retrieval.

Changes in the initial aerosol particle concentration influence the IWC all over the vertical extent of the system, as seen in **Figure 5.16**. A reduction of the initial aerosol particle number results in a reduction of the mean vertical IWC up to 14 %. The lowest time-averaged mean IWC is found for the profile of BK1, which has also the lowest maximum values of IWC during certain times (i.e. at 8:20 UTC) in the studied time period, as seen in **Table 5.2**a, or similar to BK2 (i.e. at 9:20 UTC).

The largest difference in the IWC profiles of the three simulations is found at lower altitudes (i.e. 3 km to 5.5 km), whereas the profiles of REF and BK2 are almost similar in certain higher altitudes (i.e. from 8 km to 9 km). Nevertheless, IWC profile of the RASTA retrieval remains the one with the lowest values, except altitudes > 9 km.

A similar analysis is also made using all data, in order to investigate the influence of the aforementioned limitation to the calculation of the mean vertical IWC profiles, but also to better highlight the impact of the aerosol particles on the total IWC of the convective system. Indeed, considering all data, higher IWC values are found for all model simulations, as seen in **Figure 5.17**a. This analysis shows that simulation BK1 has higher values of time-averaged IWC than BK2 at levels from 3.3 km to 5.8 km which is not the case in the previous analysis with with $Z_{Ray} < 35$ dBZ. Also, from 8:40 UTC to 9:20 UTC, the maximum IWC is higher in BK1 than in BK2 (see **Table 5.2**b). According to the analysis using all data, the initial aerosol particle number results in a reduction of the mean vertical IWC up to 10 %. To better understand those differences, the mean vertical RWC is also

calculated, both for levels with reflectivity < 35 dBZ and using all data, and presented in **Figure 5.17**b.

Maximum IWC (g m^{-3})			
(a)	**REF**	**BK1**	**BK2**
8:00 UTC	0.70	0.61	0.60
8:20 UTC	0.82	0.64	0.73
8:40 UTC	0.64	0.57	0.58
9:00 UTC	0.54	0.54	0.52
9:20 UTC	0.57	0.50	0.49
(b)	**REF (all data)**	**BK1 (all data)**	**BK2 (all data)**
8:00 UTC	0.88	0.65	0.76
8:20 UTC	0.89	0.75	0.80
8:40 UTC	0.75	0.82	0.64
9:00 UTC	0.61	0.69	0.59
9:20 UTC	0.62	0.63	0.55

Table 5.2: Maximum values of time averaged (8:00 UTC – 9:20 UTC) mean vertical IWC (in g m^{-3}) for simulations REF, BK1 and BK2 (a) from profiles calculated for levels with $Z_{Ray} < 35$ dBZ and (b) from profiles calculated using all data.

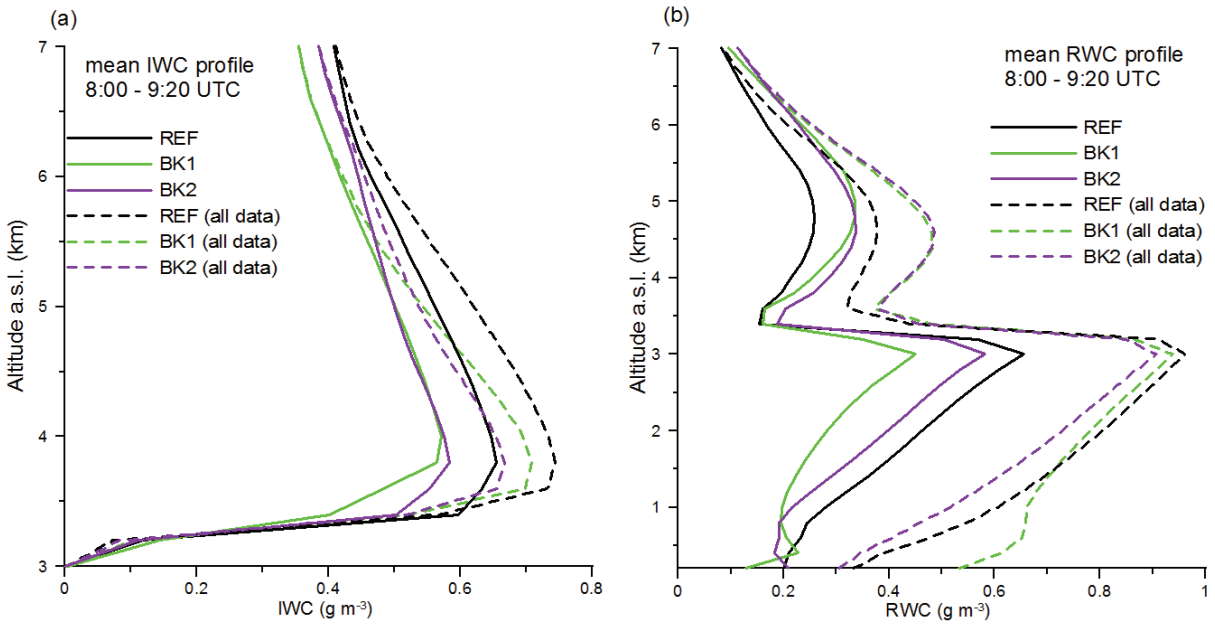

Figure 5.17: (a) Time-averaged mean vertical profiles of IWC (in g m-3) in the time period 8:00 UTC – 9:20 UTC for simulations REF, BK1 and BK2 for levels with $Z_{Ray} < 35$ dBZ (solid lines) and for all data (dashed lines). (b) Time-averaged mean vertical profiles of RWC (in g m-3) in the time period 8:00 UTC – 9:20 UTC for simulations REF, BK1 and BK2 for levels with $Z_{Ray} < 35$ dBZ (solid lines) and for all data (dashed lines).

Looking only at the profiles calculated using all data (dashed lines), it is clear that for BK1 there is 40 % higher RWC than REF and BK2 at low altitudes (≤ 1 km). Between 1 km and 3.2 km, RWC is highest for REF and lowest for BK2. Time-averaged RWC at levels higher than 3.5 km is up to 30 % higher in background simulations (i.e. BK1 and BK2) than in REF. The highest maximum of RWC is found BK1 after 8:40 UTC, as seen in **Table 5.3**b. The steep variation of RWC at 3.2 km reminds that this altitude is where melting level is found.

Maximum RWC (g m^{-3})			
(a)	**REF**	**BK1**	**BK2**
8:00 UTC	0.60	0.53	0.49
8:20 UTC	0.76	0.45	0.65
8:40 UTC	0.66	0.45	0.62
9:00 UTC	0.62	0.45	0.58
9:20 UTC	0.63	0.41	0.50
(b)	**REF (all data)**	**BK1 (all data)**	**BK2 (all data)**
8:00 UTC	0.97	0.71	0.88
8:20 UTC	1.12	0.88	1.04
8:40 UTC	1.02	1.06	0.96
9:00 UTC	0.86	1.05	0.86
9:20 UTC	0.83	0.98	0.78

Table 5.3: Maximum values of time averaged (8:00 UTC – 9:20 UTC) mean vertical RWC (in g m^{-3}) for simulations REF, BK1 and BK2 (a) from profiles calculated for levels with $Z_{Ray} < 35$ dBZ and (b) from profiles calculated using all data.

Time-averaged mean vertical RWC is also calculated for levels with reflectivity lower than 35 dBZ. Those profiles have same behavior with the respective IWC profiles for altitudes under the melting level. Above this altitude, RWC is higher in background simulation than in REF, which is in contrast to IWC profiles. In this case, maximum values of mean vertical IWC are found rather for simulation BK2 (see **Table 5.3**a).

Overall, in this section it is found that changes in the initial aerosol particle number influence also the vertical structure of the convective system, namely the IWC and the RWC, as expected. A reduction of the initial aerosol particle concentration results to an increase of RWC in the cloud at altitudes above the melting level but a reduction of IWC all over the vertical extension of the system. More numerous droplets are found at altitudes higher than the melting level for REF simulation than for background simulations (e.g. up to 80 % more droplets at altitudes between 4.4 and 5.7 km, not shown). However, more numerous droplets signify an environment of lower

supersaturation, therefore these droplets stay small and evaporate easily. On the contrary, less numerous droplets can grow larger and contain more RWC. As a consequence, RWC is higher in background simulations at the aforementioned altitudes. However, as bigger droplets fall faster due to gravity, they can evaporate while falling. This is the reason why RWC is reduced in lower altitudes for background simulations. Accordingly, the freezing of bigger droplets is more difficult, therefore there is less IWC in the background simulations than in REF simulation.

This chapter ends with a study of the influence of changes in the aerosol particle number together with modifications of the large-scale model domain on the precipitation field.

5.4 Impact of the initial aerosol properties on the SSD simulations

As discussed in **chapter 4**, the consideration of a smaller outermost domain that is also shifted with respect to the outermost domain of the REF simulation can influence the temporal and spatial evolution of the convective system. In this section, sensitivity simulations are performed taking into account both changes on the initial aerosol particle number (as for cases BK1 and BK2) and on the large-scale set-up (as in SSD simulation). Consequently, a simulation called “background 1 SSD” and a simulation named “background 2 SSD” take place. Firstly, the initial properties of these sensitivity simulations are described and then, their results, i.e. rain accumulation, radar reflectivity, IWC and RWC, are compared to the reference simulations results. Moreover, all examined modeled variables are also compared to HYMEX observations.

5.4.1 Description of the initial properties

For the present study, two sensitivity simulations take place. For the simulation “background 1 SSD”, which will hereafter refer to “BK1_SSD”, the same aerosol particle properties used for the simulation BK1 are applied (see **Figure 5.2** and **Table 5.1**). Respectively, for the simulation “background 2 SSD”, which hereafter will be called as “BK2_SSD”, the model is initialized with the same aerosol particle properties of case BK2 (see also **Table 5.1** and **Figure 5.3**). For both simulations BK1_SSD and BK2_SSD, the large scale configuration of DESCAM-3D corresponds to one applied for simulation SSD (see section **4.3.1**). Overall, in BK1_SSD and BK2_SSD, the initial aerosol particle

concentration is lower than in simulation REF and at the same time, the outermost domain is smaller and shifted to the west. This section continues with the analysis of the results from the aforementioned sensitivity simulations concerning the precipitation field (cumulative rainfall and X-band radar reflectivity).

5.4.2 Impact on the precipitation field

The influence of both changes in the initial aerosol particle number and large-scale configuration on the rainfall are examined first. **Figure 5.18** compares the rain accumulation at the ground until 11:00 UTC for simulations SSD, BK1_SSD and BK2_SSD along with the REF simulations and the observations (KED QPE).

Comparing BK1_SSD (**Figure 5.18**e) with SSD (**Figure 5.18**c) results, it is seen that the orientation of the system is almost similar for these two simulations, as well as for BK2_SSD (**Figure 5.18**g). Nevertheless, the spatial distribution of the precipitation is quite different. The small cell that appears in SSD at the north (over Vivarais Mountains) is more pronounced in BK1_SSD, as well as the secondary cell at the south (at the east of Alès). The maximum cumulative rainfall in BK1_SSD is 128 mm locally (about 5 % higher than in SSD) and for BK2_SSD is 117 mm locally (about 4 % less than in SSD), according to **Table 5.4**. The location of the maximum cumulative rainfall is similar in the SSD simulations and it is found Vivarais Mountains, shifted by 5 km to the south-west with regard to REF simulations and KED QPE (**Figure 5.18**a).

KED QPE	REF	BK1	BK2	SSD	BK1_SSD	BK2_SSD
115	118	117	153	122	128	117

Table 5.4: Maximum values of rain accumulation (in mm) from 00:00 to 11:00 UTC for KED QPE and for all DESCAM simulations (REF and SSD).

Nevertheless, it is seen that comparing BK1 with BK1_SSD, the maximum rain accumulation is about 8 % higher in the second one. In contrast to this, the maximum value for BK2 is 24 % higher than in BK2_SSD.

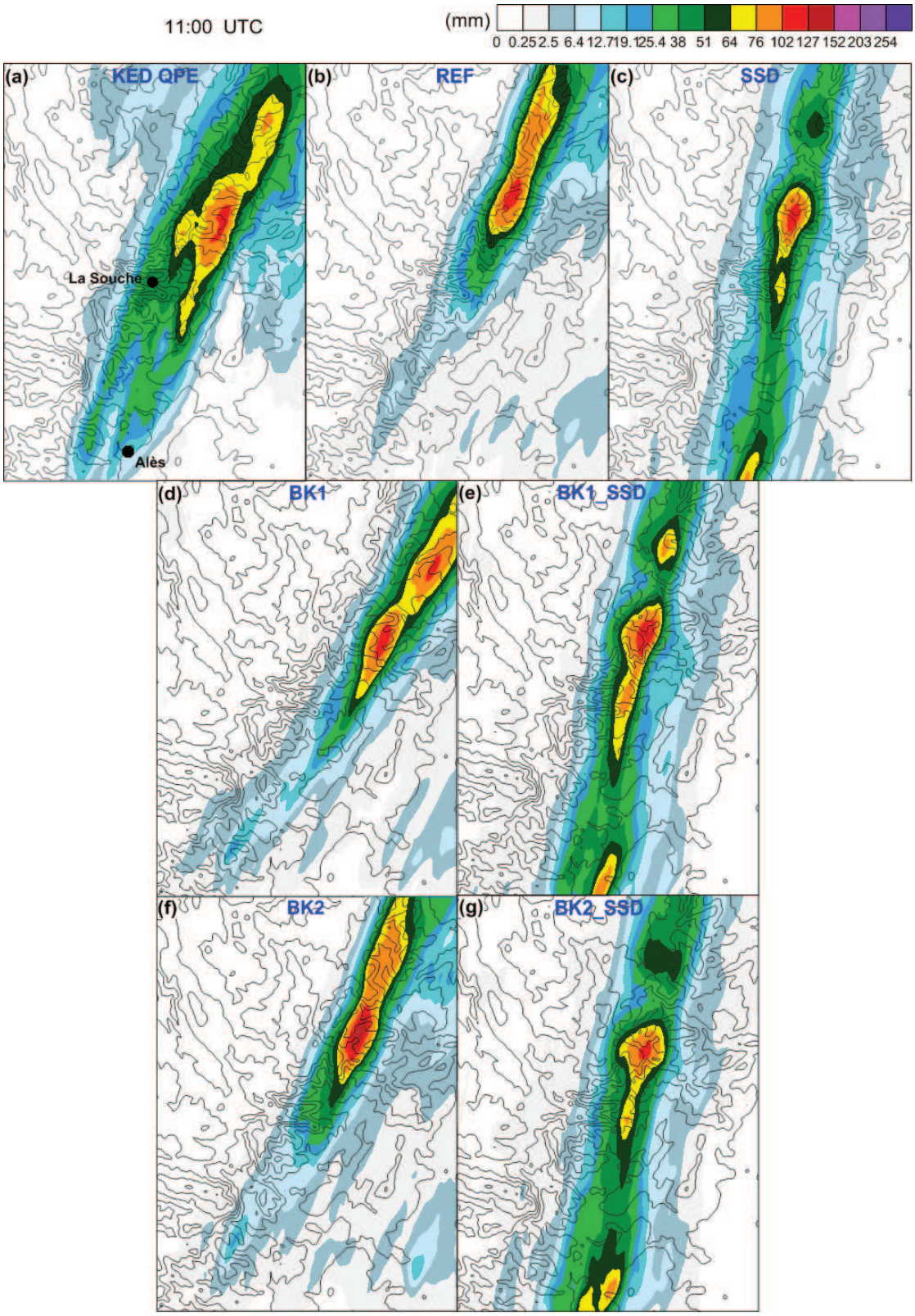

Figure 5.18: Cumulative rainfall on the ground (in mm) from 00:00 UTC to 11:00 UTC of the 26th September 2012 (a) from the observations (KED QPE), for REF simulations (b, d, f) and for SSD simulations (c, e, g).

It is remarkable to note that the total rain amount on the ground until 11:00 UTC (considering the part of the D3 that is in common for REF and SSD) in all SSD simulations is higher than in REF, BK1 and BK2 simulations, as shown in **Figure 5.19**.

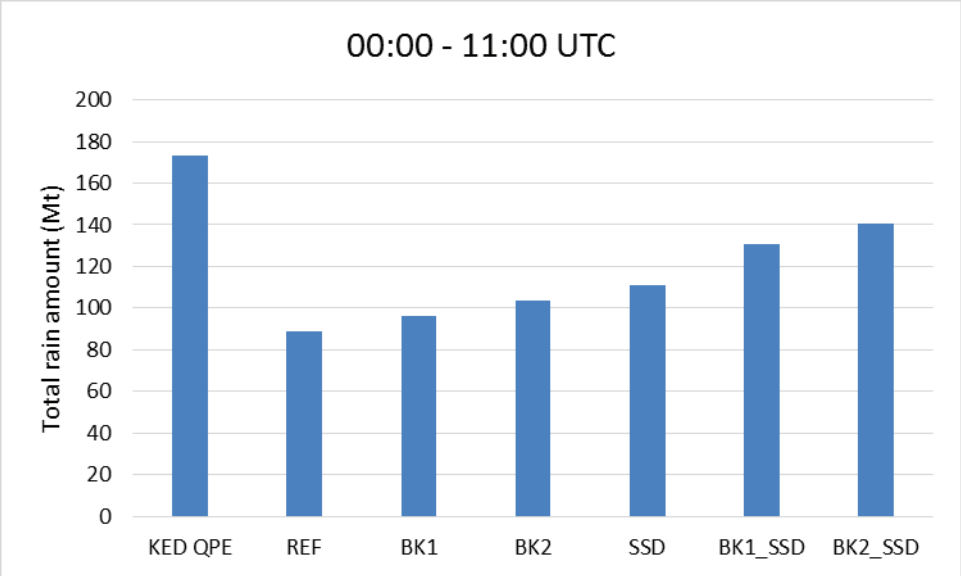

Figure 5.19: Total rain amount on the ground (in Mt) from 00:00 UTC to 11:00 UTC according to the KED QPE, the REF model simulations (REF, BK1 and BK2) and the SSD model simulations (SSD, BK1_SSD and BK2_SSD) inside their geographical region in common.

Higher total rain amount in all SSD simulations is explained by their different spatial distribution. Indeed, as seen in **Figure 5.18**c, e and g, there is more rainfall at the southern part of the domain (i.e. at the east of Cévennes Mountains) in SSD results than in reference simulations. This finding can be also seen from the statistical comparison of precipitation accumulation between different simulations and observations until 11:00 UTC in **Figure 5.20**.

Rain spots in the range of 20 mm to 60 mm appear more frequently in all SSD simulations. Nevertheless, strong rain spots (> 80 mm) are rather appeared mostly for REF, BK1 and BK2 simulations. It is also seen that the highest maximum rainfall is found for BK2 and BK1_SSD.

Focusing on the period between 6:40 UTC and 10:00 UTC, the probability density function of the X-band radar reflectivity for all model simulations and observations is presented in **Figure 5.21**. According to this distribution, reflectivity in the range 25 to 60 dBZ appears more frequently for SSD than for reference simulations. However, values from 10 to 20 dBZ that correspond to light rain appear more frequently in reference simulations.

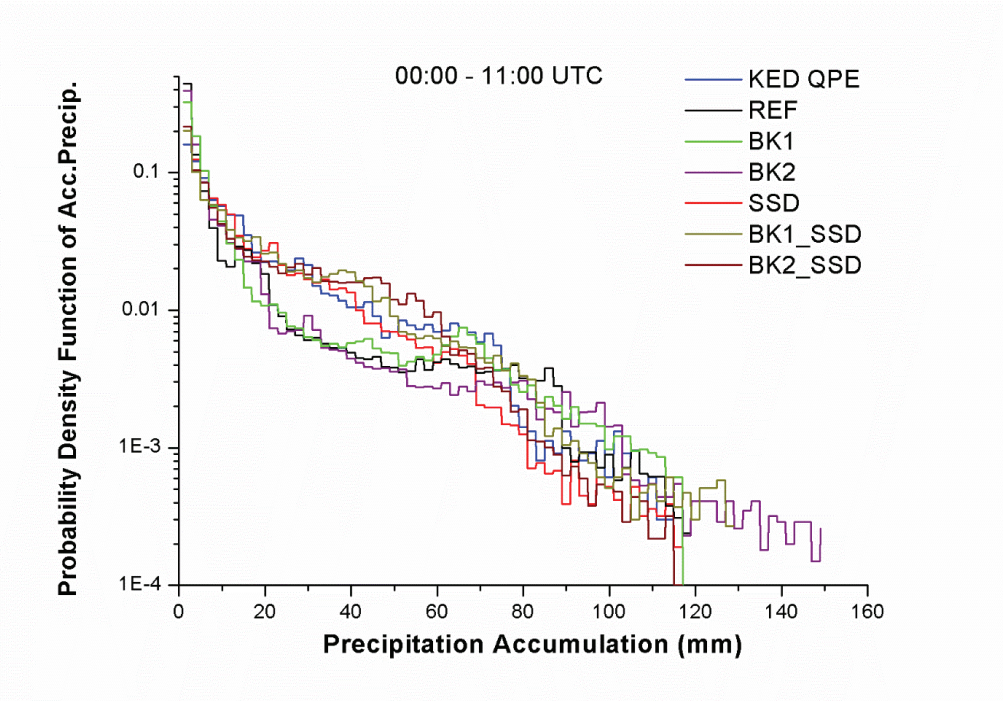

Figure 5.20: Probability density function of the rain accumulation on the surface between 00:00 UTC and 11:00 UTC of the 26th September 2012 calculated for the QPE observations (blue line), the model results of the REF simulations and the SSD simulations.

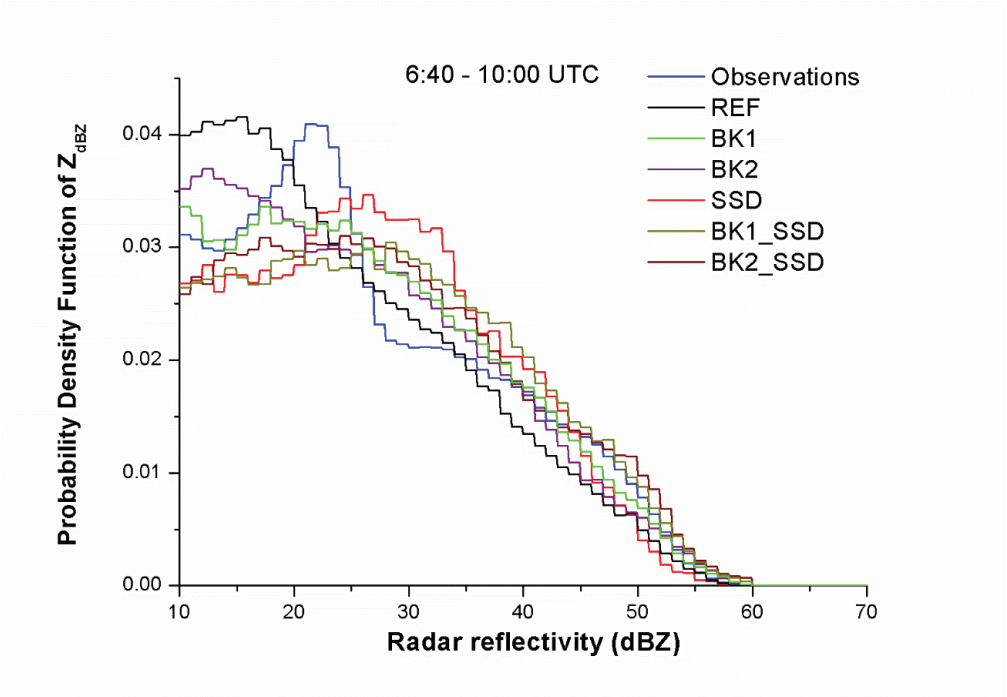

Figure 5.21: Averaged probability density function of the X-band radar reflectivity observations (blue line) and the respective model results of the REF simulations and the SSD simulations for the time period of 6:40 UTC – 10:00 UTC.

To conclude, a reduction on the initial aerosol concentration together with the consideration of a modified outermost model domain results in higher total rain amount on the ground and differences in the spatial distribution of the rain field. Nevertheless, the magnitude of impact of each of these aspects in cloud features is not the same. A single reduction in the initial concentration of aerosol particles influences mainly the rain quantity by an increase in the total rain amount in the cloud (e.g. comparing REF and BK2). On the other hand, a single modification of the large-scale configuration, affects mostly the spatial distribution and orientation of the precipitating system, but results also in an increase of the total rain amount in the whole innermost domain (e.g. comparing REF and SSD. However, the consideration of both modifications in the model initialization leads to higher impact in the total rainfall amount, as well as changes in the orientation of the system and spatial distribution of the precipitation (e.g. comparing REF and BK1_SSD).

6 Conclusions and Perspectives

In the general framework of a climate change which is in progress since the previous century, intensity of meteorological phenomena (i.e. heavy rainfall episodes) can vary significantly and/or unexpectedly. NWP models provide pretty accurate predictions of such phenomena in the time frame of 3 days. However, improvements must be done in order to obtain more accurate forecasts regarding temporal and spatial evolution of intense meteorological phenomena. The 10-year international program of HYMEX aiming to the improvement of the prediction of heavy precipitation events, provides a large set of observations from various ground-based and on-board instruments during such events in the western part of the Mediterranean Sea. The South of France is affected by heavy precipitation episodes in the beginning of autumn. A French region that is constantly influenced heavy rainfall in autumn is Cévennes-Vivarais. "Cévenols", as these episodes are called, can cause natural disasters, economical loss and casualties. It is, therefore, essential to improve their prediction. A better understanding of the microphysics of heavy precipitation episodes in Cévennes-Vivarais attributes to the improvement of their prediction by NWP models. For this reason, DESCAM, a cloud model with detailed microphysics was used to simulate and study one of the observed during HYMEX heavy precipitation events, IOP7a, in a 3D-field. The objectives of the present thesis were the following:

- Detailed analysis of the available HYMEX observations during IOP7a and their quality check.
- Simulation of IOP7a with DESCAM-3D and evaluation of the model results by comparing them to the respective HYMEX observations.
- Study of the role of atmospheric pollution, by means of the initial aerosol particle concentration, in the development and evolution of the intense precipitation episode of IOP7a. In particular, study of the influence of the initial aerosol particle

number on the precipitation field, but also in the vertical structure of the system, regarding ice phase and liquid phase.

A synopsis of the present study together with its main conclusions is presented hereafter.

6.1 Conclusions

Chapter 2 was dedicated to the state-of-the-art of cloud modeling. An up-to-date literature review of modeling of cloud dynamics at different scales has been presented. Differences regarding microphysics in various models were discussed, pointing out the two main types of its representation: the “bulk” and the “bin-resolved”. Emphasis was given to aerosol-cloud interactions and ice nucleation processes, as challenging topics in cloud microphysics. DESCAM, a model with bin-resolved microphysics, was used for the study of the heavy precipitation episode of IOP7a. As fundamental tool for the present thesis, the detailed microphysics of DESCAM was described separately, as well as the 3D dynamics of Clark and Hall model, which was coupled to DESCAM for this study.

Another fundamental aspect for this work was the observation data from HYMEX. In chapter 3, the HYMEX experiment was presented, during which the heavy rainfall episode of IOP7a, study case of this thesis, was observed. Special features of IOP7a (e.g. prevailing synoptic conditions, rain intensity), as well as its spatial and temporal evolution provided by HYMEX observations was detailed. Afterwards, instruments available during IOP7a in the area of interest (Cévennes-Vivarais) were described together with their products. As for ground-based measurements, the quantitative precipitation estimation from OHM-CV merging rain gauge and radar observations provided data for rain accumulation in Cévennes-Vivarais during IOP7a with a resolution of 1 km x 1 km. Intensity of rainfall during IOP7a was confirmed by rain rate data from the rain gauge network of Météo-France, but also from Parsivel disdrometers installed in the area of interest by LaMP and LTHE. Disdrometers also provided DSDs from which information about rain spectra during IOP7a was obtained. A MRR from LTHE was also operating during IOP7a providing DSD measurements which permitted additional retrieval of rain rates. Finally, X-band radars from LaMP were installed at locations affected by strong rainfall, permitting to record high-resolved reflectivity measurements. Nevertheless, the different position of each individual instrument combined with the different time of the passage of the precipitating system presented difficulties for the evaluation of the observations, since comparison of their observations was not always feasible. However, two disdrometers, a MMR and one X-band radar where selected to be

used in this study, as well as the products of quantitative precipitation estimation from OHM-CV. During IOP7a, aircraft measurements were also available. Hydrometeor microphysics probes (PIP and 2D-S), as well as the 95 GHz cloud radar RASTA were on-board the French research aircraft Falcon 20 which flew over Cévennes-Vivarais during the time period of the precipitation. RASTA provided cloud reflectivity observations, as well as a retrieval of IWC, whereas instruments 2D-S and PIP measured cloud hydrometeors. The last provided data showing that the majority of observed particles were solid hydrometeors. Therefore, these measurements provided information about ice crystal spectra. Another French research aircraft, ATR-42, performed a flight in the morning of the same day providing information about aerosol particles in the atmosphere over sea at the south of the strong precipitation area. Aerosol particle properties were obtained from SMPS and GRIMM OPC instruments on-board the ATR-42 and used for the initialization of the cloud model.

The intense precipitation episode of the IOP7a was simulated with DESCAM-3D cloud microphysics model. The model was initiated using ECMWF IFS synoptic data at midnight of 26th September 2012 and aerosol particle properties from ATR-42 observations close to the surface. Chapter 4 presents a detailed analysis of the results of this simulation named reference (REF). DESCAM-3D reproduced satisfactorily the evolution of the IOP7a heavy precipitating system. The comparison between model results and ground-based observations, namely the rain accumulation from KED QPE and X-band radar reflectivity, showed that the location and orientation of the precipitating system was reasonably simulated by DESCAM-3D. The magnitude of these modeled values was also in accordance with the observations. However, since spatial resolution differs between model results and observations, small differences are rather expected. The horizontal extension of the system was somewhat underestimated by the model, as well as amount of rainfall at Cévennes Mountains. Also, a time shift of about one hour was observed compared to the observations. Nevertheless, the intensity and quantity of the modeled rain, as seen in results for cumulative rainfall and X-band radar reflectivity, was reasonable. Modeled rain spectra were rather in agreement with observations from disdrometers (Parsivel 10 and Parsivel S), but with an underestimation of the number of small rain drops (< 1 mm), as well as of their mass. However, it is possible that Parsivel S observed extremely high number of rain drops because it was close to the cloud base. Similar comparison between simulated rain spectra and those observed by the MRR10, showed that the instrument was probably influenced by dynamical factors, such as vertical wind, since only few and small (< 2 mm) rain drops were detected. Ice crystal spectra were in agreement with those observed by hydrometeor probes, but with an underestimation of the number of small ice crystals (< 200 μm) and rather at 6.6 km, whereas the observations took place between 5.1 km and 5.7 km. Time-averaged mean

vertical profiles of IWC were obtained from RASTA retrievals, as well as from observations by PIP and 2D-S. Comparing these profiles to the modeled ones, it was found that RASTA shows lower values all over the vertical extent, except high altitudes (> 9 km). At the same time, the IWC profile for hydrometeor probes showed a large variation with very high values between 5 km and 6 km and very small values in the layer from 7 km and 8 km. The analysis of data from RASTA showed that attenuation can influence its observation products.

In order to investigate sensitivity of the model large-scale configuration, the outermost domain was modified and another simulation performed, named SSD (for "smaller shifter domain"). It was found that the size, position and orientation of the outermost model domain are critical factors for the simulation of an intense rainfall event, since such a modification results in the consideration of a different dynamic field. Reference simulation results concerning the precipitation field (i.e. rain accumulation and X-band radar reflectivity) were closer to the observations than SSD results.

The role of "pollution" on the formation and evolution of the heavy precipitation episode of IOP7a was studied in chapter 5. For this purpose, the initial aerosol concentration was modified in the DESCAM configuration and two additional simulations were performed using the same ECMWF IFS data as in REF. The first simulation, named "background 1" (BK1) was initialized with aerosol particle properties observed during HYMEX IOP16 over sea, close to the surface. For the initialization of the second simulation, namely "background 2" (BK2), aerosol properties from observations at the Puy de Dôme (PDD) research station (Central France) in autumn were used. The initial total aerosol particle number of cases BK1 and BK2 was 1704 cm^{-3} and 1010 cm^{-3} respectively. The results of these two simulations showed that a reduction of the initial AP influences the spatial distribution of the precipitation on the ground and leads to an increase of maximum rain accumulation, as well as of the total rain amount. However, this influence is not always proportional; the least polluted case, BK2, simulated the highest maximum of rain accumulation, however total rain amount was larger for BK1 simulation. Regarding numbers inside the innermost model domain, a reduction of a factor of 2 in the initial aerosol particle number with respect to REF leads up to 4 % of increase in maximum rain accumulation and up to 28 % in total rain amount until the end of the precipitation episode (BK1). Nevertheless, a decrease of 66 % in the initial aerosol particle number gives 22 % higher maximum cumulative rainfall, but only 10 % higher total rain amount (BK2). A reduction in the initial aerosol particle concentration will also alter the IWC and RWC regime inside the cloud. In particular, it results in a decrease of the time-averaged mean vertical IWC at all altitudes and an increase by 30 % of the mean RWC above the melting level.

Finally, the role of “pollution” coupled to the large-scale configuration on the precipitation field was examined. For this purpose, simulations BK1 and BK2 were performed with DESCAM-3D using the domain configuration of SSD. Thus, the two new simulations were named “BK1_SSD” and “BK2_SSD” and their results for cumulative rainfall were compared with SSD, REF, BK1 and BK2 results. It was found that both modifications influence the spatial distribution of the precipitation and the total rain amount was more increased than if a single modification is applied (i.e. only a reduction of the initial aerosol particle number).

To sum up, a detailed analysis of HYMEX observations during IOP7a was made together with an evaluation of instruments and observation products. Simulation of IOP7a with DESCAM-3D was reasonable compared to the available observations. The role of “pollution” by means of initial number of aerosol particles in the beginning of the simulation influences spatial distribution, quantity and intensity of rainfall during a heavy precipitation episode. Mean vertical IWC changes proportionally to modifications in the initial aerosol concentration, whereas opposite behavior is observed for RWC at levels higher than the melting level. Large-scale model configuration is also important and its selection must be done carefully, as it is linked to the consideration of dynamics in the simulation.

6.2 Perspectives

The present work provided also a critical view on the observations during HYMEX IOP7a from individual instruments (e.g. disdrometers, X-band radars, MRR, cloud radar). This analysis suggests that calibration of certain instruments may need to be reconsidered. For example, X-band observations from radar X4 seems to indicate a systematic overestimation of reflectivity. It is also suggested that the placement of MRR instruments at locations which can be affected by strong vertical wind (e.g. mountain slopes) should be avoided for observations of orographic precipitation because it is still impossible to correct the MRR data unless a vertically pointing wind radar is deployed at the same site. Finally, attenuation appears to be a non-negligible factor that needs to be carefully considered when treating RASTA products.

IOP7a was quite well reproduced by DESCAM-3D. Nevertheless, an underestimation of small hydrometeors by the model suggests that the nucleation processes can still be improved. However, further comparisons between modeled and observed rain and ice crystal spectra during similar heavy precipitation episodes should be done before reconsidering new representations in the model. The small deviations in

the spatial distribution of precipitation at the surface are still present between observations and simulation results suggesting that additional sensitivity studies can be performed in order to erase them (i.e. using new initial synoptic conditions, such as ERA5). Finally, not only the concentration of the aerosol particles, but also how their solubility can impact the formation and evolution of heavy precipitation episodes.

It will also be interesting to evaluate how a NWP model, such as WRF among others, reproduce the IOP7a system using the same set-up as defined in our reference simulations. Another model intercomparison study for the IOP7a is performed and highlighted the difficulties of the WRF model to reproduce/forecast this kind of intense precipitation system. Indeed, using the same set-up as in the REF case described in this thesis, the WRF model does not allow to reproduce the intensity and the distribution of the observed precipitation and so using either the Thompson or the Morrison microphysics scheme (Arteaga Rojas et. al, in preparation). This study, as well as other studies presented in the literature, highlight the overall quality of the DESCAM-3D simulations for the analysis and understanding of cloud and precipitation episodes. Even though there is still room for improvement.

Appendix

Rain rate observations by rain gauges of **Figure 3.2.**

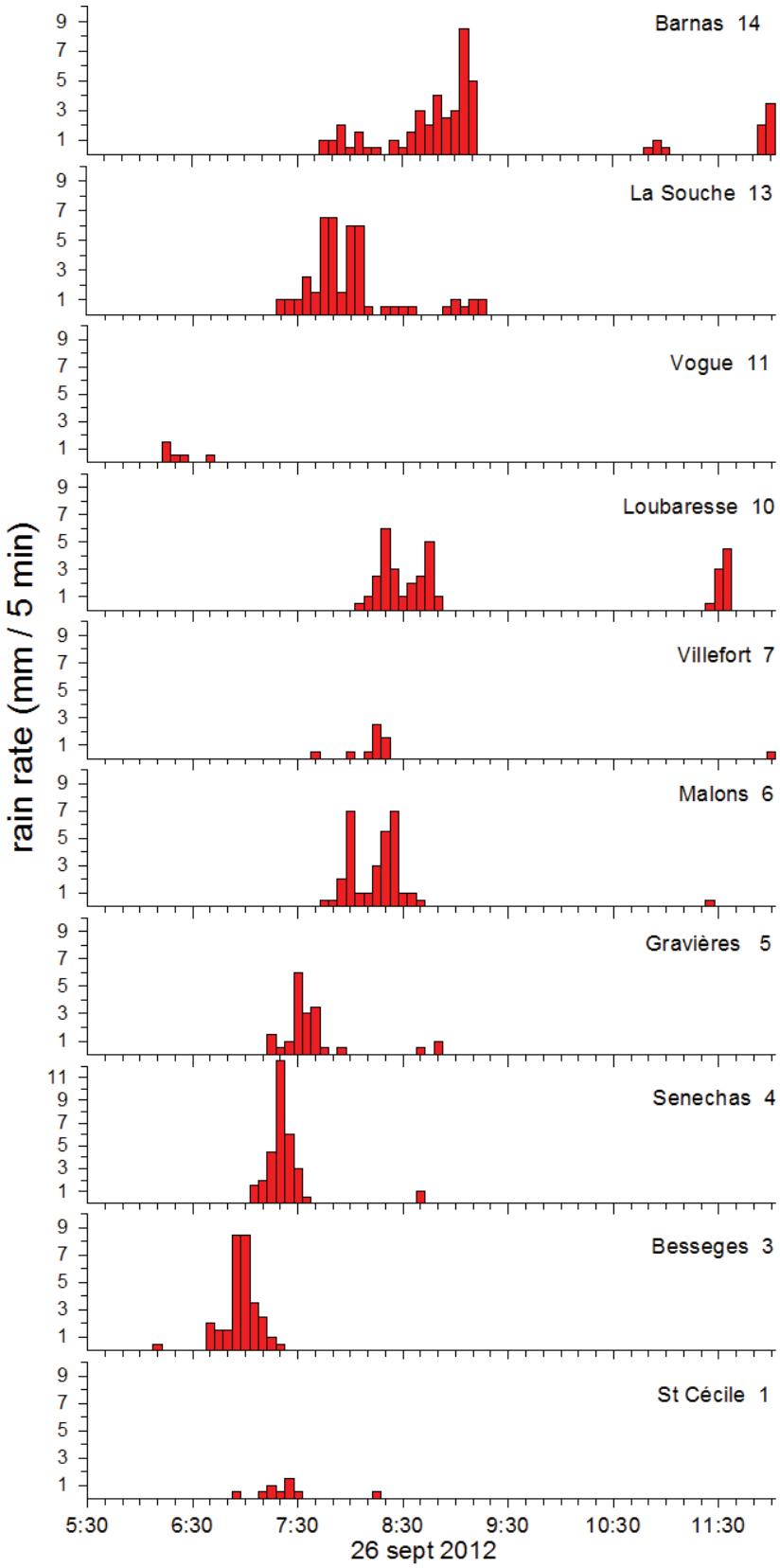

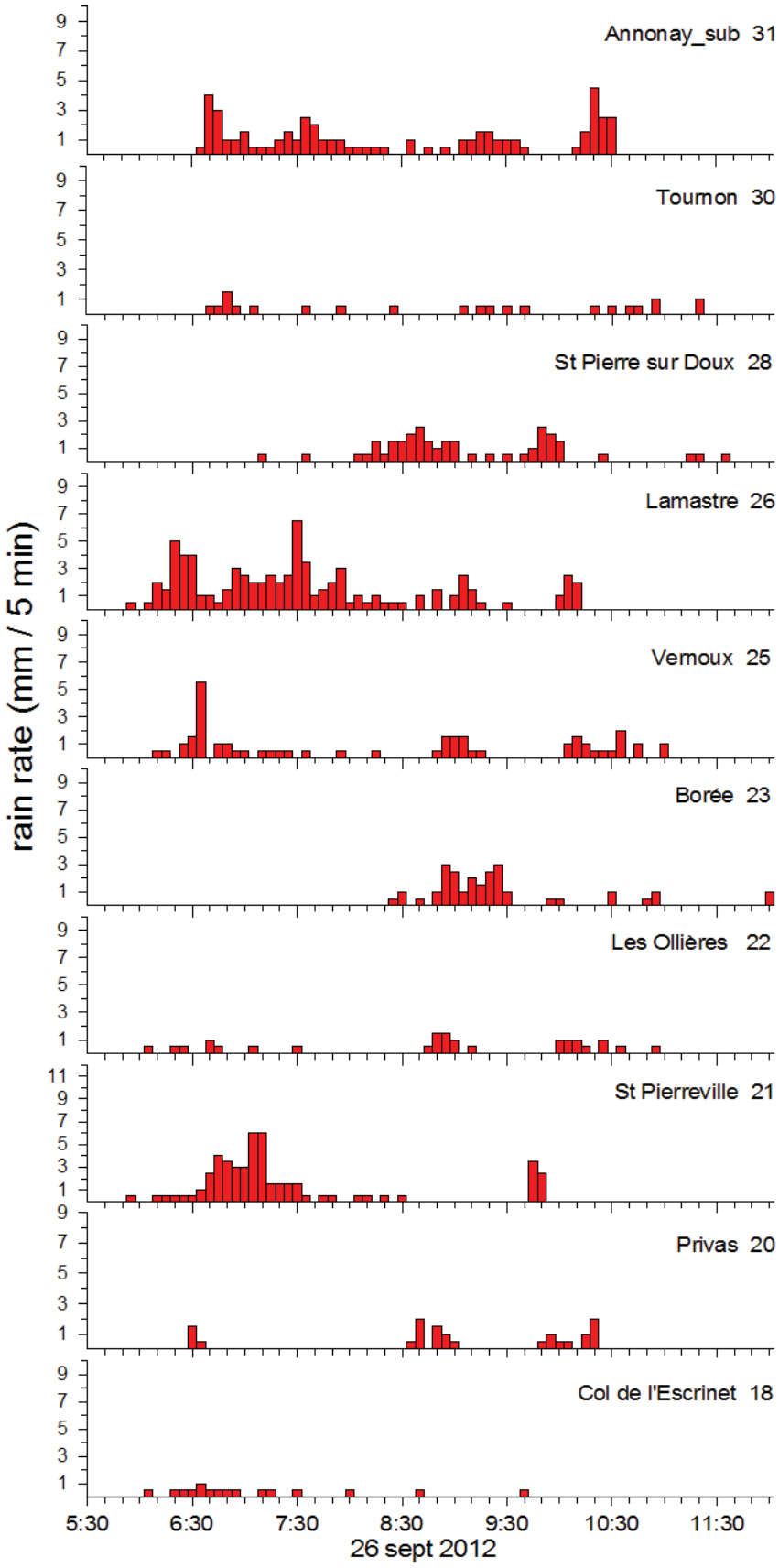
Annonay_sub 31
Tournon 30
St Pierre sur Doux 28
Lamastre 26
Vernoux 25
Borée 23
Les Ollières 22
St Pierreville 21
Privas 20
Col de l'Escrinet 18
rain rate (mm / 5 min)
5:30
6:30
7:30
8:30
9:30
10:30
11:30
26 sept 2012

List of figures

List of tables

List of symbols

$\|K_i\|^2$	Di-electrical constant for ice
$\|K_w\|^2$	Di-electrical constant for water
$\overline{\boldsymbol{\tau_{ij}}}$	Stress tensor
D_m	Mean volume weight diameter
D_{max}	Maximum dimension of the hydrometeor
D_v^*	Diffusion of water vapor in the air
$\overline{IWC}$	Averaged ice water content
J_{hom}	Homogeneous ice nucleation rate coefficient
K_M	Eddy mixing coefficient
L_e	Latent heat from evaporation
M_w	Molecular weight of water
N^*	Scaled number distribution of hydrometeors
N_{IN}	Number of pristine ice crystals (in DESCAM)
S_i	Ice saturation ratio
S_w	Supersaturation with respect to water
$\vec{V}$	Wind velocity
$Z^*_{aircraft}$	Altitude of the aircraft
Z_{dBZ}	Normalized radar reflectivity
c_p	Specific heat at constant pressure
c_v	Specific heat at constant volume
$e_{sat,w}$	Saturation vapor pressure with respect to liquid water
f_{AP}	Moist aerosol particle number distribution function
f_d	Number density distribution function of droplets
f_i	Number density distribution function of ice crystals
g_{APd}	Distribution function of aerosol particle mass inside droplets
k_r^*	Thermal conductivity of air
$\bar{m}$	Mean aerosol particle mass
m_i	Ice crystal mass
n_{Cooper}	Number of ice crystals (Cooper, 1986)
n_{id}	Number of ice crystals (Meyers et. al 1992)
q_v	Water vapor mixing ratio
r_N	Mean dry radius of wet aerosol particles inside drops
r_{act}	Critical radius for activation

$s_{v,w}$	Supersaturation with respect to liquid water
$z_{95,atten}$	Attenuated 95 GHz cloud radar reflectivity
z_{95GHz}	95 GHz cloud radar reflectivity
z_e	Equivalent radar reflectivity
$\vec{\Omega}$	Earth's rotation velocity
α_w	Water activity
α_w^i	Water activity of a solution in equilibrium with ice
δ_{ij}	Kronecker delta
ζ_0	Flight level
ζ_T	Level of cloud target
ρ_i	Density of ice
ρ_w	Density of water
σ_B	Backscattering coefficient
σ_{ext}	Extinction coefficient
σ_i	Geometric standard deviation
$\Delta\alpha_w$	Water-activity criterion for homogeneous ice nucleation
A	One-way attenuation factor
CWC	Condensed water content
D	Diameter of hydrometeors
IWC	Ice water content
L	Latent heat
N	Number concentration of hydrometeors
P	Atmospheric pressure
R	Gas constant
RR	Rain rate
RWC	Rain water content
T	Temperature
V	Terminal velocity of hydrometeors
Z	Radar reflectivity
r	Drop radius
θ	Air potential temperature
λ	Slope parameter of gamma distribution (Chapter 2)
λ	Radar wavelength (Chapter 4)
μ	Shape parameter of gamma distribution
ρ	Density of air

References

Albrecht BA (1989) Aerosols, Cloud Microphysics, and Fractional Cloudiness. Science 245:1227–1230. doi: 10.1126/science.245.4923.1227

Asai T, Kasahara A (1967) A Theoretical Study of the Compensating Downward Motions Associated with Cumulus Clouds. J Atmos Sci 24:487–496. doi: 10.1175/1520-0469(1967)024<0487:ATSOTC>2.0.CO;2

Atlas D, Srivastava RC, Sekhon RS (1973) Doppler radar characteristics of precipitation at vertical incidence. Reviews of Geophysics 11:1. doi: 10.1029/RG011i001p00001

Baba Y, Takahashi K, Sugimura T, Goto K (2010) Dynamical Core of an Atmospheric General Circulation Model on a Yin–Yang Grid. Monthly Weather Review 138:3988–4005. doi: 10.1175/2010MWR3375.1

Battaglia A, Rustemeier E, Tokay A, et al (2010) PARSIVEL Snow Observations: A Critical Assessment. Journal of Atmospheric and Oceanic Technology 27:333–344. doi: 10.1175/2009JTECHA1332.1

Baumgardner D, Korolev A (1997) Airspeed Corrections for Optical Array Probe Sample Volumes. J Atmos Oceanic Technol 14:1224–1229. doi: 10.1175/1520-0426(1997)014<1224:ACFOAP>2.0.CO;2

Beard KV (1976) Terminal Velocity and Shape of Cloud and Precipitation Drops Aloft. J Atmos Sci 33:851–864. doi: 10.1175/1520-0469(1976)033<0851:TVASOC>2.0.CO;2

Bigg EK (1953) The formation of atmospheric ice crystals by the freezing of droplets. Quarterly Journal of the Royal Meteorological Society 79:510–519. doi: 10.1002/qj.49707934207

Bott A (1998) A Flux Method for the Numerical Solution of the Stochastic Collection Equation. Journal of the Atmospheric Sciences 55:2284–2293. doi: 10.1175/1520-0469(1998)055<2284:AFMFTN>2.0.CO;2

Boudevillain B, Delrieu G, Galabertier B, et al (2011) The Cévennes-Vivarais Mediterranean Hydrometeorological Observatory database: DATA AND ANALYSIS NOTE. Water Resources Research 47:. doi: 10.1029/2010WR010353

Boudevillain B, Delrieu G, Wijbrans A, Confoland A (2016) A high-resolution rainfall re-analysis based on radar–raingauge merging in the Cévennes-Vivarais region, France. Journal of Hydrology 541:14–23. doi: 10.1016/j.jhydrol.2016.03.058

Bouniol D, Protat A, Plana-Fattori A, et al (2008) Comparison of Airborne and Spaceborne 95-GHz Radar Reflectivities and Evaluation of Multiple Scattering Effects in Spaceborne Measurements. Journal of Atmospheric and Oceanic Technology 25:1983–1995. doi: 10.1175/2008JTECHA1011.1

Bray M, Han D, Xuan Y, et al (2010) Rainfall uncertainty for extreme events in NWP downscaling model. Hydrological Processes 25:1397–1406. doi: 10.1002/hyp.7905

Bresson E, Ducrocq V, Nuissier O, et al (2012) Idealized numerical simulations of quasi-stationary convective systems over the Northwestern Mediterranean complex terrain. Quarterly Journal of the Royal Meteorological Society 138:1751–1763. doi: 10.1002/qj.1911

Brousseau P, Seity Y, Ricard D, Léger J (2016) Improvement of the forecast of convective activity from the AROME-France system: Improvement of Convective Activity Forecasts from AROME-France. Quarterly Journal of the Royal Meteorological Society 142:2231–2243. doi: 10.1002/qj.2822

Caniaux G, Redelsperger J-L, Lafore J-P (1994) A Numerical Study of the Stratiform Region of a Fast-Moving Squall Line. Part I: General Description and Water and Heat Budgets. Journal of the Atmospheric Sciences 51:2046–2074. doi: 10.1175/1520-0469(1994)051<2046:ANSOTS>2.0.CO;2

Chu Q, Xu Z, Chen Y, Han D (2017) Evaluation of the WRF model with different domain configurations and spin-up time in reproducing a sub-daily extreme rainfall event in Beijing, China. Hydrology and Earth System Sciences Discussions 1–32. doi: 10.5194/hess-2017-363

Clark T, Hall W, Coen J (1996) Source Code Documentation for the Clark-Hall Cloud-scale Model Code Version G3CH01. UCAR/NCAR

Clark TL (1977) A small-scale dynamic model using a terrain-following coordinate transformation. Journal of Computational Physics 24:186–215. doi: 10.1016/0021-9991(77)90057-2

Clark TL (1979) Numerical Simulations with a Three-Dimensional Cloud Model: Lateral Boundary Condition Experiments and Multicellular Severe Storm Simulations. Journal of the Atmospheric Sciences 36:2191–2215. doi: 10.1175/1520-0469(1979)036<2191:NSWATD>2.0.CO;2

Clark TL, Farley RD (1984) Severe Downslope Windstorm Calculations in Two and Three Spatial Dimensions Using Anelastic Interactive Grid Nesting: A Possible Mechanism for Gustiness. Journal of the Atmospheric Sciences 41:329–350. doi: 10.1175/1520-0469(1984)041<0329:SDWCIT>2.0.CO;2

Clark TL, Hall WD (1991) Multi-domain simulations of the time dependent navier-stokes equations: Benchmark error analysis of some nesting procedures. Journal of Computational Physics 92:456–481. doi: 10.1016/0021-9991(91)90218-A

Cohard J-M, Pinty J-P (2000) A comprehensive two-moment warm microphysical bulk scheme. I: Description and tests. Quarterly Journal of the Royal Meteorological Society 126:1815–1842. doi: 10.1256/smsqj.56613

Cohard J-M, Pinty J-P, Bedos C (1998) Extending Twomey's Analytical Estimate of Nucleated Cloud Droplet Concentrations from CCN Spectra. Journal of the

Atmospheric Sciences 55:3348–3357. doi: 10.1175/1520-0469(1998)055<3348:ETSAEO>2.0.CO;2

Colarco P, Silva A da, Chin M, Diehl T (2010) Online simulations of global aerosol distributions in the NASA GEOS-4 model and comparisons to satellite and ground-based aerosol optical depth. Journal of Geophysical Research: Atmospheres 115:. doi: 10.1029/2009JD012820

Collins M, Tett SFB, Cooper C (2001) The internal climate variability of HadCM3, a version of the Hadley Centre coupled model without flux adjustments. Climate Dynamics 17:61–81. doi: 10.1007/s003820000094

Cooper WA (1986) Ice Initiation in Natural Clouds. Meteorological Monographs 43:29–32. doi: 10.1175/0065-9401-21.43.29

Crumeyrolle S, Manninen HE, Sellegri K, et al (2010) New particle formation events measured on board the ATR-42 aircraft during the EUCAARI campaign. Atmospheric Chemistry and Physics 10:6721–6735. doi: 10.5194/acp-10-6721-2010

Dayan U, Nissen K, Ulbrich U (2015) Review Article: Atmospheric conditions inducing extreme precipitation over the eastern and western Mediterranean. Natural Hazards and Earth System Sciences 15:2525–2544. doi: 10.5194/nhess-15-2525-2015

Delanoë J, Protat A, Bouniol D, et al (2007) The Characterization of Ice Cloud Properties from Doppler Radar Measurements. Journal of Applied Meteorology and Climatology 46:1682–1698. doi: 10.1175/JAM2543.1

Delanoë J, Protat A, Testud J, et al (2005) Statistical properties of the normalized ice particle size distribution. Journal of Geophysical Research: Atmospheres 110:D10201. doi: 10.1029/2004JD005405

Delanoë J, Protat A, Vinson J-P, et al (2012) RASTA: The airborne cloud radar, a tool for studying cloud and precipitation during HyMeX SOP1.1. In: 6th HyMeX Workshop. Primosten, Croatia

Delanoë JME, Heymsfield AJ, Protat A, et al (2014) Normalized particle size distribution for remote sensing application. Journal of Geophysical Research: Atmospheres 119:4204–4227. doi: 10.1002/2013JD020700

Delanoë Julien, Hogan Robin J. (2008) A variational scheme for retrieving ice cloud properties from combined radar, lidar, and infrared radiometer. Journal of Geophysical Research: Atmospheres 113:. doi: 10.1029/2007JD009000

Delrieu G, Bonnifait L, Kirstetter P-E, Boudevillain B (2014) Dependence of radar quantitative precipitation estimation error on the rain intensity in the Cévennes region, France. Hydrological Sciences Journal 59:1308–1319. doi: 10.1080/02626667.2013.827337

Déqué M, Dreveton C, Braun A, Cariolle D (1994) The ARPEGE/IFS atmosphere model: a contribution to the French community climate modelling. Climate Dynamics 10:249–266. doi: 10.1007/BF00208992

Déqué M, Piedelievre JP (1995) High resolution climate simulation over Europe. Climate Dynamics 11:321–339. doi: 10.1007/BF00215735

Drigeard E, Fontaine E, Wobrock W, et al (2015) A Comparison of Airborne In Situ Cloud Microphysical Measurement with Ground-Based C-Band Radar Observations in Deep Stratiform Regions of African Squall Lines. Journal of Applied Meteorology and Climatology 54:2461–2477. doi: 10.1175/JAMC-D-14-0262.1

Drobinski P, Ducrocq V, Alpert P, et al (2014) HyMeX: A 10-Year Multidisciplinary Program on the Mediterranean Water Cycle. Bulletin of the American Meteorological Society 95:1063–1082. doi: 10.1175/BAMS-D-12-00242.1

Ducrocq V, Braud I, Davolio S, et al (2014) HyMeX-SOP1: The Field Campaign Dedicated to Heavy Precipitation and Flash Flooding in the Northwestern Mediterranean. Bulletin of the American Meteorological Society 95:1083–1100. doi: 10.1175/BAMS-D-12-00244.1

Estournel C, Testor P, Damien P, et al (2016) High resolution modeling of dense water formation in the north-western Mediterranean during winter 2012-2013: Processes and budget: MODELING OF DENSE WATER CONVECTION. Journal of Geophysical Research: Oceans 121:5367–5392. doi: 10.1002/2016JC011935

Fan J, Wang Y, Rosenfeld D, Liu X (2016) Review of Aerosol–Cloud Interactions: Mechanisms, Significance, and Challenges. Journal of the Atmospheric Sciences 73:4221–4252. doi: 10.1175/JAS-D-16-0037.1

Feingold G, Heymsfield AJ (1992) Parameterizations of Condensational Growth of Droplets for Use in General Circulation Models. J Atmos Sci 49:2325–2342. doi: 10.1175/1520-0469(1992)049<2325:POCGOD>2.0.CO;2

Flossmann AI, Hall WD, Pruppacher HR (1985) A Theoretical Study of the Wet Removal of Atmospheric Pollutants. Part I: The Redistribution of Aerosol Particles Captured through Nucleation and Impaction Scavenging by Growing Cloud Drops. Journal of the Atmospheric Sciences 42:583–606. doi: 10.1175/1520-0469(1985)042<0583:ATSOTW>2.0.CO;2

Flossmann AI, Wobrock W (2010) A review of our understanding of the aerosol–cloud interaction from the perspective of a bin resolved cloud scale modelling. Atmospheric Research 97:478–497. doi: 10.1016/j.atmosres.2010.05.008

Fontaine E, Schwarzenboeck A, Delanoë J, et al (2014) Constraining mass–diameter relations from hydrometeor images and cloud radar reflectivities in tropical continental and oceanic convective anvils. Atmospheric Chemistry and Physics 14:11367–11392. doi: 10.5194/acp-14-11367-2014

Fourrié N, Bresson E, Nuret M, et al (2015) AROME-WMED, a real-time mesoscale model designed for the HyMeX special observation periods. Geoscientific Model Development 8:1919–1941. doi: 10.5194/gmd-8-1919-2015

Frei, Schär (1998) A precipitation climatology of the Alps from high-resolution rain-gauge observations. International Journal of Climatology 18:873–900. doi: 10.1002/(SICI)1097-0088(19980630)18:8<873::AID-JOC255>3.0.CO;2-9

Gibelin A-L, Déqué M (2003) Anthropogenic climate change over the Mediterranean region simulated by a global variable resolution model. Climate Dynamics 20:327–339. doi: 10.1007/s00382-002-0277-1

Gong W, Stroud C, Zhang L (2011) Cloud Processing of Gases and Aerosols in Air Quality Modeling. Atmosphere 2:567–616. doi: 10.3390/atmos2040567

Gordon C, Cooper C, Senior CA, et al (2000) The simulation of SST, sea ice extents and ocean heat transports in a version of the Hadley Centre coupled model without flux adjustments. Climate Dynamics 16:147–168. doi: 10.1007/s003820050010

Gosset M, Sauvageot H (1992) A Dual-Wavelength Radar Method for Ice-Water Characterization in Mixed-Phase Clouds. J Atmos Oceanic Technol 9:538–547. doi: 10.1175/1520-0426(1992)009<0538:ADWRMF>2.0.CO;2

Grandey BS, Rothenberg D, Avramov A, et al (2018) Effective radiative forcing in the aerosol–climate model CAM5.3-MARC-ARG. Atmospheric Chemistry and Physics Discussions 1–39. doi: 10.5194/acp-2018-118

Guo X, Fu D, Guo X, Zhang C (2014) A case study of aerosol impacts on summer convective clouds and precipitation over northern China. Atmospheric Research 142:142–157. doi: 10.1016/j.atmosres.2013.10.006

Hiron T, Flossmann AI (2015) A Study of the Role of the Parameterization of Heterogeneous Ice Nucleation for the Modeling of Microphysics and Precipitation of a Convective Cloud. Journal of the Atmospheric Sciences 72:3322–3339. doi: 10.1175/JAS-D-15-0026.1

Ilotoviz E, Khain A (2016) Application of a new scheme of cloud base droplet nucleation in a spectral (bin) microphysics cloud model: sensitivity to aerosol size distribution. Atmospheric Chemistry and Physics 16:14317–14329. doi: 10.5194/acp-16-14317-2016

IPCC (2018) Global warming of 1.5°C. Available online: http://www.ipcc.ch/report/sr15/

Iribarne JV, Cho HR (1989) Models of cloud chemistry. Tellus B 41B:2–23. doi: 10.1111/j.1600-0889.1989.tb00121.x

Jung G, Prange M, Schulz M (2015) Model simulation output data (CCSM3) related to uplift of African topography and the intensification of upwelling in the Benguela region. Supplement to: Jung, G et al. (2014): Uplift of Africa as a potential cause for Neogene intensification of the Benguela upwelling system. Nature Geoscience, 7(10), 741-747, https://doi.org/10.1038/ngeo2249

Kessler E (1969) On the Distribution and Continuity of Water Substance in Atmospheric Circulations. In: On the Distribution and Continuity of Water Substance in Atmospheric Circulations. American Meteorological Society, Boston, MA, pp 1–84

Khain A, Lynn B, Dudhia J (2010) Aerosol Effects on Intensity of Landfalling Hurricanes as Seen from Simulations with the WRF Model with Spectral Bin Microphysics. J Atmos Sci 67:365–384. doi: 10.1175/2009JAS3210.1

Khain A, Pokrovsky A, Pinsky M, et al (2004) Simulation of Effects of Atmospheric Aerosols on Deep Turbulent Convective Clouds Using a Spectral Microphysics Mixed-Phase Cumulus Cloud Model. Part I: Model Description and Possible Applications. J Atmos Sci 61:2963–2982. doi: 10.1175/JAS-3350.1

Khain AP (2009) Notes on state-of-the-art investigations of aerosol effects on precipitation: a critical review. Environmental Research Letters 4:015004. doi: 10.1088/1748-9326/4/1/015004

Khain AP, Leung LR, Lynn B, Ghan S (2009) Effects of aerosols on the dynamics and microphysics of squall lines simulated by spectral bin and bulk parameterization schemes. Journal of Geophysical Research 114:. doi: 10.1029/2009JD011902

Kogan Y (2012) A Cumulus Cloud Microphysics Parameterization for Cloud-Resolving Models. J Atmos Sci 70:1423–1436. doi: 10.1175/JAS-D-12-0183.1

Kogan YL, Mechem DB, Choi K (2012) Effects of Sea-Salt Aerosols on Precipitation in Simulations of Shallow Cumulus. Journal of the Atmospheric Sciences 69:463–483. doi: 10.1175/JAS-D-11-031.1

Köhler H (1936) The nucleus in and the growth of hygroscopic droplets. Trans Faraday Soc 32:1152–1161. doi: 10.1039/TF9363201152

Koop T, Luo B, Tsias A, Peter T (2000) Water activity as the determinant for homogeneous ice nucleation in aqueous solutions. Nature 406:611–614. doi: 10.1038/35020537

Labbouz L, Van Baelen J, Tridon F, et al (2013) Precipitation on the lee side of the Vosges Mountains: Multi-instrumental study of one case from the COPS campaign. Meteorologische Zeitschrift 413–432. doi: 10.1127/0941-2948/2013/0413

Lafore JP, Stein J, Asencio N, et al (1998) The Meso-NH Atmospheric Simulation System. Part I: adiabatic formulation and control simulations. Annales Geophysicae 16:90–109. doi: 10.1007/s00585-997-0090-6

Lawson RP, O'Connor D, Zmarzly P, et al (2006) The 2D-S (Stereo) Probe: Design and Preliminary Tests of a New Airborne, High-Speed, High-Resolution Particle Imaging Probe. Journal of Atmospheric and Oceanic Technology 23:1462–1477. doi: 10.1175/JTECH1927.1

Lebo ZJ, Morrison H (2013) A Novel Scheme for Parameterizing Aerosol Processing in Warm Clouds. J Atmos Sci 70:3576–3598. doi: 10.1175/JAS-D-13-045.1

Leroy D (2007) Développement d'un modèle tridimensionnel à microphysique détaillée. Application à la simulation de cas de convection moyenne et profonde. Thèse de doctorat, Université Blaise Pascal

Leroy D, Fontaine E, Schwarzenboeck A, Strapp JW (2016) Ice Crystal Sizes in High Ice Water Content Clouds. Part I: On the Computation of Median Mass Diameter from In Situ Measurements. J Atmos Oceanic Technol 33:2461–2476. doi: 10.1175/JTECH-D-15-0151.1

Leroy D, Monier M, Wobrock W, Flossmann AI (2006) A numerical study of the effects of the aerosol particle spectrum on the development of the ice phase and

precipitation formation. Atmospheric Research 80:15–45. doi: 10.1016/j.atmosres.2005.06.007

Leroy D, Wobrock W, Flossmann AI (2007) On the influence of the treatment of aerosol particles in different bin microphysical models: A comparison between two different schemes. Atmospheric Research 85:269–287. doi: 10.1016/j.atmosres.2007.01.003

Leroy D, Wobrock W, Flossmann AI (2009) The role of boundary layer aerosol particles for the development of deep convective clouds: A high-resolution 3D model with detailed (bin) microphysics applied to CRYSTAL-FACE. Atmospheric Research 91:62–78. doi: 10.1016/j.atmosres.2008.06.001

Liebe HJ (1985) An updated model for millimeter wave propagation in moist air. Radio Science 20:1069–1089. doi: 10.1029/RS020i005p01069

Lim K-SS, Hong S-Y (2009) Development of an Effective Double-Moment Cloud Microphysics Scheme with Prognostic Cloud Condensation Nuclei (CCN) for Weather and Climate Models. Mon Wea Rev 138:1587–1612. doi: 10.1175/2009MWR2968.1

Lin Y-L, Farley RD, Orville HD (1983) Bulk Parameterization of the Snow Field in a Cloud Model. J Climate Appl Meteor 22:1065–1092. doi: 10.1175/1520-0450(1983)022<1065:BPOTSF>2.0.CO;2

Liu X, Easter RC, Ghan SJ, et al (2012) Toward a minimal representation of aerosols in climate models: description and evaluation in the Community Atmosphere Model CAM5. Geoscientific Model Development 5:709–739. doi: 10.5194/gmd-5-709-2012

Llasat MC, Llasat-Botija M, Petrucci O, et al (2013) Towards a database on societal impact of Mediterranean floods within the framework of the HYMEX project. Natural Hazards and Earth System Sciences 13:1337–1350. doi: 10.5194/nhess-13-1337-2013

Löffler-Mang M, Joss J (2000) An Optical Disdrometer for Measuring Size and Velocity of Hydrometeors. Journal of Atmospheric and Oceanic Technology 17:130–139. doi: 10.1175/1520-0426(2000)017<0130:AODFMS>2.0.CO;2

Lynn BH, Khain AP, Dudhia J, et al (2005) Spectral (Bin) Microphysics Coupled with a Mesoscale Model (MM5). Part I: Model Description and First Results. Mon Wea Rev 133:44–58. doi: 10.1175/MWR-2840.1

Marshall JS, Palmer WMK (1948) The distribution of raindrops with size. J Meteor 5:165–166. doi: 10.1175/1520-0469(1948)005<0165:TDORWS>2.0.CO;2

Meyers MP, DeMott PJ, Cotton WR (1992) New Primary Ice-Nucleation Parameterizations in an Explicit Cloud Model. Journal of Applied Meteorology 31:708–721. doi: 10.1175/1520-0450(1992)031<0708:NPINPI>2.0.CO;2

Mie G (1908) Beiträge zur Optik trüber Medien, speziell kolloidaler Metallösungen. Annalen der Physik 330:377–445. doi: 10.1002/andp.19083300302

Milbrandt JA, McTaggart-Cowan R (2010) Sedimentation-Induced Errors in Bulk Microphysics Schemes. Journal of the Atmospheric Sciences 67:3931–3948. doi: 10.1175/2010JAS3541.1

Milbrandt JA, Yau MK (2005) A Multimoment Bulk Microphysics Parameterization. Part I: Analysis of the Role of the Spectral Shape Parameter. Journal of the Atmospheric Sciences 62:14

Monier M (2003) Développement d'un modèle de cirrus à microphysique détaillée. Thèse de doctorat, Université Blaise Pascal

Monier M, Wobrock W, Gayet J-F, Flossmann A (2006) Development of a Detailed Microphysics Cirrus Model Tracking Aerosol Particles' Histories for Interpretation of the Recent INCA Campaign. Journal of the Atmospheric Sciences 63:504–525. doi: 10.1175/JAS3656.1

Morrison H, Thompson G, Tatarskii V (2008) Impact of Cloud Microphysics on the Development of Trailing Stratiform Precipitation in a Simulated Squall Line: Comparison of One- and Two-Moment Schemes. Monthly Weather Review 137:991–1007. doi: 10.1175/2008MWR2556.1

Nuissier O, Ducrocq V, Ricard D, et al (2008) A numerical study of three catastrophic precipitating events over southern France. I: Numerical framework and synoptic ingredients. Quarterly Journal of the Royal Meteorological Society 134:111–130. doi: 10.1002/qj.200

Onishi R, Takahashi K (2011) A Warm-Bin–Cold-Bulk Hybrid Cloud Microphysical Model*. Journal of the Atmospheric Sciences 69:1474–1497. doi: 10.1175/JAS-D-11-0166.1

Penide G (2010) Mise en place de simulateurs d'instruments de télédétection dans un modèle méso-échelle (BRAMS): Application à l'étude d'un système convectif observé pendant la campagne AMMA. Thèse de doctorat, Université Blaise Pascal - Clermont-Ferrand II

Peters G, Fischer B, Andersson T (2002) Rain observations with a vertically looking Micro Rain Radar (MRR). 7:10

Peters G, Fischer B, Münster H, et al (2005) Profiles of Raindrop Size Distributions as Retrieved by Microrain Radars. Journal of Applied Meteorology 44:1930–1949. doi: 10.1175/JAM2316.1

Petters MD, Kreidenweis SM (2007) A single parameter representation of hygroscopic growth and cloud condensation nucleus activity. Atmos Chem Phys 11

Phillips VTJ, DeMott PJ, Andronache C (2008) An Empirical Parameterization of Heterogeneous Ice Nucleation for Multiple Chemical Species of Aerosol. Journal of the Atmospheric Sciences 65:2757–2783. doi: 10.1175/2007JAS2546.1

Phillips VTJ, Demott PJ, Andronache C, et al (2013) Improvements to an Empirical Parameterization of Heterogeneous Ice Nucleation and Its Comparison with Observations. Journal of the Atmospheric Sciences 70:378–409. doi: 10.1175/JAS-D-12-080.1

Pinty J-P, Jabouille P (1998) A mixed-phase cloud parameterization for use in a mesoscale non-hydrostatic model: simulations of a squall line and of orographic precipitation. in: Conf on Cloud Physics, 17–21 August 1998, Everett, Washington

Planche C (2011) Développement et évaluation d'un modèle tridimensionnel de nuage mixte à microphysique détaillée: application aux précipitations orographiques. Thèse de doctorat, Université Blaise Pascal

Planche C, Wobrock W, Flossmann AI, et al (2010) The influence of aerosol particle number and hygroscopicity on the evolution of convective cloud systems and their precipitation: A numerical study based on the COPS observations on 12 August 2007. Atmospheric Research 98:40–56. doi: 10.1016/j.atmosres.2010.05.003

Planche C, Wobrock W, Flossmann AI (2014) The continuous melting process in a cloud-scale model using a bin microphysics scheme: Continuous Melting Process in Bin Microphysics Scheme. Quarterly Journal of the Royal Meteorological Society 140:1986–1996. doi: 10.1002/qj.2265

Planche C, Wobrock W, Flossmann AI, et al (2013) Small scale topography influence on the formation of three convective systems observed during COPS over the Vosges Mountains. Meteorologische Zeitschrift 395–411. doi: 10.1127/0941-2948/2013/0402

Pruppacher HR, Klett JD (1997) Microphysics of Clouds and Precipitation, 2 edition. Springer, Dordrecht

Raupach TH, Berne A (2015) Correction of raindrop size distributions measured by Parsivel disdrometers, using a two-dimensional video disdrometer as a reference. Atmospheric Measurement Techniques 8:343–365. doi: 10.5194/amt-8-343-2015

Ray PS (1972) Broadband Complex Refractive Indices of Ice and Water. Appl Opt, AO 11:1836–1844. doi: 10.1364/AO.11.001836

Rogers RR, Yau MK (1989) A short course in cloud physics. Pergamon Press

Rose C (2014) Nucléation et formation de nouvelles particules à haute altitude. Thèse de doctorat, Université Blaise Pascal - Clermont-Ferrand II

Rose C, Sellegri K, Freney E, et al (2015) Airborne measurements of new particle formation in the free troposphere above the Mediterranean Sea during the HYMEX campaign. Atmospheric Chemistry and Physics Discussions 15:8151–8189. doi: 10.5194/acpd-15-8151-2015

Saleeby SM, van den Heever SC (2013) Developments in the CSU-RAMS Aerosol Model: Emissions, Nucleation, Regeneration, Deposition, and Radiation. Journal of Applied Meteorology and Climatology 52:2601–2622. doi: 10.1175/JAMC-D-12-0312.1

Seifert et. al (2009) COSMO General Meeting, WG3-Session, 7 Sep Cloud microphysics in the COSMO model: New parameterizations of ice nucleation and melting of snow. - ppt download. http://slideplayer.com/slide/9770871/. Accessed 19 Apr 2018

Seity Y, Brousseau P, Malardel S, et al (2011) The AROME-France Convective-Scale Operational Model. Monthly Weather Review 139:976–991. doi: 10.1175/2010MWR3425.1

Simonin D, Pierce C, Roberts N, et al (2017) Performance of Met Office hourly cycling NWP-based nowcasting for precipitation forecasts. Quarterly Journal of the Royal Meteorological Society 143:2862–2873. doi: 10.1002/qj.3136

Skamarock C, Klemp B, Dudhia J, et al (2008) A Description of the Advanced Research WRF Version 3. doi: 10.5065/D68S4MVH

Smagorinsky J (1963) General circulation experiments with the primitive equations. Mon Wea Rev 91:99–164. doi: 10.1175/1520-0493(1963)091<0099:GCEWTP>2.3.CO;2

Sokol Z, Bližňák V, Zacharov P, Skripniková K (2016) Nowcasting of hailstorms simulated by the NWP model COSMO for the area of the Czech Republic. Atmospheric Research 171:66–76. doi: 10.1016/j.atmosres.2015.12.006

Stevens B, Feingold G (2009) Untangling aerosol effects on clouds and precipitation in a buffered system. Nature 461:607–613. doi: 10.1038/nature08281

Sun J, Xue M, Wilson JW, et al (2014) Use of NWP for Nowcasting Convective Precipitation: Recent Progress and Challenges. Bulletin of the American Meteorological Society 95:409–426. doi: 10.1175/BAMS-D-11-00263.1

Tabary P, Augros C, Champeaux J-L, et al (2013) Le réseau et les produits radars de Météo-France. La Météorologie 8:15. doi: 10.4267/2042/52050

Tao W-K, Chen J-P, Li Z, et al (2012) Impact of aerosols on convective clouds and precipitation: Aerosol impact on convective clouds. Reviews of Geophysics 50:. doi: 10.1029/2011RG000369

Teller A, Levin Z (2006) The effects of aerosols on precipitation and dimensions of subtropical clouds: a sensitivity study using a numerical cloud model. Atmos Chem Phys 14

Thompson G, Eidhammer T (2014) A Study of Aerosol Impacts on Clouds and Precipitation Development in a Large Winter Cyclone. J Atmos Sci 71:3636–3658. doi: 10.1175/JAS-D-13-0305.1

Thompson G, Field PR, Rasmussen RM, Hall WD (2008) Explicit Forecasts of Winter Precipitation Using an Improved Bulk Microphysics Scheme. Part II: Implementation of a New Snow Parameterization. Mon Wea Rev 136:5095–5115. doi: 10.1175/2008MWR2387.1

Thompson G, Rasmussen RM, Manning K (2004) Explicit Forecasts of Winter Precipitation Using an Improved Bulk Microphysics Scheme. Part I: Description and Sensitivity Analysis. Mon Wea Rev 132:519–542. doi: 10.1175/1520-0493(2004)132<0519:EFOWPU>2.0.CO;2

Tridon F, Van Baelen J, Pointin Y (2011) Aliasing in Micro Rain Radar data due to strong vertical winds: wind aliasing in MRR data. Geophysical Research Letters 38:. doi: 10.1029/2010GL046018

Twomey S (1977) The Influence of Pollution on the Shortwave Albedo of Clouds. Journal of the Atmospheric Sciences 34:1149–1152. doi: 10.1175/1520-0469(1977)034<1149:TIOPOT>2.0.CO;2

Twomey S (1974) Pollution and the planetary albedo. Atmospheric Environment (1967) 8:1251–1256. doi: 10.1016/0004-6981(74)90004-3

Vali G (2015) Interactive comment on "Ice nucleation terminology" by G. Vali et al. Discussion Paper 20

Van Baelen J, Pointin Y, Wobrock W, et al (2009) Precipitation and microphysical studies with a low cost high resolution X-band radar: an innovative project prospective. Advances in Geosciences 20:25–32. doi: 10.5194/adgeo-20-25-2009

Venzac H, Sellegri K, Villani P, et al (2009) Seasonal variation of aerosol size distributions in the free troposphere and residual layer at the puy de Doˆme station, France. Atmos Chem Phys 14

Vié B, Pinty J-P, Berthet S, Leriche M (2016) LIMA (v1.0): A quasi two-moment microphysical scheme driven by a multimodal population of cloud condensation and ice freezing nuclei. Geoscientific Model Development 9:567–586. doi: 10.5194/gmd-9-567-2016

Villarini G, Mandapaka PV, Krajewski WF, Moore RJ (2008) Rainfall and sampling uncertainties: A rain gauge perspective. Journal of Geophysical Research 113:. doi: 10.1029/2007JD009214

Wall C, Zipser E, Liu C (2013) An Investigation of the Aerosol Indirect Effect on Convective Intensity Using Satellite Observations. J Atmos Sci 71:430–447. doi: 10.1175/JAS-D-13-0158.1

Wang H, Lei H, Yang J (2017) Microphysical processes of a stratiform precipitation event over eastern China: analysis using micro rain radar data. Advances in Atmospheric Sciences 34:1472–1482. doi: 10.1007/s00376-017-7005-6

Warren SG (1984) Optical constants of ice from the ultraviolet to the microwave. Applied Optics 23:1206. doi: 10.1364/AO.23.001206

Zwiebel J (2015) Etude de l'impact orographique sur la structure microphysique horizontale et verticale des précipitations. Thèse de doctorat, Université Blaise Pascal - Clermont-Ferrand II

Detailed microphysics modeling of the intense precipitation episode IOP7a observed during HYMEX experiment: Study of the impact of pollution

ABSTRACT:

The French coastline in the Mediterranean Sea is affected by heavy rainfall episodes especially in autumn. Cévennes – Vivarais, which is part of the Massif Central Mountains, is one of the affected regions. The associated heavy precipitation episodes (HPE), namely "Cévenols", can cause natural disasters with important economic damages and life losses. The prediction of such episodes by Numerical Weather Prediction (NWP) models has been significantly improved; uncertainties remain though, regarding their occurrence and strength. The improvement of microphysical parameterizations in NWP models is one key-component for the reduction of forecast errors. The aim of this study was provide a better understanding of the microphysical processes that govern HPE and their interaction with atmospheric aerosol particles (APs) by exploiting observations from the HYMEX research program.

The present study focused on the HPE from the HYMEX Intense Observation Period (IOP) 7a, whose observations were assessed and compared with modelling results from the bin-resolved microphysics scheme DEtailed SCAvenging Model (DESCAM, Flossmann and Wobrock; 2010) with 3D dynamics. This research model uses a detailed representation of the APs. Observations from ground-based instruments, as well as in-situ measurements were used for the evaluation of the model's performance. The ground-based dataset consists of X-band Radars, Micro-Rain Radars (MRR), disdrometers, but also a rainfall reanalysis by rain gauges and operational radars (Boudevillain et al. 2016). Moreover, hydrometeor probes and the 95GHz cloud radar RASTA provided observations on-board of the French research aircraft Falcon-20.

The role of pollution on the development and evolution of the HPE of IOP7a was investigated, as well. Considering that the highest AP concentrations were observed during IOP7a, the followed strategy was to perform model simulations by using less polluted observed AP spectra with lower total number concentrations. The results showed that the initial AP concentration influences the spatial distribution and quantity of rainfall, as well as the vertical properties of the rain water content and the ice water content of the precipitating cloud system. For the studied cases, with increasing the initial number concentration of APs, the total rain amount was decreased. Finally, the present study revealed a critical role of the model's large-scale configuration necessary to correctly represent the dynamics.

KEYWORDS: Mediterranean, heavy precipitation, detailed numerical modeling, cloud microphysics, aerosol-cloud-precipitation interactions

Modélisation microphysique détaillée de l'épisode de précipitation intense IOP7a observé lors de l'expérience HYMEX : Etude de l'impact de la pollution

RÉSUMÉ :

Le littoral méditerranéen français est fréquemment affecté en automne par des épisodes de forte pluie. La région montagneuse des Cévennes – Vivarais (Massif Central) est une des régions affectées par ces épisodes de précipitations intenses (appelés Cévenols) qui peuvent provoquer des catastrophes naturelles entraînant des dommages économiques importants et des pertes de vies humaines. La prévision de tels épisodes par les modèles numériques de prévision du temps a été considérablement améliorée; cependant, des incertitudes en ce qui concerne leur intensité demeurent. L'amélioration des paramétrisations microphysiques dans ces modèles de prévision est un élément clé pour la réduction des erreurs. Le but de cette étude était de mieux comprendre les processus microphysiques qui régissent les épisodes de fortes précipitations et l'impact des particules d'aérosol atmosphériques sur ces précipitations en exploitant les observations du programme de recherche HYMEX et de la campagne de mesures associée qui s'est déroulée en 2012 dans le Sud de la France.

L'étude s'est portée sur l'épisode de précipitation intense observé le 26 Sept. 2012 lors de la Période d'Observations Intenses (POI) 7a. Les observations disponibles ont été évaluées et comparées aux résultats de simulations effectuées avec le DEtailed SCAvenging Model (DESCAM, Flossmann and Wobrock; 2010) qui est un modèle tridimensionnelle utilisant un schéma bin pour représenter de manière détaillée la microphysique nuageuse ainsi que les interactions entre les particules d'aérosols et les nuages. Les observations utilisées ont été faites à partir d'instruments au sol et des mesures aéroportées in situ et permettent d'évaluer le modèle. Les observations au sol sont issues de radars en bande X, de Micro-Rain Radars (MRR), de disdromètres, mais également d'une réanalyse statistique des mesures de pluie par pluviomètres et radars opérationnels (Boudevillain et al. 2016). Les observations aéroportées in-situ ont été réalisées à l'aide de sondes microphysiques et du radar nuage RASTA embarqués à bord de l'avion de recherche français, le Falcon-20.

Le rôle de la pollution sur le développement et l'évolution de l'épisode de précipitation intense du POI7a a été étudié en modifiant la concentration des particules d'aérosol à l'aide de spectres en aérosols observés lors de la campagne de mesures. Les résultats ont montré que la concentration initiale des particules d'aérosol influence la distribution spatiale et la quantité des précipitations, ainsi que le contenu vertical en eau de pluie et en eau glacée du système nuageux précipitant. Pour le cas étudié, une augmentation de la concentration initiale en nombre de particules d'aérosol diminue la quantité totale de pluie au sol. Enfin, une étude de sensibilité supplémentaire sur le choix du domaine de simulation a permis de montrer le rôle essentiel de la dynamique et de l'humidité des basses couches atmosphériques de grande échelle sur la représentation du système précipitant.

MOTS CLÉS : Méditerranée, précipitation intense, modélisation numérique détaillée, microphysique des nuages, interactions aérosols-nuages-précipitation